MARINE PHYSICAL LABORATORY

SCRIPPS INSTITUTION OF OCEANOGRAPHY

San Diego, California 92152

AD-A220 008

**THE MARINE PHYSICAL LABORATORY
MULTI-DISCIPLINARY OCEAN SCIENCE
& TECHNOLOGY PROGRAM**

DTIC
S ELECTE
APRO 3 1990
B D

*Final Report for Office of Naval Research
Contract N00014-79-C-0472*

MPL-U-27/89

Approved for public release; distribution unlimited.

90 04 02 183

REPORT DOCUMENTATION PAGE	Form Approved OMB No. 0704-0188

1a. REPORT SECURITY CLASSIFICATION UNCLASSIFIED	1b. RESTRICTIVE MARKINGS

2a. SECURITY CLASSIFICATION AUTHORITY	3. DISTRIBUTION/AVAILABILITY OF REPORT
2b. DECLASSIFICATION/DOWNGRADING SCHEDULE	Approved for public release; distribution unlimited.

4. PERFORMING ORGANIZATION REPORT NUMBER(S)	5. MONITORING ORGANIZATION REPORT NUMBER(S)
MPL-U-27/89	

6a. NAME OF PERFORMING ORGANIZATION University of California, San Diego	6b. OFFICE SYMBOL (If applicable) MPL	7a. NAME OF MONITORING ORGANIZATION Office of Naval Research Department of the Navy

6c. ADDRESS (City, State, and ZIP Code) Marine Physical Laboratory Scripps Institution of Oceanography San Diego, California 92152	7b. ADDRESS (City, State, and ZIP Code) 800 North Quincy Street Arlington, VA 22217-5000

8a. NAME OF FUNDING/SPONSORING ORGANIZATION Office of Naval Research	8b. OFFICE SYMBOL (If applicable) ONR	9. PROCUREMENT INSTRUMENT IDENTIFICATION NUMBER N00014-79-C-0472

8c. ADDRESS (City, State, and ZIP Code) 800 North Quincy Street Arlington, VA 22217-5000	10. SOURCE OF FUNDING NUMBERS

PROGRAM ELEMENT NO.	PROJECT NO.	TASK NO.	WORK UNIT ACCESSION NO.

11. TITLE (Include Security Classification)
The Marine Physical Laboratory Multi-Disciplinary Ocean Science & Technology Program

12. PERSONAL AUTHOR(S)
Kenneth M. Watson and Victor C. Anderson (Principal Investigators)

13a. TYPE OF REPORT Final Report	13b. TIME COVERED FROM _____ TO _____	14. DATE OF REPORT (Year, Month, Day) October 1989	15. PAGE COUNT 126

16. SUPPLEMENTARY NOTATION

17. COSATI CODES			18. SUBJECT TERMS (Continue on reverse if necessary and identify by block number)
FIELD	GROUP	SUB-GROUP	ocean technology, swath bathymetry, internal waves; ambient noise; sound absorption

19. ABSTRACT (Continue on reverse if necessary and identify by block number)

This report contains summaries of the research performed at the Marine Physical Laboratory under ONR Contract N00014-79-C-0472 from FY 1980 through 1988. Brief descriptions of the research and bibliographies of the publications resulting therefrom are included. In pursuing basic research we must meet the high standards of the academic arena and at the same time satisfy the overall objectives inherent in our Navy mission statement.

Under our mission statement, we have a broad ranging threefold charter: "*to investigate and apply knowledge about the ocean, its boundaries and their surrounding media to the solution of the Navy's problems in anti-submarine and pro-submarine warfare; to provide research training of students in areas of oceanography and ocean technology which have application to Navy requirements; to maintain certain special ocean engineering, research and development capabilities which are essential to the Navy.*"

The general areas of our research include: Ocean Environmental Acoustics, Marine Physics, Marine Geophysics, Signal Processing, Ocean Technology, Platform Development and Support, and Technical Assistance and Technology Transfer.

20. DISTRIBUTION/AVAILABILITY OF ABSTRACT ☐ UNCLASSIFIED/UNLIMITED ☒ SAME AS RPT. ☐ DTIC USERS	21. ABSTRACT SECURITY CLASSIFICATION UNCLASSIFIED	
22a. NAME OF RESPONSIBLE INDIVIDUAL Kenneth M. Watson	22b. TELEPHONE (Include Area Code) (619) 534-1803	22c. OFFICE SYMBOL MPL

DD Form 1473, JUN 86   *Previous editions are obsolete*

In pursuing basic research related to understanding oceanic processes and interactions, especially as related to sound propagation, we gain a more definitive measure of the limitations Mother Nature places on what we can do with of our knowledge. The Navy is interested in exploring and exploiting these limitations with respect to improving their capabilities with respect to the feasibility and cost of new equipments as well as making better and more effective use of current assets. In this way, Navy needs and Navy support of basic research within the academic community provide a means for a mutually productive and satisfying interaction of the Navy with academia. In the following, brief descriptions are given of some of the ways in which academic basic research projects (see Bibliography) under this contract provide benefits to the Navy.

The experimental (Pinkel et al.) and theoretical (Watson, Abarbanel) research on internal waves, non-linear processes and upper ocean dynamics, important areas of physical oceanography, couple strongly into non-acoustic ASW in providing a base for understanding natural versus man-made phenomena vis-a-vis wake detection. Pinkel's Doppler sonars also provide a means by which we can investigate surface acoustic reverberation processes, an area of increasing importance with respect to low frequency active (LFA) sonars and lower frequency ship sonars.
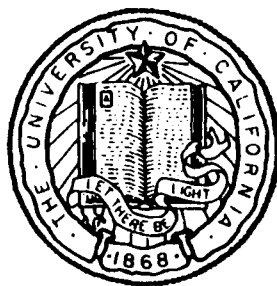
Swath bathymetric research (deMoustier et al. and Tyce) ties in with bottom acoustic reverberation in that efforts to provide quantitative scattering estimates of sea bottom roughness as well a topography are needed to assess background contamination in LFA as well in new active ship sonars. Understanding the morphology and general characteristics of various bottom regions (Lonsdale, Spiess, et al.) provides a basis for estimating reverberation of regions for which quantitive Sea Beam swath are unavailable.

Effects of sub-bottom topography and sediments on acoustic propagation and signal processing (Hodgkiss et al.) are important for the exploitation of all acoustic multipaths (coherent recombination) at lower frequencies in improving signal to noise performance for potential detection systems. Watson's work on detection and estimation ties in with these areas. Brienzo's work on coherent recombination included results for bottom attenuation coefficients for sediments as a function of frequency.

Anderson's investigation of ambient noise with the ADA array yielded characteristics of surface noise relevant to the operation of DIMUS and other passive sonars. Surface noise investigations and biological noise are relevant to the general problem of improving signal to noise and detection capabilities.

Fisher and Hsu's measurements of sound absorption in seawater and magnesium sulfate solutions provides data for the design of sonars, particularly at higher frequencies and deep depths common to side-looking sonars.

Finally, support for MPL research facilities, FLIP and the Tower, made it possible to perform some of the research described above.

THE MARINE PHYSICAL LABORATORY
MULTI-DISCIPLINARY OCEAN SCIENCE
& TECHNOLOGY PROGRAM

*Final Report for Office of Naval Research
Contract N00014-79-C-0472*

MPL-U-27/89

Approved for public release; distribution unlimited.

TABLE OF CONTENTS

Project *(Principal Investigator(s))*

Marine Physical Laboratory

THE MARINE PHYSICAL LABORATORY MULTI-DISCIPLINARY OCEAN SCIENCE & TECHNOLOGY PROGRAM

Final Report for Office of Naval Research
Contract N00014-79-C-0472

INTRODUCTION

This report contains summaries of the research performed at the Marine Physical Laboratory under ONR Contract N00014-79-C-0472 from FY 1980 through 1988. Brief descriptions of the research and bibliographies of the publications resulting therefrom are included. In pursuing basic research we must meet the high standards of the academic arena and at the same time satisfy the overall objectives inherent in our Navy mission statement.

Under our mission statement, we have a broad ranging threefold charter:

> *"to investigate and apply knowledge about the ocean, its boundaries and their surrounding media to the solution of the Navy's problems in anti-submarine and pro-submarine warfare; to provide research training of students in areas of oceanography and ocean technology which have application to Navy requirements; to maintain certain special ocean engineering, research and development capabilities which are essential to the Navy."*

The general areas of our research include: Ocean Environmental Acoustics, Marine Physics, Marine Geophysics, Signal Processing, Ocean Technology, Platform Development and Support, and Technical Assistance and Technology Transfer.

In pursuing basic research related to understanding oceanic processes and interactions, especially as related to sound propagation, we gain a more definitive measure of the limitations Mother Nature places on what we can do with of our knowledge. The Navy is interested in exploring and exploiting these limitations with respect to improving their capabilities with respect to the feasibility and cost of new equipments as well as making better and more effective use of current assets. In this way, Navy needs and Navy support of basic research within the academic community provide a means for a mutually productive and satisfying interaction of the Navy with

1

academia. In the following, brief descriptions are given of some of the ways in which academic basic research projects (see Bibliography) under this contract provide benefits to the Navy.

The experimental (Pinkel et al.) and theoretical (Watson, Abarbanel) research on internal waves, non-linear processes and upper ocean dynamics, important areas of physical oceanography, couple strongly into non-acoustic ASW in providing a base for understanding natural versus man-made phenomena vis-a-vis wake detection. Pinkel's Doppler sonars also provide a means by which we can investigate surface acoustic reverberation processes, an area of increasing importance with respect to low frequency active (LFA) sonars and lower frequency ship sonars.

Swath bathymetric research (deMoustier et al. and Tyce) ties in with bottom acoustic reverberation in that efforts to provide quantitative scattering estimates of sea bottom roughness as well a topography are needed to assess background contamination in LFA as well in new active ship sonars. Understanding the morphology and general characteristics of various bottom regions (Lonsdale, Spiess, et al.) provides a basis for estimating reverberation of regions for which quantitive Sea Beam swath are unavailable.

Effects of sub-bottom topography and sediments on acoustic propagation and signal processing (Hodgkiss et al.) are important for the exploitation of all acoustic multipaths (coherent recombination) at lower frequencies in improving signal to noise performance for potential detection systems. Watson's work on detection and estimation ties in with these areas. Brienzo's work on coherent recombination included results for bottom attenuation coefficients for sediments as a function of frequency.

Anderson's investigation of ambient noise with the ADA array yielded characteristics of surface noise relevant to the operation of DIMUS and other passive sonars. Surface noise investigations and biological noise are relevant to the general problem of improving signal to noise and detection capabilities.

Fisher and Hsu's measurements of sound absorption in seawater and magnesium sulfate solutions provides data for the design of sonars, particularly at higher frequencies and deep depths common to side-looking sonars.

Finally, support for MPL research facilities, FLIP and the Tower, made it possible to perform some of the research described above.

PROJECT   Upper Ocean Physics

PROJECT LEADER: Robert Pinkel
TELEPHONE NUMBER: (619) 534-2056

INTRODUCTION

The Upper Ocean Physics Group at the Marine Physical Laboratory has been engaged in a continuing program to observe and understand the physics of the upper ocean. Significant achievement was also made in the development of Doppler sonar technology. Initially observations of the ocean were made by repeatedly profiling thermometers which were suspended from booms mounted on the Research Platform FLIP. Subsequently, Doppler scattering was developed, to enable measurements to be made at greater horizontal distances from FLIP than could be achieved with booms. In 1975 preliminary measurements were made out to 400 m range, using a borrowed sonar. By 1977 the maximum useful range was doubled to 800 m. Two and a half weeks of continuous open ocean measurements were obtained in January 1977. In 1979, using a new Doppler scattering sonar, developed under ONR Code 480 sponsorship, measurements to a range of 1600 m were achieved. This new sonar, coupled with suitable signal processing equipment was complementary to a wide range of oceanographic studies and gave a multi-dimensional look at the motions in the upper part of the sea.

SUMMARY

Initially, ONR funds were directed toward the construction of a special purpose Doppler sonar system, for use from the Research Platform FLIP. This system was to be the first oceanographic research system not derived from a converted ships log or echo sounder. It operated at a peak power of 32 kw, transmitting simultaneously on four beams. In May 1980, the system was used at sea for the first time. An excellent data set was obtained resulting in a string of publications on the form of the internal wave spectrum.

Subsequently the system geometry was altered. A four beam downward looking array was configured, for improved resolution of the internal wavefield. Two additional narrow beams were directed horizontally in the mixed layer, for observing the near surface velocity field. Refinements in the system electronics increased the maximum range from 800 m to 1500 m between 1980 and the 1983 Mixed Layer Dynamics Experiment (MILDEX) MILDEX was conducted in October and November 1983, in conjunction with investigators from Oregon State University, Woods Hole, and the Naval Postgraduate School. The MILDEX internal wavefield was found to be similar to that seen in 1980, with the exception of significantly reduced near inertial currents (Appendix A). Mixed layer measurements revealed a highly

3

developed structure of Langmuir cells. These were seen in both the Doppler sonars and in a vertical array of current meters operated by Dr. Robert Weller of Woods Hole. The diurnal heating of the top several meters of the sea was well observed by the various FLIP based sensors. These measurements lead to the first accurate model of the diurnal effect, developed by Price, Weller and Pinkel (1986)[20]. The model has proved useful in interpretation remote sensing data, particularly sea surface temperature. Surface temperature can differ from deeper mixed layer temperature by several degrees centigrade during periods of sun and calm. To estimate the mixed layer temperature remotely, one must properly account for the diurnal effect.

A significant finding in MILDEX was that acoustic scattering from the underside of the sea surface resulted in water velocity estimates of a quality comparable to the deep volume scattering measurements. Near surface bubbles, rather than zooplankton, are the acoustic scatterers. This discovery lead to the development of Doppler sonar systems for the study of surface waves and currents. This measurement breakthrough is still being actively explored.

Following the success of MILDEX, preparations were initiated on a pair of subsequent experiments. In 1985, a small commercial sonar was deployed in the Beaufort Sea, in conjunction with the Arctic Internal Waves Experiment, AIWEX. While the deployment was executed flawlessly, the sonar performed somewhat mysteriously. Preliminary analysis revealed wave motions of great beauty, with intermittent depth-time zones of poor data. The editing of this data is now being done and has proved to be a challenge.

In 1986, the FLIP based system was further modified. The two horizontal sonar beams were each split into an over-under pair of beams, separated by 3° in the vertical. The lower beams of each pair were directed horizontally and the upper beams grazed the underside of the sea surface. This modified array was fielded in November 1986 in the PATCHEX Experiment. The goal of PATCHEX was to detect and monitor patches of small scale mixing in the thermocline, and relay the patch parameters to larger scale features of the flow, such as the background shear. The down-looking sonars on FLIP were to measure the shear, while simultaneous microstructure measurements were performed by Dr. Mike Gregg of the University of Washington.

For most of the duration of the PATCHEX observations the weather was calm. The large shears in the thermocline occurred at depths greater than 200 m. These were associated with a downward propogating near inertial wave packet generated by a wind event which occurred at the beginning of the experiment. If persistent microstructure patches were associated with these shears, they were beyond the operating depth of the AMP profiler being used to obtain the microstructure data.

Nevertheless, a great deal was learned from the FLIP sensors about shear and strain in the thermocline. A variety of mixed layer phenomena were observed on the horizontal and surface scattering systems, as well. These data are now being prepared for publication.

----

1.   J. A. Smith and R. Pinkel, "Observations of waves and Langmuir circulation with Doppler sonars," in *Dynamics of the Oceanic Surface Mixed Layer*, edited by P. Muller and D. Henderson (Honolulu, Hawaii, 1977). Proceedings of the 'Aha Huliko'a, Hawaii Winter Workshop on Internal Waves and Small Scale Turbulence.

2.   R. Pinkel, "Acoustic Doppler techniques," in *Air-Sea Interaction*, edited by F. Dobson, L. Hasse, R. Davis (Plenum Publ. Corp., 1980), pp. 171-199.

3.   R. Pinkel, "Observations of the near-surface internal wavefield," J. Phys. Oceanogr. **11**, 1248-1257 (1981).

4.   R. Pinkel, "On the use of Doppler sonar for internal wave measurements," Deep-Sea Res. **28A**, 269-289 (1981).

5.   R. Pinkel, "The wavenumber frequency spectrum of the internal wavefield," 2nd Annual Aha Huliko's Hawaiian Winter Workshop on Internal Waves and Small Scale Turbulence, 113-127 (1984).

6.   R. Pinkel, "Doppler sonar observations of internal waves: the wavenumber frequency spectrum," J. Phys. Oceanogr. **14**, 1249-1270 (1984).

7.   R. Pinkel, A. J. Plueddemann, and R. G. Williams, "Internal wave observations from FLIP in MILDEX," EOS, Am. Geophys. Un. **66**, 1281 (1985).

8.   J. Smith, R. Pinkel, and R. Weller, "Observations of small scale structure in the surface layer," EOS, Am. Geophys. Un. **66**, 1281 (1985). Presentation given at Ocean Science Meeting, New Orleans, 1986 January.

9.   R. Pinkel, "A wavenumber-frequency spectrum of upper ocean shear," J. Phys. Oceanogr. **15**, 1453-1469 (1985).

10.   S. Beck, R. Pinkel, and J. Morison, "Doppler acoustic velocity profiling in the Arctic," EOS, Trans. Amer. Geophys. Union **67** (1986).

11.   R. Pinkel, A. Plueddemann, and R. Williams, "Doppler sonar observation from FLIP in MILDEX," EOS, Trans. Amer. Geophys. Union **67**, 1060 (1986).

12.   R. Pinkel and J. A. Smith, "Surface wave detection by Doppler sonar," EOS, Trans. Amer. Geophys. Union **67**, 1060 (1986).

13.   J. Sherman and R. Pinkel, "Investigation of fine scale shear with a coherent Doppler sonar," EOS, Trans. Amer. Geophys. Union **67**, 1060 (1986).

14.   R. Pinkel, S. Beck, and J. Morison, "Doppler acoustic velocity profiling in the Arctic," Proceedings IEEE Third Working Conference on Current Measurements **CH2305-1**, 163-168 (1986).

15.   J. F. Price, R. A. Weller, and R. Pinkel, "Diurnal cycling: Observations and models of the upper ocean response to diurnal heating, cooling, and wind mixing," J. Geophys. Res. **91**, 8411-8427 (1986).

16.   J. A. Smith and R. Pinkel, "Open ocean surface wave measurement using Doppler sonar," J. Geophys. Res. **92**, 12,967-12,973 (1987).

17.   Jerome Smith, Robert Pinkel, and Robert Weller, "Velocity structure in the mixed layer during MILDEX," J. Phys. Oceanogr. **17**, 425-439 (1987).

18.   R. Pinkel, A. Plueddemann, and R. Williams, "Internal wave observations from FLIP in MILDEX," J. Phys. Oceanogr. **17**, 1737-1757 (1988).

19. A. J. Plueddemann and R. Pinkel, "Biasing of the covariance-based spectral mean estimator in the presence of correlated noise," J. Atmos. Oceanic Technol. (submitted - revision).

20. J. A. Smith and R. Pinkel, "Observations of waves and Langmuir circulation with Doppler sonars," Proceedings of the 'Aha Huliko'a, Hawaii Winter Workshop on Internal Waves and Small Scale Turbulence (submitted).

| PROJECT | The Energy Balance of the Ocean Internal Wavefield |

PROJECT LEADER: Kenneth M. Watson
TELEPHONE NUMBER: (619) 534-1803

INTRODUCTION

This project focussed on the role of mesoscale currents in the development of the internal wave spectrum. The work represented an extension of previous studies of energy transport and energy sources and sinks within the ocean internal wavefields.

The research had two thrusts. The first was directed towards the study of internal wave interactions with mesoscale flow and the resulting exchange of energy. The second portion of the research will apply available techniques in transport theory to make a global investigation of:

1. Net energy transport in wavenumber-frequency space throughout the internal wave spectrum;

2. Identification of energy sources and sinks required to maintain stationarity;

3. Transport of energy in physical space-particularly in the vertical direction.

SUMMARY

The first investigation, completed during the contract year, was published in Watson[1], which is attached in Appendix A. Here an internal "test wave" was set in interaction with a mesoscale field and the relaxation rate evaluated.

A more elaborate analysis aimed at calculating the generation of internal wave energy by mesoscale flows was begun. This work was completed under the Internal Wave Transport Processes project.

Watson, K. M. Relaxation Processes for Internal Waves in Mesoscale Flow. Proc. Natl. Acad. Sci. USA, 80, 1144-1146 (1983).

Marine Physical Laboratory

<table>
<tr><td align="right">**PROJECT**</td><td>Project A: III.A. Generation of Internal Waves
by Surface Waves</td></tr>
</table>

<table>
<tr><td align="right">**PROJECT LEADER:**</td><td>Kenneth M. Watson</td></tr>
<tr><td align="right">**TELEPHONE NUMBER:**</td><td>(619) 534-1803</td></tr>
</table>

INTRODUCTION

SUMMARY

Phase I of this involved the so-called "modulation mechanism" for surface wave generation of internal waves. A report of this work is referenced in Watson[1]. This work was interupted due to shut-down of the computer being used.

It has been continued under the current ONR Contract N00014-87-K-0010 and is nearly complete. The conclusion are that for winds under 15 m/s the internal wave field is rather strongly damped by surface wave. For higher winds this effect is reached and strong growth of the internal wave field is predicted.

Incidental to this project, an investigation of the damping of surface wave "patterns" [such as the Kelvin wake of a ship] was conducted. This work is described in Watson[2].

[1] Watson, K. M. The Coupling of Surface and Internal Waves: Revisited. J. Phys. Oceanogr. (submitted).

[2] Watson, K. M. Persistence of a Pattern of Surface Gravity Waves. J. Geophys. Res., 91, 2607-2615 (1986) (Appendix A).

Marine Physical Laboratory

PROJECT   Project A:II.B. Internal Wave Transport Processes

PROJECT LEADER: Kenneth M. Watson
TELEPHONE NUMBER: (619) 534-1803

INTRODUCTION

This program addressed some questions to the internal wave transport model. First, there was a needed understanding of the effects of spatial and temporal variability int he mesoscale field. What is the transient response of the IW field? How does it propagate horizontally and vertically in the presence of varying mesoscale activity? What is the relative importance of wave propagation and diffusion in spatial transport of IW's.

SUMMARY

This investigation of internal wave generation by mesoscale flows led to the conclusion that much of the internal wave field arises from this mechanism. The work is described in Watson[1].

[1] Watson, K. M. Interaction between internal waves and mesoscale flow. J. Phys. Oceanogr., 15, 1296-1311 (1985).

[2] Watson, K. M. Interactions of internal waves of near inertial frequencies. Presented at the Aha Huliko's Winter Workshop, Honolulu, Hawaii (1984).

[3] Watson, K. M. A model for nonlinear wave interactions. Pure Appl. Geophys., 121(3), 401-415 (1983).

PROJECT   Project A: IV. Swallow Float/Lagrangian
               Drifter Experiment

PROJECT LEADER: Kenneth M. Watson
TELEPHONE NUMBER: (619) 534-1803

INTRODUCTION

The MPL Swallow float array was developed to measure ambient ocean acoustic noise in the 1-10 Hz range. An acoustic transponder system provides a continuous record of the position (to within one to a few meters, depending on rate of recording). A study was conducted of the utility of this array for observations of internal waves and so-called "vortical modes". During acoustic measurements with the MPL Swallow float array research objectives would be to: (1) determine the scale of vertical vorticity and correlate this with shear, (2) obtain new information concerning the internal wave spectrum, and (3) possibly determine new information relating to the linearity and Gaussian nataure of the internal wave field.

SUMMARY

Several calculations were made relating to the ballasting of the MPL Swallow float array. Estimates of the dispersion of the array due to internal wave and mesoscale flows were also made. These were made in collaboration with William Hodgkiss. This wcrk was not published, but was used in plans for the deployment of the array.

PROJECT Large Scale Ocean Circulation and the Interaction
of Internal Waves with Mesoscale Circulation

PROJECT LEADER: Henry D. I. Abarbanel
TELEPHONE NUMBER: (619) 534-5590

INTRODUCTION

The major effort of research was directed toward the study of **sources** of
energy for the internal wave field and a description of the **transport** of that energy
(or action) through the field. Through this study a convincing model of the internal
wave field could be established and explored on its own as a nonlinear dynamical
system of some oceanograhic importance.

SUMMARY

The results of the last stage of this work are included in Appendix A of this
report. Several earlier reports have been filed with the program managers.

----

1. H. D. I. Abarbanel, "Stability of inviscid stratified flows under nonlinear perturbations,"
    Proc. of the Hawiian Winter Aha Huliko'a Workshop, 263-276 (1984).

2. H. D. I. Abarbanel, D. D. Holm, J. E. Mardsen, and T. Ratiu, "Richardson number criterion
    for the nonlinear stability of stratified flow," Phys. Rev. Lett. **52**, 2352-2355 (1984).

3. H. D. I. Abarbanel, "Hamiltonian description of nearly geostropic flow," Geophys.
    Astrophys. Fluid Dyn. **33**, 145-171 (1985).

4. H.D.I. Abarbanel, S. Buchsbaum, and J. Keeler, "A low dimensional interated map with an
    apparent continuum of attractors," in *Perspectives in Nonlinear Dynamics*, edited by M.
    F. Shlesinger, R. Cawley, A. W. Saenz, and W. Zachary (World Scientific Publishing Co. Pte
    Ltd, 1986), pp. 167-208.

5. H.D.I. Abarbanel, "Chaos across disciplines," Proc. Navy Dynamics Institute Conf. on
    Perspectives on Nonlinear Dynamics (1986).

6. H. D. I. Abarbanel, "Nonlinear stability of inviscid fluid equilibria," Fourth Symposium of
    Energy Engineering Sciences (1986).

7. H.D.I. Abarbanel, S. Buchsbaum, J. Keeler, and Y-M Yang, "Transient dissipative behavior in Hamiltonian dynamics," Physica D. (in prep).

8. H.D.I. Abarbanel and S. Rouhi, "Phase space density representation of inviscid fluid dynamics," J. Fluid Mech. (in prep).

9. H.D.I. Abarbanel and B. Long, "Nonlinear stability of cyclostrophic flows," J. Phys. Oceanogr. (in prep).

10. H.D.I. Abarbanel and E. A. Frieman, "Renormalized theory of homogenous turbulence," Phys. Fl. (in prep).

11. Henry D.I. Abarbanel and Darryl D. Holm, "Nonlinear stability analysis of inviscid flows in three dimensions: Incompressible fluids and barotropic fluids fluids," Physics of Fluids (in press).

12. H.D.I. Abarbanel and D. D. Holm, "Conservation laws and nonlinear stability of three dimensional fluids," J. Fluid Mech. (submitted).

PROJECT   Sea Beam Acoustics - Backscatter Angular Dependence Function, Near Real Time Processing and Displays

PROJECT LEADER: Christian de Moustier
TELEPHONE NUMBER: (619) 534-6322

INTRODUCTION

The goals of this research were to determine how one could use the acoustic returns received by a multibeam echo-sounder, such as the Sea Beam system manufactured by the General Instrument Corporation, to characterize seafloor terrains by extracting more information from the returns than simply the time of arrival of the bottom echo.

A system was developed to record digitally the detected echo envelopes of Sea Beam's 16 preformed beams over a variety of seafloor environments, and to process these data to determine whether the acoustics held sufficient information to differentiate between bottom types.

The results of this work were written into a PhD thesis[1].

SUMMARY OF PROJECT RESULTS

The operational characteristics of the Sea Beam system were reviewed and the recorded acoustic data were used to take an in-depth look at the system's performance as a mapping tool[2]. Although the system works well under most circumstances, several bathymetric artifacts were observed in the contoured outputs. The artifacts were analyzed and their causes were identified by examining the character of the bottom echoes received and processed by the system. The analysis led to recommendations for improving bathymetric data quality.

Amplitude variations of the echo signals received by Sea Beam were used to produce a sidescan image of the seafloor surveyed. This new application of the Sea Beam system enhanced its usefulness during geological investigations of the seafloor, by complementing the standard bathymetric contouring with a qualitative measure of bottom acoustic backscatter which is related to the texture of the seafloor[3] (Appendix A).

[1] de Moustier, Christian. Deep Seafloor Acoustic Backscattering Measurements Using SEABEAM. SIO Reference 85-33, Scripps Institution of Oceanography, San Diego, California (1985).
[2] de Moustier, Christian and Kleinrock, Martin C. Bathymetric Artifacts in Sea Beam Data: How to Recognize Them and What Causes Them. J. Geophys. Res., 91, B3, pp. 3407-3424 (1986).
[3] de Moustier, C. Approaches to Acoustic Backscattering Measurements from the Deep Seafloor. Trans. Am. Soc. Mechanical Engineers, OED-11, pp. 137-143 (1986); also reprinted in Trans. of the ASME, J. Energy Resources Tech., Vol. 110,pp.77-84, (1988).

Marine Physical Laboratory

An attempt was made at relating the character of the acoustic backscatter to the geological processes that cause them[4]. The variations of the peak amplitude of Sea Beam's near-specular return along the ship's track were compared with the density of the coverage of manganese nodules at at a mining site in the Northeastern Tropical Pacific. A 98% qualitative agreement was found between manganese nodule coverage inferences obtained with Sea Beam acoustic data and the bottom photographs taken by the Deep Tow instrument package in the same area.

Expansion of the analysis of Sea Beam acoustic data to non-specular beams was investigated. Measurements from three geologically different areas were compared.[5] Acoustic backscattering boundaries were mapped both along and across the ship's track by following trend changes in the total energy of the acoustic returns over many transmission cycles. A partial angular-dependence function of backscattering shows marked differences in the overall acoustic energy level recorded at each site. Application of Rician statistics to the distribution of peak amplitude in the near-specular direction gives clues to the roughness character of each area, and provides a means to differentiate them.

[4] de Moustier, C. Inference of Manganese Nodule Coverage from Sea Beam Acoustic Backscattering Data. Geophysics, 50, 6, pp. 989-1001 (1985).
[5] de Moustier, Christian. Beyond Bathymetry: Mapping Acoustic Backscattering from the Deep Seafloor with Sea Beam. J. Acoust. Soc. Am., 79(2), pp. 316-331 (1986).

PROJECT   Sea Beam Acoustics

PROJECT LEADERS: Christian de Moustier, Dimitri Alexandrou, V.C. Anderson
TELEPHONE NUMBER: (619) 534-6322

INTRODUCTION

Based on earlier work with acoustic data recorded from a Sea Beam multibeam echo-sounder, it was determined that sidelobe interference inherent to the multibeam geometry hindered one's ability to process echoes received on individual beams if only the envelope of the return were available. Computer simulations of the echoes showed that provided the full wave form was available, the sidelobe interference could be removed by filtering using adaptive noise cancellation techniques. The ability to obtain acoustic returns free of sidelobe interference means that one is able to derive an angular dependence function of seafloor acoustic backscatter. Such a function is expected to vary with seafloor types and could therefore serve as one element towards remote classification of seafloors.

The goal of the work were to design and build a data acquisition system to record both the amplitude and the phase of the Sea Beam system's 16 preformed beams, and to implement the sidelobe interference filtering scheme tested through computer simulations. In addition, real-time displays of the acoustic data were implemented following ideas derived from earlier work[1].

SUMMARY OF PROJECT RESULTS

To preserve the amplitude and the phase of the beamformed echo signals received by the Sea Beam system, a complex acoustic data acquisition system was designed and built. The signals at the output of the beamformer are base-banded, quadrature-sampled, digitized and recorded on magnetic tape for subsequent processing[2].

This system was used to record data on three different vessels equipped with a Sea Beam system: the R.V.'s *Thomas Washington, Atlantis II* and *Jean Charcot.*

Adaptive noise cancelling applied to the recorded complex acoustic data provided satisfactory sidelobe interference cancellation with no noticeable degradation of the true bottom returns[3].

A stand alone interface between the Sea Beam system and a 4-bit grey scale linescan recorder was built to allow real-time output of sidescan images derived

[1] de Moustier, Christian. Deep Seafloor Acoustic Backscattering Measurements Using Sea Beam. SIO Reference 85-33, Scripps Institution of Oceanography, San Diego, California (1985).
[2] de Moustier, C. and Pavlicek, F. V. A Fully Transportable Sea Beam Complex Acoustic Data Acquistion System. Offshore Tech. Conf. Proc., Houston, TX, OTC #5514, pp.269-274, (1987).
[3] Alexandrou, D. and de Moustier, C. Adaptive Noise Cancelling Applied to Sea Beam Sidelbe Interference Rejection. IEEE J. Oceanic Eng., Vol. 13, No. 2, pp.70-76, (1988).

form the Sea Beam acoustic data[4]. Such displays provide important textural information about the seafloor surveyed and complement the standard contoured bathymetric output of the Sea Beam system to help in geomorphological interpretations of the terrain.

---

[4] de Moustier, C. and Pavlicek, V. On-line Sea Beam acoustic imaging. Proc. MTS/IEEE Oceans'87. pp. 1197-1201 (1987).

PROJECT   Seabeam Research

PROJECT LEADER: Robert C. Tyce

The principal results from the research funded under this contract has been the improvements in hardware and software related to the Sea beam system on the R.V. *Thomas Washington.* Work lead by Dr. Tyce at the Marine Physical Laboratory and by J. L. Abbott at the Shipboard Computer Group at Scripps was devoted to organizing and presenting the high resolution bathymetric data in a coherent mutually consistent format. This included the development of software to manipulate swath data and navigation data to display bathymetry in geographical coordinates on a 32" wide four pen plotter.

The software developed under this contract and in conjunction with the Scripps Shipboard Computer Group is the core of software for processing Sea Beam bathymetric data throughout the United States. This represents a very valuable and currently useful benefit of the research performed under this contract. Since 1984, Sea Beam software development at Scripps has been carried out mostly by members of the Shipboard Computer Group with institutional funds. Copies of the current version of this software may be obtained at no charge, except shipping and handling, from Scripps through Dr. Christian de Moustier, Scientific Advisor to the Shipboard Computer Group.

Dr. Christian de Moustier's PhD thesis research was funded under this project and a brief summary of his contributions are delineated below.

PROJECT   *Alvin* Study of Young and Cratered
Seamounts on the East Pacific Rise

PROJECT LEADER: Peter F. Lonsdale
TELEPHONE NUMBER: (619) 534-2855

INTRODUCTION

Two young seamounts near the crest of the East Pacific Rise received intensive volcanologic study. The principal tool in the field work, following up deep two and Sea Beam surveys paid for by other projects, will be the submersible *Alvin*. Studies of tectonic, volanic and hydrothermal phenomena at mid-ocean spreading centers have been among the most effective geological uses of research submersibles, fully exploiting their capability for close-up observation and directional sampling.

SUMMARY

Alteration of ship schedules because of engineering problems forced reallocation of all dives to the 21°N area of the East Pacific Rise, omitting the proposed 9°N dive sites. Ten dives were made for geologic sampling and observation on three volcanoes which had been mapped with the Sea Beam echosounder. These dives were fully successful in their objective of geologic mapping of three young cratered seamounts near the rise crest. The rock types encountered (including large amounts of fragmented rocks) provided new insight on submarine eruption mechanisms, and the petrology of the lavas clarified the chemistry and supply pathways of molten mantle material near the East Pacific Rise crest. In addition, the dives discovered and sampled an active oxide-precipitating hydrothermal system (now known to be common on off-axis volcanoes, but this was the first examined in detail), and a large inactive sulfide-depositing hydrothermal system, which made an instructive comparison to the known rise-axis hydrothermal sites (See Appendix A).

---

[1] Lonsdale, P., Batiza, R. and Simkin, T. Metallogenesis at seamounts on the East Pacific Rise. Marine Techn. Soc. J., V. 16, pp. 54-61, 1982.

[2] Batiza, R., Fornari, D., Vanki, D., and Lonsdale, P. Craters, calderas and hydroclastites on young Pacific seamounts. J. Geophys. Res., V. 89, pp. 8371-8390, 1984.

[3] Alt, J., Lonsdale, P., Haymon, R., and Muehlenbachs, K. Hydrothermal sulfide and oxide deposites on seamounts near 21°N, East Pacific Rise. Gerol. Soc. Am. Bull., V. 98, pp. 157-168, 1987.

[4] Allan, J., Batiza, R., and Lonsdale, P. Petrology and chemistry of lavas from seamounts flanking the East Pacific Rise axis, 21°N: Implications concerning the mantle source composition for both seamount and adjacent EPR lavas. AGU Geophysical Monography, 43, pp. 255-282, 1987.

Marine Physical Laboratory

SUPPORT **REQUESTED FOR:**	Origin and Evolution of Seamounts, and Young and Cratered Seamounts

PROJECT LEADER:	Peter F. Lonsdale and F. N. Spiess
TELEPHONE NUMBER:	(619) 534-2855 / (619) 534-1621

INTRODUCTION

Several submerged volcanoes in the Baja California seamount province, west of San Diego, were examined using surface-ship surveying (Seabeam bathymetry, magnetics, seismic profiling and gravity) and Deep Tow. The data was processed and interpreted in preparation for submersible diving programs *Alvin* and Turtle.

SUMMARY

Several volcanoes in a chain of major seamounts west of California were surveyed. The chain was shown to be the result of hotspot activity 20-5 million years ago, but it has numerous unusual features. These include a chemical bimodality in the eruption products, both alkali basalts and tholeiites; episodes of superficial, small scale volcanisms long after the main shield-building stage; and the abaundance of ultramafic xenoliths (fragments of the underlying mantle) included in some lavas.

[1] Gee, J., Tauxe, L., Hildebrand, J., Staudigel, H., and Lonsdale, P. Nonuniform magnetization of Jasper Seamount. J. Geophys. Res., V. 93, pp. 12159-12175, 1988.

[2] Lonsdale, P. Structural patterns of the Pacific floor offshore of peninsular California. Am. Assn. Petroleum Geol. Memoir 47, in press, 1989.

Marine Physical Laboratory

SUPPORT REQUESTED FOR:	Submersible Studies in Mexican Waters

PROJECT LEADER:	Peter F. Lonsdale
TELEPHONE NUMBER:	(619) 534-2855

SUMMARY

Technical problems with the U.S. Navy's submersibles *Turtle* and *Seacliff*, and their support ship prevented execution of the proposed field program. By agreement with the ONR program managers the work plan was rearranged and the funding reallocated to prepare for a series of Turtle dives in Fieberling Guyot, a large seamount 500 miles west of San Diego. These dives are scheduled to take place in October, 1989.

PROJECT   Studies of Bedforms and the
Benthic Boundary Layer

PROJECT LEADER: Fred N. Spiess and Peter Lonsdale
TELEPHONE NUMBER: (619) 534-1621 / (619) 534-2855

INTRODUCTION

Support was provided to study the various aspects of the fine scale nature of the ocean floor using the Deep Tow system. This consisted primarily of at-sea expeditions in support of the High Energy Benthic Boundary Layer Experiment (HEBBLE) in the Atlantic and studies of the origin and structure of seamounts in the Pacific.

SUMMARY

Within this contract the principal addition to the measurement capabilities of the Deep Tow system was an optical transmissometer, used to map the structure of dense near-bottom turbid layers intermittently present at 5,000 m depth in the HEBBLE site area. Both the HEBBLE and seamount work utilized nearly all of the full range of existing system capabilities - precision echo sounder, 4-6 kHz subbottom sounder, side-looking sonar, CTD, transmissometer, magnetometer, cameras and transponder navigation.

The group was involved in both data collection and interpretation by P. Lonsdale and F. Spiess. Much of the HEBBLE data output was reported directly to the HEBBLE planning committees, in which Lonsdale was a participant.

PROJECT   Coherent Recombination of Sediment Borne
and Water Path Acoustic Signals

Coherence and Attenuation Data Analysis

PROJECT LEADER: William S. Hodgkiss
TELEPHONE NUMBER: (619) 534-1798

INTRODUCTION

In April 1981, the Marine Physical Laboratory (MPL) conducted an experiment investigating acoustic signal propagation in thick sediments. The experiment involved the deployment of a 20-element array from FLIP in an area of thick sediments (2.5 km) on the Monterey Fan. The hydrophone array which had equal sensor spacing and a total aperture of 500 m was placed at mid-depth in the 3 km deep water column. Utilizing both shallow (300' SUS) and deep (6000' SUS + 256# TNT) explosive sources, shooting runs were made at ranges to 35 km from the array.

A majority of the effort under these programs has been devoted to an attenuation analysis of the data in order to derive values of sediment acoustic attenuation as a function of both depth and frequency. As indicated below, several publications and a Ph.D. thesis has resulted from this work.

[1]   W. S. Hodgkiss and R. Brienzo, "Coherent recombination of sediment borne and water path acoustic signals," 1984 IEEE Intl. Conf. on Acoust., Speech, Signal Process, pp. 24.5.1-24.5.2 (1984).

[2]   R. K. Brienzo, "Iterative method for the estimation of shot and sea floor depths using hydrophone streamer data," MPL TM-398, Marine Physical Laboratory, Scripps Institution of Oceanography, San Diego, CA (1988).

[3]   R. K. Brienzo, "Velocity and attenuation profiles in the Monterey deep-sea fan," SIO Reference 87-28, Scripps Institution of Oceanography, La Jolla, CA, (1987) (Ph.D. dissertation).

[4]   R. K. Brienzo, "Velocity and attenuation profiles in the Monterey deep-sea fan, Part I: Velocity profile," J. Acoust. Soc. Am. (1988) (submitted).

[5]   R. K. Brienzo, "Velocity and attenuation profiles in the Monterey deep-sea fan, Part II: Attenuation profile," J. Acoust. Soc. Am. (1988) (submitted).

PROJECT   Detection & Estimation in the
Presence of Boundary Reverberation

PROJECT LEADER: Kenneth M. Watson
TELEPHONE NUMBER: (619) 534-1793

INTRODUCTION

The objective of this program has been the derivation and performance evaluation of optimal detection and estimation processors operating in an environment where boundary reverberation is the major factor limiting processor performance. As indicated below, several publications have resulted from this work. In addition, a Ph.D. thesis by D. Almagor was completed[4].

[1]   W. S. Hodgkiss and D. Almagor, "Element-level reverberation time series synthesis," 1988 IEEE Int'l Conf. Acoustics, Speech and Sign. Proc., pp. 2701-2704 (1988).

[2]   W. S. Hodgkiss and D. Almagor, "A pole-zero complex adaptive joint process least-squares lattice," IEEE Conf. Acoust., Speech, and Sign. Proc., pp. 2789-2792 (1988).

[3]   W. S. Hodgkiss and D. Almagor, "Oceanic reverberation time series synthesis," IEEE J. Oceanic Eng. (1988) (submitted).

[4]   D. Almagor "Least Squares Adaptive and Bayes Optimal Array Processors for the active sonar problem," SIO Reference 89-16, Scripps Institution of Oceanography, San Diego, CA. (1989).

PROJECT   ADA Ambient Noise Data Analysis

PROJECT LEADER: Victor C. Anderson
TELEPHONE NUMBER: (619) 534-1793

INTRODUCTION

Data was collected during a December 1980 ADA (**A**dvanced **D**etection **A**rray) sea trip at low to moderate wind speeds and a low sea state environment with ADA suspended at a depth of 70 meters. The new data would have some relevance to the mechanisms of ambient wind generated surface noise.

SUMMARY

Data analysis carried out under this project centered on the December 1980 ADA sea trip. In particular, a 2 hour sequence during which the wind increased steadily from 3 knots to 17 knots was selected for close scrutiny. Kalman filter tracking on the noise structure was attempted. However, the noise structure was too diffuse for the algorithm to develop realistic tracks. The time bearing data was transformed to generate a surface distance vs time display in order to more readily interpret the observed wind wave acoustic structure. In this display the general time varying tracks of more intense noise regions could be seen to grow in intensity and number with the increasing wind speed. This particular display along with another high speed time bearing waterfall plot showing noise bursts at low wind speeds was the stimulus for the referenced publication[1] (Appendix A), as well as the follow on surface noise instrument development project.

---

[1] Shang. E. C. and Anderson. V. C. Surface-generated Noise under Low Wind Speed at Kilohertz Frequencies. J. Acoust. Soc. Am., 79(4), pp. 964-971 (1986).

Marine Physical Laboratory

PROJECT	Wind Generated Surface Noise

PROJECT LEADER:	Victor C. Anderson
TELEPHONE NUMBER:	(619) 534-1793

INTRODUCTION

Observations made with the large aperture acoustic array ADA in December 1980 indicated the existence of individual discrete noise sources at the sea surface under very low wind speed conditions (3 knots). These sources were of very short duration-within the 50 ms integration time of the broad band energy detection receiver of the ADA DIMUS beamformer. Furthermore, they appeared to be correlated with swell periods and also to have a space time dependence that indicated a transport rate on the order of .5 m/sec, a rate that corresponds to typical surface currents observed in that area.

These observations stimulated the design and construction of a Synoptic Surface Noise Instrument (Figure 1), to observe acoustic events from a subsurface vantage point at close range.

SUMMARY

Description of the observations made of ADA in a joint paper with Professor Er-Chang Shang[1]. Also indicated, is a possible mechanism - that of cavitation collapse of bubbles in saturated or supersaturated water, stimulated by the turbulent presence fluctuations in the near surface region.

The SSNI has been completed and operated at sea. Data collected with the instrument provided the basis of a recent paper presented at the Acoustical Society of America[2]. The data from this experiment will be the basis for Mr. Updegraff's doctoral thesis in preparation.

[1] Shang, E. C. and Anderson, V. C. Surface-generated Noise under Low Wind Speed at Kilohertz Frequencies. J. Acoust. Soc. Am., 79(4), pp. 964-971 (1986).
[2] Updegraff, Garr E. and Anderson, Victor C. *In Situ* Acoustic Signature of Low Sea State Micro-breaking. J. Acoust. Soc. Am., (1989).

[3] Updegraff, Garr E. *In Situ* Investigation of Sea Surface Noise from a Depth of One Meter. SIO Reference 89-21. Scripps Institution of Oceanography, San Diego, CA. (November 1989).

PROJECT   Low Frequency Bioacoustics

PROJECT LEADER: F. N. Spiess / V. C. Anderson
ASSOCIATE INVESTIGATOR: William C. Cummings
TELEPHONE NUMBER: (619) 534-1621 / (619) 534-1793

INTRODUCTION

Two specific objectives were planned for the next year: an updating and completion of a world-wide catalog of fish sounds, and a study on the feasibility of determining the function of sounds (other than those presumed to be of echolocation) from killer whales, *Orcinus orca*.

SUMMARY

Low-frequency moaning sounds were recorded by Bryde whales (*Balaenoptera edeni*) off Loreto, Mexico, in the Gulf of California. These utterances averaged 0.4 sec in duration with most of the energy at about 124 Hz. In a more northern region of the Gulf, we recorded about low-frequency moans from approximately 35 feeding finback whales (*B. physalus*). The finbacks' most outstanding sound was a long moan with a 1.9-sec component at 68 Hz and a 1.6-sec component at 34 Hz. Locations, dates, and number of whales are tabulated.

Full documentation of the results of this work can be found in the report listed below[1].

---

[1]. Cummings, William C. and Thompson, Paul. O. Sounds from Bryde and Finback Whales in the Gulf of California. Marine Physical Laboratory Technical Report MPL-U-39/81, Scripps Institution of Oceanography, San Diego, CA. (1981).

PROJECT   Differential Sound Absorption: A Method to
Study Pressure Dependent Ion-Pairing in Seawater

PROJECT LEADER: Fred H. Fisher
TELEPHONE NUMBER: (619) 534-1796

INTRODUCTION

Two research objectives were investigated under ONR sponsorship: (1) Laboratory acoustic measurements were made in sea water to resolve the conflict between the sound absorption results obtained by Bezdek at sea to a depth of 3350 meters and the laboratory work of Fisher in 0.5 Molar solutions of MgSO4 to an equivalent depth of 10,000 meters; (2) To understand the physical chemistry of the electrolytes involved in chemical sound absorption related to MgSO4.

SUMMARY

The first objective was achieved by making measurements in the !aboratory of the sound absorption of seawater as a function of pressure and temperature, up to equivalent depths of 3070 meters. The principle reason for the discrepancy cited in objective 1 is the fact that the decrease of sound absorption with pressure is a strong function of temperature; at freezing temperatures, the effect of pressure is much larger than at room temperatures. These results were reported at an Acoustical Society meeting.

The second objective was studied extensively and the source of difficulty was laid out in the paper by Fisher. which treated the worst case of interactions of the $MgSO_4$ relaxation with other electrolytes, namely hydrochloric and sulfuric acids. For seawater, interaction with sodium chloride gives rise to coupled chemical reactions with the magnesium sulfate which leads to a decrease in sound absorption as sodium chloride is added to a magnesium sulfate solution. Originally, Kurtze and Tamm had shown a quantitative relationship between absorption of magnesium sulfate and the amount of added sodium chloride and Fisher had reinterpreted the results in terms of ion association effects. However, in extending the concepts to acid-magnesium sulfate mixtures, it was realized that because of competing, coupled pressure dependent reactions, it not only would take a substantial theoretical effort to solve the coupled reaction problem quantitatively, it would also take even a greater effort inasmuch as the original models for multistate dissociation by Eigen and Tamm were off by a factor of three in the overall association constant (Appendix A).

----

1. C. C. Hsu and F. H. Fisher, "Differential sound absorption technique for ion-pairing studies in $MgSO_4$-NaCl solutions," J. Acoust. Soc. Am. **68**, S107 (1980).

2. C. C. Hsu and F. H. Fisher, "Observation of Q of 1 million in a water-filled 100-liter titanium spherical resonator at 25 kHz," J. Acoust. Soc. Am. **69**, S44 (1981).

3. C. C. Hsu and F. H. Fisher, "Sound absorption in a 0.02 M $MgSo_4$ solutions and in a 0.02 M $MgSO_4$-0.6 NaCl mixture at $25^{\circ}C$ and pressures up to 307 atm," J. Acoust. Soc. Am. **70**, S90 (1981).

4. C. C. Hsu and F. H. Fisher, "Sound absorption in seawater at pressures up to 307 atmospheres," J. Acoust. Soc. Am. **69**, S45 (1981).

5. C. C. Hsu and F. H. Fisher, "Sound absorption in sodium sulfate (1 atm) and sodium chloride (1-307 atm) solutions from 30 to 300 kHz," J. Acoust. Soc. Am. **69**, S45 (1981).

6. F. H. Fisher, J. M. Gieskes, and C. C. Hsu, "$MgSO_4$ ion association in seawater," Mar. Chem. **11**, 279-283 (1982).

7. C. Neuberger, C. C. Hsu, and F. H. Fisher, "Effect of ionic strength and ion pairing on sound absorption in aqueous solutions of $MgSO_4$ and NaCl," SIO Reference 82-9, (1982).

8. F. H. Fisher, J. M. Gieskes, and C. C. Hsu, "Analysis of Johnson's response to our paper '$MgSo_4$ ion association in seawater'," Mar. Chem. **11**, 287-288 (1982).

9. C. C. Hsu and F. H. Fisher, "Effect of pressure on sound absorption in synthetic seawater and in aqueous solutions of $MgSO_4$," J. Acoust. Soc. Am. **74**, 564-569 (1983).

PROJECT   Research Tower Operation and Support

PROJECT LEADER: Kenneth M. Watson
TELEPHONE NUMBER: (619) 534-1801

INTRODUCTION

Support was provided for the scientific use of the ONR Research Tower located offshore of Mission Beach, San Diego, California.

SUMMARY

The Oceanographic Research Tower was restored to operational status by repairing worn and damaged structural items, improving personnel safety installations; providing on-board repair and communication equipment; and establishing scheduled maintenance and boat transport services. The work was completed in time to support several scientific experiments on the Tower, and was continued under ONR Contract N00014-87-C-0127.

PROJECT   FLIP Overhaul

PROJECT LEADER: Kenneth M. Watson
TELEPHONE NUMBER: (619) 534-1801

INTRODUCTION

Research Platform FLIP (Floating Laboratory Instrument Platform) is a U.S. Government public vessel assigned to the plant account of the Chief of Naval Research. It's operation and administration are assigned to the Scripps Institution of Oceanography, University of California, San Diego. A thorough overhaul was required in order to effectively and safely support scheduled research operations.

SUMMARY

Research Plataform FLIP was overhauled at Southwest Marine Shipyard, San Diego, California from 23 Marach to 23 April 1982. The work included:

1. A thorough preservation and painting of the hull, ballast tanks and air flasks;
2. Replacement of worn and corroded fittings;
3. Ventilation and survival equipment improvements;
4. Sea valves overhauled;
5. Acquisition and installation of automatic fire protection system in engine room;
6. Modern radio communication and electronic navigation system.

APPENDIX A

Phase space density representation of inviscid fluid dynamics

Henry D. I. Abarbanel[a]

Marine Physical Laboratory, A-013, Scripps Institution of Oceanography and Department of Physics, University of California, San Diego, La Jolla, California 92093

A. Rouhi[a]

Department of Physics, B-019, University of California, San Diego, La Jolla, California 92093

A formulation of inviscid fluid dynamics based on the density $F(\mathbf{x},\mathbf{v},t)$ in a *single-particle phase space* $[\mathbf{x} = (x_1,x_2,x_3), \mathbf{v} = (v_1,v_2,v_3)]$ is presented. This density evolves in time according to a Poisson bracket of F with $H(\mathbf{x},\mathbf{v},t)$—a Hamiltonian in the same single-particle phase space. Compressible flows of barotropic fluid and homogeneous, incompressible flows are discussed. The main advantage of the phase space density formulation over either Euler or Lagrange formulations is the algebraic and conceptual ease in making fully Hamiltonian approximations to the flow by altering $H(\mathbf{x},\mathbf{v},t)$ and the Poisson brackets appropriately. The example of a shallow layer of rapidly rotating fluid where a Rossby number expansion is desired will be discussed in some detail. Changes of phase space coordinates that give an approximate H (expanded in Rossby number) and *exact* Poisson brackets will be exhibited. The resulting quasigeostrophic equations for F are two-dimensional partial differential equations to every order in Rossby number. The extension to multiple layers will be presented.

I. INTRODUCTION

Inviscid fluids possess an energy functional that is conserved with the fluid motion. Indeed one may regard the existence of such an energy functional as the definition of an inviscid fluid. What is perhaps somewhat less well known is that this energy functional acts as a Hamiltonian functional, in the usual sense of the word, on the infinite-dimensional phase space of the fluid. This holds true for both the Lagrangian and Eulerian descriptions of the fluid flow. We will proceed now to discuss this description of Lagrangian and Eulerian views of inviscid fluid dynamics as "Hamiltonian field theories." We do this (even though we will not need this description of inviscid fluids in the main body of the paper) for two reasons. First, because the existence of this Hamiltonian description motivated us initially to carry out the investigation presented in this paper and, second, to contrast the Lagrangian and Eulerian viewpoints with a third, rather different viewpoint we shall describe and use later.

In the Lagrangian description of fluid flow one requires the position $\mathbf{Y}(\mathbf{l},t)$ of a fluid particle together with the conjugate momentum $\mathbf{P}(\mathbf{l},t)$, where $\mathbf{l}$ is a continuous label that, for example, can be (but does not have to be) the initial position of the fluid particle, that is, $\mathbf{Y}(\mathbf{l},t=0) = \mathbf{l}$. For definiteness, we consider the specific case of an inviscid barotropic fluid in which the energy density ϵ or equivalently the pressure are functions of mass density ρ alone. The equations of motion for $\mathbf{Y}(\mathbf{l},t)$, which are just the continuum limit of n-particle Newtonian dynamics, can be shown to follow from an action principle[1-4]

$$\delta \mathcal{S} = 0, \tag{1a}$$

where

$$\mathcal{S} = \int_{t_1}^{t_2} dt \int d^3l\, \rho_0(\mathbf{l}) \left[\frac{1}{2}\left(\frac{\partial \mathbf{Y}(\mathbf{l},t)}{\partial t}\right)^2 - \epsilon(\rho(\mathbf{Y}(\mathbf{l},t))) \right]. \tag{1b}$$

In Eq. (1a) $\mathcal{S}$ is extremized over all variations in $\mathbf{Y}$ that vanish at t_1 and t_2. In Eq. (1b), $\rho_0(\mathbf{l})$ is the mass density of the fluid at $t = 0$ and $\rho(\mathbf{Y}(\mathbf{l},t))$ is the mass density at position $\mathbf{Y}$ at time t. The law of conservation of mass can be stated simply as

$$\rho_0(\mathbf{l})d^3l = \rho(\mathbf{Y})d^3Y$$

or

$$\rho(\mathbf{Y}) = \frac{\partial(\mathbf{l})}{\partial(\mathbf{Y})}\rho_0(\mathbf{l}), \tag{2}$$

where $\partial(\mathbf{l})/\partial(\mathbf{Y})$ is the Jacobian of the transformation

$$\mathbf{l} \to \mathbf{Y}(\mathbf{l},t).$$

One may recover the more familiar Eulerian version of the law of conservation of mass by applying $\partial/\partial t$ to Eq. (2); these matters are elaborated on more fully in the references.[1-4]

One may now proceed to the Hamiltonian description in the usual fashion, defining the Lagrangian density $\mathcal{L}$ through Eq. (1b) by

$$\mathcal{S} = \int_{t_1}^{t_2} dt \int d^3l\, \mathcal{L}(Y,\dot{Y}).$$

We have the canonical momentum defined by

$$P_i(\mathbf{l},t) = \frac{\partial \mathcal{L}}{\partial \dot{Y}_i(\mathbf{l},t)} = \rho_0(\mathbf{l})\frac{\partial Y_i(\mathbf{l},t)}{\partial t}.$$

The Hamiltonian functional is defined as usual by

$$\mathscr{H} = \int d^3 l (\mathbf{P}\cdot\dot{\mathbf{Y}} - \mathscr{L}(Y,\dot{Y}))$$

$$= \int d^3 l \left(\frac{1}{2\rho_0(l)} (\mathbf{P}(l,t))^2 + \rho_0(l)\epsilon(\rho(\mathbf{Y})) \right). \quad (3)$$

The fundamental Poisson brackets are the canonical brackets

$$\{Y_i(l,t)Y_j(l',t)\} = 0,$$

$$\{Y_i(l,t),P_j(l',t)\} = \delta_{ij}\delta^3(l - l'),$$

$$\{P_i(l,t),P_j(l',t)\} = 0,$$

in other words, the Poisson bracket between any two functionals A and B of $\mathbf{Y}$ and $\mathbf{P}$ given by

$$\{A,B\} = \int d^3 l \left(\frac{\delta A}{\delta \mathbf{Y}}\cdot\frac{\delta B}{\delta \mathbf{P}} - \frac{\delta B}{\delta \mathbf{Y}}\cdot\frac{\delta A}{\delta \mathbf{P}} \right). \quad (4)$$

The dynamics for any functional A proceeds accordingly to the usual equation

$$\frac{\partial A}{\partial t} = \{A,H\}, \quad (5)$$

where H is given by Eq. (3) and the Poisson bracket $\{\cdot,\cdot\}$ is defined by Eq. (4). For example, substitution of $P_a(l,t)$ for F would lead to the momentum equation and substitution of $\rho(\mathbf{Y})$ would lead to the continuity equation. It is important to note that in these expressions the derivative with respect to time is taken with the label l held fixed. It is easy to show that in Eulerian variables this corresponds to the usual convective derivative[2-4]

$$\left.\frac{\partial}{\partial t}\right|_{l \text{ fixed}} = \left.\frac{\partial}{\partial t}\right|_{x \text{ fixed}} + \mathbf{v}(x,t)\cdot\frac{\partial}{\partial x},$$

where x is the Eulerian position coordinate and v the Eulerian velocity. Below, where we discuss the Hamiltonian formulation of the Eulerian description of fluid dynamics, $\partial/\partial t$ will have its usual meaning, that is, the derivative is taken with x kept fixed. This ends our brief discussion of the Hamiltonian formulation of inviscid fluid dynamics in Lagrangian coordinates; the interested reader may refer to the references for more detailed accounts.[1-4]

The Hamiltonian formulation of inviscid fluid dynamics in Eulerian coordinates is considerably more subtle. Indeed, it is not *a priori* obvious that such a formulation need exist since the connection of Eulerian fluid dynamics with Newtonian n-particle dynamics is less direct than its Lagrangian counterpart. Returning to the barotropic case we note that the Lagrangian specification requires knowledge of six independent fields $Y_a(l,t),P_a(l,t)$, namely the particle positions and momenta for $a = 1,2,3$. In the Eulerian specification, however, knowledge of four independent fields, namely the mass density $\rho(x,t)$ and the three components of the Eulerian velocity $v_a(x,t)$, is sufficient. Simple counting shows then that the Eulerian variables cannot be related to the Lagrangian variables by a canonical transformation. Then $\rho(x,t)$ and $v_a(x,t)$ are noncanonical coordinates in the infinite-dimensional phase space of the fluid. Not only are they noncanonical, however, they are also "reduced" coordinates in some sense since they describe essentially the same dynamics as the Lagrangian variables using fewer

fields. The fact that such a reduced description is possible in the first place and also that the reduced description also admits of a Hamiltonian formulation both have to do with a fundamental symmetry present in the full $(\mathbf{Y},\mathbf{P})$ phase space of the fluid, namely the freedom to relabel the fluid particles in arbitrary fashion subject to the action (1b) remaining fixed.[5] The preceding statement is far from self-evident; however, it does not touch upon the material in the main part of this paper directly. The interested reader may consult Ref. 5 and the references cited therein for full details. We content ourselves with reproducing the Poisson brackets and the Hamiltonian in the barotropic case.[5] The Hamiltonian functional is

$$\mathscr{H}[\rho,v] = \int d^3x \left(\frac{1}{2}\rho v^2 + \rho\epsilon(\rho) \right). \quad (6)$$

The Poisson bracket among any two functions A and B of ρ and $\mathbf{M}$ where $\mathbf{M} = \rho v$, is given by

$$\{A[\rho,\mathbf{M}],B[\rho,\mathbf{M}]\} = \int d^3x \left(\mathbf{M}\cdot\left[\left(\frac{\delta B}{\delta \mathbf{M}}\cdot\nabla\right)\frac{\delta A}{\delta \mathbf{M}} - (A\leftrightarrow B) \right] \right.$$
$$\left. + \rho\left[\left(\frac{\delta B}{\delta \mathbf{M}}\cdot\nabla\right)\frac{\delta A}{\delta \rho} - (A\leftrightarrow B) \right] \right). \quad (7)$$

It is easy to see that Eq. (7) satisfies all the required properties for being a Poisson bracket, namely, antisymmetry, linearity in each of the entries, and the Jacobi identity. One can verify easily from (6) and (7) that the fluid equations result from the usual Poisson bracket with the Hamiltonian, that is, mass conservation

$$\frac{\partial \rho(x,t)}{\partial t} = \{\rho(x,t),\mathscr{H}\} = -\nabla\cdot(\rho(x,t)\mathbf{v}(x,t)),$$

and the momentum equation

$$\frac{\partial \mathbf{v}(x,t)}{\partial t} = \{\mathbf{v}(x,t),\mathscr{H}\} = -(\mathbf{v}\cdot\nabla)\mathbf{v} - \frac{\nabla p(\rho)}{\rho},$$

where the pressure p is related to the energy density ϵ by

$$\epsilon(\rho) = \int^\rho \frac{dp}{dp'}\frac{d\rho'}{\rho'}.$$

The existence of these Hamiltonian formulations for inviscid fluids leads us to speculate on whether the powerful and efficient methods of Hamiltonian perturbation theory could be applied to make physically motivated approximations to inviscid fluid systems. Hamiltonian perturbation theory has several marked advantages compared to direct manipulation of the equations of motion when devising approximation schemes. First, one deals with a single scalar function instead of the vector equations of motion. Second, Hamiltonian perturbation theory is a systematic procedure; if the approximation involves expansion in some small parameter one may proceed to arbitrary order in the expansion parameter. Third, at each stage of the approximation one retains an approximate Hamiltonian conserved exactly by the approximated equations of motion. Related to this is the fact that if one takes care to preserve symmetries present in the original Hamiltonian then one retains also conserved quantities associated with the symmetries in the approximated system automatically.

Neither the Lagrangian nor Eulerian descriptions outlined above turn out to be suitable for this purpose, at least for the application the authors had in mind (Sec. V). Instead a third view of the same dynamics seems to allow one to connect rather simply into the methods of Hamiltonian perturbation theory *for a single particle*. This view is founded on a phase density function $F(\mathbf{x},\mathbf{v},t)$ which gives the number of fluid particles in the six-dimensional volume $d^3x\, d^3v$ around $\mathbf{x}$ and $\mathbf{v}$ at the observation time t. Such a function, albeit for a set of N discrete particles rather than a fluid continuum, is familiar in plasma physics as the Klimontovich or Dupree function.[6] It carries less information about the N-particle dynamics than the Liouville function, which is defined on $6N$-dimensional phase space, but much more than the single-particle Vlasov or Boltzmann distribution function $f_1(\mathbf{x},\mathbf{v},t)$, which provides the essential tool for the kinetic theory of the N-particle system.

In the case of an N-particle system with coordinates $\mathbf{Y}(i,t)$, $i = 1,2,...,N$, and velocities $\mathbf{U}(i,t)$, $i = 1,2,...,N$, the phase space density is defined as

$$F_N(\mathbf{x},\mathbf{v},t) = \sum_{i=1}^{N} \delta^3[\mathbf{x} - \mathbf{Y}(i,t)]\delta^3[\mathbf{v} - \mathbf{U}(i,t)], \quad (8)$$

and it satisfies

$$\frac{\partial}{\partial t} F_N + \mathbf{v}\cdot\frac{\partial}{\partial \mathbf{x}} F_N + \mathscr{F}(\mathbf{x},\mathbf{v},t)\cdot\frac{\partial}{\partial \mathbf{v}} F_N = 0, \quad (9a)$$

with $\mathscr{F}$ the forces seen by a particle at $(\mathbf{x},\mathbf{v})$ caused by all other particles. This $\mathscr{F}$ is a functional of F_N, so (9a) is a complicated nonlinear equation in general.

The advantage of studying the evolution of F_N rather than the Liouville function or the fluid equations coming from averages over the Liouville function lies in the ability to write (9a) as

$$\frac{\partial}{\partial t} F_N + \{F_N, H\}_{(\mathbf{x},\mathbf{v})} = 0, \quad (9b)$$

with $H(\mathbf{x},\mathbf{v},t)$ a Hamiltonian living in six-dimensional $(\mathbf{x},\mathbf{v})$ phase space and $\{\ ,\ \}_{(\mathbf{x},\mathbf{v})}$ a Poisson bracket among ordinary functions, *not functionals*, of these noncanonical variables. We stress here that H is an ordinary function of six variables $(\mathbf{x},\mathbf{v})$ here and not a functional over the entire fluid as in Eq. (3) or Eq. (6) and the Poisson bracket in Eq. (9b) is on single-particle $(\mathbf{x},\mathbf{v})$ space. This is the simplifying feature compared to the Eulerian and Lagrangian formulations that allow us to tap into the methods of Hamiltonian perturbation theory with relative ease. We mention here another possible advantage of the phase space density formulation not directly related to Hamiltonian perturbation theory; this has to do with numerical simulations. Plasma physicists have devised efficient "particle pushing" schemes for numerical integration of equations like Eq. (9b)[6,7] in a setting very much like our example in Sec. V. In our present case of fluid motion this is a purely speculative comment, however. The details of the advantages or disadvantages of integrating Eq. (9b) as opposed to the usual fluid equations await future investigation, which the authors will present in the near future.

In this paper we will show how to generalize these phase space density functions to a fluid continuum. In the next section we will discuss how one proceeds in the case of the shallow water equations in a rotating frame. This is the motivating example, and we consider it in some detail. We also generalize the discussion to many shallow layers. The Rossby number expansion of this set of examples is one of the goals of this work. In this we again rely on the experience in treating a similar problem in the plasma physics literature: the guiding center expansion of a strongly magnetized plasma.

After these examples, we turn to the three-dimensional inviscid flow of compressible barotropic fluids. Incompressible flow is also treated.

II. PHASE SPACE DENSITY DESCRIPTION OF THE SHALLOW WATER EQUATIONS; ONE LAYER AND MANY LAYERS

The equations governing a flat basin of homogeneous shallow, rotating fluid are described in many texts.[7,8] The presumed large ratio of horizontal to vertical scales is used to eliminate the vertical velocity w from the momentum equations so that only a hydrostatic balance

$$0 = -\frac{\partial p}{\partial z} - g \quad (10)$$

is enforced. (The overall uniform density is set to unity.) Mass conservation in the form

$$\frac{\partial w}{\partial z} + \nabla\cdot\mathbf{u} = 0, \quad (11)$$

where $\nabla = (\partial_x, \partial_y)$ and $\mathbf{u} = (u,v)$ determines $w(x,y,z,t)$ from $\nabla\cdot\mathbf{u}$, when $\mathbf{u}$ is taken to be independent of z. The height of the fluid, $h(\mathbf{x},t)$ [$\mathbf{x} = (x,y)$], is the remaining dynamical variable. In a frame that rotates at $f(\mathbf{x})/2$ about the z axis, $\mathbf{u}$ and h satisfy

$$\frac{\partial}{\partial t}\mathbf{u} + \mathbf{u}\cdot\nabla\mathbf{u} = -g\nabla h + \mathbf{u}\times\hat{z}f(\mathbf{x}) \quad (12)$$

and

$$\frac{\partial}{\partial t} h + \nabla\cdot(\mathbf{u}h) = 0, \quad (13)$$

when the bottom of the fluid is flat at $z = 0$. These evolution equations are just those of a barotropic fluid with "density" $h(\mathbf{x},t)$ and pressure $p(h) = \frac{1}{2} gh^2$. The conserved energy that acts as the Hamiltonian *functional* for these Eulerian equations is

$$\mathscr{H} = \int d^2x\left(h\frac{\mathbf{u}^2}{2} + g\frac{h^2}{2}\right). \quad (14)$$

Though we shall derive the needed result in a later section, we now introduce in an *ad hoc* fashion the shallow water phase space density function $F(\mathbf{x},\mathbf{v},t)$ [$\mathbf{v} = (v_1,v_2)$],

$$F(\mathbf{x},\mathbf{v},t) = h(\mathbf{x},t)\delta^2[\mathbf{v} - \mathbf{u}(\mathbf{x},t)]. \quad (15)$$

Next consider $\partial F/\partial t$:

$$\frac{\partial F}{\partial t} = \frac{\partial h}{\partial t}\delta^2[\mathbf{v} - \mathbf{u}(\mathbf{x},t)] + h\frac{\partial u_a}{\partial t}\frac{\partial}{\partial u_a}\delta^2[\mathbf{v} - \mathbf{u}(\mathbf{x},t)] \tag{16}$$

$$= -\left(\frac{\partial}{\partial x_b}(u_b h)\right)\delta^2(\mathbf{v} - \mathbf{u})$$

$$- hu_b\frac{\partial u_a}{\partial x_b}\frac{\partial}{\partial u_a}\delta^2(\mathbf{v} - \mathbf{u})$$

$$+ h[-g\nabla_a h + \epsilon_{ac}u_c f]\frac{\partial}{\partial u_a}\delta^2(\mathbf{v} - \mathbf{u}) \tag{17}$$

$$= -\frac{\partial}{\partial x_b}[u_b h\delta^2(\mathbf{v} - \mathbf{u})]$$

$$- \frac{\partial}{\partial v_a}[h(\mathbf{x},t)\delta^2(\mathbf{v} - \mathbf{u})][-g\nabla_a h + \epsilon_{ac}v_c f] \tag{18}$$

on using the equations of motion for h and $\mathbf{u}$ and properties of $\delta^2(\mathbf{v} - \mathbf{u})$. Noting that

$$\frac{\partial}{\partial x_b}\{u_b h\delta^2[\mathbf{v} - \mathbf{u}(\mathbf{x},t)]\} = \mathbf{v}\cdot\frac{\partial}{\partial \mathbf{x}}[h\delta^2(\mathbf{v} - \mathbf{u})], \tag{19}$$

we may write

$$\frac{\partial F}{\partial t} + \mathbf{v}\cdot\frac{\partial}{\partial \mathbf{x}}F + \mathscr{F}_{\text{shallow}}(\mathbf{x},\mathbf{v},t)\cdot\frac{\partial}{\partial \mathbf{v}}F = 0,$$

where

$$\mathscr{F}_{\text{shallow}} = -g\nabla h + (\mathbf{v}\times\hat{z})f. \tag{20}$$

Finally, we introduce the Hamilton function $H(\mathbf{x},\mathbf{v},t)$,

$$H(\mathbf{x},\mathbf{v},t) = v^2/2 + gh(\mathbf{x},t), \tag{21}$$

and the noncanonical Poisson brackets $(a,b = 1,2)$,

$$\{x_a, x_b\} = 0, \tag{22}$$

$$\{x_a, v_b\} = \delta_{ab}, \tag{23}$$

$$\{v_a, v_b\} = \epsilon_{ab}f(\mathbf{x}). \tag{24}$$

These noncanonical variables $\mathbf{x}$ and $\mathbf{v}$ are simply related to the more familiar canonical coordinates by $\mathbf{q} = \mathbf{x}$ and $\mathbf{p} = \mathbf{v} + \mathbf{R}$ with $f(\mathbf{x}) = \hat{z}\cdot\text{curl }\mathbf{R}$. With these brackets we find

$$\frac{\partial F}{\partial t} + \{F,H\}_{\mathbf{x},\mathbf{v}} = 0, \tag{25}$$

where, for any two functions of $\mathbf{x}$ and $\mathbf{v}$,

$$\{A,B\}_{\mathbf{x},\mathbf{v}} = \frac{\partial A}{\partial x_a}\{x_a, v_b\}\frac{\partial B}{\partial v_b}$$

$$+ \frac{\partial A}{\partial v_b}\{v_b, x_a\}\frac{\partial B}{\partial x_a} + \frac{\partial A}{\partial v_a}\{v_a, v_b\}\frac{\partial B}{\partial v_b}. \tag{26}$$

This evolution equation for $F(\mathbf{x},\mathbf{v},t)$ is our starting point for the analysis of the Rossby number expansion of the shallow water equations. The details will be presented below, but the key idea is that the equation for F is governed by the single-particle phase space Hamilton function $H(\mathbf{x},\mathbf{v},t)$. Approximations to H, which consist of an expansion in Rossby
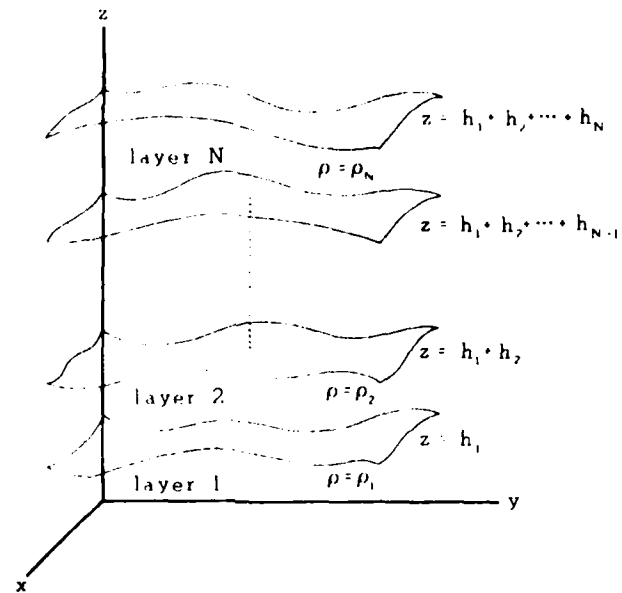

FIG. 1. Many shallow layers of different densities.

number in our example, immediately give *approximate but still Hamiltonian* evolution rules for F.

Many shallow layers of different density may be treated in the same fashion.[7] We choose N layers with density ρ_l and thickness h_l. The bottom layer lies between $0 < z < h_1$ and has density ρ_1. The second layer, of density ρ_2, lies between $h_1 < z < h_1 + h_2$. The top layer has density ρ_N and lies in $h_1 + \cdots + h_{N-1} < z < h_1 + h_2 + \cdots + h_N$. (See Fig. 1 for these definitions.) In each layer, the thickness acts as the effective "density" and satisfies a continuity equation of the form

$$\frac{\partial}{\partial t}h_l(\mathbf{x},t) + \nabla\cdot(\mathbf{u}^{(l)}h_l) = 0, \tag{27}$$

where we note that h_l depends only on $\mathbf{x}$ and t as does the horizontal velocity $\mathbf{u}^l(\mathbf{x},t)$ in layer l. The horizontal momentum equation in each layer is

$$\frac{\partial}{\partial t}\mathbf{u}^{(l)} + \mathbf{u}^{(l)}\cdot\nabla\mathbf{u}^l = -\frac{\nabla P_l(\mathbf{x},t)}{\rho_l} + \mathbf{u}^{(l)}\times\hat{z}f(\mathbf{x}), \tag{28}$$

where

$$P_l = g\sum_{m=l+1}^{N}\rho_m h_m + g\rho_l\sum_{m=1}^{l}h_m. \tag{29}$$

The pressure in layer l is $P_l(\mathbf{x},t) - g\rho_l z$.

We may replace the N equations for the $\mathbf{u}^{(l)}$ and h_l by equations for the N phase space densities

$$F_l(\mathbf{x},\mathbf{v},t) = h_l(\mathbf{x},t)\delta^2[\mathbf{v} - \mathbf{u}^{(l)}(\mathbf{x},t)], \tag{30}$$

which satisfy

$$\frac{\partial}{\partial t}F_l(\mathbf{x},\mathbf{v},t) + \{F_l, H_l\}_{\mathbf{x},\mathbf{v}} = 0, \tag{31}$$

with the lth layer Hamiltonian defined to be

$$H_l = v^2/2 + P_l/\rho_l, \tag{32}$$

as some straightforward algebra will verify. The Poisson brackets here are as in Eq. (24).

III. ANOTHER EXAMPLE

To illustrate further the phase space density technique we consider a rotating, incompressible, Boussinesq fluid, assuming the vertical momentum equation is well approximated by the hydrostatic balance.[9] We choose $\mathbf{x} = (x,y)$ and z as spatial labels on our Eulerian fields. The velocity $\mathbf{u} = (u,v,w)$ splits into a horizontal velocity $\mathbf{u}_H = (u,v)$ and w. The horizontal momentum equations in Boussinesq approximation are

$$\frac{\partial}{\partial t}\mathbf{u}_H + w\frac{\partial}{\partial z}\mathbf{u}_H + \mathbf{u}_H\cdot\nabla\mathbf{u}_H = -\frac{1}{\rho_0}\nabla_p + \mathbf{u}_H\times\hat{z}f(\mathbf{x}),$$

$$(33)$$

where $\nabla = (\partial_x,\partial_y)$ while the vertical momentum equation is simply

$$0 = -\frac{\partial p}{\partial z} - \rho g. \tag{34}$$

Incompressibility and continuity are as usual

$$(\partial_t + w\,\partial_z + \mathbf{u}_H\cdot\nabla)\rho = 0 \tag{35}$$

and

$$\partial_z w + \nabla\cdot\mathbf{u}_H = 0. \tag{36}$$

Now change to isopycnal coordinates where ρ replaces z as an independent variable. For this to make sense $\rho(z)$ must be monotonic. This enables us to eliminate the vertical velocity in terms of the depth $h(\mathbf{x},\rho,t)$ defined by

$$h(\mathbf{x},\rho,t) = \int^\rho d\rho'\left(\frac{1}{(\partial\rho/\partial z)(\mathbf{x},\rho',t)}\right), \tag{37}$$

via

$$w = \frac{\partial h}{\partial t} + \mathbf{u}_H\cdot\nabla h, \tag{38}$$

and $\mathbf{u}_H$ is to be considered a function of $\mathbf{x}$ and ρ while now ∇ means derivatives at fixed ρ.

With this change of coordinates the Euler equations become

$$\left(\frac{\partial}{\partial t} + \mathbf{u}_H\cdot\nabla\right)\mathbf{u}_H(\mathbf{x},\rho,t) = -\nabla\frac{\Psi}{\rho_0} + \mathbf{u}_H\hat{z}f(\mathbf{x}), \tag{39}$$

where

$$\Psi(\mathbf{x},\rho,t) = p(\mathbf{x},\rho,t) + \rho gh. \tag{40}$$

The hydrostatic balance is now

$$\Psi_\rho = gh, \tag{41}$$

and the solenoidal nature of $\mathbf{u}$ translates into

$$\partial_t h_\rho + \nabla\cdot(\mathbf{u}_H h_\rho) = 0, \tag{42}$$

where

$$h_\rho = \frac{\partial}{\partial\rho}h(\mathbf{x},\rho,t). \tag{43}$$

Now this is very much like the shallow water equations with h_ρ playing the role of density and Ψ the role of pressure. The hydrostatic balance is a nondynamical relation true at every t. We observe then that the phase space density

$$F(\mathbf{x},\rho,\mathbf{v},t) = h_\rho(\mathbf{x},\rho,t)\delta^2[\mathbf{v} - \mathbf{u}_H(\mathbf{x},\rho,t)] \tag{44}$$

satisfies

$$\frac{\partial F}{\partial t} + \{H,F\}_{\mathbf{x},\mathbf{v}} = 0 \tag{45}$$

with

$$H = \mathbf{v}^2/2 + \Psi(\mathbf{x},\rho,t)/\rho_0 \tag{46}$$

and the usual Poisson brackets, Eqs. (22)–(24). The function Ψ entering the evolution equation for F is determined by F itself through the solution of

$$\Psi_{\rho\rho} = g\int d^2v\,F = gh_\rho, \tag{47}$$

and this is the source of nonlinear behavior here.

IV. THE GENERAL CONSTRUCTION

To this point we have made apparently *ad hoc* statements about the phase space density $F(\mathbf{x},\mathbf{v},t)$ to be used in our examples; now we derive the general form for it. We begin by considering a collection of N particles with the three dimensional coordinates $\mathbf{Y}(i,t)$ and velocities $\mathbf{U}(i,t)$, where $i = 1,2,...,N$. The number of particles in the phase space volume $\int_{\gamma} d^3x\,d^3v$ is clearly

$$\int_{\gamma} d^3x\,d^3v\,F(\mathbf{x},\mathbf{v},t), \tag{48}$$

where the phase space density is[6]

$$F(\mathbf{x},\mathbf{v},t) = \sum_{i=1}^{N}\delta^3[\mathbf{x} - \mathbf{Y}(i,t)]\delta^3[\mathbf{v} - \mathbf{U}(i,t)]. \tag{49}$$

The integral counts the particles with orbits that have reached the phase volume γ at time t.

Next we take the continuum limit of this by considering the number of particles N to go to infinity. The label i becomes a continuous label $\mathbf{l}$, the coordinates and velocities become functions of $\mathbf{l}$,

$$\mathbf{Y}(i,t)\to\mathbf{Y}(\mathbf{l},t), \quad \mathbf{U}(i,t)\to\mathbf{U}(\mathbf{l},t), \tag{50}$$

and the phase space density has the form

$$F(\mathbf{x},\mathbf{v},t) = \int d^3l\,\rho_0(\mathbf{l})\delta^3[\mathbf{x} - \mathbf{Y}(\mathbf{l},t)]\delta^3[\mathbf{v} - \mathbf{U}(\mathbf{l},t)], \tag{51}$$

where $\rho_0(\mathbf{l})$ simply provides a weight for the label space.

We recognize $\mathbf{Y}(\mathbf{l},t)$ and $\mathbf{U}(\mathbf{l},t)$ with

$$\frac{\partial}{\partial t}\mathbf{Y}(\mathbf{l},t)\bigg|_{\mathbf{l}\text{ fixed}} = \mathbf{U}(\mathbf{l},t) \tag{52}$$

to be the Lagrangian fluid particle position and velocity, with $\mathbf{l}$ some appropriate means of labeling the continuum of fluid particles.[4] To go from the Lagrangian description to Eulerian variables, we identify the Eulerian label $\mathbf{x}$ as the position reached by the fluid particle with label $\mathbf{L}(\mathbf{x},t)$ defined by

$$\mathbf{x} = \mathbf{Y}[\mathbf{L}(\mathbf{x},t),t]. \tag{53}$$

The velocity $\mathbf{U}(\mathbf{l},t)$ at this labeled position is just the Eulerian velocity $\mathbf{u}(\mathbf{x},t) = \mathbf{U}[\mathbf{L}(\mathbf{x},t),t]$. Mass conservation in Lagrange variables tells us that the particles with label $\mathbf{l}$ in $d^3\mathbf{l}$ at some time, say $t = 0$, must equal the number that reach $\mathbf{Y}$ in d^3Y at time t. Thus we have the density in d^3Y given by

$$\rho[\mathbf{Y}(\mathbf{l},t),t] = \frac{\partial(\mathbf{l})}{\partial\mathbf{Y}}\rho_0(\mathbf{l}). \tag{54}$$

This satisfies

$$\frac{\partial}{\partial t}\rho[Y(l,t),t]\bigg|_{l\text{ fixed}} = -\rho(Y,t)\frac{\partial}{\partial Y}\cdot U. \quad (55)$$

If we evaluate (54) at $l = L(x,t)$, then $\rho(x,t) = \rho(Y(L(x,t),t),t)$ satisfies

$$\frac{\partial}{\partial t}\rho(x,t) + \nabla_x\cdot(\rho u) = 0, \quad (56)$$

since

$$\frac{\partial}{\partial t}\bigg|_l = \frac{\partial}{\partial t}\bigg|_x + u\cdot\nabla_x. \quad (57)$$

These observations allow us to do the integral over d^3l in the definition of the phase space density by using the first delta function: $\delta^3[x - Y(l,t)]$. The resulting $F(x,v,t)$ is precisely

$$F(x,v,t) = \rho(x,t)\delta^3[v - u(x,t)], \quad (58)$$

with ρ and u the Eulerian density and velocity fields.

The equation satisfied by $F(x,v,t)$ depends on the Euler equation of the fluid. If we have

$$\frac{\partial u(x,t)}{\partial t} + u\cdot\nabla u = -\frac{\nabla p}{\rho} + u\times f(x) + \mathscr{G}_F, \quad (59)$$

and

$$\frac{\partial\rho}{\partial t} + \nabla\cdot(u\rho) = 0, \quad (60)$$

then F satisfies

$$\frac{\partial}{\partial t}F(x,v,t) + v\cdot\nabla_x F + \mathscr{G}\cdot\nabla_v F = 0 \quad (61)$$

with $\mathscr{G} = $ the right-hand side of (59). In (59), $\mathscr{G}_F$ represents other forces, internal and external.

Our ability to write (61) in the form

$$\frac{\partial}{\partial t}F(x,v,t) + \{F,H\}_{x,v} = 0 \quad (62)$$

turns entirely on the possibility of finding Poisson brackets in (x,v) space such that

$$\{x_a,x_b\}\frac{\partial H}{\partial x_b} + \{x_a,v_b\}\frac{\partial H}{\partial v_b} = v_a,$$
$$\{v_a,x_b\}\frac{\partial H}{\partial x_b} + \{v_a,v_b\}\frac{\partial H}{\partial v_b} = \mathscr{G}_a. \quad (63)$$

We now concentrate on several special cases: (1) *barotropic fluid*, where p depends only on ρ; and (2) homogeneous fluid, where ρ is constant. In case (1) we may accomplish our task with the Hamiltonian

$$H = v^2/2 + h(\rho) + \Phi(x,t), \quad (64)$$

where

$$h(\rho) = \int^\rho \frac{dp}{d\rho'}\frac{d\rho'}{\rho'} \quad (65)$$

and we assume the forces $\mathscr{G}_F$ are derivable from a potential, $\mathscr{G}_F = -\nabla\Phi$. The Poisson brackets are

$$\{x_a,x_b\} = 0, \quad \{x_a,v_b\} = \delta_{ab}, \quad (66)$$

and

$$\{v_a,v_b\} = \epsilon_{abc}f_c(x),$$

with $\nabla_x\cdot f(x) = 0$ in analogy with the situation of a charged particle in a magnetic field. The evolution equation for F is now (62) and is nonlinear in F since we must replace ρ and u in the equation by

$$\rho(x,t) = \int d^3v\, F(x,v,t) \quad (67)$$

and

$$u(x,t) = \frac{\int d^3v\, vF(x,v,t)}{\rho(x,t)}.$$

In the second case of constant density, $\rho(x,t) = \rho_0$, we can use the time-independent constraint div $u = 0$ to determine the pressure in terms of u alone. This requires

$$\nabla^2(p/\rho_0 + u^2/2) = \nabla\cdot[u\times(f + \text{curl } u)], \quad (68)$$

at all t. With $\rho_0 u = \int d^3v\, Fv$, we again turn (62) into an equation for F alone.

V. ROSSBY NUMBER EXPANSION OF THE SHALLOW WATER EQUATIONS

In this section we apply the ideas of the previous sections, together with some work of Littlejohn,[10] to derive an equation of motion describing the slow time scale evolution of the phase space density function for the shallow water equations in a rotating frame. Such equations, describing "almost geostrophic" fluid motion, are of considerable geophysical interest for the description of mesoscale phenomena in the atmosphere and ocean.

We start with the shallow water equations describing the motion of a thin, rapidly rotating layer of fluid. The reader is referred to Sec. II and the references for a discussion of the equations.[7,8] We repeat them here for convenience. The evolution of the horizontal velocity $u(x,t)$ and the height $h(x,t)$ are given by the momentum equation

$$R\left(\frac{\partial u}{\partial t} + u\cdot\nabla u\right) = -g\nabla h + (u\times\hat{z})f(x) \quad (69)$$

and mass conservation

$$\frac{\partial}{\partial t}h + \nabla\cdot(uh) = 0. \quad (70)$$

In these equations $x = (x,y)$ are the horizontal coordinates and the frame rotates about the z axis at $f(x)/2$. The Rossby number R introduced into Eq. (69) results from standard scalings of the shallow water equations. We will have more to say about the Rossby number in a moment.

As shown in Sec. II, the phase space density function $F = F(x,v,t)$, defined by

$$F(x,v,t) = h(x,t)\delta^2(v - u(x,t)), \quad (71)$$

obeys the following evolution equation:

$$\frac{\partial F}{\partial t} + \{F,H\}_{x,v} = 0. \quad (72a)$$

Where H is a *single-particle* Hamiltonian given by

$$H(x,v,t) = v^2/2 + gh(x,t)/R \quad (72b)$$

and $\{\cdot,\cdot\}_{x,v}$ is a noncanonical *single-particle* Poisson bracket, where the Poisson bracket of any two phase functions A and

2957   Phys. Fluids, Vol. 30, No. 10, October 1987

H. D. I. Abarbanel and A. Rouhi   2957

B is given by

$$\{A,B\}_{\mathbf{x},\mathbf{v}} = \frac{\partial A}{\partial \mathbf{x}} \cdot \frac{\partial b}{\partial \mathbf{v}} - \frac{\partial A}{\partial \mathbf{v}} \cdot \frac{\partial B}{\partial \mathbf{x}} + \frac{f}{R}\left(\frac{\partial A}{\partial \mathbf{v}} \times \frac{\partial B}{\partial \mathbf{v}}\right) \cdot \hat{z}. \tag{72c}$$

We will be making *time-dependent* noncanonical transformations in the $(\mathbf{x},\mathbf{v})$ phase space. This gives rise to certain difficulties which we circumvent by the use of the well-known device of extended phase space in which the time t is treated as an additional coordinate with $-k$ its conjugate momentum, where k is the value of the physical Hamiltonian (72b) on particle trajectories. On the extended phase space $(\mathbf{x},\mathbf{v},t,k)$ we define a Hamiltonian $H(\mathbf{x},\mathbf{v},t,k)$ and Poisson brackets $\{\cdot,\cdot\}_{\mathbf{x},\mathbf{v},t,k}$ that describe exactly the same dynamics as Eqs. (72):

$$H(\mathbf{x},\mathbf{v},t,k) = H(\mathbf{x},\mathbf{v},t) - k, \tag{73a}$$

$$\{\overline{A},\overline{B}\}_{\mathbf{x},\mathbf{v},t,k} = \{\overline{A},\overline{B}\}_{\mathbf{x},\mathbf{v}} - \frac{\partial \overline{A}}{\partial t} \frac{\partial \overline{B}}{\partial k} + \frac{\partial \overline{A}}{\partial k} \frac{\partial \overline{B}}{\partial t}. \tag{73b}$$

Here $(\mathbf{x},\mathbf{v},t)$ and $\{\cdot,\cdot\}_{\mathbf{x},\mathbf{v}}$ are given by Eqs. (72) and $\overline{A}$ and $\overline{B}$ are any functions of the extended variables $\{\mathbf{x},\mathbf{v},t,k\}$. From here on, the *symbols H and $\{\cdot,\cdot\}$ will refer to the extended phase space variables*. We also let the symbol s parametrize orbits in the extended phase space, so that for any $\psi(\mathbf{x},\mathbf{v},t,k)$ the evolution of ψ is governed by

$$\frac{d\psi}{ds} = \{\psi,H\}. \tag{73c}$$

Note that in the extended variables Eq. (72a) simply becomes

$$\{F,H\} = 0. \tag{74}$$

We now turn to the discussion of the physical significance of the Rossby number. This will also serve to motivate the transformations that we will carry out on the shallow water phase space density function later. The Rossby number for a particular fluid motion measures the ratio of inertial to Coriolis accelerations for that motion. Thus fluid motions in which the Rossby number is small are ones in which the fluid has time to feel the effects of rotation; in particular, time scales of such motions are of order $\gg 1/f$. The motion in which inertial effects are completely ignored is geostrophic. This we reach by setting R equal to zero in Eq. (69). Geostrophy is then a balance between hydrostatic and Coriolis forces. If strict geostrophy is in effect, we can easily solve for the velocity in terms of the gradient of h and the Coriolis parameter f. This velocity we denote by $\mathbf{G}(\mathbf{x},t)$:

$$\mathbf{G}(\mathbf{x},t) = g(\hat{z} \times \nabla_{\mathbf{x}} h(\mathbf{x},t))/f(\mathbf{x}). \tag{75}$$

In this section we derive evolution equations where solutions show almost geostrophic behavior and where departures from geostrophy are calculable to any order in R one may desire. The distribution function view of the fluid is the natural setting for this since the description in terms of a one-particle Hamiltonian with one-particle Poisson brackets will allow us to make use of powerful techniques.

The single-particle equations of motion for s, $\mathbf{x}$, and $\mathbf{v}$ that follow from the use of the Hamiltonian (73a) and the

given Poisson brackets are

$$\frac{ds}{dt} = 1, \tag{76a}$$

$$\frac{d\mathbf{x}}{ds} = \frac{d\mathbf{x}}{dt} = \mathbf{v}, \tag{76b}$$

$$\frac{d\mathbf{x}}{ds} = \frac{d\mathbf{v}}{dt} = \frac{1}{R}(-g\nabla h + (\mathbf{v}\times\hat{z})f). \tag{76c}$$

What makes this particle a *fluid* particle is the particular form of the distribution function and the fact that $h(\mathbf{x},t)$ is an integral over the velocities of this distribution function

$$h(\mathbf{x},t) = \int d^2v\, F(\mathbf{x},\mathbf{v},t). \tag{77}$$

In what follows, though, we may ignore this for the most part and treat $h(\mathbf{x},t)$ as if externally imposed and given. There is an analogy in (76) to the motion of a charged particle in strong electric and magnetic fields in two dimensions, with h playing the role of the electrostatic potential and f the magnetic field perpendicular to the plane of motion (we also take $f > 0$ everywhere). In the limit of infinitely strong fields ($R = 0$), we obtain, solving $\mathbf{v}$ in Eq. (76), what is known as the "$\mathbf{E}\times\mathbf{B}$ drift" in electromagnetic language,

$$\mathbf{v}_D = (\mathbf{E}\times\mathbf{B})/|\mathbf{B}|^2. \tag{78}$$

This, of course, is the exact analog of the geostrophic velocity [Eq. (75)]. The problem of finding evolution equations involving slow variations only and describing departures from geostrophy or $\mathbf{E}\times\mathbf{B}$ drift order by order in R was dealt with by Littlejohn,[10] and it is his method we will follow. He treated single-particle motion only and did not need the connection with a continuum fluid theory that we use here. The procedure falls roughly into *three* parts. The *first* part consists of changes of variables in the single-particle Hamiltonian and in the Poisson brackets. These new variables identify the *fast* variable θ whose inverse time scales are of order f/R. At this stage the equations of motion will still involve a mixture of slow and fast variables. The *second* part consists of further changes of variables that decouple slow variables from the fast variable in the sense that the Poisson brackets of the new variables among themselves will be functions only of the slow variables. The new variables will be known in terms of the old ones as power series in R. The inspiration for this change of variables comes from the proof of Darboux's theorem so we will call it the Darboux transformation. The *third* stage consists of Lie transformations in which further variable changes are made putting the fast variable dependence of the Hamiltonian into higher and higher orders of R. The crucial observation here is that Lie transformations, being symplectic transformations, will not change the form of the Poisson brackets[11,12]; in other words, these Lie transforms of the phase space coordinates will not destroy the decoupling of fast and slow variables that we achieved by the Darboux transformation. We will not carry out the third stage involving Lie transformations in this paper since, as a result of fortuitous cancellations, θ dependence does not appear in the Hamiltonian in the first two orders of expansion in R after the Darboux transformation. This will allow us to write an equation for the phase space

density function valid to $O(R^2)$ immediately after the Darboux transformation.[12-14] In principle, one could use the technique of Lie transformations to proceed to higher orders in R. With Poisson brackets decoupled and the fast variable appearing say only at order R^n or higher in the Hamiltonian, we are guaranteed that the evolution equations for the slow variables will be decoupled from the fast variable to the same order. Having expressions in terms of power series in R of the new Darboux-transformed, Lie-transformed variables in terms of the old variables and exact expressions for the Poisson brackets of the new variables among themselves, we can express the distribution function and the equation of motion it satisfies in terms of these new variables. We shall see that this will amount to the elimination of the fast variable from the distribution function to any order desired. We can then solve (numerically) the decoupled evolution equation for the distribution function and recover the fluid height and velocity as its zeroth and first moments. We shall discuss the issues arising from the singular nature of the distribution function in a later paper.

A. Preliminary changes of variables

Since we are interested in small deviations from geostrophy, it is natural to introduce a variable V that measures the difference between velocity and geostrophic velocity:

$$V = v - G, \qquad (79)$$

with G given by Eq. (75).

From the analogy with the electromagnetic case we know that the particle exhibits fast, almost circular motion, superposed on a slow drift. We therefore introduce the variables V and θ through

$$V_1 = -V\sin\theta, \quad V_2 = -V\cos\theta. \qquad (80)$$

For convenience we introduce also the three unit vectors

$$\hat{a}(\theta) = (\cos\theta, -\sin\theta, 0),$$
$$\hat{b} = \hat{z}, \qquad (81)$$
$$\hat{c}(\theta) = (-\sin\theta, -\cos\theta, 0) = \hat{a}\times\hat{b}.$$

We also have

$$V = V\hat{c}(\theta).$$

Thus in a frame moving with the geostrophic velocity we have the picture shown in Fig. 2.

Making a change of variables form the set (x, v) to the set (x, θ, V), we may calculate the Hamiltonian and the Pois-
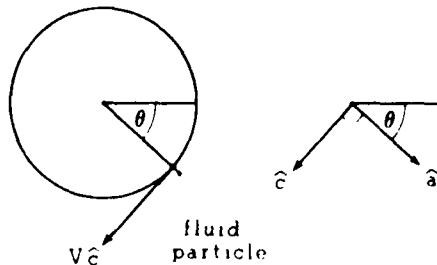

FIG. 2. A fluid particle in a frame moving with velocity G.

son brackets [from Eq. (73)] in terms of the new variables:

$$H(x, V, \theta, t, k) = \frac{V^2}{2} + \hat{c}\cdot GV + \frac{G^2}{2} + \frac{gh(x,t)}{R} - k; \qquad (82)$$

$$\{x, V\} = \hat{c}(\theta), \quad \{x, \theta\} = -\frac{\hat{a}(\theta)}{V}, \quad \{\theta, V\} = \frac{\mathscr{I}}{RV}, \qquad (83)$$

$$\{V, k\} = \hat{c}\cdot\frac{\partial G}{\partial t}, \quad \{\theta, k\} = -\frac{\hat{a}}{V}\cdot\frac{\partial G}{\partial t}, \quad \{t, k\} = -1.$$

All other brackets vanish. We have also introduced $\mathscr{I}$,

$$\mathscr{I} = f + R(\nabla\times G)\cdot\hat{z}. \qquad (84)$$

Now the equations of motion for our new phase space variables using this Hamiltonian and these Poisson brackets become

$$\frac{dx}{dt} = V\hat{c}(\theta) + G, \qquad (85)$$

$$\frac{d\theta}{dt} = \frac{f}{R} + O(R^n), \qquad (86)$$

$$\frac{dV}{dt} = -\hat{c}\cdot[\nabla G\cdot(V\hat{c} + G)] + (\hat{c}\cdot\nabla h)(\nabla\times G)\cdot\hat{b} - \hat{c}\cdot\frac{\partial G}{\partial t}. \qquad (87)$$

Equation (85) is just a reminder of the definition of the velocity v in terms of the new variables (x, θ, V). Equation (86) exhibits the high frequency evolution of θ and identifies it as the fast variable. In any case all these equations contain a mixture of fast and slow variables, in particular θ enters in the right-hand sides of Eqs. (85) and (87).

B. The Darboux transformation

The proof of Darboux's theorem is the inspiration for the change of variables we are going to perform next. We will not go into a detailed discussion of Darboux's theorem here, for this the reader may refer to Arnol'd[14] or Littlejohn.[10] This change of variables will decouple order by order in R, the fast (θ) and slow variables. In any case, we wish to accomplish the following. Let $z = (x, \theta, V, t, k)$. We seek a coordinate transformation $z \to z'(z)$, with $z' = (Z_1, Z_2, \theta, J, t, K)$ such that

$$\{\theta, J\} = 1/R, \qquad (88)$$
$$\{Z_\alpha, \theta\} = 0, \qquad (89)$$
$$\{Z_\alpha, J\} = 0, \qquad (90)$$
$$\{t, \theta\} = 0, \qquad (91)$$
$$\{t, J\} = 0, \qquad (92)$$
$$\{K, \theta\} = 0, \qquad (93)$$
$$\{K, J\} = 0, \qquad (94)$$

for $\alpha = 1, 2$. Darboux's theorem asserts that if there exists a closed nondegenerate two-form on the phase space manifold (in our case the inverse of the Poisson tensor $\{z, z\}$ is such a two-form), then a solution to Eqs. (88)-(94) can be found. Darboux's theorem also guarantees that the Poisson brackets not appearing in (88)-(94), i.e., those of the coordinates (Z_1, Z_2, t, K), among each other will be independent of θ and

J and only a function of (Z_1, Z_2, t, K). We should mention that Darboux's theorem guarantees the existence of a *local* coordinate transformation that, in the presence of a closed, nondegenerate two-form on the phase space manifold, takes a general noncanonical set of coordinates to a fully canonical one. Equations (88)-(94) are the starting point for the iterative (and constructive) proof of the theorem. In the proof of the theorem, one then goes on to observe that the phase space submanifold coordinatized by (Z, t, K) also satisfies the conditions of the theorem, so it can be transformed to two canonical pairs. (Of course for a $2N$-dimensional phase space, N iterations are required to transform the noncanonical set to a canonical one.) Our purpose is achieved by going "halfway" (and only halfway) in the Darboux construction, the desirable feature being the form of the Poisson brackets (88)-(94) at this stage. Also note that in Eq. (88) we take $\{\theta, J\} = 1/R$ not 1, this is a trivial modification for physical reasons having to do with the orderings we desire.

The proof of Darboux's theorem also points the way to the actual construction of $z' = (Z, \theta, J, t, K)$ in terms of the old coordinates $z = (x, \theta, V, t, k)$. We leave the details of the construction to the Appendix. Here we just state that Eqs. (88)-(94) constitute a set of partial differential equations of the new coordinates z' as a function of the old coordinates z, which may be solved formally by the method of characteristics. The results of the calculations presented in the Appendix are

$$Z = e^{RVL} x,$$ (95)

$$J(z) = \left(\sum_{n=0}^{\infty} \frac{(-R)^n V^{n+2}}{(n+2)!} L^n \right) \frac{1}{\mathscr{F}},$$ (96)

$$K(z) = k + \frac{RV}{f} \hat{a} \cdot \frac{\partial G}{\partial t} + O(R^2),$$ (97)

where L is the Lie operator

$$L = \frac{1}{\mathscr{F}(x)} \hat{a} \cdot \frac{\partial}{\partial x}.$$ (98)

Note that in (96) the leading term is $V^2/2f$, which is the familiar first-order adiabatic invariant for this problem. We point out that t and θ are unchanged by the Darboux transformation. Also in Eqs. (95)-(97) k appears only in Eq. (97) and there only as the leading term in a power series expansion in R. In view of this we immediately have

$$\{t, Z\} = 0,$$ (99)

$$\{t, J\} = 0,$$ (100)

$$\{t, \theta\} = 0,$$ (101)

$$\{t, K\} = -1.$$ (102)

It remains to calculate the Poisson brackets $\{Z_1, Z_2\}$ and $\{Z, K\}$ to complete our description of phase space in terms of the new variables (z, θ, J, t, K). It is sufficient to calculate these to first order in V and then let V go to zero. The result thus obtained will be true throughout phase space[10]:

$$\{Z_1, Z_2\} = \lim_{V \to 0} \{(1 - RVL)x_1, (1 - RVL)x_2\}.$$ (103)

The Poisson brackets required to do the calculation are given

in (83). We obtain

$$\{Z_1, Z_2\} = -\lim_{V \to 0} [R/\mathscr{F}(x, t)]$$

$$= -R/\mathscr{F}(Z, t).$$ (104)

We also mention that Z calculated to order R gives

$$Z(x, \theta, V) = x - [VR/f(x)] \hat{a}(\theta) + O(R^2),$$ (105)

which are the guiding center coordinates familiar in the electromagnetic problem. The Poisson bracket $\{Z, K\}$ is obtained using (95) and (97) in a similar fashion:

$$\{Z, K\} = -\frac{R}{\mathscr{F}(Z, t)} \hat{b} \times \frac{\partial G(Z, t)}{\partial t}.$$ (106)

Note that we have now in Eqs. (88)-(94), (99)-(102), and (104)-(106) an *exact* set of Poisson brackets amongst the Darboux variables (Z, θ, J, t, K).

C. The phase space density equation

As mentioned earlier a cancellation of θ-dependent terms at order R^0 in the Hamiltonian will allow us to proceed directly to an almost geostrophic equation for the phase space density function. In this section we let z denote

$$z = (x, v, t, k),$$ (107)

and denote

$$z' = (Z, \theta, J, t, K).$$ (108)

Similarly we denote the Hamiltonian and phase space density functions in the z' coordinates by H' and F', respectively:

$$H'(z') = H(z),$$ (109)

$$F'(z') = F(z).$$ (110)

Using Eqs. (99) and (106) we obtain

$$H'(z') = (1/R)H_0'(Z, J, t, K) + RH_1'(Z, \theta, J, t) + O(R^2),$$ (111)

where

$$H_0' = gh(Z, t) + R[\mathscr{F}(Z, t)J + |G(Z, t)|^2/2 - K].$$ (112)

The function H_1' is a complicated function of z' which we do not need here in order to proceed to our lowest-order almost geostrophic approximation. We will require it later to find the height and horizontal velocities from the lowest-order expression for $F'(z')$. Note, however, that the order-R^1 and order-R^0 terms in H' are independent of θ.

Now $F'(z')$ satisfies

$$\{F', H'\} = 0,$$ (113)

and using the Poisson brackets (88)-(94), (99)-(102), (104), and (106) and Eq. (111), we may write this as

$$\frac{\partial F'}{\partial t} + \frac{1}{R^2} \frac{\partial F'}{\partial \theta} \frac{\partial H_0'}{\partial J} + \frac{1}{\mathscr{F}} (\nabla_z H_0' \times \nabla_z F') \cdot \hat{b}$$

$$\nabla_z F' \cdot \{Z, K\}$$

$$+ \frac{\partial F'}{\partial \theta} \frac{\partial H_1'}{\partial J} - \frac{\partial F'}{\partial J} \frac{\partial H_1'}{\partial \theta} + O(R) = 0.$$ (114)

2960   Phys. Fluids, Vol. 30, No. 10, October 1987

H. D. I. Abarbanel and A. Rouhi   2960

We expand F' itself in powers of R:

$$F' = F_0' + R F_1' + R^2 F_2' + \cdots. \qquad (115)$$

Inserting this into (114), we obtain at order R^{-1}

$$\mathscr{F}(\mathbf{Z}) \frac{\partial F_0'}{\partial \theta} = 0, \qquad (116)$$

which means that F_0' is independent of θ. Using this, we have at order R^0

$$\frac{\partial F_0'}{\partial t} + \frac{1}{\mathscr{F}} (\nabla H_0' \times \nabla F_0') \cdot \hat{b} - \nabla_z F' \cdot (\mathbf{Z}, K)$$

$$+ \mathscr{F} \frac{\partial F_1'}{\partial \theta} - \frac{\partial F_0'}{\partial J} \frac{\partial H_1'}{\partial \theta} = 0. \qquad (117)$$

Now $\partial H_1'/\partial \theta$ is certainly purely oscillatory (i.e., its θ average vanishes). We demand that F_1' be periodic, in which case $\partial F_1'/\partial \theta$ is also purely oscillatory. In this case the θ-dependent and θ-independent parts in Eq. (117) must vanish individually; in particular, for the θ-independent parts

$$\frac{\partial F_0'(J,\mathbf{Z},t)}{\partial t} + \frac{1}{\mathscr{F}(\mathbf{Z})} (\nabla_z H_0' \times \nabla_z F_0'(J,\mathbf{Z},t)) \cdot \hat{b}$$
$$- \nabla_z F' \cdot \{\mathbf{Z}, K\} = 0 \qquad (118)$$

or

$$\frac{\partial F_0'}{\partial t} + \frac{1}{\mathscr{F}} \times \left[g\nabla h + R \left(\nabla \frac{|\mathbf{G}|^2}{2} + \frac{\partial \mathbf{G}}{\partial t} + J\nabla \mathscr{F} \right) \right]$$
$$\cdot \nabla F_0' = 0. \qquad (119)$$

This is our near geostrophic equation for $F_0'(J,\mathbf{Z},t)$. To close the system we must give h at each instance in time in terms of F_0'. We have

$$h(\mathbf{y},t) = \int d^4 z \, \delta^2(\mathbf{x} - \mathbf{y}) F(\mathbf{z}). \qquad (120)$$

We have added the extra integrations over $\mathbf{x}$, which are removed by the delta function, in order to make the following formulas somewhat simpler. In the integral we change variables to the $\mathbf{z}'$ coordinates:

$$h(\mathbf{y},t) = \int d^2 Z \, dJ \, d\theta \, \frac{\partial(\mathbf{z})}{\partial(\mathbf{z}')} \delta^2(\mathbf{x}(\mathbf{z}') - \mathbf{y}) F'(\mathbf{z}'). \qquad (121)$$

Using Eqs. (99) and (106) we write Eq. (116) as

$$h(\mathbf{y},t) = \int d^2 Z \, d\theta \, dJ \, \mathscr{F} \, \delta^2(\mathbf{Z} - \mathbf{y}) F_0'(\mathbf{Z},J,t) + O(R^2). \qquad (122)$$

Note that all $O(R)$ terms vanish because of the θ integration. Equation (122) can then be written in the following simple fashion:

$$h(\mathbf{Z},t) = 2\pi \mathscr{F}(\mathbf{Z}) \int dJ \, F_0'(\mathbf{Z},J,t). \qquad (123)$$

Equations (118) [or (119)] and (123) constitute our almost geostrophic equations for the phase space density. Though we will not do so in this paper, we mention that one may easily (albeit laboriously), with these as starting points, derive slow time scale evolution equations valid to higher orders in R using the technique of Lie transformations.[14] This is dealt with extensively in a context similar to our own in the paper by Dubin et al.[15]

VI. SUMMARY

Our work in this paper has achieved two major goals.

(1) We provided a formulation of inviscid fluid flow based on a density function in phase space, $F(\mathbf{x},\mathbf{v},t)$, in terms of which the momentum and continuity equations read

$$\frac{\partial F(\mathbf{x},\mathbf{v},t)}{\partial t} + \{F(\mathbf{x},\mathbf{v},t), H(\mathbf{x},\mathbf{v},t)\}_{\mathbf{x},\mathbf{v}} = 0, \qquad (124)$$

where $H(\mathbf{x},\mathbf{v},t)$ is a scalar Hamiltonian in $(\mathbf{x},\mathbf{v})$ space, and $\{\cdot,\cdot\}_{\mathbf{x},\mathbf{v}}$ are Poisson brackets among the (generally) noncanonical $(\mathbf{x},\mathbf{v})$. Further, we have given a derivation of $F(\mathbf{x},\mathbf{v},t)$ that identifies it as the number of "fluid particles" in $d^2x \, d^2v$ at time t and shows it to be

$$F(\mathbf{x},\mathbf{v},t) = \rho(\mathbf{x},t) \delta^2(\mathbf{v} - \mathbf{u}(\mathbf{x},t)) \qquad (125)$$

in terms of the familiar Eulerian density $\rho(\mathbf{x},t)$ and Eulerian fluid velocity $\mathbf{u}(\mathbf{x},t)$.

(2) We applied this phase space density formulation to the Rossby number expansion of the motions of a single shallow layer of rapidly rotating fluid. Such a fluid is a two-dimensional barotropic medium with the height of the fluid $h(\mathbf{x},t)$ acting as the "density" and the pressure given as $\frac{1}{2}gh^2$.

Our method is presented in detail in Sec. V of the paper. By moving into a frame going along at the local geostrophic velocity $g(\hat{z} \times \nabla h)/f(\mathbf{x})$, we were able to decouple, order by order in Rossby number, the fast evolution of an angular variable θ and the slow evolution of the two-dimensional location $\mathbf{Z}$ of the center of geostrophy. The distribution function to every order in R is independent of θ. It depends on $\mathbf{Z}$ and the slow coordinate conjugate to θ which we call J, since it is an *action variable*.

In the body of the paper we presented the evolution equation for $F_0(\mathbf{Z},J,t)$ (called F_0' there) correct to order R^0 and R^1. It reads

$$\{F_0(\mathbf{Z},J,t), H_0(\mathbf{Z},J,t,K)\} = 0, \qquad (126)$$

where

$$H_0(\mathbf{Z},J,t,K) = \frac{gh(\mathbf{Z},t)}{R} + \left(\mathscr{F}(\mathbf{Z},t)J + \frac{|\mathbf{G}(\mathbf{Z},t)|^2}{2} \right) - K, \qquad (127)$$

in which the height is a function of $\mathbf{Z} = (Z_1, Z_2)$ and time, and

$$\mathbf{G}(\mathbf{Z},t) = g[\hat{z} \times \nabla_z h(\mathbf{Z},t)]/f(\mathbf{Z}) \qquad (128)$$

is the local geostrophic velocity in a system rotating about the $\hat{z}$ axis at a rate $f(\mathbf{Z})/2$. The total vorticity

$$\mathscr{F}(\mathbf{Z},t) = f(\mathbf{Z}) + R\hat{z} \cdot \text{curl}_z \, \mathbf{G}(\mathbf{Z},t) \qquad (129)$$

enters as well.

In (126) the Poisson brackets are

$$\{Z_a, Z_b\} = -\epsilon_{ab} R/\mathscr{F}(\mathbf{Z},t), \quad a,b = 1 \text{ or } 2,$$

$$\{\mathbf{Z}, K\} = \frac{R}{\mathscr{F}} \hat{b} \times \frac{\partial \mathbf{G}}{\partial t}, \qquad (130)$$

$$\{t, K\} = -1.$$

These Poisson brackets are correct to all orders in R while H_0 and F_0 each have corrections of order R. The fact that the Poisson brackets are known to all orders in R means that whatever approximations are made to the Hamiltonian to

arrive at approximate equations of motion those equations retain the full symplectic structure essential in Hamiltonian systems. Direct expansion of the equations of motion, though formally accurate to the same apparent order in Rossby number, will fail to maintain the Hamiltonian structure.

This is a nonlinear equation for $F_0(\mathbf{Z},J,t)$ alone when we recall that $h(\mathbf{Z},t)$ is determined by

$$h(\mathbf{Z},t) = 2\pi\mathscr{F}(\mathbf{Z},t)\int dJ\, F_0(\mathbf{Z},J,t) + O(R). \quad (131)$$

The equation for $F_0(\mathbf{Z},J,t)$ requires solving for a scalar function over a two-dimensional set of coordinates.

If we have, in fact, solved for $F_0(\mathbf{Z},J,t)$, how do we reconstruct the original Eulerian height and horizontal velocity? The height $h(\mathbf{x},t)$ is given directly by the previous equation [131]. The horizontal velocity is recovered by

$$\mathbf{u}(\mathbf{x},t) = \frac{1}{h(\mathbf{x},t)}\int d^2v\, \mathbf{v}F(\mathbf{x},\mathbf{v},t) \quad (132)$$

$$= \frac{1}{h(\mathbf{x},t)}\int d^2v\, d^2y\, \mathbf{v}\delta^2(\mathbf{x}-\mathbf{y})F(\mathbf{y},\mathbf{v},t). \quad (133)$$

The geostrophic velocity $\mathbf{G}(\mathbf{x},t)$ we can obtain directly from $h(\mathbf{x},t)$ itself through (131). However, we would like to know the order-R departures of the velocity from the geostrophic velocity in terms of our Darboux-transformed phase space density function $F_0(\mathbf{z},t)$. In terms of the original variables $\mathbf{z} = (\mathbf{x},\mathbf{v})$ the difference between the fluid velocity and geostrophic velocity is given by

$$h(\mathbf{y},t)\{\mathbf{u}(\mathbf{y},t)-\mathbf{G}(\mathbf{y},t)\} = \int d^4z\,\delta^2(\mathbf{x}-\mathbf{y})\mathbf{V}F(\mathbf{x},\mathbf{v},t). \quad (134)$$

Transforming the integral to the $\mathbf{z}' = (\mathbf{Z},\theta,J)$ variables, this becomes

$$h(\mathbf{y},t)\{\mathbf{u}(\mathbf{y},t)-\mathbf{G}(\mathbf{y},t)\}$$
$$= \int d^2Z\, d\theta\, dJ\, \frac{\partial(\mathbf{z})}{\partial(\mathbf{z}')}V^2(\mathbf{z}')\hat{c}(\theta)$$
$$\times\delta^2(\mathbf{x}(\mathbf{z}')-\mathbf{y})F(\mathbf{z}'), \quad (135)$$

where $V^2(\mathbf{z}')$ is given by Eq. (103). Now using our power series expansions giving $\mathbf{z}'$ as a function of $\mathbf{z}$ through Eqs. (99) and (103), we obtain as functions of $\mathbf{z}'$ each of $\partial(\mathbf{z})/\partial(\mathbf{z}')$, $V^2(\mathbf{z}')$, and $\delta^2(\mathbf{x}(\mathbf{z}')-\mathbf{y})$ up to order R.

The order-R contributions of $F(\mathbf{z}')$ to the integral require a little more care but fortunately are expressible wholly in terms of $F_0(\mathbf{z}')$. We have

$$F(\mathbf{z}') = F_0(\mathbf{Z},J,t) + RF_1(\mathbf{Z},\theta,J,t) + O(R^2). \quad (136)$$

From Eq. (117), F_1 satisfies

$$F_1(\mathbf{Z},J,\theta,t) = \frac{1}{\mathscr{F}(\mathbf{Z},t)}\frac{\partial F_0(\mathbf{Z},J,t)}{\partial J} H'_1(\mathbf{Z},J,\theta,t)$$
$$+ \phi_1(\mathbf{Z},J,t), \quad (137)$$

where ϕ_1 is an unknown function of $\mathbf{Z}$ and J only. In fact, the only θ dependence of f_1 arises from H'_1, which has the explicit expression

$H'_1(\mathbf{Z},\theta,J,t)$
$$= \frac{(2\mathscr{F}J)^{3/2}}{3\mathscr{F}^2}\hat{a}\cdot\nabla\mathscr{F} + \frac{(2\mathscr{F}J)^{1/2}}{\mathscr{F}}\mathbf{G}\cdot([\hat{a}\cdot\nabla_\mathbf{z}]\mathbf{G})$$
$$+ 2Ja_ic_j\left(\frac{\partial G_j}{\partial Z_i} + \frac{G_j}{3\mathscr{F}}\frac{\partial\mathscr{F}}{\partial Z_i}\right)$$
$$+ \frac{gJ}{\mathscr{F}}a_ia_j\left(\frac{\partial^2h}{\partial z_i\partial Z_j} - \frac{1}{3\mathscr{F}}\frac{\partial\mathscr{F}}{\partial Z_i}\frac{\partial h}{\partial Z_j}\right)$$
$$- \frac{g}{\mathscr{F}^2}(2\mathscr{F}J)^{1/2}\hat{b}\cdot(\nabla_\mathbf{z}\times\mathbf{G})\hat{a}\cdot\nabla h, \quad (138)$$

with sums over repeated indices understood.

Now in each of $\partial(\mathbf{z})/\partial(\mathbf{z}')$, $V^2(\mathbf{z}')$, and $\delta^2(\mathbf{x}(\mathbf{z}')-\mathbf{y})$, when expressed as functions of $\mathbf{z}'$, θ dependence appears only at order R. Thus in (135), $\phi_1(\mathbf{Z},J,t)$ makes no contributions at order R to the integral [its θ integral vanishes because of the presence of the $\hat{c}(\theta)$ factor]. Armed with these facts, we return to (135). The integrations over $\mathbf{Z}$ are carried out using the delta function; θ may also be integrated over since the θ dependence of all factors is known explicitly (at order R). We find, for the corrections to the geostrophic velocity,

$$h(\mathbf{y},t)\{\mathbf{u}(\mathbf{y},t)-\mathbf{G}(\mathbf{y},t)\}$$
$$= \frac{Rh(\mathbf{y},t)}{\mathscr{F}(\mathbf{y})}\{\hat{b}\times\mathbf{G}(\mathbf{y},t)\cdot\nabla_\mathbf{y}\mathbf{G}(\mathbf{y},t)\}$$
$$+ 2\pi R\hat{b}\times\left[\nabla_\mathbf{y}\left(\mathscr{F}(\mathbf{y})\int dJ\, JF_0(\mathbf{y},J,t)\right)\right]$$
$$+ O(R^2). \quad (139)$$

In formulating the phase space density description of inviscid fluids we were able to describe *barotropic* fluids where the pressure is a function only of a density $D(\mathbf{x},t)$, which satisfies

$$\frac{\partial}{\partial t}D(\mathbf{x},t) + \nabla_\mathbf{x}\cdot\{\mathbf{u}(\mathbf{x},t)D(\mathbf{x},t)\} = 0. \quad (140)$$

We were also able to describe *incompressible* fluids. The "density" that appears in different fluid problems was either the shallow water height $h(\mathbf{x},t)$, the isopycnal depth $h_\rho(\mathbf{x},\rho,t)$ or the mass density itself.

One wonders whether a general, isentropic or isothermal inviscid flow satisfying

$$\left(\frac{\partial}{\partial t}+\mathbf{u}\cdot\nabla_\mathbf{x}\right)\mathbf{u} = -\frac{1}{\rho}\nabla_\mathbf{x}p(\rho,\chi) + \mathbf{u}\times\mathbf{\Omega}(\mathbf{x}) - \nabla\Phi(\mathbf{x}), \quad (141)$$

$$\frac{\partial}{\partial t}\rho(\mathbf{x},t) + \nabla_\mathbf{x}\cdot(\mathbf{u}\rho) = 0, \quad (142)$$

and

$$\left(\frac{\partial}{\partial t}+\mathbf{u}\cdot\nabla_\mathbf{x}\right)\chi(\mathbf{x},t) = 0 \quad (143)$$

can be described in the same fashion. In these equations $\chi(\mathbf{x},t)$ is a specific entropy for isentropic flows or temperature for isothermal flows, Φ is a potential, and $\Omega(\mathbf{x})/2$ is the rotation rate of the frame.

The answer to the question comes down to this geometric problem: if $z = (x,v)$ are six-dimensional phase space coordinates and one is given the vector field on z,

$$V_\alpha(z) = \begin{cases} v, & \alpha = 1,2,3, \\ -1/\rho(x) + v \times \Omega(x) - \nabla\Phi(x), & \alpha = 4,5,6, \end{cases}$$

(144)

can one find a Hamiltonian $H(z)$ and Poisson brackets $\{z_\alpha, z_\beta\}$ such that

$$\{z_\alpha, z_\beta\}\frac{\partial H}{\partial z_\beta} = V_\alpha(z)?$$

(145)

The answer is that one may always do this *locally* in z space provided the Poisson tensor $\sigma_{\alpha\beta}(z) = \{z_\alpha, z_\beta\}$ is nondegenerate; that is, $\det \sigma(z) \neq 0$. Whether one can find $H(z)$ and $\sigma_{\alpha\beta}(z)$ *globally* is a harder issue. Both these matters will be taken up in detail in a forthcoming article by the present authors.

While it may prove to be of value in other investigations of the Hamiltonian or symplectic structure of inviscid flows, we have seen already in the detailed application to the Rossby number expansion of a rapidly rotating layer of shallow water that the phase space density representation provides a very convenient template upon which to make physically motivated approximations to the dynamical equations of inviscid flows.

ACKNOWLEDGMENTS

APPENDIX: FORMAL SOLUTIONS TO EQS. (88), (89), AND (93) OF SEC. V

We think of the Darboux coordinates Z, J, and K as functions of the old variables (x,θ,V,T,k) and write out Eqs. (88), (89), and (93) correspondingly:

$$\{Z_\alpha, \theta\} = 0 = \{x,\theta\}\cdot\frac{\partial Z_\alpha}{\partial x} + \{V,\theta\}\frac{\partial Z_\alpha}{\partial V},$$

(A1)

$$\{J,\theta\} = -\frac{1}{R} = \frac{\partial J}{\partial V}\{V,\theta\} + \{x,\theta\}\cdot\frac{\partial J}{\partial x},$$

(A2)

$$\{K,\theta\} = 0 = \{k,\theta\} + \frac{\partial K}{\partial V}\{V,\theta\} + \{x,\theta\}\cdot\frac{\partial K}{\partial x}.$$

(A3)

In writing these equations we have assumed $\partial Z_\alpha/\partial k = \partial J/\partial k = 0$ and $\partial K/\partial k = 1$. We can do this consistently since the Poisson brackets (83) do not depend on k. Using (83), Eqs.

(A1)–(A3) may be written

$$\frac{\partial Z_\alpha}{\partial V} = -\frac{R\hat{a}}{\mathscr{F}}\cdot\nabla_x Z_\alpha,$$

(A4)

$$\frac{\partial J}{\partial V} + \frac{R\hat{a}}{\mathscr{F}}\cdot\nabla_x J = \frac{V}{\mathscr{F}},$$

(A5)

$$\frac{\partial K}{\partial V} + \frac{R\hat{a}}{\mathscr{F}}\cdot\nabla_x K = \frac{R\hat{a}}{\mathscr{F}}\cdot\frac{\partial G}{\partial t}.$$

(A6)

We can write a formal solution to Eq. (A4) easily by expanding Z_α in a power series,

$$Z_\alpha(x,v,\theta,t) = \sum_{n=0}^{\infty} \frac{V^n}{n!}\left(\frac{\partial^n Z_\alpha}{\partial V^n}\right)_{V=0}.$$

(A7)

From Eq. (A4) this is just

$$Z_\alpha = \sum_{n=0}^{\infty}\frac{(-1)^n}{n!}(VRL)^n Z_\alpha\Big|_{V=0}$$

$$= e^{-VRL}Z_\alpha\big|_{V=0},$$

where

$$L = (\hat{a}/\mathscr{F})\cdot\nabla_x.$$

(A8)

Finally we set $Z_\alpha|_{V=0} = x_\alpha$, for physical reasons elaborated on in the text, so that

$$Z_\alpha = e^{-VRL}x_\alpha.$$

(A9)

For Eqs. (A5) and (A6) we proceed in a slightly different fashion. We consider the ordinary differential equation

$$\frac{dx}{dV} = \frac{R\hat{a}}{\mathscr{F}}.$$

(A10)

By the same method by which we obtained (A9) we can write down a formal solution to (A10):

$$x = e^{VRL}x_0,$$

(A11)

where $x_0 = x|_{V=0}$. In fact, for any function $\phi(x(V))$ of x we have, by the same reasoning,

$$\phi(x) = e^{VRL}\phi(x_0).$$

(A12)

Now using (A10) and (A12) we can write (A5) and (A6) as

$$\frac{dJ}{dV} = Ve^{VRL}\frac{1}{\mathscr{F}(x_0)},$$

(A13)

$$\frac{dK}{dV} = Re^{VRL}\frac{\hat{a}}{\mathscr{F}(x_0)}\cdot\frac{\partial G(x_0)}{\partial t}.$$

(A14)

We do not indicate θ and t dependences in the right-hand sides of (A13) and (A14) as these play an entirely passive role here. In (A13) and (A14) the V dependence is now explicit since x_0 does not depend on V, so we can formally integrate these equations to obtain

$$J = \frac{1 + RVLe^{RVL} - e^{RVL}}{(RL)^2}\frac{1}{\mathscr{F}(x_0)},$$

(A15)

$$K = k + R\frac{e^{RVL}-1}{RL}\frac{\hat{a}}{\mathscr{F}(x_0)}\cdot\frac{\partial G(x_0)}{\partial t},$$

(A16)

where we have made the choices $J|_{V=0} = 0$ and $K|_{V=0} = k$. The reason for these choices is elaborated on in the text. Note that the appearance of the operator L in the denominators in (A15) and (A16) causes no ambiguity as the numerators are defined by their power series expansions,

2963   Phys. Fluids, Vol. 30, No. 10, October 1987

H. D. I. Abarbanel and A. Rouhi   2963

which begin at L^2 and L, respectively, in (A15) and (A16). Finally in (A15) and (A16) we have J and K as functions of (x_0, θ, V, t, k) whereas we want them as functions of (x, θ, V, t, k). This is easily obtained using the inverse (A12) for any $\phi(x_0)$:

$$\phi(x_0) = e^{-VRt \cdot} \phi(x).$$

(A17)

Using this in (A15) and (A16) we have

$$J = \frac{e^{-RVt} - 1 + RVL}{(RL)^2} \frac{1}{\mathscr{F}(x)}$$

$$= \left(\sum_{n=0}^{\cdot} \frac{(-R)^n V^{n+2} L^n}{(n+2)!} \right) \frac{1}{\mathscr{F}(x)},$$

(A18)

and

$$K = k + R \cdot \frac{1 - e^{-RVt}}{RL} \frac{\hat{a}}{\mathscr{F}(x)} \cdot \frac{\partial G(x)}{\partial t}$$

$$= k + \left(R \sum_{n=0}^{\cdot} \frac{(-R)^n V^{n+1} L^n}{(n+1)!} \right) \frac{\hat{a}}{\mathscr{F}(x)} \cdot \frac{\partial G(x)}{\partial t}.$$

(A19)

Equations (A9), (A18), and (A19) constitute then our power series expressions for the Darboux coordinates in terms of the old coordinates.

[1]C. Eckart, Phys. Fluids 3, 421 (1960).
[2]R. Salmon, in *Mathematical Methods in Hydrodynamics and Integrability in Dynamical Systems, Conference Proceedings 811225*, edited by M. Tabor and Y. M. Treve (American Institute of Physics, New York, 1982), Vol. 88, p. 127.
[3]R. Salmon, J. Fluid Mech. 132, 431 (1983).
[4]H. D. I. Abarbanel and D. D. Holm, Phys. Fluids, in press.
[5]D. D. Holm, J. E. Marsden, T. Ratiu, and A. Weinstein, Phys. Rep. 123, (1985).
[6]W. W. Lee, Phys. Fluids 26, 556 (1983).
[7]W. W. Lee, J. A. Krommes, C. R. Oberman, and R. A. Smith, Phys. Fluids 27, 2652 (1984).
[8]A. E. Gill, *Atmosphere-Ocean Dynamics* (Academic, New York, 1982).
[9]This example was suggested to us by Bruce Long, with whom we had most fruitful discussions on its physical content.
[10]R. G. Littlejohn, J. Math. Phys. 20, 2445 (1979).
[11]E. C. G. Sudarshan and N. Mukunda, *Classical Dynamics: A Modern Perspective* (Krieger, Malabar, FL, 1974).
[12]R. Abraham, and J. E. Marsden, *Foundations of Mechanics* (Benjamin, Reading, MA, 1978), 2nd ed.
[13]A. J. Lichtenberg and M. A. Lieberman, *Regular and Stochastic Motion* (Springer, New York, 1983), Chap. 3.
[14]V. I. Arnol'd, *Mathematical Methods of Classical Mechanics* (Springer, New York, 1978).
[15]D. H. E. Dubin, J. A. Krommes, C. Oberman, and W. W. Lee, Phys. Fluids 26, 3524 (1983).

APPROACHES TO ACOUSTIC BACKSCATTERING MEASUREMENTS FROM
THE DEEP SEAFLOOR

C. de Moustier

Marine Physical Laboratory
Scripps Institution of Oceanography
University of California, San Diego
La Jolla, California

1. ABSTRACT

Because the average ocean depth is four kilometers, seafloor investigations are mostly remote sensing operations. The primary means to determine the morphology, the structure, and the texture of the seafloor are acoustic. This paper considers the current seafloor remote sensing approaches involving acoustic backscattering. The physical constraints imposed by the ocean as a propagation medium, by the seafloor as a backscattering boundary, and by the measuring instruments are briefly reviewed. The sonar systems currently used by the oceanographic community for deep seafloor acoustic backscattering measurements deal with these constraints differently depending on their specific application and on whether they are towed behind a ship or mounted on her hull.

Towed sidescan systems such as Gloria II (U.K.), the Sea Mapping and Remote Characterization (Sea MARC) I and II, the Deep Tow system of the Marine Physical Laboratory (MPL), and hull-mounted systems such as Swathmap all give a qualitative measure of backscattering by converting echo amplitudes to gray levels to produce a sidescan image of the seafloor. A new approach is presented which uses a Sea Beam multibeam echo-sounder to produce similar acoustic images.

Quantitative measurements of backscattering have been attempted in recent experiments using the Deep Tow system and Sea Beam. Such measurements provide some insight into the geological properties responsible for the acoustic backscatter, with useful applications for geologists as well as designers and operators of bottom-interacting sonars.

2. INTRODUCTION

With an average depth of four kilometers, the ocean floor is only accessible by special purpose submersibles from which observations are limited by the aperture of a view port. For this reason, most seafloor investigations are remote sensing operations which use underwater sound as their primary tool and core or grab sample as well as bottom photography as ground truth. Seafloor acoustic measurements are commonly divided in two broad categories: low frequency (< 100 Hz) seismic measurements in reflection or refraction work, and high frequency (> 3 kHz) reflectivity or backscattering measurements. This paper focuses on the high frequency seafloor acoustic backscatter which is on one hand a noise background against which active sonars must operate, and on the other hand a source of information for geologists because its variations are caused by changes in bottom type or bottom microroughness.

The systems currently used by the oceanographic community to measure acoustic backscatter from the deep seafloor are most often sidescan sonars or echo-sounders, and occasionally specially designed multifrequency arrays. Sidescan sonars give a qualitative measure of backscattering by converting echo amplitudes to gray levels in the process of forming an acoustic image of the seafloor, and their resolution depends on a combination of parameters such as frequency, pulse length, beamwidth ... [1]. The same parameters apply to echo-sounders whose primary output is numerical bathymetry. However, broad-beam ($\geqslant 30°$) echo-sounders have been used to obtain quantitative normal-incidence measurements in an effort to classify bottom types [2] or bottom microroughness [3]. Based on the author's work, this paper shows that multi-narrowbeam echo-sounders such as Sea Beam [4], [5] provide a means to obtain both quantitative seafloor acoustic backscattering measurements at discrete angles of incidence and qualitative measures in an acoustic imaging mode which is new to such systems.

In the following, the physical constraints which condition the performance of sonar systems are reviewed briefly. The approaches taken in the design of several operational systems are compared, and recent experiments involving Sea Beam and multifrequency arrays are presented.

3. SONAR DESIGN CONSTRAINTS

This section briefly reviews the constraints imposed by the ocean as a propagating medium, by the seafloor as a backscattering boundary and by the physical characteristics of the sonar on the design of systems to measure seafloor acoustic backscatter. More exhaustive treatments on the subject may be found in references [6] and [7].

As sound waves propagate through the water column, they are attenuated due to spherical spreading and absorption. The former increases as the square of range and the latter increases roughly as the square of frequency. This frequency dependence is usually imbedded in a logarithmic absorption coefficient α in decibels per meter (e.g., $\alpha \sim 10^{-3}$ dB/m at 10 kHz) which sets limits on the operating frequency of a sonar for a given range. The deep-water ambient-noise level is also frequency dependent and decreases 5 to 6 dB per octave in the interval 1-100 kHz. At long ranges, attenuation dominates and adversely counterbalances improvements in ambient-noise characteristics obtained by using higher frequencies. Expressed in decibels, the attenuation terms add into a transmission loss:

$$TL = 20log_{10} r + \alpha r \qquad (1)$$

where the slant range r is in meters. The propagation medium also imposes horizontal range limitations on sound waves as they are refracted

due to variations in the sound velocity with temperature and pressure. In practice, the range limitation due to ray-bending depends on water depth and bottom relief. At oceanic depths ($\geqslant 4$ km) the maximum horizontal range attainable with a sonar at the sea surface is between 30 and 40 km [8].

Bottom relief enters as a geometrical parameter in the range limitation, but for a given relief, bottom type and bottom microroughness condition the backscattering process. Whether a body backscatters sound effectively depends on how its density and compressibility differ from those of the surrounding ocean, and how its roughness scale compares to the acoustic wavelength. There is no simple theory to predict the level of seafloor-backscattered sound waves, and one relies on reported measurements (mostly done in shallow water, e.g., references [9], and [10]) and geoacoustic models [11] to derive empirical expressions for bottom back-scattering strength as a function of grazing angle and/or frequency for various types of substrates.

In practice, the bottom backscattering strength BS, in decibels, is expressed as the sum of a backscattering strength per unit area ($1m^2$) S_B and an effective scattering area A :

$$BS = S_B + A \qquad (2)$$

with $S_B = S_0 + 10log_{10} \sin^K\alpha$ and $A = 10log_{10}(\dfrac{r\theta c\tau}{2cos\alpha})$

where as indicated in Fig. 1, r is the slant range, θ the horizontal beamwidth of the transducer, α the grazing angle. τ is the transmitted pulse length, $c = 1500m/s$ the sound speed, and S_0 is a scattering coefficient independent of grazing angle. For most sidescan sonar or echo-sounder applications, a square law dependence on $\sin\alpha$ ($K = 2$) is a reasonable match to existing shallow-water measurements and by extrapolation to the few measurements existing for the deep seafloor [6]. The
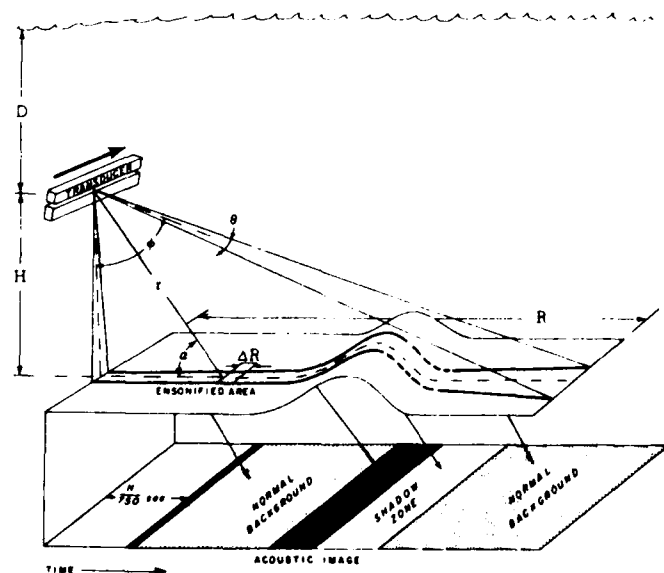
Fig. 1 SIDESCAN GEOMETRY. A transducer array at depth D and elevation H above the seafloor has a beam pattern with angular dimensions θ (horizontal) and Φ (vertical). It ensonifies a strip of seafloor out to horizontal range R at right angle to the direction of travel (arrow). A portion of the strip (broken line) is not ensonified as it is shadowed by the hill. Backscattered acoustic intensities received at the transducer are converted to gray levels and mapped at increasing times of arrival (or slant range r). In this case, the first return is received H/750 s after transmission. On the acoustic image, specular returns appear darker than the normal background and shadow zones are white. Δ R is the cross-track resolution, and α is the grazing angle.

dependence of backscattering on bottom type is taken into account in the scattering coefficient S_0 which increases by nearly 25 dB from clay, through silt and sand to rock; and bottom roughness can cause variations of several dB in S_0 for the same bottom type [9].

As mentioned above, the effects of bottom roughness depend on the operating characteristics of the sonar. To sample the small scale roughness rather than bottom slopes requires a system with narrow horizontal beamwidth and large bandwidth. These parameters are constrained by the physical characteristics of the transducer used.

The bandwidth capability of the transducer is usually limited to 10-15% of the center frequency [12]. Since the range resolution of a system with bandwidth w is $\Delta R = c/2w$, the incentive is to use high frequencies for greater bandwidth and higher range resolution, but attenuation imposes horizontal range limitations and it becomes necessary to operate close to the bottom. The most common and simplest way of acheiving range resolution in sonars is to use short pulsed continuous wave signals (CW) but the shortest acheivable pluse length τ is limited to $\tau = 1/w$. An alternative approach is to use long frequency-modulated (FM) pulses with $w\tau > 1$ and process the returns through matched filters. The advantages of this method are the possibility to use lower frequencies and still maintain adequate range resolution, and a theoretical signal to noise power gain over short CW pulses with equal source level of $10log_{10}(w\tau)$ [1]. However implementation of the correlation processor adds complexity and cost to the overall sonar system design.

The beamwidth requirements are constrained by the size of the transducer array and by its operating frequency. Defining the beamwidth as the width of the mainlobe of the radiation pattern 3 dB down from its on-axis response, the beamwidth θ in radians is roughly the reciprocal of the number of wavelength across the effective aperture of the array i.e. $\theta = \lambda/L$ with $\lambda = c/f$. L is the length of the aperture in meters, λ is the acoustic wavelength in meters and f is the acoustic frequency in Hertz. Consequently, for a given frequency, the longer the array the narrower the beamwidth. However the optimum size of a transducer is a compromise between its directionality and its acoustic-power output capability.

The maximum strain bearable by the transducer and cavitation limit the maximum power to which the transducer can be excited. These constrains set a lower limit on the size of the effective aperture necessary to keep the radiated power per unit area below the cavitation threshold. The power P per unit area necessary to produce cavitation increases as the square of the ambient pressure P_a: $P = P_a^2/2\rho c$ watts/cm^2 where $\rho c = 1.5 \ 10^5 g \ cm^{-2}s^{-1}$ is the acoustic impedance of water [13]. A substantial gain in cavitation threshold is therefore achieved by operating an array a few decameters below the surface with the added advantage of reduced refraction effects as one goes below the thermocline. This technique is used in most shallow-towed sidescan arrays.

In the case of sidescan sonar arrays mounted on either side of a towed vehicle for port-starboard coverage, an additional constraint is imposed on the choice of operating frequency by the existence of mutual interference (cross-talk) between the arrays due to radiation of sound from the back of each array. As a result, a mirror image of returns on one side is mapped on the other side (for examples, see [14]). In general, this problem is alleviated by using slightly different operating frequencies on each side.

Finally, an estimate of the echo-to-noise ratio EN measurable with a given sonar system is obtained through the sonar equation which combines the various aforementioned design parameters. In decibel units, this equation has the form:

$$EN = SL - 2TL - (NL + 10log_{10}w) + BS + 20log_{10}b \ (\Phi) \qquad (3)$$

where SL is the source level, 2TL accounts for the round-trip transmission loss (Eq. 1) between the sonar and the bottom, $(NL + 10log_{10}w)$ is the noise level in the bandwidth w, BS is the backscattering strength (Eq. 2) and $20log_{10}b \ (\Phi)$ accounts for the transducer's vertical directivity.

For most sidescan systems the amplitude corresponding to the echo level is converted to a gray level and output on a linescan recorder to create an acoustic image of the seafloor surveyed. In the process, it is

138

Table 1 OPERATIONAL CHARACTERISTICS

System	Gloria	Swathmap	Sea MARC II	Sea MARC I	Sea Beam	Deep Tow
Frequency (kHz)	P 6.5, S 6.7	3.5	P 11, S 12	P 27, S 30	12 158	110
	FM sweep	FM sweep	CW	CW	CW	CW
Pulse Length τ	2, 4 sec		25-10 ms	15-3 2 ms	7 ms	2, 5 ms
Pulse rep. (sec)	20-40	40-48	1, 2, 4, 8, 16	5, 1, 2 or 4	1-22	1
Bandwidth W	100 Hz		2 kHz→ 100 Hz	5 kHz→ 200 Hz	225 Hz	10 kHz
Beamwidth (deg) θ, Φ	2.7, 30		2, 40	1.7, 50	T 2.7, 54 R 16(20, 2.7)	.75, 60
Cross-track resolution ΔR	20 m		5 m	5 m		.15 m
Tow depth D	30-60 m	hull mount	50-100 m	up to 6 km	hull mount	up to 7.5 km
Tow altitude H				12-1250 m		10-100 m
Horizontal range (km) R	15-30	up to 36	5, 1, 2.5, 5	.25, 5, 1, 2.5	3/8 water depth	5
Speed (knots)	up to 11	up to 20	up to 10	1-3	up to 15	1-2
Array length (m)	5.33		3.8	1.5	T 2.8, R 2.8	1.25
Array width (m)	18		2	2	T .16, R .4	.08
Vehicle length (m)	7.75		5.5	3		2
Vehicle width (m)	8		1.3	1.2		.7

customary to multiply the amplitudes by a time-varied-gain to compensate for transmission losses and keep the returns within the dynamic range of the recording instrument.

4. CURRENT SYSTEMS

The design constraints outlined above are dealt with differently depending on the intended application of the sonar system. In this section, several systems currently used by the oceanographic community are compared on the basis of their design approach, and of the characteristics of the acoustic measurements obtained.

Six systems covering a wide spectrum of ranges in deep-ocean work have been chosen for this comparison. They are the British system Gloria II [15], [16], Swathmap [8], [17], [18], the Sea Mapping and Remote Characterization systems (Sea MARC I and II) [19], [20], [21], Sea Beam and the Deep Tow instrument package [22], [23]. The operating characteristics of these systems are listed in Table 1 where symbols appearing in Section 3 and Fig. 1 have been repeated for ease of correspondence.

Gloria II, Sea MARC I and II and Deep Tow are original sidescan sonar systems whereas Sea Beam is a multibeam echo-sounder and Swathmap is a sidescan application of the SQS-26 ASW sonar used aboard U. S. Navy frigates. The table is incomplete for Swathmap because some of the technical details of the system are classified. In the Swathmap design, a beam is steered to one side of the ship's track only with a maximum horizontal range of about 36 km and a cross-track resolution of several hundred meters. The high ship speed results in a poor along track resolution as transmit cycles are spaced 400 to 500 m apart at 20 knots (~10m/s). This system is primarily a reconnaissance tool designed to map at a rapid rate the large scale seafloor relief such as seamounts or fracture zones, and the intermediate relief (50-100m) typical of abyssal hills. Although the acoustic backscatter measured with Swathmap is modulated by bottom texture, it is dominated by slope effects, and the records are qualitative representations of bottom slopes and regional trends.

Similar measurements, with greater along and across-track resolution, are obtained with Gloria II which records acoustic backscattering from both sides of a shallow-towed vehicle. Different frequencies are used in the port and starboard arrays to avoid cross-talk between them. To enhance its signal to noise characteristics, this system uses a long transmit pulse and processes the echoes by match-filtering techniques. The records are automatically corrected from slant range to horizontal range by projecting slant range onto a horizontal plane at the mean depth below the vehicle [Searle, personal communication]. Measurements are qualitative and recorded acoustic returns are usually dominated by bottom slopes with marginal indication of textural changes [25]. The strength of this systems is its ability to map with sufficient detail large swaths of seafloor (30 km or more) at an average tow speed of 8 knots.

The Sea MARC II system is also a shallow-tow vehicle with port-starboard coverage and a tow-speed capability comparable to that of Gloria II. It operates at higher frequencies and uses short transmit pulses resulting in better cross-track resolution but reduced horizontal ranges (Table 1). In order to maintain even spacing between data points in the sidescan image, the bottom returns are sampled more rapidly at close ranges than at far ranges. As with Gloria II, the records are automatically corrected for slant range by assuming a flat plane at the mean depth below the vehicle. Due to its finer resolution, the qualitative bottom backscattering measurements obtained from Sea MARC II images are useful for bottom slope and texture determination on a scale of acoustic wavelengths (~12 cm), and for large scale regional trend determination. Sea MARC II uses a pair of transducer arrays (e.g. Fig. 1) on each side of the vehicle. By measuring the phase difference between the outputs of the two arrays, it is possible to determine the angle of arrival of a given return and therefore compute the corresponding depth and cross-track distance. In a post-processing operation, approximately one hundred such pairs of depths and cross-track distances are computed for every transmission cycle, and are used to produce a contour map of the swath of seafloor surveyed. This bathymetry is an important element in the interpretation of backscattering measurements made with the system, because it offers the potential to remove bottom slope effects from the data while in principle retaining the effects of bottom composition and microroughness.

The Sea MARC I system is a deep-towed version of Sea MARC II with a lesser swath width (5 km maximum). Its use of higher frequencies and short pulse lengths yields sub-meter cross-track resolution; and its inherent slow speed over the bottom yields an along-track resolution between .5 and 5 m, depending on the pulse repetition rate (Table 1). Although this system uses the same transducer array pair configuration as Sea MARC II, the phase measurement technique is not implemented. Without numerical bathymetry, it is therefore not possible to correct the backscattering measurements for bottom slope. Nontheless, the fine resolution of the sonar allows detection of changes in bottom texture over areas of constant slope between 10 and 100 m in extent depending on the swath width chosen.

Through a combination of frequency, pulse length and tow speed, the sidescan sonars of the Deep Tow instrument package achieve the highest resolution of all the systems listed in Table 1. The lateral coverage to port and starboard is inherently limited to a swath about 1 km wide. This system is primarily intended for fine scale studies of the seafloor down to depths in excess of 7 km. The backscatter measurements are qualitative gray scale displays uncorrected for slant range. Changes in bottom texture are readily observable and micro-relief ($\leqslant 1m$) such as small fissures is resolvable on such displays. However, the limited coverage of the sonars make the system marginally useful for regional trend assess-

ment as it requires long and costly surveys. The strength of the Deep Tow instrument package is its versatility as environmental (e.g. temperature, conductivity) and other geophysical (e.g. magnetics, subbottom profiles) data can be collected simultaneously with the sidescan data; and bottom photographs can be taken on the same lowering [22]. The phase measurement technique mentioned above is feasible but not implemented on the Deep Tow system.

5. NEW APPROACHES

The systems described in section 4 all operate as sidescan sonars. As such they provide qualitative acoustic backscattering measurements of the deep seafloor. This section looks at new measurement approaches using multibeam echo-sounders such as Sea Beam or experimental multifrequency acoustic arrays mounted on instrument packages such as Deep Tow [24].

Sidescan sonars typically transmit and receive with the same fan-shaped beam which is narrow along track and broad across track (Fig. 1). The Sea Beam system transmits with a similar geometry, but it receives with sixteen narrow beams spaced 2° 2/3 apart athwartships within ± 20° incidence. Each receive beam is 2° 2/3 wide. With this geometry, the system is able to process backscattered returns (Fig. 2) at discrete angles of incidence and calculate a set of depths and cross-track distances for each transmission cycle. This numerical bathymetry is then output in near real-time as a contoured chart of the swath of seafloor surveyed.

Sea Beam processes the acoustic signals to determine depths but has no internal provision for recording the actual waveform. To preserve these signals, requires a parallel acoustic data acquisition system which records digitally the echo envelopes on magnetic tape for later processing and analysis. Such a system developed at MPL was used by the author to record Sea Beam acoustic data [26]. A typical set of returns corresponding to one transmission cycle is illustrated in Fig. 2. These data make it possible to obtain quantitative backscattering measurements at discrete angles of incidence. Because variations in bottom characteristics cause fluctuations in the acoustic backscatter, and because numerical bathymetry allows corrections for slope effects to be made, the geological characteristics of the seafloor (e.g. microroughness or bottom type) can be inferred in part from these measurements [27], [28], [29].

In a new application of Sea Beam system, the acoustic returns it receives are used in a sidescan-like mode by combining echoes on either side of vertical incidence. Working with digitally recorded Sea Beam acoustic data (Fig. 2) a peak detection process is used to obtain echo

amplitudes at incremental slant ranges to port and starboard. This process starts at the first arrival of each transmission cycle. An example of the resulting acoustic image is shown in Fig. 3 along with the corresponding Sea Beam bathymetry, and a Sea MARC I image of the same region included for comparison. In this example, the Sea Beam acoustic image is not corrected for slant range or for angle of incidence. However, as Sea Beam computes a cross-track bathymetric profile every transmission cycle, slant range corrections can be performed without the ambiguities inherent to the conventional horizontal plane method mentioned previously. The correction for angle of incidence entails ampl ng a time-varied-gain to the signals displayed in order to compensate for the drop in backscatter as a function of angle. Such a correction is performed in most sidescan systems and yields an acoustic image having nearly uniform resolution out to the edges.

This new acoustic imaging application of Sea Beam gives textural information about the seafloor and brings out seafloor features not discernible in the contoured bathymetry. Unlike conventional sidescan images (Fig. 1), acoustic images obtained with Sea Beam do not contain shadows because angles of incidence are limited to the range ± 20°, (note that most sidescan sonars do not record data in this angular sector). The qualitative measure of backscatter given by these images is therefore representative of seafloor microroughness and bottom slopes. The effect of bottom slopes can also be removed from the backscatter data given that quantitative slope information is available in Sea Beam's bathymetry.

The advantage of Sea Beam's discrete narrow beams can also be preserved by outputting the echo character on each beam in a gray level display such as that of Fig. 4. Although this display is more difficult to interpret than conventional sidescan images, it gives bottom structural details which are smoothed out in the processing used to create the acoustic image of Fig. 3b.

As mentioned in Section 3, the effects of the seafloor as an acoustic backscattering boundary are difficult to predict, and one relies on measured data to derive empirical backscattering models usable by designers of sonar systems [30]. However, there is a definite need for deep seafloor measurements as the existing data base is very limited. Systems such as Sea Beam give access to quantitative measurements as a function of angle of incidence within the limits of the available beamwidth. Recent experiments to obtain quantitative measurements as a function of frequency have also been carried out using multifrequency arrays (4.5, 9, 15, 28, 60, 110, 160 kHz) mounted on the stern of the Deep Tow instrument package, and projecting fan beams pointing aft [24].

In general single frequency measurements give non-unique answers about the nature of the seafloor because there is an infinite combination of roughness and bottom type influencing the backscattering process, and measurements need to be validated by direct bottom sampling or by bottom photographs or television. On the other hand, multiple frequency systems allow simultaneous sampling of several roughness scales thereby giving some indication of the respective contribution of roughness and bottom type in the backscattering process. Such measurements may eventually help geologists to acoustically differentiate between bottom types, or determine the size of bottom microrelief (e.g. furrows, manganese nodules, etc.). Similar multifrequency measurements have been obtained with conventional hull-mounted echo-sounders in an effort to determine the size of polymetallic nodules [31].

6. CONCLUSIONS

In the remote sensing of the deep seafloor, acoustic backscattering can be measured with sidescan sonars or echo-sounders. Sidescan sonars usually provide qualitative measurements of backscattering which allow geologists to make regional structural analysis and textural assessments of the seafloor, with a resolution depending on the operating characteristics of the sonar. A new application of the Sea Beam system in an acoustic imaging mode has been shown to yield similar qualitative measurements whose usefulness is enhanced by the precision numerical bathymetry normally available with this system. The Sea Beam also offers the potential to obtain quantitative backscattering measurements as a function of angle

Fig. 2 ENVELOPES OF ECHOES RECEIVED BY SEA BEAM'S 16 BEAMS. Beams are equally spaced 2° 2/3 apart within ± 20° of the ship's vertical axis. In this display, returns are not compensated for ship's roll. Time is in seconds after transmission. Amplitudes have been corrected for transmission loss by a time-varied-gain and are displayed in volts.

Fig. 3 ACOUSTIC IMAGES AND BATHYMETRY. (a) Slant-range corrected SeaMARC I image of the crest of the East Pacific Rise at 10° N [32]. Distances are true horizontal distances. (b) Uncorrected Sea Beam image of the same area; the dashed line in (a) represents the corresponding Sea Beam track. The cross-track dimension is in seconds from first arrival (differential slant range). (c) Corresponding swath of Sea Beam bathymetry at 10 m contour interval. Tick marks point downhill.
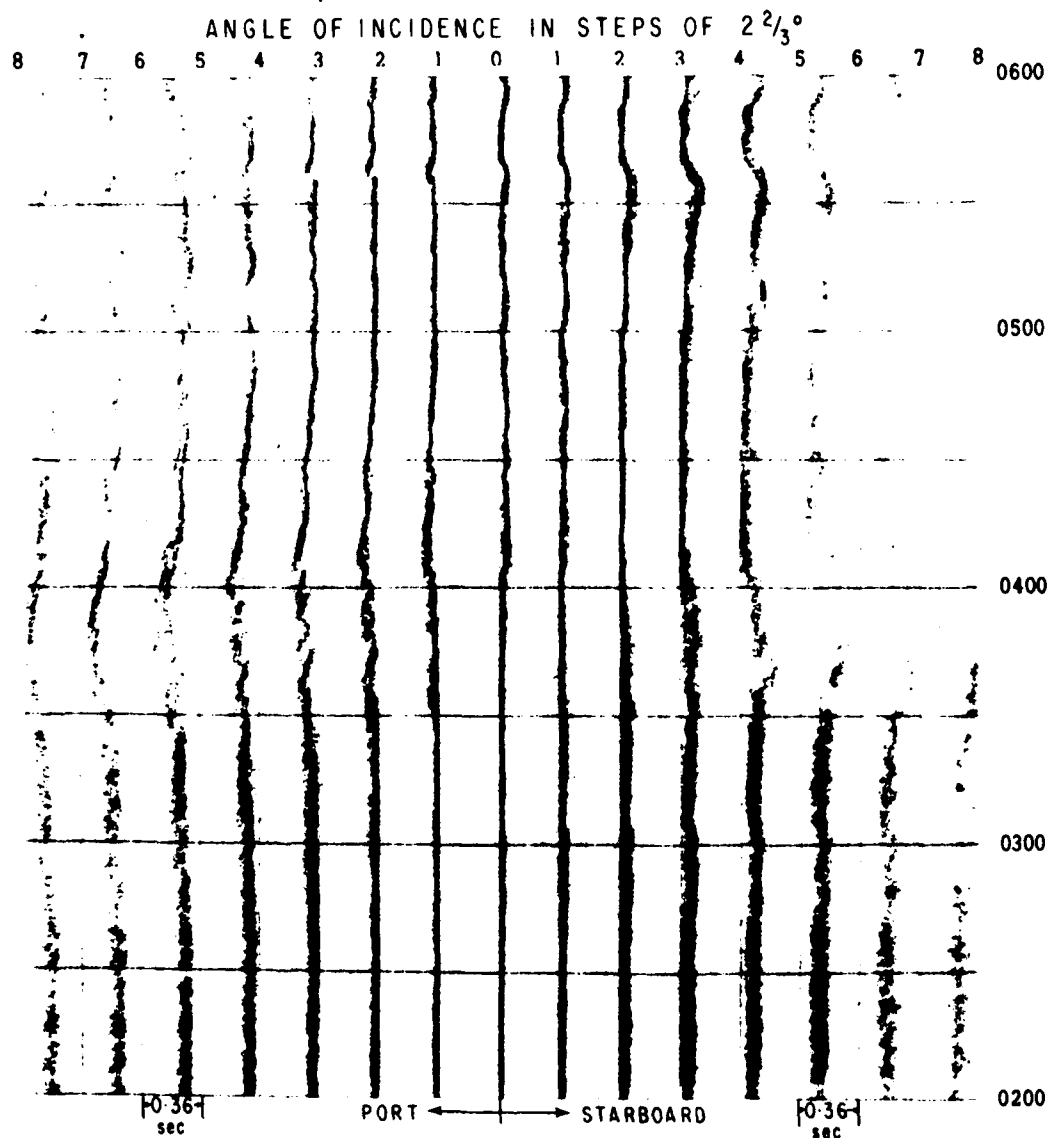
Fig. 4 ECHO CHARACTER OF INDIVIDUAL ROLL-COMPENSATED BEAMS. Same Sea Beam acoustic data as that of Fig. 3. At each angle of incidence, vertical grid lines mark the time of first arrival for each transmission cycle, and echoes are displayed in bins .36s wide. The gap between a grid line and the corresponding return is the differential slant range.

142

of incidence. Because of the complicated nature of the seafloor back-scattering process, these measurements do not give a unique answer about the nature of the seafloor, but they constitute a necessary step towards the understanding of the processes at work, and towards the construction of empirical formulas for sonar design purposes.

Further insight into the processes influencing the seafloor acoustic backscatter are obtainable with multifrequency arrays as they allow simultaneous sampling of several bottom roughness scales. However acoustic measurements alone may never be sufficient to give the exact nature of the seafloor, and ground truth from some other sensing technique (e.g. bottom sampling or photography) may still be necessary.

7. ACKNOWLEDGMENTS

References

[1] A. R. Stubbs, Sidescan sonar, *IEE Proc*, Vol. 131, Part F No. 3, 1984, pp 243-256

[2] L. Breslau, Classification of sea-floor sediments with a shipborne acoustical system, *Woods Hole Ocean. Inst. Contribution No. 1678*, 1967.

[3] T. K. Stanton, Sonar estimates of seafloor microroughness, *J. Acoust. Soc. Am.*, Vol 75-3, 1984, pp 809-818.

[4] H. K. Farr, Multibeam bathymetric sonar: Sea Beam and Hydrochart, *Marine Geodesy*, Vol. 4, No. 2, 1980, pp 77-93.

[5] V. Renard and J. P. Allenou, Seabeam, multi-beam echo-sounding in "Jean Charcot". Description, evaluation and first results, *Internat'l. Hydrogr. Rev. LVI(1)*, 1979, pp 35-67.

[6] R. J. Urick, Principles of underwater sound (3rd ed.), McGraw-Hill, 1983.

[7] C. S. Clay and H. Medwin, Acoustical Oceanography: Principles and Applications, *Wiley Interscience*, 1977.

[8] J. E. Andrews and P. B. Humphrey, Swathmap: Long range sidescan sonar mapping of the deep seafloor, *Marine Geodesy*, Vol. 4, No. 2, 1980, pp 141-159.

[9] H. K. Wong and W. D. Chesterman, Bottom backscattering near grazing incidence in shallow water, *J. Acoust. Soc. Am.* Vol. 44, 1968, pp 1713-1718

[10] C. M. McKinney and C. D. Anderson, Measurements of backscattering of sound from the ocean bottom, *J. Acoust. Soc. Am.*, Vol. 36, 1964, pp 158-163.

[11] E. L. Hamilton, Geoacoustic modeling of the sea floor, *J. Acoust. Soc. of Am.*, Vol. 68, No. 5, 1980, pp 1313-1340.

[12] J. G. Kosalos, Ocean bottom imaging, *OTC 4717*, *Proc. Offshore Technology Conf.*, 1984, pp 65-72.

[13] V. M. Albers, Underwater acoustics Handbook II, The Pennsylvania State University Press, 1965.

[14] R. H. Belderson, N. H. Kenyon, A. H. Stride, and A. R. Stubbs, Sonographs of sea floor, A picture atlas, Elsevier Publishing Co., 1972

[15] M. L. Somers, R. M. Carson, J. A. Revie, R. H. Edge, B. J. Barrow, and A. G. Andrews, Gloria II, an improved long range sidescan sonar, *Oceanology International*, Technical Session J, London, BPS Exhibitions, Ltd., 1978, pp 16-24.

[16] A. S. Laughton, The first decade of Gloria, *J. Geol. Research*, Vol. 86, No. 812, 1981, pp 11511-11534.

[17] P. B. Humphrey, Circular structures observed in the deep sea by the Swathmap long-range side scan sonar, *Bottom-Interacting Ocean Acoustics*, Plenum Publ. Co., New York, N.Y., 1980, pp 111-117.

[18] J. E. Andrews, J. D. Graig and W. A. Hardy, Investigations of the deep-sea floor by side-scan sonar techniques: Central Eastern Pacific, *Deep Sea Research*, Vol. 24, 1977, pp 975-985.

[19] J. G. Blackinton, D. M. Hussong and J. G. Kosalos, First results from a combination side-scan and seafloor mapping system (SEA MARC II), OTC 4478, *Proc. Offshore Technology Conf., Vol. 1, 1983, pp 307-314.*

[20] D. M. Hussong, P. Fryer, Back-arc seamounts and the SEA MARC II seafloor mapping system, *Trans. Am. Geophys. Union*, Vol. 64, No. 45, 1983, pp 627-632.

[21] J. G. Kosalos and D. N. Chayes, A portable system for ocean bottom imaging and charting, *Proc. Oceans '83*, 1983, pp 649-656.

[22] F. N. Spiess and P. F. Lonsdale, Deep Tow rise crest exploration techniques, *Marine Tech. Soc. Journal*, Vol. 16, No. 3, 1982, pp 67-75.

[23] F. N. Spiess and R. C. Tyce, Marine Physical Laboratory Deep Tow instrumentation system, *Scripps Inst. of Oceanog. Ref. 73-4*, 1973.

[24] F. N. Spiess, R. Hessler, G. Wilson, M. Weydert, and P. Rude, Echo I Cruise Report, *Scripps Inst. of Oceanog., Ref. 84-3*, 1984.

[25] P. G. Teleki, D. G. Roberts, P. S. Chavez, M. L. Somers, and D. C. Twichell, Sonar survey of the U.S. Atlantic Continental Slope: Acoustic characteristics and image processing techniques, OTC 4017, *Proc. Offshore Technology Conference*, 1981, pp 93-102.

[26] C. de Moustier, A Sea Beam acoustic data acquisition system, MPL TM-379, *Scripps Inst. of Oceanog. Ref. 85-*, 1985.

[27] C. de Moustier, Inference of manganese nodule coverage from Sea Beam acoustic backscattering data, *Geophysics*, Vol. 50, 1985, pp 989-1001.

[28] C. de Moustier, Beyond bathymetry: Mapping acoustic backscattering from the deep seafloor with Sea Beam, J. Acoust. Soc. Am., (in press).

[29] R. B. Patterson, Relationships between acoustic backscatter and geological characteristics of the deep ocean floor, *J. Acoust. Soc. Am.*, Vol. 46, No. 3, 1967, pp 756-761.

[30] H. Weinberg, Generic sonar model, *Tech. document 5971-C*, Naval Underwater Systems Center, 1981.

[31] Sumitomo Metal Mining Co., Multi-frequency exploration system (MFES), *Techn. info.*, 24-8, 4-Chrome Shimbashi, 1981.

[32] Rise Axis Tectonic Team, An along strike Sea Beam and Sea Marc I perspective of the axis of the East Pacific Rise: Implications for the accretion of oceanic lithosphere, *International Lithosphere Congress*, Texas A&M Univ., 1983.

Internal Wave Observations from *FLIP* in MILDEX

ROBERT PINKEL, ALBERT PLUEDDEMANN* AND ROBIN WILLIAMS**

Marine Physical Laboratory, Scripps Institution of Oceanography, University of California–San Diego, La Jolla, CA 92093

ABSTRACT

During October–November 1983, the Research Platform *FLIP* participated in the Mixed Layer Dynamics Experiment (MILDEX), off the coast of Southern California. Included among the equipment on board was an array of six Doppler sonars and a repeatedly profiling CTD. The sonars operate at frequencies between 67 and 80 kHz, with peak transmitted power of order 2 kW each. Four of the sonars were directed downward 53°, obtaining velocity profiles to depths in excess of 1100 m. The CTD was profiled to a depth of 320 m every 3 minutes. Approximately 6000 CTD profiles were obtained during MILDEX.

The MILDEX internal wavefield is slightly less energetic than the Garrett-Munk canonical standard, except in the near inertial frequency band. Here very low energy levels are seen. The semidiurnal baroclinic tide dominates the spectra of both horizontal and vertical velocity.

In this work, slant velocity estimates from back-to-back sonar beams are combined to form estimates of horizontal velocity and its vertical derivative, shear. These are compared with isopycnal vertical displacement and strain, derived from the CTD measurements over a 10-day period, in the depth range 200–300 m. Power spectra of shear, strain, and geocentric acceleration are presented, along with more customary spectral quantities. The shear and strain spectra are of approximate $\omega^{-1/2}$ form, with weak inertial and tidal peaks. Vertical coherences of horizontal and vertical velocity are also of similar form during the 10-day comparison period. There is little need to hypothesize the existence of an added class of motions to explain a disparity in the coherences. However, near the beginning and end of the cruise, when *FLIP* was being more rapidly advected through the water, the vertical coherence of horizontal velocity was significantly reduced relative to that of vertical velocity, particularly at high frequency. The ratios of clockwise to counterclockwise horizontal velocity and shear variance are consistent with linear internal wave theory. Ratios of the vertical to horizontal velocity variance are also consistent, except in the tidal and twice tidal frequency bands. Here approximately four times as much vertical velocity variance is seen as would be predicted from the horizontal velocity measurements. This is found to be a "near field" effect associated with the reflection of the baroclinic tide from the sea surface. Scale vertical wavenumbers are defined from the ratio of the strain to vertical displacement spectra, as well as shear to horizontal velocity spectra. These show characteristic vertical wavelengths of 300–500 m throughout the internal wave band, except at tidal and twice tidal frequencies, where the typical wavelengths are much longer (800 m) and at inertial and subinertial frequencies, where they are much shorter (~200 m). Horizontal wavenumber scales can be derived from the ratios of strain to horizontal velocity and shear to vertical displacement. The derivation depends on the validity of linear shear-free internal wave theory in the WKB approximation. The two scales show an interesting pattern as a function of frequency, but agreement between them is poor.

1. Introduction

In October and November 1983 the research platform *FLIP* was one of three vessels participating in the Mixed Layer Dynamics Experiment (MILDEX) off the coast of Southern California. On board *FLIP*, the velocity and density structure of the mixed layer was investigated in a series of experiments conducted by Dr. R. Weller (W.H.O.I.) and ourselves (Smith et al., 1987). Vector measuring current meters, a profiling CTD, expendable drifters, and two Doppler sonars were used in this effort. In addition, four Doppler sonars were directed downward into the thermocline. These provided velocity and shear information at depths between

100 and 1000 m, with 17.85 m nominal depth resolution. The profiling CTD was operated from the surface to 320 m every 3 minutes. Approximately 6000 profiles were obtained. From these data a set of 320 isopycnal surfaces was tracked, to indicate the vertical displacement of the internal wavefield.

The MILDEX data are unique in that both horizontal velocity, vertical displacement, *and* their vertical derivatives (henceforth referred to as shear and strain) are reasonably well measured in the same volume of ocean at the same time. Following a brief description of the experiment and a depth–time presentation of the raw data, this co-occurrence is exploited to investigate the statistical properties of the observed motions and to quantify the degree of consistency with linear, shear-free internal wave theory. Attention is focused on the depth range 200–300 m, below the depth where significant intrusive effects can be seen in the CTD

* Present affiliation: Woods Hole Oceanographic Institution.

** Present affiliation: R. D. Instruments, Inc. San Diego, California.

data. A ten-day period in the center of the experiment, during which both the CTD and the sonars were functioning, is considered.

Power spectra of vertical strain, shear, geocentric acceleration and the horizontal Laplacian of pressure are presented, along with more conventional spectral products. The vertical coherence of horizontal and vertical velocity is compared. The consistency of the motions with linear internal wave theory is then examined, and vertical and horizontal scale wavenumbers are estimated, as a function of frequency.

It will be shown that internal waves seen in MILDEX are, for the most part, typical of those seen in other open ocean experiments. Horizontal kinetic energy spectral levels are approximately a factor of 2 less than the canonical Garrett–Munk (1972, 1975) levels, and comparable with the 1973 IWEX experiment (Müller et al., 1978, henceforth M78). Notably absent are the energetic near inertial packets which often dominate the horizontal kinetic energy spectrum. Near-inertial energy is a factor of eight less than in a previous *FLIP* cruise in May 1980 (Pinkel, 1984, 1985). In contrast, the energy of the baroclinic semidiurnal lunar tide (henceforth referred to as "the tide") is typical of California coastal measurements. Given the relative absence of near-inertial energy, the tide dominates the spectrum of both horizontal and vertical motion. The first harmonic of the tide is clearly seen in the spectra.

These tidal currents significantly affect the drift of *FLIP*. The measurements are thus made in a coordinate system that is not only accelerating with respect to the deep sea, but accelerating in fixed phase with the observed signals. This problem is discussed briefly, following a description of the experiment. A depth–time description of the motion field is then presented, followed by a statistical description of the motions in the 200–300 m depth range.

2. Experiment

FLIP departed San Diego on 19 October 1983 for a position at 34°N, 127°W, approximately 500 km west of Point Conception. From this position *FLIP* drifted first to the east and then north and west (Fig. 1). Both Transit Satellite and Loran-C Navigation were used to document the drift. The Loran C, an Internav Model 404, was recorded at 4 sec intervals and subsequently averaged for use in correcting the relative velocity measurements from the sonars. A representative Väisälä profile for the MILDEX region is presented in Fig. 2.

In addition to many devices for sensing atmospheric, sea surface and mixed layer conditions, a profiling CTD and four downward looking Doppler sonars were on board (Fig. 3). The CTD was a standard Sea Bird Instruments Model SBE-9 which was slightly repackaged to facilitate repeated profiling at a 4 m s⁻¹ drop rate. A pitot tube was added to minimize errors in the pressure measurement due to motion. The CTD was profiled from just below the surface to 320 m every three minutes, starting on 29 October. In all, approximately six thousand profiles were obtained, corresponding to nearly 4000 km of vertical sampling. Data were sampled at a 12 Hz rate for display and recording on magnetic tape. A simple filtering technique was used to match the time response of the temperature and conductivity cells (appendix A).

Salinity, potential temperature and potential density profiles were calculated from the filtered records. For the present analysis, a set of potential density surfaces was followed, whose mean depths over a 12-day period were centered at one-meter intervals from the surface to 320 m. These form the basis of the subsequent analysis.

The four downward looking Doppler sonars of interest in this study (Fig. 4) were part of a six-sonar cluster mounted at a depth of 38 m on *FLIP*'s hull. The sonars were pointed at 90° intervals in azimuth and directed 52.5° down from horizontal. Throughout the experiment, an azimuth orientation control system was used to keep the beams pointing in the cardinal compass directions. When major shifts of wind direction necessitated reorientation of the ship, azimuth changes were effected in 90° increments, such that the four cardinal time series were preserved. Two of the downward looking sonars were operated in frequency bands centered at 67.5 kHz and two at 71.5 kHz. Each sonar transmitted a burst of four 30 ms tones within its band every 2 sec. The maximum range sampled was 1410 m, corresponding to a maximum depth of 1162 m. The signal processing of the acoustic data is discussed briefly in appendix B.

Profiles of velocity from a pair of back–to–back sonar beams are presented in Fig. 5. Note that a given vertical velocity results in a Doppler shift of the same sign for both beams, while a horizontal velocity will be seen as a positive velocity in one beam and negative in the other. Under the assumption that most of the measured velocity results from horizontal motion, one set of profiles in Fig. 5 has been reversed, to facilitate comparison. Differences in the three min averaged velocities sensed by these beams are less than 1 cm s⁻¹ in the first 1 km of range. Velocity precision degrades at ranges greater than 1 km as the acoustic intensity of the return echo falls to a level comparable to system electrical noise. In the near ranges, precision is adequate to distinguish significant differences in the velocity signals from the two beams. These difference signals (in the reversed beams) indicate either vertical velocity or lateral variation in the horizontal velocity field between the beams. The difference signal can be used to infer the propagation direction of the waves. This will be attempted in future work.

For the present, information from the back–to–back beams is combined to form laterally averaged series of east and north horizontal velocity. What is obtained,
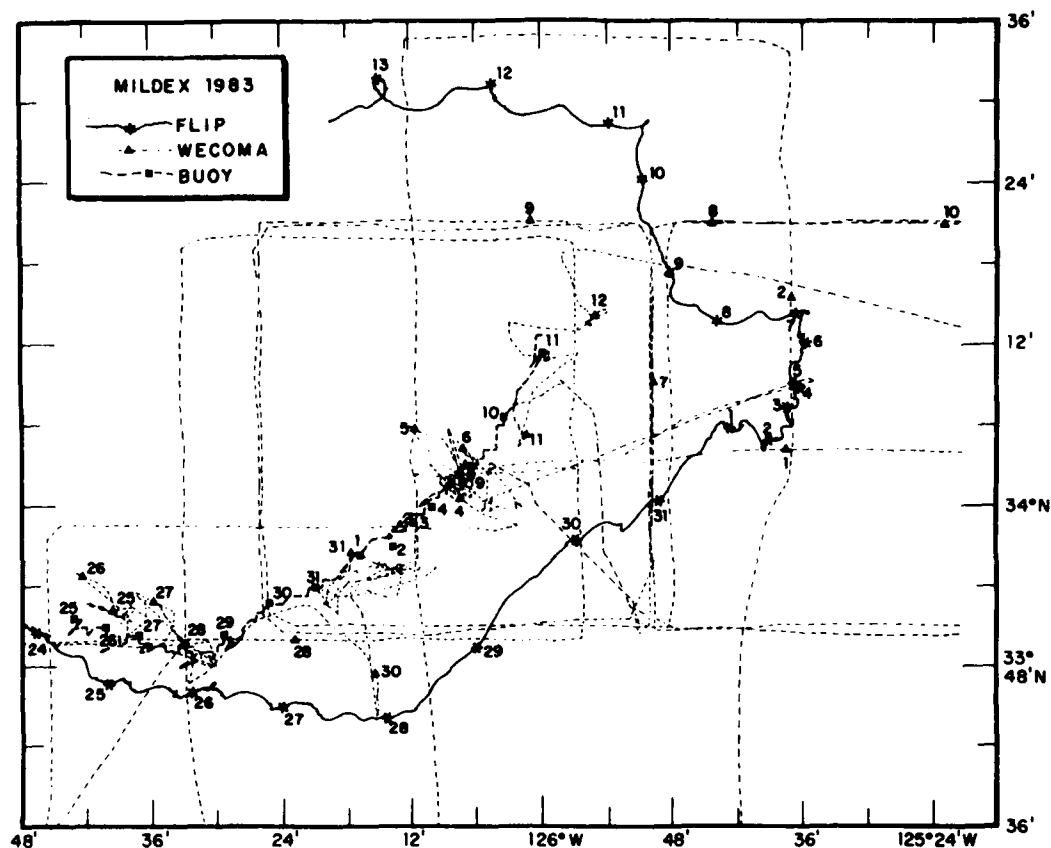
FIG. 1. The drift track of *FLIP* (solid line) and a drifting float deployed by Oregon State University (dark dashed line). The light dashed line gives the path of the R.V. *Wecoma* while doing thermistor chain tows during MILDEX. Numbers refer to the local date during October–November 1983. Drift variance is less than the total observed variance of horizontal velocity in the 200–300 m region, although comparable to the variance of deeper motions.
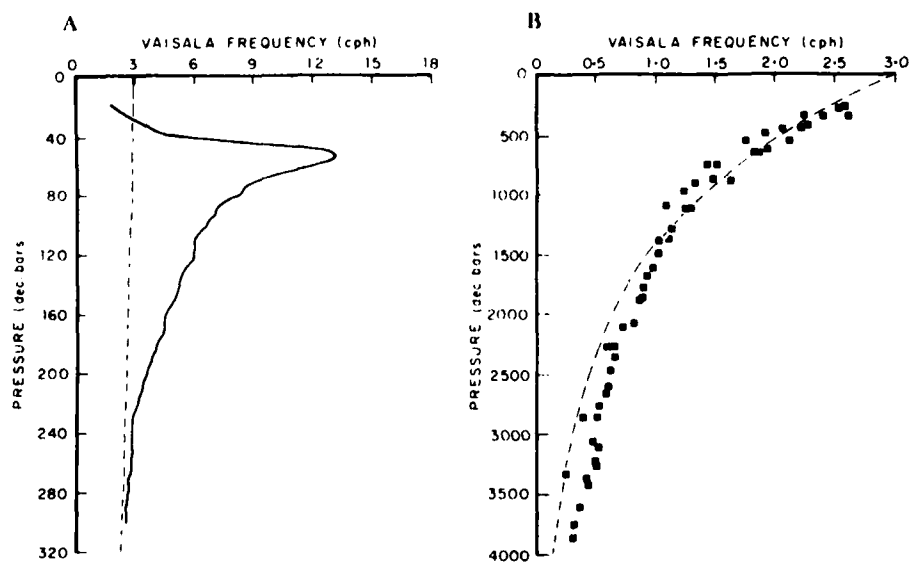

FIG. 2. Near-surface and deep Väisälä profiles from the MILDEX site. Dashed line represents an exponential model of the profile, with 3 cph surface intercept and 1.3 km scale depth.
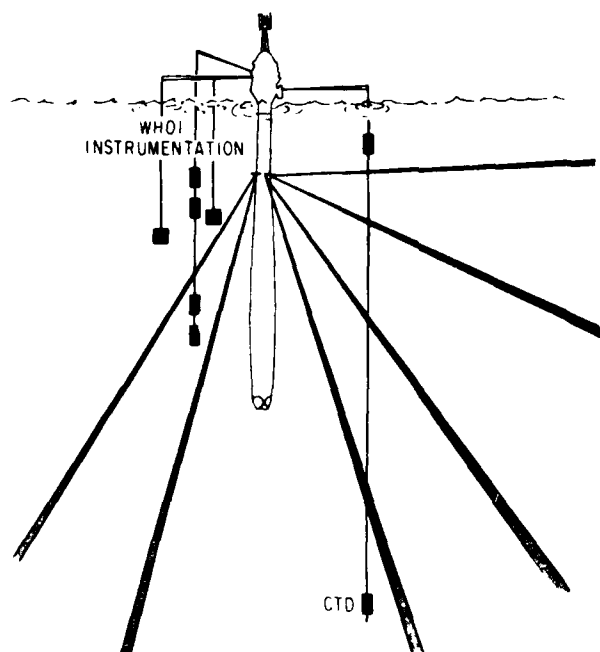
FIG. 3. Schematic diagram of the 1983 *FLIP* experiment. Sonar beam orientation is illustrated by the shaded regions. CTD profiles are obtained to a depth of 320 m every 3 min. A profiling current meter array, as well as other instrumentation, was operated by R. Weller of Woods Hole Oceanographic Institution. This work is concerned only with data from the four downlooking sonars and the CTD.

of course, is velocity relative to the drifting *FLIP*. In fixed coordinates, one expects to see baroclinic velocities which are relatively large near the surface and which decrease in magnitude in proportion to the square root of the Väisälä frequency as depth increases. The energetic, near-surface horizontal motions are those that advect *FLIP*. Thus a strong northward (relative to the earth) baroclinic current is seen by the sonars as weak near-surface current, with increasingly strong southward flow at depth. Any correction to these data, to account for *FLIP*'s drift will be comparable to or larger than the measured near-surface relative velocities, and nearly equal but opposite to the deep measured velocities. At depth, the estimated velocity field relative to the earth is thus a small difference of two larger numbers, the measured velocity and *FLIP*'s drift velocity.

Two techniques have been used to correct for *FLIP*'s drift. The first uses the Loran C information, adding the observed Loran C velocity to that sensed by the sonars. This method introduces barotropic signals into the measurements, as well as baroclinic. Also, the Loran velocities are seen to be slightly noisier at night than during the day (Fig. 1). A simpler correction method is to use the sonar information to navigate *FLIP* relative to the average water motion in the top quarter of the sea. This is done by subtracting the vertically averaged

velocity from the measured flow at each depth, as a function of time. This procedure effectively removes not only *FLIP*'s drift, but also barotropic signals and all baroclinic signals with vertical wavelength long compared to the averaging interval. The vertical depth range 200–800 m has been used to determine the vertically averaged velocity in most of the analyses presented here.

The concern is that errors in either the Loran C or vertical mean removal (henceforth VMR) corrections significantly affect the resulting calculations. If this is the case, the error is common to both techniques since the two methods result in surprisingly similar velocity corrections. The spectrum of the *difference* between the drift velocities estimated by the two methods is presented later in Fig. 11c. This measure of uncertainty in the correction is typically a factor of ten smaller than the corrected spectra, in spite of the fact that each of the corrections are comparable in magnitude to the absolute velocity estimates.

Note, however, the tidal and twice-tidal peaks in the difference spectrum. This might result from the inclusion of barotropic signals in the Loran C correction which are not seen either in the relative velocity measurements or the inferred depth-averaged drift. Also note that neither correction method will negate the effects of Doppler shifting which has resulted from *FLIP*'s drift. Finally, there is concern that because the drift is in fixed phase with the measured motions, nonlinear effects might be introduced into the sampling. These could result in the appearance of spectral harmonics (Pinkel 1981, 1984) which might not be seen in spectra from moored sensors. Simple numerical simulations were performed which confirm the presence of nonlinear, drift-related effects. However, the modeled harmonics which resulted were too small to explain the various irregularities seen in the drifting measurements.

In the depth–time and statistical analyses presented below, both Loran C and VMR methods are used to correct for *FLIP*'s drift. For the most part, no significant differences are seen in the results. Where interesting differences occur, they are noted or presented in the figures.

3. Depth–time analysis

It is useful to present a depth–time picture of the full dataset to give a qualitative sense of the motions observed and to motivate the subsequent statistical discussion.

From the CTD, a plot of the depth variations of surfaces of constant σ_θ is a useful means of visualization (Fig. 6). Here, 320 isopycnals are followed for the first 5 days of the CTD time series. The isopycnals are chosen such that their mean vertical separation is one meter over the duration of the 12-day series. Particularly apparent in the record is the baroclinic semidiurnal
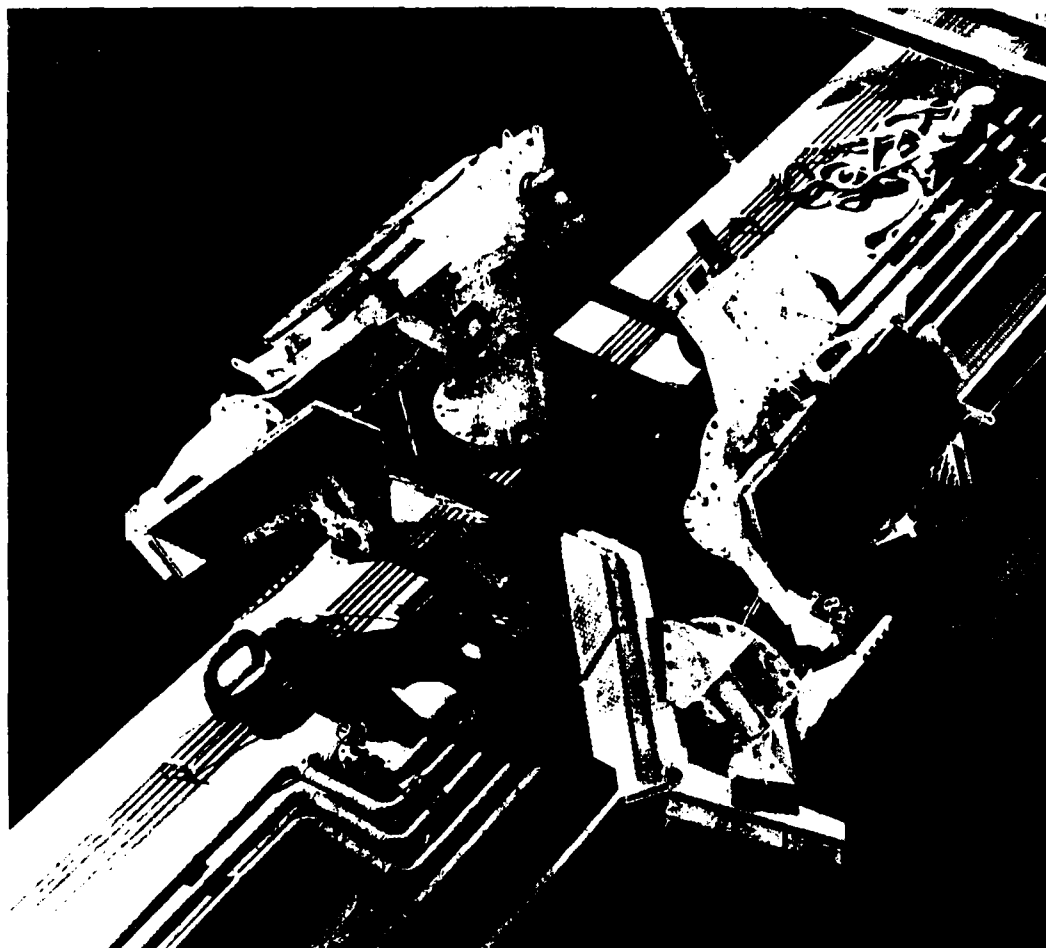
FIG. 4. The six sonar array cluster, mounted at a depth of 38 m when *FLIP* is vertical.
The four smaller downlooking sonars are in the lower left part of the picture.

tide. Vertical displacements of the tide are often of order ±15 m. The long vertical wavelength of the tide is striking. Note the distinctly nonsinusoidal, sawtooth pattern in the tidal waveform which is apparent in the deepest records of Fig. 6.

The high-frequency wavefield is also dominated by motions of low vertical mode, as has been reported by Zalkan (1970) and others. The attenuation of the highest frequency motions can be seen at great depth, where the wave frequency exceeds the local Väisälä frequency.

A variety of displays can be used to illustrate the horizontal velocity field seen by the sonars. A particularly useful technique is to generate "synthetic shadowgraphs". These are created by combining data from the back-to-back sonar beams to form time series of north and east horizontal velocity at each depth. The series are then band pass filtered using the simple but imprecise technique of forward and reverse Fourier transformation. The frequency bandwidth of filtered data series is ±0.5 cpd. Sixteen independent Fourier coefficients are included in the inverse transform used

to produce each series at each depth. The frequency-filtered profiles are then Väisälä stretched using the Garrett–Munk exponential profile with a scale depth of 1300 m. Successive profiles of the north component of velocity are plotted at 48 min intervals for the 1, 2 and 4 cpd bands in Figs. 7, 8 and 9. VMR drift correction is used. The depth derivative of these profiles is also plotted as a measure of the vertical shear. Plots based on Loran C navigation and plots of the east component of velocity are very similar.

The shadowgraph effect is achieved by careful choice of plotting scales. The profiles are plotted so close together that significant changes in velocity over the 48 min interval results in a given profile overplotting its neighbor. Thus, excessively dark (or light) regions of the figures correspond to unusually large positive (or negative) acceleration. Whereas wave "crests" are often defined as regions of maximal velocity or vertical displacement, here maxima of acceleration are followed.

The shadowgraph of the near-inertial velocity field shows a confused internal sea (Fig. 7, top). The her-
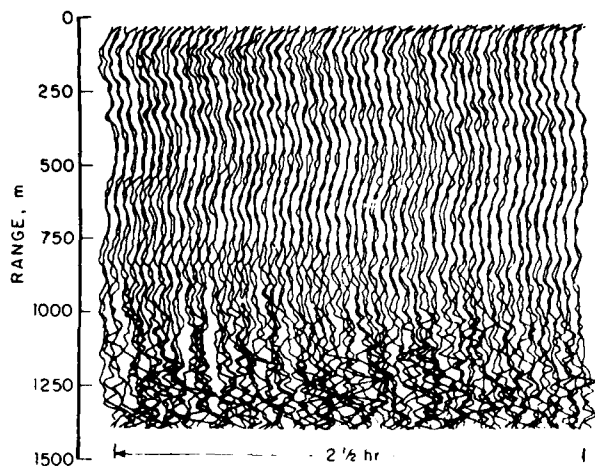
FIG. 5. A comparison of velocity profiles from back-to-back sonar beams. One of the profiles is plotted with reversed sign. Successive profile pairs are offset by 5 cm s⁻¹ in velocity and 3 min in time. The profiles should be identical if the observed velocity field is purely horizontal motion, unvarying across the array. Deterministic differences of a few cm s⁻¹ in the profiles can be detected to a range of 1 km. Hourly averaged profiles are precise to a greater range. The calibrated average of these back-to-back profiles is defined to be the horizontal velocity used in this study.

ringbone pattern characteristic of standing waves is seen in the top three hundred meters and also in the 800 m depth range. Between these depths occasional indications of propagation are seen. The dominant vertical scale of the motions is of order 200 m. Toward the end of the experiment a very long vertical wavelength motion becomes apparent, perhaps in the aftermath of strong wind forcing which began on 8 November.

The near-inertial shear field (Fig. 7, bottom) emphasizes a smaller vertical scale than velocity (~100 m) but is otherwise similar. At great depths there is a

marked decrease in vertical scale, perhaps associated with improper Väisälä stretching. One can infer from visual inspection that the vertical wavenumber spectrum of these near-inertial motions is band limited. Weighting the vertical wavenumber spectrum by a factor of k_z^2 (in the conversion from velocity to shear) shifts the spectral maximum by only a factor of two in wavenumber.

The semidiurnal tide (Fig. 8, top), in contrast, is dominated by motions of extremely long (~800 m) vertical wavelength. Clear indications of vertical phase propagation are seen, but the pattern does not stay fixed for more than a few days at a time. This might be due, in part, to the proximity of the sea surface. Downward phase (upward energy propagation) is seen on 30–31 October, 4–5 and 9–10 November. These episodes are followed by upward phase (downward energy) propagation immediately thereafter (1–2, 6–7 and 11–12 November) as if a reflection from the sea surface is occurring. Independent analyses by Williams (1985) and Levine (personal communication) have demonstrated that the various wave packets comprising this signal are coming from different azimuthal directions.

The dominant tidal shear (Fig. 8, bottom) is at ~80 m vertical scale, a factor of ten less than that of velocity. This disparity suggests a wavenumber spectral form that is essentially red, with a high wavenumber spectral shoulder (Pinkel, 1975–84) which contains the shear. Both upward and downward propagating crests can be tracked in the high-shear waves.

Shadowgraphs of the velocity and shear in the 4 cpd band are presented in Fig. 9. These, as well as higher frequency bands, resemble the tidal more than the inertial signals in that very long wavelength motions dominate in velocity, but not shear. Caution is advised in that this particular frequency band is the first harmonic of the tide and might not be representative of
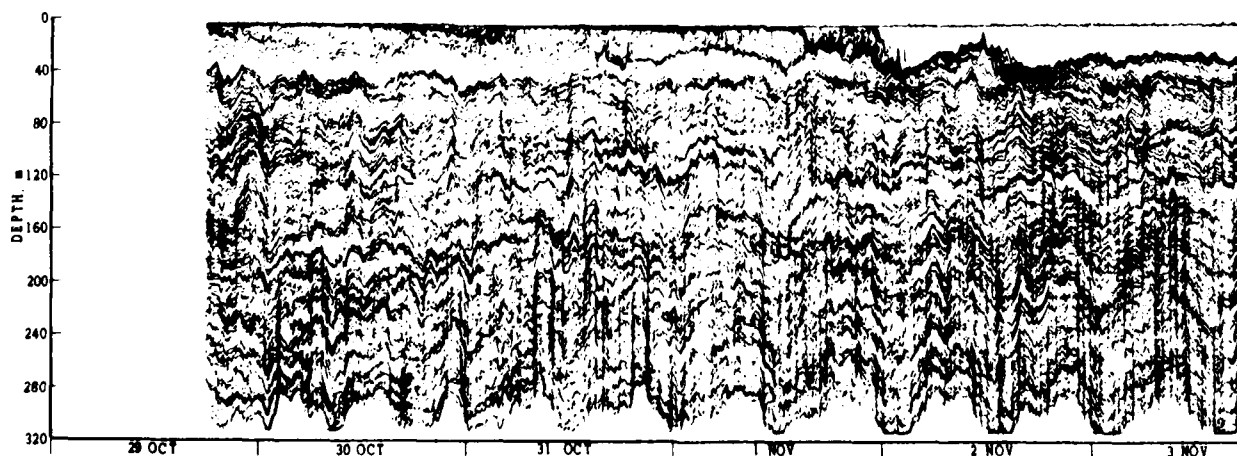

FIG. 6. A five-day sample of the depth variation of a set of selected isopycnals. The average separation between plotted isopycnals, over the course of the study, is 2 m. A denser set, with 1 m separation is used in the analysis. Note the saw-tooth nature of the semidiurnal baroclinic tide seen in the deep isopycnals.

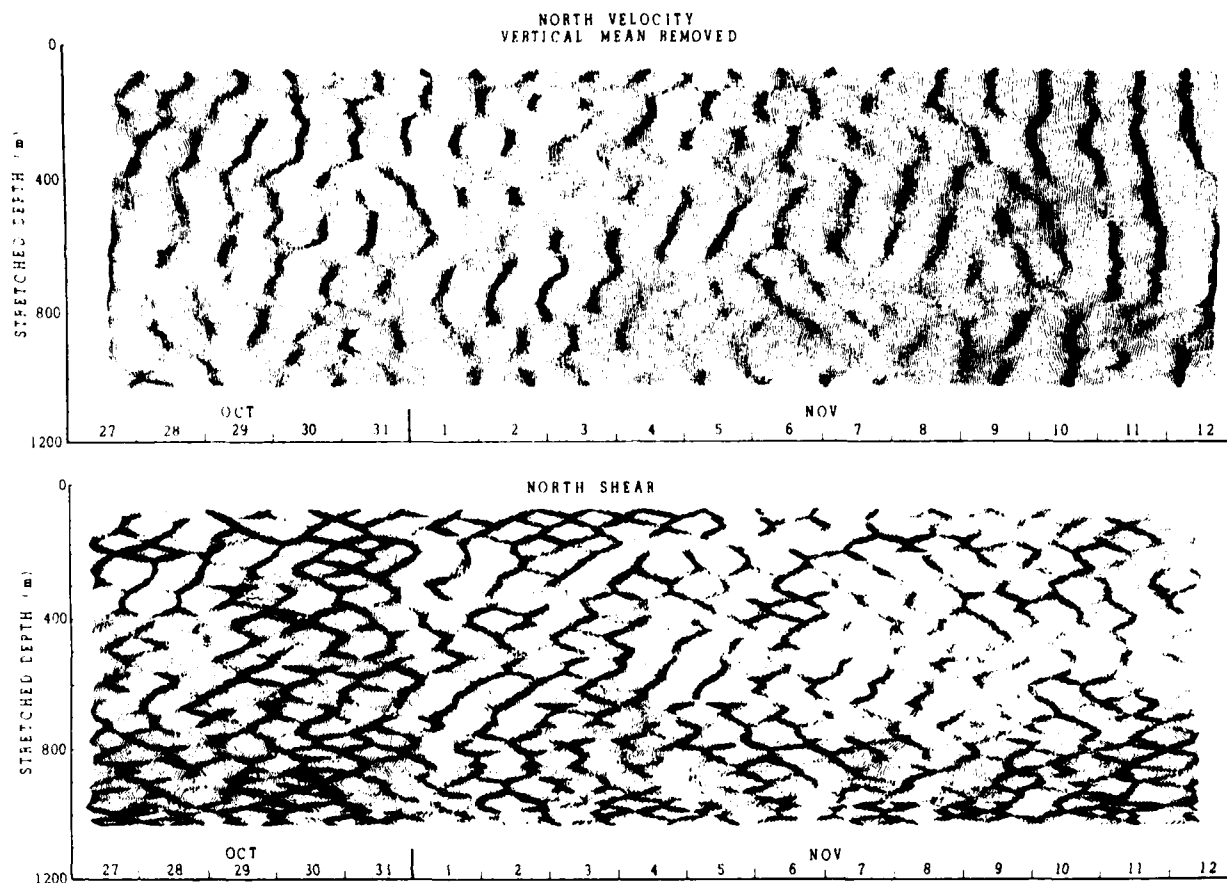NORTH VELOCITY
VERTICAL MEAN REMOVED

NORTH SHEAR

FIG. 7. Profiles of Väisälä stretched horizontal velocity (top) and shear (bottom) plotted vs stretched depth and time for the frequency band 0.5–1.5 cpd. Excessively dark or light regions can be used to trace wave crests on this confused near-inertial sea. For a discussion, see text. Note the pronounced change in the dominant vertical scale of the velocity which occurs after the wind increases on 8 November.

neighboring nonharmonic frequencies (Pinkel, 1984). Also, it should be noted that the process of removing the vertically-averaged velocity from each of the profiles in these figures also removes the signature of motions whose wavelength is long compared to the vertical extent of the measurements. Thus the 800-m wavelength motions seen at semidiurnal tidal frequency are the longest that can be seen by this method, and not necessarily the dominant long wavelength motions. When Loran C navigation is used to correct the profiles for FLIP's drift, longer wavelength motions are present, although not clearly dominant. The interesting patterns of vertical phase propagation are somewhat obscured in the Loran C shadowgraphs as barotropic tidal motions are now included.

4. Statistical analysis

Here the objective is to document the observed energy levels and to quantify the extent to which the observed motions are consistent with linear, shear free internal wave theory, in the spirit of Fofonoff (1969). To proceed, the north and east sonar time series were divided into three 8.5 day subseries. Successive subseries were overlapped 50% in time. Six-minute time averages of velocity at 60 depths (separated by 17.85 m) were used. A single ten-day record of isopycnal vertical displacement was produced, using isopycnals with mean depths separated by 1 m. Successive vertical displacement data were averaged together in time to produce 6 min displacement values, which correspond to the 6 min averages of sonar velocity. Both sonar and CTD data series were first differenced in time, multiplied by a triangular data window, and Fourier transformed. Fourier coefficients were produced at 0.1 cpd intervals.

The Fourier coefficients are used as the basis for the statistical analyses which follow. Statistical stability is achieved through a combination of cross-frequency and cross-depth averaging. The cross-frequency averaging is implemented in terms of successive passes of a running mean filter applied with smoothing widths of 2, 4, 8, 16, 32, 64 and 128 bands starting at frequencies of 0.1, 3, 4.5, 8.5, 16.5, 32.5 and 64.5 cpd. Note that adjacent Fourier bands are not independent, due to the frequency window broadening associated with the

NORTH VELOCITY
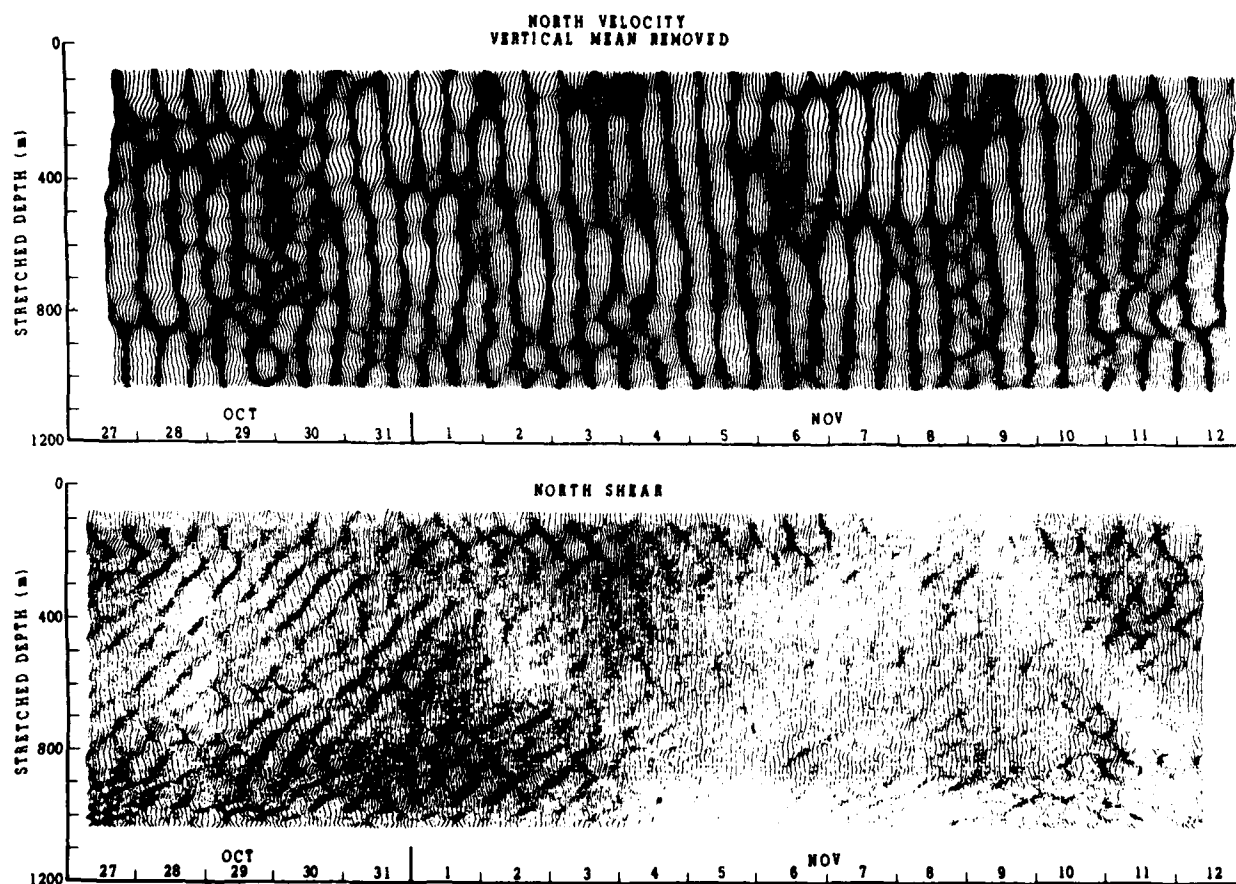VERTICAL MEAN REMOVED

NORTH SHEAR

FIG. 8. As in Fig. 7, except for the semidiurnal tidal band, 1.5–2.5 cpd. Note the extremely long vertical wavelengths seen in the velocity field as compared to Fig. 7. The scale of the shear, in contrast seems shorter. There is a mix of upward and downward phase propagation, as individual groups reflect off the sea surface.

triangular time window (as well as the 8.5-day record length of the sonar velocity series). Recoloring and weighting of the various spectral estimates is performed after the cross-frequency averaging.

Ensemble averaging over the three 8.5-day velocity series was initially used to increase the statistical stability of the velocity spectra. However, in forming intercomparisons with the 10-day CTD record, it was found that data from the center 8.5-day sonar series (which coincided in time with the CTD record) agreed much better with the CTD data than the results from the sum of the three records. Hence, this analysis features the sonar and CTD data in the space time interval in which they coincide. Specifically, the depth region from 200 to 300 m is considered over the time interval 29 October–9 November (CTD), and 1–9 November (Sonar). In addition to the standard spectral-analysis products such as power spectra and vertical coherence of horizontal and vertical velocity, spectra of horizontal acceleration, geocentric acceleration, the vertical shear of horizontal velocity and the vertical strain of vertical displacement are discussed. From comparisons of these spectra, estimates of the horizontal as well as vertical

wavenumber of the motions are obtained as a function of frequency. Estimates of the suspected nonwave spectral levels are also produced.

a. Power spectra

Spectra of horizontal velocity and acceleration, vertical displacement, shear, and strain are presented in Fig. 10a–f. Each estimate is a vertical average of the information between 200–300 m. This corresponds to averaging the results from five sonar range bins or 100 CTD isopycnal surfaces. The vertical dashed line in each figure indicates the frequency of the tide, while the dotted line gives the local inertial frequency, f.

A rotary spectrum of horizontal velocity, derived from the combined north and east time series, is presented in Fig. 10a. The clockwise (viewed from above) rotary motion shows dual peaks at the inertial and tidal frequencies, with smaller peaks at $M_2 + f$ and $2M_2$. The spectral form is approximately ω^{-2} for frequencies greater than M_2. The spectrum of counterclockwise motion also has a strong tidal peak, although no inertial

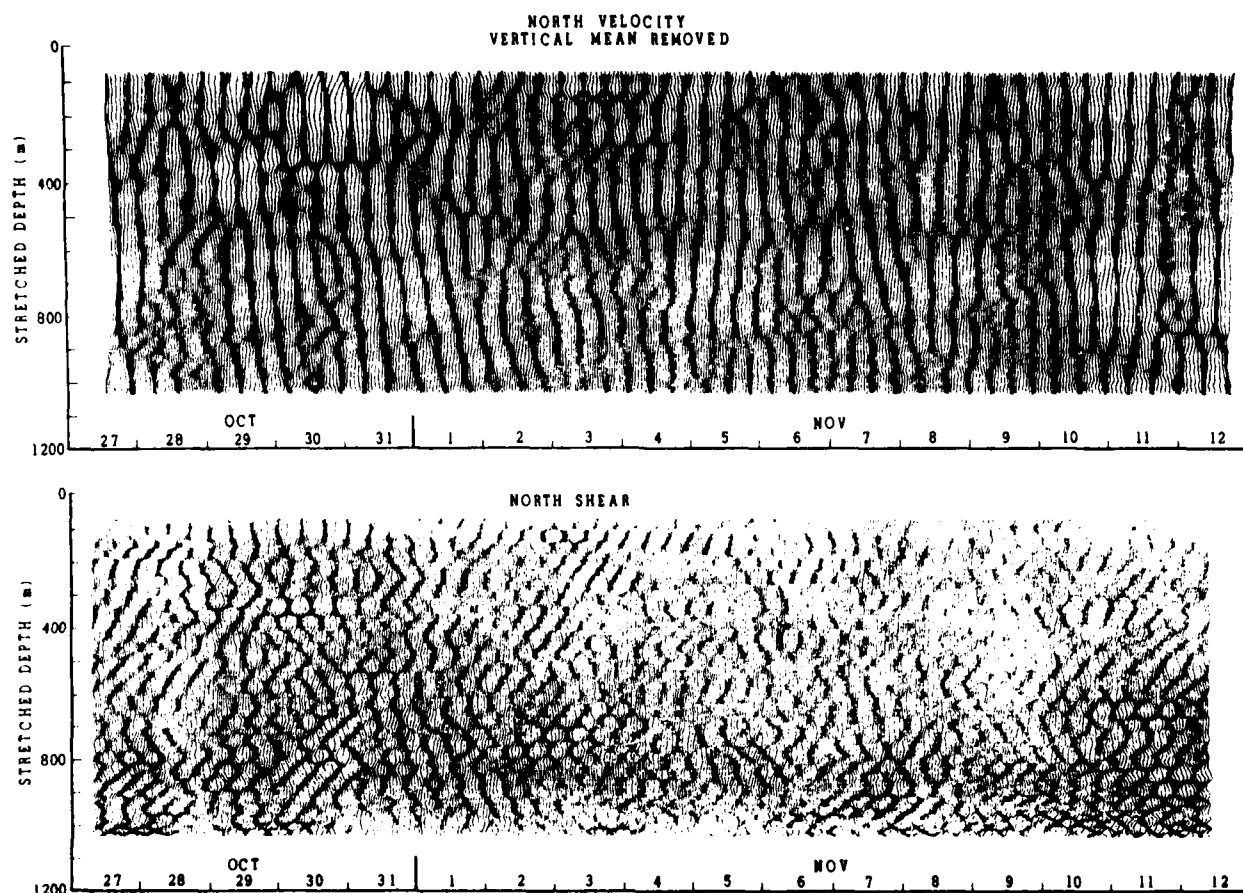NORTH VELOCITY
VERTICAL MEAN REMOVED

NORTH SHEAR

FIG. 9. As in Fig. 7, except for the twice-tidal frequency band, 3.5–4.5 cpd. The vertical scale of the velocity field is comparable to the tidal, but the shear appears to occur at yet smaller scales.

peak. The form of this spectrum is more nearly ω^{-1} at low frequency. When clockwise and counterclockwise spectra are combined to form a "horizontal kinetic energy" (HKE) spectrum, the tidal peak is seen to be significantly more energetic than the inertial. Note that the barotropic tide contributes little variance here, as the vertical mean velocity over 200–800 m has been removed in these data. Also, the slope of the combined HKE spectrum (Fig. 11b) is significantly less than ω^{-2}, due to the influence of the counterclockwise contribution.

The rotary shear spectrum is derived by subtracting Fourier coefficients separated by two range bins (Δz = 36 m) prior to squaring, averaging and recoloring. The inertial peak is now much more energetic than the tidal. Most of the tidal velocity variance is in very long vertical wavelengths, which are associated with little shear. Peaks are again seen at $M_2 + f$ and $2M_2$. The clockwise spectrum is again nearly of ω^{-2} form to 0.6 cph, after which it rapidly drops. The counterclockwise spectrum has significantly less slope than the clockwise. Again, there is no sign of an inertial peak. The tide and higher frequency peaks curiously fail to line up with their clockwise counterparts. Counter-

clockwise shear variance levels are significantly less than clockwise out to frequencies of 0.5 cph, ten times the inertial.

Spectra of the east–west component of acceleration, $\langle(\partial u/\partial t)^2\rangle$ and geocentric acceleration $\langle(\partial u/\partial t - fv)^2\rangle$ are plotted in Fig. 10b. The component acceleration rises 20 db from low frequency to a near-inertial peak, and then rises further at the tidal peak. A reasonably regular set of harmonics is visible, with peaks at f, M_2, $f + M_2$, $2M_2$, $2(f + M_2)$ or $3M_2$, and $4M_2$. The geocentric acceleration shows similar behavior, except at low frequency. The near-inertial peak is greatly reduced compared to the component acceleration, while sub-inertial frequencies are elevated.

The disparity in the two spectral estimates at high frequency is a result of a difference in spectral analysis technique, not oceanic motion. The geocentric acceleration is estimated using the first difference of 6 min average velocities. This is a good approximation of true acceleration at low frequency, but it underestimates the true acceleration at frequencies near the Nyquist. The component acceleration is correctly weighted to account for this effect. It is first divided by the factor $[2 - 2\cos(\pi f/f_{NY})]$ to recolor to a velocity estimate.
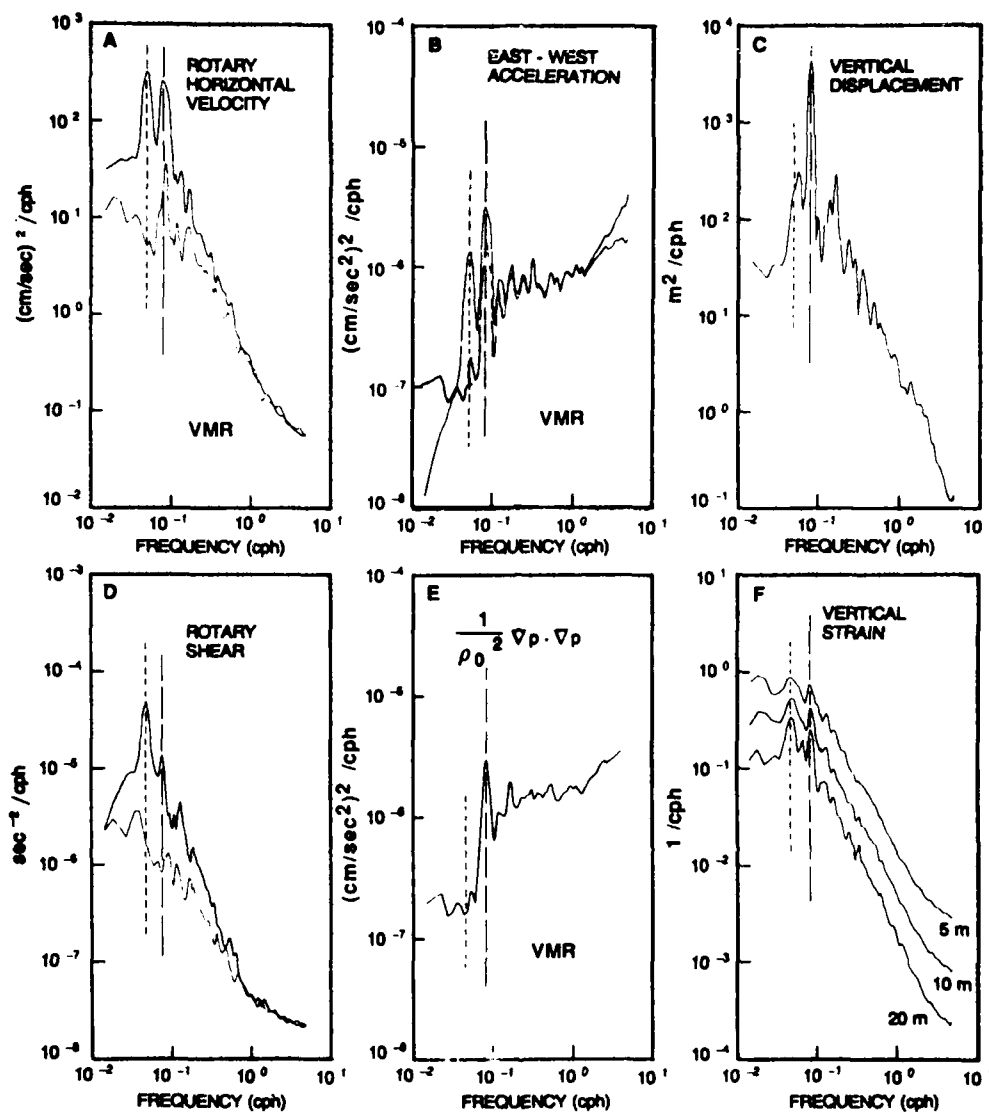
FIG. 10. A comparison of the power spectral density of various derived quantities, depth-averaged over the region 200–300 m. Dashed lines indicate inertial and semidiurnal tidal frequencies. In A and D, the dark line gives the clockwise component of motion while the light gives the counterclockwise. In B the dark line represents the component acceleration while the light line is component acceleration. The power spectrum of vertical strain (F) has an $\omega^{1.5}$ spectral form at frequencies above tidal. The shear spectrum in (D) is remarkably similar, when clockwise and counterclockwise contributions are summed.

Then it is multiplied by $(2\pi f)^2$ to reconvert to acceleration. Thus, the upper line in Fig. 10b is more appropriate for *both* component and geocentric acceleration. The blue nature of the acceleration spectrum at high frequency corresponds to the leveling off of the velocity spectrum and is a consequence of both noise and nonwave motions at high frequency.

In an unforced, inviscid, Boussinesq, linear environment the geocentric acceleration is equal to the ratio of the horizontal pressure gradient to the mean density. In Fig. 10e, the sum of the north and east geocentric acceleration spectra is presented. This can be inter-

preted as the spectral density of $1/\rho_0^2 \langle (\nabla_h p \cdot \nabla_h p) \rangle$, an index of the spectral density of the lateral pressure gradient with frequency. The tide has the greatest spectral density, followed by its harmonics. Subinertial spectral levels are a factor of five less energetic than supratidal levels, although resolved with but limited statistical precision in this short record.

The spectrum of isopycnal vertical displacement is presented in Fig. 10c. It is dominated by the tide and its first harmonic. The spectrum has an ω^{-2} form out to 1 cph, where there is a slight rise, followed by a cutoff above 2.5 cph. The high-frequency limiting value
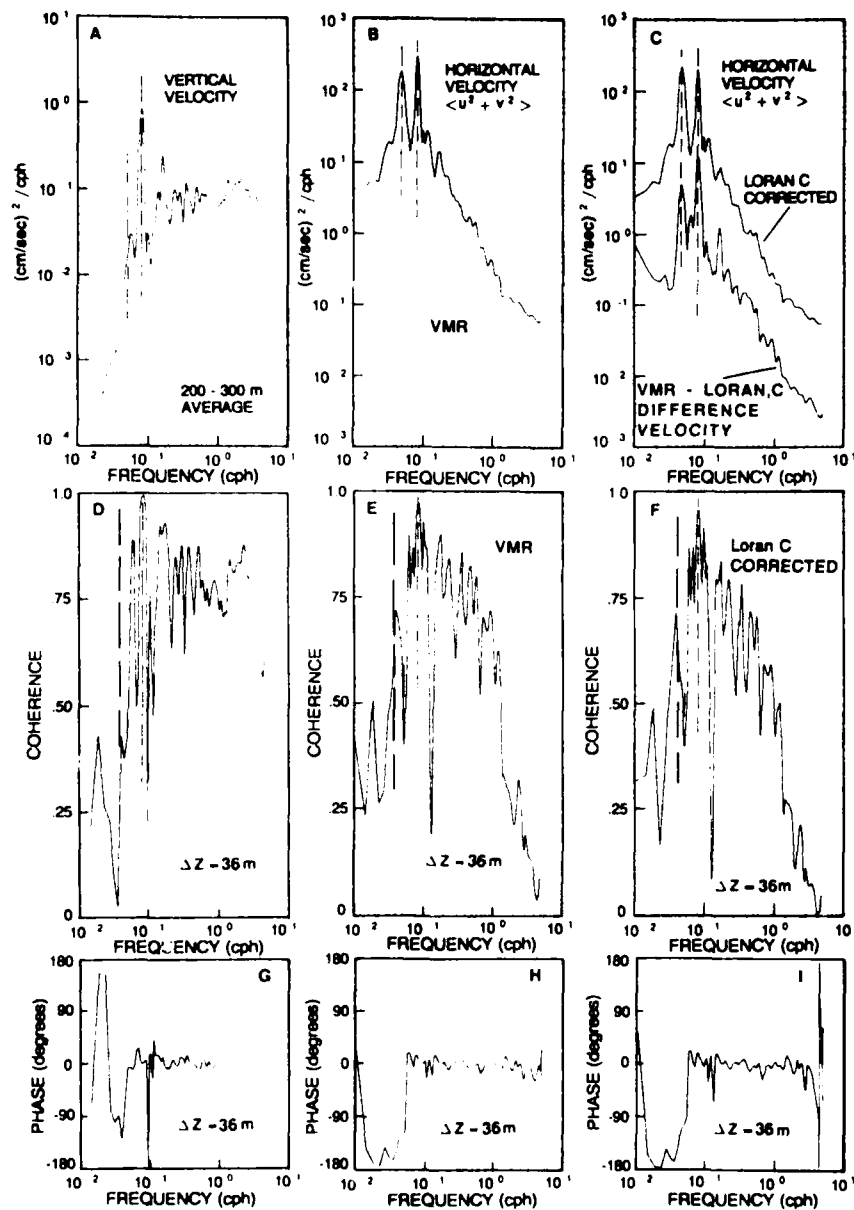
FIG. 11. Power spectra, vertical coherences and phases of vertical velocity and horizontal velocity using both Loran C and VMR drift corrections. At frequencies below 1 cph, coherence values are quite similar. Note the extremely high coherence at tidal and twice tidal frequency. Above 1 cph the vertical velocity measurements from the CTD are significantly more coherent than estimates of horizontal velocity from the sonar. The lower spectrum in C represents the difference between the VMR and Loran C drift velocities. It represents the variance at vertical scales longer than 600 m, including barotropic motions, as well as errors in navigation and velocity determination.

of the spectrum is not an index of system noise, but is rather a result of substantial aliasing. It is necessary to sample more often than once per six minutes to fully resolve the cutoff. The smaller peaks immediately adjacent to the tide might well be a result of spectral leakage from the tidal peak

Taking the first difference of the isopycnal displacement series in depth results in an estimate of the vertical straining, $\partial\eta/\partial z$, of vertical displacement, η. Vertical strain spectra are presented in Fig. 10f for three values of depth differencing interval, 5, 10 and 20 m. The forms of the spectra are nearly $\omega^{1.5}$ between tidal frequency and 1 cph. The tidal peak and the subsequent harmonics are greatly reduced in the strain (as compared to displacement) spectrum. This is a result of the unusually long vertical wavelengths of these mo-

tions. The similarity between the strain and shear (Fig. 10d) spectra is notable (particularly when both rotary components of shear are combined). The strain spectrum even has some indication of an inertial peak, although not as large as the shear peak.

It is somewhat curious that the level of the strain spectrum depends so strongly on the vertical differencing interval. If all of the motions which contribute to the strain variance have vertical wavelengths long compared to the vertical differencing interval, this would not be the case. This is seen formally by noting that the vertical wavenumber-frequency spectrum of strain is related to that of displacement by the factor k_z^2, where k_z is the vertical wavenumber. When the strain is approximated by the depth difference of two displacement time series, the resulting strain spectral estimate is related to that of displacement by the factor $\sin^2(k_z\delta z)/(\delta z)^2$. The finite difference is a good approximation to the vertical derivative only if it is taken over a vertical separation δz which is sufficiently small so that $\sin^2(k_z\delta z)/(\delta z)^2 \propto k_z^2$ for all k_z at which the displacement spectrum has significant variance. The fact that the strain spectral estimate changes as δz changes from 10 to 5 m implies that there is significant spectral variance at wavenumbers $k_z > 0.1$ m^{-1}, $\lambda_z < 60$ m. It would be interesting to note the change in strain estimates if a vertical differencing interval of 1 m rather than 5 m were used. Unfortunately, the finite resolution of the CTD limits the ability to consider smaller vertical separations.

b. Vertical coherence

Garrett and Munk (1972, 1975) have emphasized the use of vertical coherence estimates to infer the vertical wavenumber bandwidth of the internal wave spectrum. With the present measurements, which are continuous in depth as well as time, it is more convenient to estimate the vertical wavenumber–frequency spectrum directly, rather than infer its form from the coherence, (Pinkel 1984). This will be done for the MILDEX dataset in a future work.

Here attention is focused on the comparison of vertical coherences from the CTD and sonar measurements. If the observed motions are entirely due to linear internal waves and the effects of the vertical boundaries of the waveguide are unimportant, then the vertical coherences of horizontal and vertical motion should be identical. In practice, this is rarely observed. The vertical coherence of horizontal motion is generally found to be significantly less than that of vertical motion, particularly at high frequency, as the Väisälä frequency is approached. One can account for this coherence disparity, while still maintaining that the motions are entirely due to linear waves, in several ways:

1) Horizontal motion measurements, made with either in-situ or acoustic instruments are generally more noisy (less precise) than measurements of vertical mo-

tion inferred from tracking the temperature or density field.

2) Vertical motion estimates which are inferred from tracking the vertical displacement of an isotherm or isopycnal surface are not subject to so-called passive finestructure contamination of fixed-depth measurements (Phillips 1971, Garrett and Munk 1971, McKean 1974).

3) The finite thickness of the waveguide in the vertical results in the phase-locking of upward and downward propagating free waves and enables the existence of vertically standing waves (modes). This results in the possibility of a depth dependence of the ratio of horizontal to vertical coherence which could not otherwise occur (Pinkel 1981).

In the IWEX experiment, (M78), the coherence disparity was sufficiently great that it was necessary to consider a fourth explanation, namely that an additional field of nonwave, stochastic motions was present. These were presumed to be predominantly horizontal, of very flat aspect ratio, and with a vertical coherence scale small compared to 30 m.

The vertical coherences of horizontal and vertical motion in the 200–300 m comparison region can be used to repeat the IWEX investigation (Fig. 11). Here, coherences are calculated over 36 m vertical separation. The coherence of vertical velocity is relatively uniform at frequencies between tidal and 1 cph. Above 1 cph, the coherence increases from 0.75 to 0.8 and then decreases rapidly as the Väisälä frequency is approached. Strong coherence peaks are seen at tidal and twice-tidal frequency. There is also an apparent maximum between tidal and inertial frequency, which is a result of spectral sidelobe leakage from the tidal peak.

The coherence of horizontal velocity is generally similar to that of vertical, except that a valid near-inertial peak is present, as well as the tidal peak. Also, at frequencies above 1 cph the coherence drops rapidly, due to the noise levels of the velocity measurements.

c. Coherence modeling

While not the case here, it is frequently observed (Briscoe, 1975) that the vertical coherence of horizontal velocity decreases as frequency increases. The coherence of vertical velocity is usually found to remain constant, as seen here. Muller et al. (M78) hypothesized that the observed discrepancy in IWEX was due to an added contamination field which affects only the horizontal velocity field, not the vertical. The coherence disparity can then be used to model the power spectrum of the contamination. Even though little disparity is present in this dataset, we repeat the modeling effort of M78, with the objective of comparing the IWEX and MILDEX modeled contamination fields.

The key assumptions in the modeling are that the coherence should be the same if only internal waves are involved and that the CTD-derived vertical coher-

ence is in fact the true coherence of the wavefield. This second assumption is fairly reasonable. The measurement noise associated with isopycnal following is far below the internal wave signal level throughout the internal waveband. Fine structure contamination is not an issue in these "semi-Lagrangian" measurements. (Lateral advection is an error source of unknown but presumably small magnitude.)

Assuming, for the sake of notational simplicity, that all motions are statistically homogeneous in the vertical, one can model the coherence of the presumably uncontaminated CTD data as

$$R_{CTD}(\omega, \delta z) = \frac{|CR_{waves}(\omega, \delta z)|}{S_{waves}(\omega)}, \quad \delta z = 36 \text{ m}, \quad (1)$$

where S and CR are the spectrum and cross-spectrum of vertical displacement of the internal waves. At frequencies for above inertial, one can write

$$S_{sonar}(\omega) \equiv S_{waves}(\omega) + \epsilon(\omega), \quad (2)$$

where $\epsilon(\omega)$ is the spectrum of the contamination field, which is assumed to be uncorrelated over the 36 m vertical interval. The vertical coherence of the presumably contaminated sonar data is given by

$$R_{sonar}(\omega, \delta z) = \frac{|CR_{waves}(\omega, \delta z)|}{(S_{waves}(\omega) + \epsilon(\omega))}. \quad (3)$$

Thus, from the ratio of the measured coherences, the noise to signal ratio can be determined:

$$\epsilon(\omega)/S_{waves}(\omega) = R_{CTD}(\omega, \delta z)/R_{sonar}(\omega, \delta z) - 1. \quad (4)$$

From this and the measured power spectra, the contamination spectrum and the contamination-free internal wave horizontal velocity spectrum can be modeled.

Such spectra are presented in Figs. 12a and 12b for the Loran C and VMR navigation cases. Here the upper dark lines represent the signal-plus-noise spectra, the "uncorrected" horizontal velocity estimates from the sonar. The light line gives the spectrum with noise/contamination removed. Aside from the rapid decrease in the "signal only" spectrum above 1 cph, it is virtually identical to the uncorrected spectrum. The contamination spectrum is shown by the dark lower line. The line is broken at frequencies where the noise spectrum is "negative", i.e., where sonar coherence exceeds the coherence of the CTD. The noise spectrum tends to parallel the signal spectrum at low frequency, with about a factor of ten less variance. At frequencies around 1 cph the noise spectrum becomes generally white. The spectral level here is 10^{-1} (cm/s)²/cph. This corresponds to an rms noise of 0.7 cm s⁻¹ in the $(u^2 + v^2)^{1/2}$ measurement, or 0.35 cm s⁻¹ (0.58 cm s⁻¹) precision in the horizontal (slant) velocity measured by each of the four sonars. This is approximately the measurement noise level of the sonars.

This similarity in vertical coherence estimates of

horizontal and vertical motion is unusual. It is more often the case that the vertical coherence of horizontal velocity decreases monotonically with frequency, while that of vertical velocity remains roughly constant. When the vertical coherences are compared using horizontal velocity data from the early and late stages of this experiment, the familiar coherence decrease in the horizontal velocity estimates is seen. Only during the "intercomparison period" did the coherences compare well. Inspection of Fig. 1 shows that the central period of the cruise was a time of extremely low FLIP drift, as well as low inertial activity. This would reinforce the suggestion of M78 that the "contamination field" responsible for the decreased vertical coherence of horizontal velocity is advected to high "encounter frequency" by the prevailing currents. A study of the relationship between the value of vertical coherence of high frequency horizontal motion and the magnitude of the low frequency advective velocity field is called for.

d. Consistency relationships

To this point the motions have been described in terms of internal waves, which are presumed to decorrelate gradually with increasing vertical separation, and an advective field of added motions, which is assumed to be totally decorrelated over ~30 m vertical separations. It is possible to refine the definition of "internal waves" to consider not the decorrelation properties of the motion field, but rather consistency with the theoretical solutions to the linear, shear-free wave equations.

Specifically,

$$\frac{d^2W}{dz^2} + \kappa^2\left(\frac{N(z)^2 - \omega^2}{\omega^2 - f^2}\right)W = 0 \quad (5)$$

is the equation for the vertical dependence of vertical velocity of linear shear-free waves of the form $w = W(z)e^{i(\vec{k}\cdot\vec{x}-\omega t)}$ where $\kappa = |\vec{k}|$. Solutions for horizontal velocity are related to those for vertical by

$$\left.\begin{array}{l} u = i\left(\dfrac{\cos\theta - if/\omega \sin\theta}{\kappa}\right)\dfrac{dW}{dz}e^{i(\vec{k}\cdot\vec{x}-\omega t)} \\[3mm] v = i\left(\dfrac{\sin\theta + if/\omega \cos\theta}{\kappa}\right)\dfrac{dW}{dz}e^{i(\vec{k}\cdot\vec{x}-\omega t)} \end{array}\right\}, \quad (6)$$

where θ is the azimuthal angle of propagation, as set by the wave vector $\vec{k}$.

A linear superposition of wave solutions can be modeled using the "equivalent continuum" approximation of Garrett and Munk (1972):

$$w(\vec{x}, z, t) = \text{Re}\int_\omega\int_\theta\int_\kappa a(\kappa, \theta, \omega)$$

$$\times W(\kappa, \omega, z)e^{i(\vec{k}\cdot\vec{x}-\omega t)}d\kappa d\theta d\omega. \quad (7)$$

Here $a(\kappa, \theta, \omega)$ is an amplitude density function and
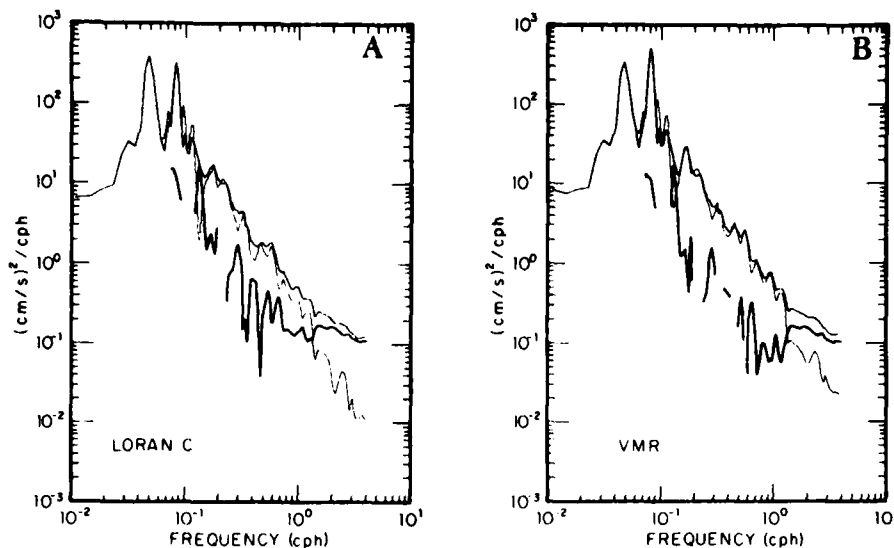
FIG. 12. Power spectra of horizontal velocity using Loran C and VMR Navigation (A, B). The upper dark line gives the measured spectra. The light line gives the spectra seen when spectra of "finestructure contamination", lower dark line, are subtracted. The contamination spectra are chosen such that the corrected spectra have the same vertical coherence as the vertical motion measurements. Missing segments of the contamination spectra represent frequency regions where the measured vertical coherence of horizontal velocity exceeded that of the vertical velocity.

the functions, W, are assumed to be suitably normalized. Stationarity and homogeneity require that

$$\langle a(\kappa,\theta,\omega)a^*(\kappa',\theta',\omega')\rangle$$
$$= A(\kappa,\theta,\omega)\delta(\kappa-\kappa')\delta(\theta-\theta')\delta(\omega-\omega'), \quad (8)$$

where A is the power spectrum and

$$\langle w^2(z)\rangle = \int_\omega\int_\theta\int_\kappa A(\kappa,\theta,\omega)|W(\kappa,\omega,z)|^2 d\kappa d\theta d\omega.[1] \quad (9)$$

From the spectral density function, corresponding spectral relations can be derived for horizontal velocity and other quantities of interest. In particular, it can be shown (Fofonoff, 1969; M78) that the ratio of counterclockwise to clockwise horizontal velocity or shear variance is equal, in theory, to $(\omega^2 - f^2)/(\omega^2 + f^2)$.

Experimentally derived ratios of counterclockwise to clockwise velocity and shear are presented in Fig.

---

[1] For a general wavefield, provision must be made for specifying waves propagating upward as well as downward. The possibility of vertically standing waves (up–down coherence) should also be considered. The existence of modes complicates the depth dependence of the various physical parameters of the wavefield, as nulls and maxima of the different modes occur at different depths. It is customary (Garrett and Munk 1972) to avoid the added complexity of these effects by assuming no up–down coherence ("topless and bottomless" boundary conditions) and that the spectrum is vertically symmetric. In this situation one can consider the spectral density, A, representing the sum of upwards and downwards propagating variance. The wave function modulus $|W|^2$ here represents the sum of the squares of the up- and down-going wave functions.

13. The spectra are averaged over the depth range 200–300 m prior to taking the ratio. The ratios agree with theory to within a factor of two, except very near the inertial frequency, where the theoretical ratio drops to zero. Loran C corrected velocity is used here, but the corresponding result using VMR velocity estimates is virtually the same.

A second test, the comparison of vertical and horizontal motions, is somewhat more interesting. Here the theoretical relationship (Fofonoff, 1969) is

$$\frac{\langle w^2\rangle}{\langle u^2+v^2\rangle} = \frac{\omega^2-f^2}{\omega^2+f^2}\frac{\omega^2}{N^2(z)-\omega^2}. \quad (10)$$

The validity of this expression requires that the WKB approximation be appropriate for the wavefield, and that vertically standing waves not dominate the motions. The ratio can be expected to vary greatly near the nulls of a single dominant mode.

In Fig. 14a, b, ratios of vertical to horizontal velocity variance are plotted, normalized such that the variance ratio will be unity if the theoretical relationship holds. Sonar and CTD estimates over the depth region 200–300 m are used, with both Loran and VMR velocities considered. When VMR velocity is used, the ratio fluctuates about unity by a factor of 3. The Loran C ratio is similar but slightly greater. The tide and twice-tidal frequency bands have four times as much vertical velocity variance as would be expected, given the observed horizontal velocity variance. A similar result is also seen in the IWEX data (M78, Fig. 3b). If one uses horizontal velocity estimates "corrected" for fine
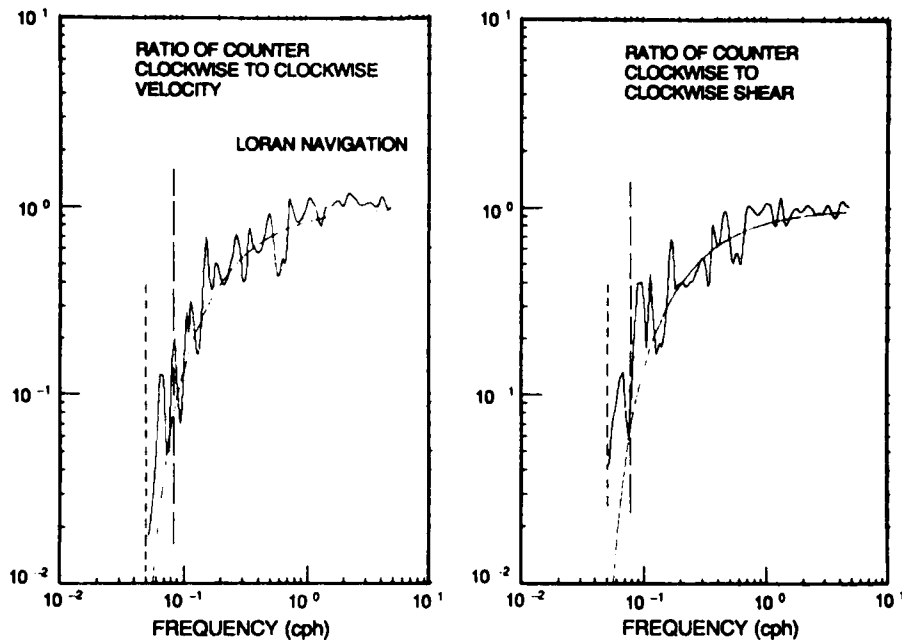
FIG. 13. The ratio of counterclockwise to clockwise horizontal velocity (and shear).
The light solid line gives the theoretical value.

structure contamination, a high value for the ratio is also seen at high frequency, above 1 cph. (Fig. 14a, b, dark line). The "uncorrected" measurements (light line) agree with theory better to about 2 cph, where

sonar measurement noise dominates the result. Thus, if one "corrects" the spectra to make the coherences more consistent, the spectra become less consistent. This is felt to be a symptom of applying the WKB
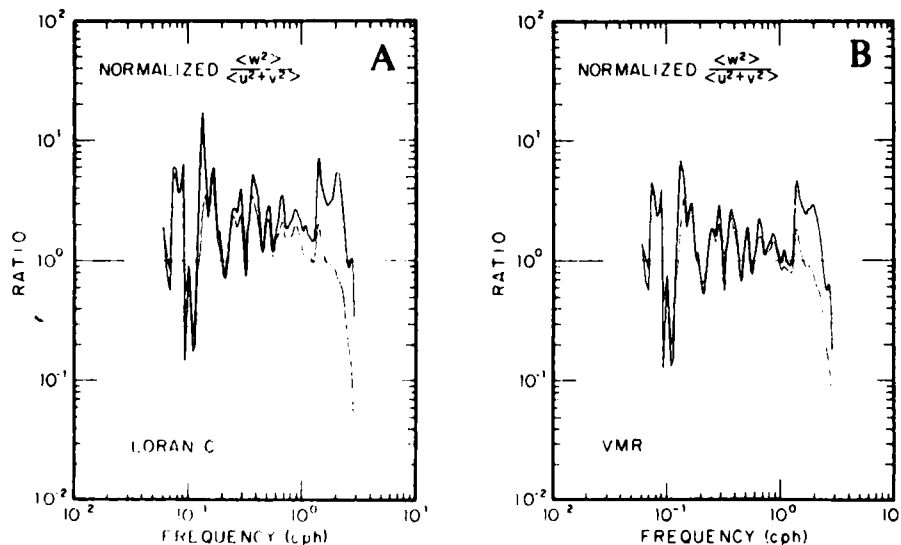
FIG. 14. The ratio of vertical to horizontal velocity variance. These are normalized such that the values should be unity if the motions are solutions to the linear shear-free internal wave equation in the WKB approximation. The light line here gives the ratio using the uncorrected spectra from Fig. 12a, b, while the dark line gives the ratio using the spectra with "contamination removed". At frequencies above 1 cph, the correction to horizontal velocity which forces the vertical coherences to agree causes the variance ratio to significantly disagree. Significant disagreement is also seen at tidal and twice-tidal frequencies. This is thought to be a near-field effect of reflection from the sea surface (see text).

approximation at high frequency, where the lowest mode dominates and the influence of the vertical boundaries of the waveguide is significant.

e. Near-surface effects

The disparity of the tidal and twice-tidal ratios is due to proximity of the measurements to the sea surface. It is seen from the shadowgraphs (Figs. 8 and 9) that these frequency bands are dominated by motions of extremely long vertical wavelength. Regardless of whether these are pure modes or whether they are free waves reflected at the sea surface, it is clear that the 200–300 m measurement zone is in the nearfield of the surface. Depending on the vertical wavenumber bandwidth of the motions in this frequency band, standing-wave behavior will be seen for some fraction of a dominant wavelength below the surface. The effect of the sea surface reflection is clearly seen by forming cascade plots of power spectra of horizontal acceleration and vertical velocity, as a function of both depth and frequency (Fig. 15). Here spectral variance density is plotted linearly on a linear frequency scale. The relative size of inertial, tidal and twice-tidal peaks is seen, as is their variation with depth.

The vertical velocity spectra from the CTD show a small tidal and twice-tidal signal in the top 100 m (Fig. 15a). These grow impressively with depth. When WKB stretching is applied (Fig. 15b) the growth is only slightly curbed. Väisälä stretched horizontal acceleration spectra (Fig. 15c, d) show large near surface tidal and twice-tidal peaks. A dip is seen in these ridges at depths of 200–400 m. This is likely a "nearfield" interference effect, associated with the reflection of the waves from the sea surface.

It is useful to consider a simple model of the wavefield near the sea surface when discussing these effects. This is done most conveniently using the vertical wavenumber–frequency spectrum. The vertical wavenumber–frequency spectrum can be easily related to $A(\kappa, \theta, \omega)$, under the assumption of horizontal isotropy and vertical symmetry.

Here

$$A(k_z, \omega) \equiv A(\kappa, \omega)\frac{dk_z}{d\kappa} = \int_0^{2\pi} A(\kappa, \theta, \omega)d\theta\frac{dk_z}{d\kappa}. \quad (11)$$

It is convenient to normalize the wavenumber dependence of the spectrum, writing

$$A(k_z, \omega) = \hat{A}(k_z, \omega)B(\omega), \quad (12)$$

where

$$\int_0^\infty \hat{A}(k_z, \omega)dk_z = 1. \quad (13)$$

The depth dependence of the velocity variance in specific frequency bands is of interest. This is most easily investigated under the assumption of constant stratification, whereby the functions W become sinu-

soids. The depth variation of velocity variance near the surface is given by

$$\left.\begin{array}{l}\langle w^2\rangle(\omega, z) = B(\omega)\int_0^\infty \hat{A}(k_z, \omega)\sin^2 k_z z\, dk_z \\[2mm] \langle U^2\rangle(\omega, z) = B'(\omega)\int_0^\infty \hat{A}(k_z, \omega)\cos^2 k_z z\, dk_z\end{array}\right\}, \quad (14)$$

where $\langle U^2\rangle \equiv \langle u^2 + v^2\rangle$. The ratio of $B(\omega)$ to $B'(\omega)$ is given by Eq. (10), if the WKB approximation is valid.

The influence of the nearfield of the sea surface is most easily seen when simple choices for $\hat{A}(k_z, \omega)$ are considered. For example, consider a band-limited white spectrum:

$$\hat{A}(k_z, \omega) = 0.5/\Delta(\omega), \quad k_0 - \Delta < k_z < k_0 + \Delta$$

$$\hat{A}(k_z, \omega) = 0, \quad \text{elsewhere.}$$

With such a wavenumber dependence it can be shown that

$$\left.\begin{array}{l}\langle w^2\rangle(\omega, z) = B(\omega)[0.5 - \cos 2k_0 z\, \sin 2\Delta z/4\Delta z] \\[2mm] \langle U^2\rangle(\omega, z) = B'(\omega)[0.5 + \cos 2k_0 z\, \sin 2\Delta z/4\Delta z]\end{array}\right\} \quad (15)$$

It is instructive to consider two simple cases.

1) A NARROW-BAND SPECTRUM $\Delta \ll k_0$:

The nearfield of the sea surface is defined here such that $\sin 2\Delta z \propto 2\Delta z - [(2\Delta z)^3/6]$ for $\Delta z \ll \pi/4$. Equations (15) become

$$\left.\begin{array}{l}\langle w^2\rangle(\omega, z) \\[1mm] \quad = B(\omega)[\sin^2(k_0 z) + (\Delta z)^2\cos(2k_0 z)/3 + \cdots] \\[2mm] \langle U^2\rangle(\omega, z) \\[1mm] \quad = B'(\omega)[\cos^2(k_0 z) - (\Delta z)^2\cos(2k_0 z)/3 + \cdots]\end{array}\right\} \quad (16)$$

The first null in horizontal velocity variance occurs near $k_0 z = \pi/2$, $z = \lambda_0/4$. A "nearly monochromatic" internal tide of vertical wavelength slightly greater than 800 m would have a minimum in horizontal velocity at depths slightly greater than 200 m.

2) A BROAD-BAND LOW WAVENUMBER SPECTRUM: $\Delta = k_0$

Here we consider uniform spectral density over vertical wavenumber $0 < k_z < 2\Delta$. Equations (15) become

$$\left.\begin{array}{l}\langle w^2\rangle(z, \omega) = B(\omega)[0.5 - \sin 4\Delta z/8\Delta z] \\[2mm] \langle U^2\rangle(z, \omega) = B'(\omega)[0.5 + \sin 4\Delta z/8\Delta z]\end{array}\right\} \quad (17)$$

Local extrema of these variances occur at depths where

$$\tan 4\Delta z = 4\Delta z.$$

The first minimum of horizontal velocity variance occurs when $4\Delta z$ is slightly less than $3\pi/2$, specifically $4\Delta z = 4.4935$. If we identify the mean vertical wavelength of the waves in the tidal band to be 800 m, $k_0 = 2\pi/800$ m^{-1}, then the depth of the first minimum
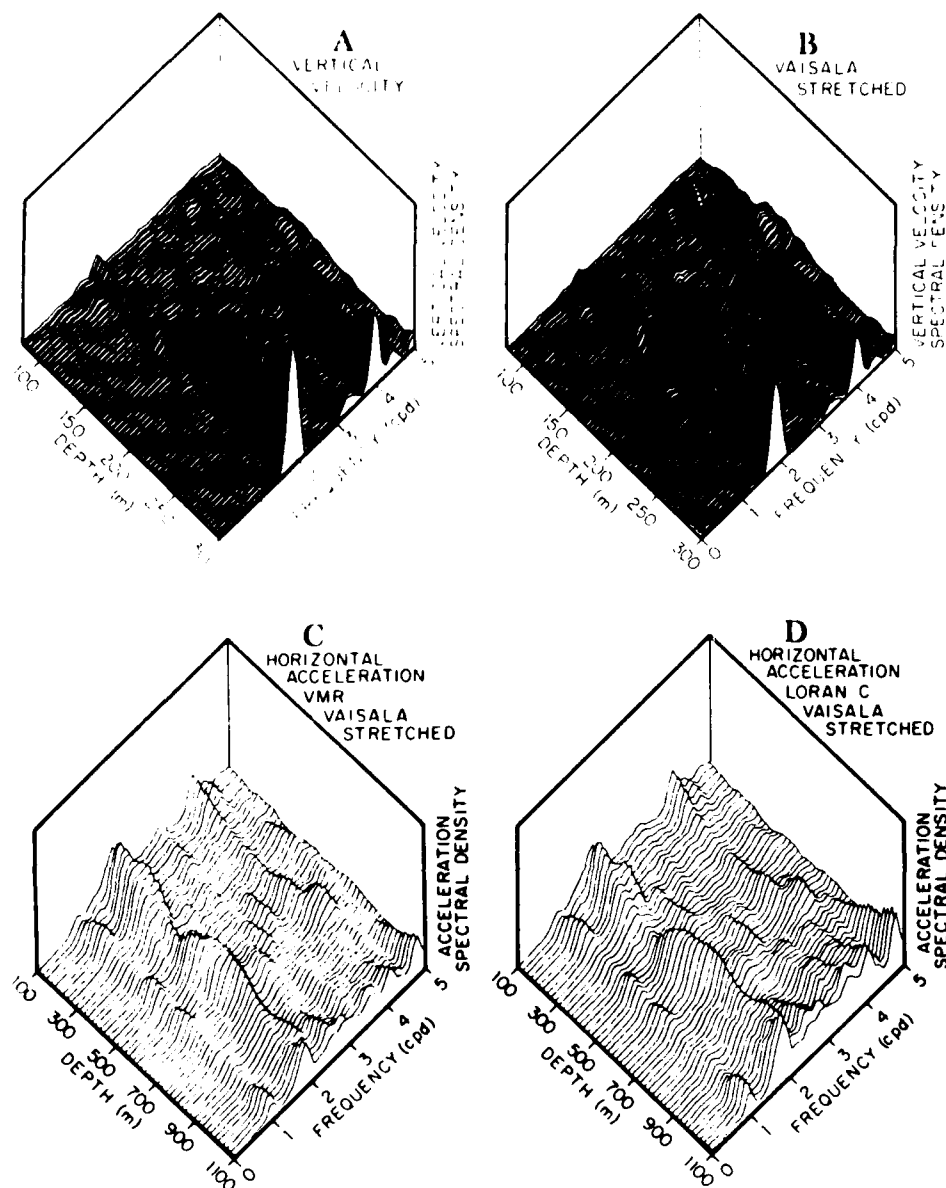
Fig. 15. The spectral density of vertical velocity (a, b) and horizontal acceleration $\langle(\partial u/\partial t)^2 + (\partial v/\partial t)^2\rangle$ (c, d), plotted on linear scales as a function of depth and frequency. Note the variation in depth of the variance at tidal and twice-tidal frequencies. The growth in the observed tidal vertical velocity variance (a) with increasing depth is only partially reduced by Väisälä scaling the spectra (b). Depth variations in Väisälä scaled horizontal acceleration (c, d) are also seen. The 200–300 m intercomparison depth zone occurs in a region of near maximal vertical velocity variance, slightly above the region of locally minimal horizontal velocity variance. A similar effect is seen at twice-tidal frequency. The ratio of vertical to horizontal velocity variance can thus be expected to oscillate about the theoretical value as a function of depth, in the near-field of the sea surface.

of horizontal velocity variance is at 143 m. It is reasonable to assume that the 800 m waves seen in Fig. 7 are the shortest energetic waves, as longer waves exceed the field of view of the sonars. With this interpretation $2k_0 = 2\Delta = 2\pi/800$ m^{-1}, and the depth of the first variance minimum of horizontal velocity is at 286 m, more consistent with the observations.

It is interesting that the modeled horizontal velocity variance only falls to 80% of the surface value in this broadband case, while in the narrowband Case 1 the decrease is much more dramatic. For example, if the value $\Delta = 0.5k_0$ is considered in the narrowband model, horizontal velocity variance is seen to fall to twenty percent of its surface value at the first minimum (al-

though this depth corresponds to $z\Delta = \pi/4$, which is beyond the domain of validity of the approximation). The exact relation, 15, gives 36% for $\Delta = 0.5k_0$. The observed variations are about 50%, suggesting an intermediate situation. Given the simplistic form chosen for the wavenumber dependence, a detailed fit of the model to the data is not to be expected.

It is curious that the $\langle w^2 \rangle / \langle U^2 \rangle$ ratio displayed similar behavior in IWEX, where measurements were made in the 600–700 m depth range (M78). Again, an apparent surplus of vertical velocity variance is seen, given the measured horizontal velocities. Interestingly, there is also the strong suggestion of a second local minimum in the horizontal acceleration variance in the MILDEX data at great depth (Fig. 15). Perhaps the coincidence of IWEX and MILDEX results is indeed a result of coincidence. Both IWEX and MILDEX measurements are near minima of horizontal velocity/ acceleration variance.

f. Parameter estimation

Various ratios of the shear, velocity, strain and displacement spectra can be used to define scale horizontal and vertical wavenumbers, as a function of frequency. Both shear and strain are estimated using a 36-m vertical differencing interval. Scale vertical wavenumbers are defined from the square root of the ratios of the shear spectrum to the velocity spectrum and strain spectrum to the displacement spectrum. This definition of a wavenumber scale as the square root of the ratio of the derivative of a quantity to the quantity itself is physically meaningful even if the observed motions are not linear internal waves.

The two spectral ratios are presented in Fig. 16. They can be interpreted as the square of a characteristic vertical wavenumber, at each frequency. At frequencies below 1 cph, the scale wavenumbers from both methods are remarkably similar, fluctuating in a region corresponding to 300–500 m vertical wavelengths. Minimum wavenumber values are seen at tidal and twice-tidal frequency, corresponding to vertical wavelengths of order 900 and 600 m. At frequencies above 1 cph the sonar derived estimates indicate a larger vertical wavenumber. This is a result of the noise in the sonar measurement, which was previously seen to be incoherent over 36-m separation. Noise contributes significantly to the vertical shear estimate at high frequencies, increasing the scale vertical wavenumber.

The CTD derived vertical wavenumber estimate stays essentially constant at all frequencies above inertial, with the exception of the tidal and harmonic excursions. The changing modal structure of the wavefield with changing frequency is accomplished in such a way that this particular parameter varies but little. Thus, even though the high-frequency wavefield is dominated by mode-one waves, the waveguide is sufficiently narrow at high frequency that the gravest-mode waves occur at the preferred vertical scale.
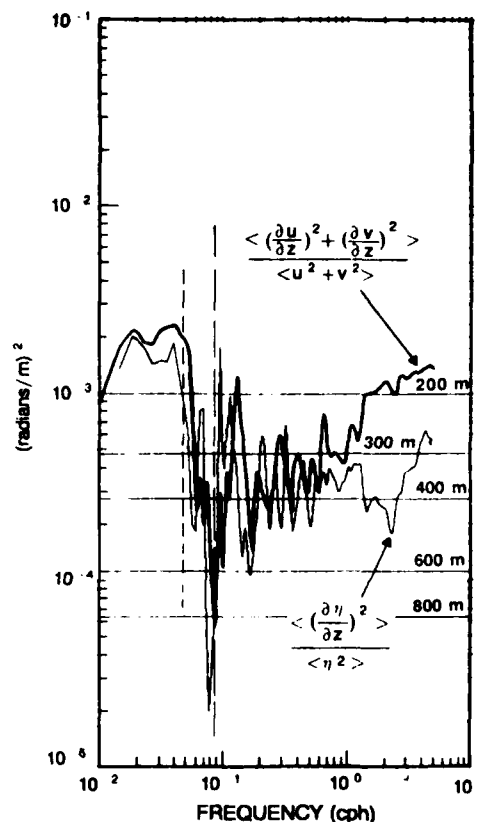

FIG. 16. The ratio of shear to horizontal velocity variance (dark line) and strain to vertical displacement variance (light line). Horizontal reference lines indicate the characteristic vertical scales implied by the ratio. Inertial and subinertial frequencies are associated with short characteristic vertical scales, tidal and twice tidal with long vertical scales. The rest of the internal wave band seems to indicate a 300–500 m characteristic scale. This corresponds to mode 10 waves at frequencies below 0.5 cph, mode 1 waves at frequencies above 2 cph.

It is of interest to note the sharp decrease in vertical scale which occurs at the inertial frequency and below, relative to the rest of the internal waveband. The scale estimates based on both vertical and horizontal motion agree well at subinertial frequencies, where internal wave theory does not apply.

The shear and strain spectra can be used to produce estimates of horizontal wavenumbers as well as vertical. Here it is necessary to assume that the observed motions are linear internal waves and to rely on the equivalent continuum description of the wavefield presented above. Using this formalism, it can be shown that if

$$\langle w^2 \rangle(\omega) = \int_\theta \int_\kappa A(\kappa, \theta, \omega) |W'|^2 d\kappa d\theta,$$

then

$$\langle w'^2 \rangle(\omega) = \int_\theta \int_\kappa A(\kappa, \theta, \omega) |W''|^2 d\kappa d\theta \qquad (18)$$

$$\langle U^2 \rangle(\omega) = \left(1 + \frac{f^2}{\omega^2}\right) \int_\theta \int_\kappa \frac{A(\kappa, \theta, \omega)}{\kappa^2} |W''|^2 d\kappa d\theta \qquad (19)$$

$$\langle U'^2\rangle(\omega) = \left(1 + \frac{f^2}{\omega^2}\right)$$

$$\times \left[\frac{N^2 - \omega^2}{\omega^2 - f^2}\right]\!\int_\theta\!\int_\kappa \kappa^2 A(\kappa, \theta, \omega)|W'|^2 d\kappa d\theta. \quad (20)$$

The primes denote differentiation with respect to depth. One can define scale horizontal wavenumbers from the ratios:

$$K_1^2(\omega) = \left(\frac{\omega^2}{\omega^2 + f^2}\right)\!\left(\frac{\omega^2 - f^2}{N^2 - \omega^2}\right)\frac{\langle U'^2\rangle(\omega)}{\langle w'^2\rangle(\omega)} \quad (21)$$

$$K_2^2(\omega) = \left(\frac{\omega^2 + f^2}{\omega^2}\right)\frac{\langle w'^2\rangle(\omega)}{\langle U^2\rangle(\omega)}. \quad (22)$$

Note that if the WKB approximation is valid, implying

$$|W''|^2 = \kappa^2\!\left(\frac{N^2 - \omega^2}{\omega^2 - f^2}\right)|W'|^2. \quad (23)$$

then these two horizontal wavenumber scales should be identical.

In Fig. 17, the two scales are presented as a function of frequency. Data from 200–300 m are averaged to form these estimates. Also shown is the approximate position of the mode 1 dispersion line, as determined from historical Eastern Pacific hydrographic data. The wavenumber scale $K_1(\omega)$ derived from the shear to vertical velocity ratio generally parallels the mode 1 reference line. However, the actual ratio of the two power spectra is of nearly uniform $\omega^{-1.5}$ form as a function of frequency. The apparent agreement with theory is due to the deterministic weighting applied. The irregularity at low frequency is a result of the variation in the $\langle w^2\rangle$ spectrum. Tidal and twice-tidal features have significantly smaller horizontal wavenumbers than their low frequency neighbors, consistent with information previously presented.

The second wavenumber scale, derived from the strain to horizontal velocity spectral ratio, has an entirely different character. Here the variation is nearly linear with frequency. A scale horizontal group velocity of 30 cm/sec is indicated by the slope of the line. The magnitude of this estimate is remarkably similar to direct estimates obtained in previous experiments from the ratio of isotherm slope to displacement (Pinkel, 1975, Fig. 10). The disparity between the K_1 and K_2 scales would be decreased if there were more horizontal velocity and/or more horizontal shear for the given vertical motions observed. Also, at tidal and twice-tidal frequencies, the near-field effect of the sea surface might be playing some role.

5. Summary

During October and November 1983 a series of sonar and CTD measurements were obtained from the Research Platform *FLIP*. These are displayed and analyzed with the objective of understanding the physics of the upper ocean internal wavefield. Interpretation of the measurements is complicated by the fact that *FLIP* is drifting with a velocity determined by upper ocean currents as well as the wind. There is a strong semidiurnal component to the drift, dominating a continuous drift velocity spectrum. Sonar velocities are corrected by either using Loran C navigation, which introduces a barotropic component to the measurements, or by subtracting a vertically averaged velocity, which reduces the barotropic contribution. Little difference is seen in analyses of velocity corrected by the two methods.

The near inertial currents observed are less energetic than usual in the Eastern Pacific. They are a factor of eight less energetic than in a previous *FLIP* cruise. Characteristic vertical wavelengths of the near inertial velocities are 200 m, while near inertial shear has a
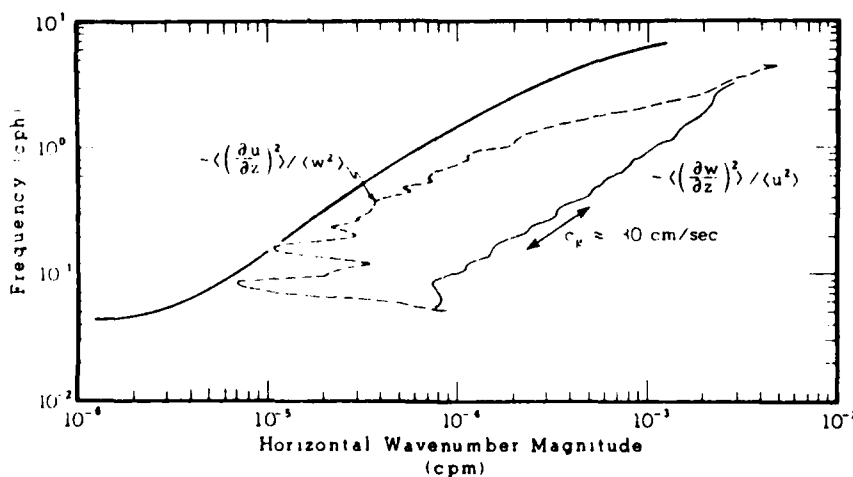

FIG. 17. Scale horizontal wavenumber as a function of frequency, given by the ratio of shear to vertical velocity variance (dashed) and vertical strain rate to horizontal velocity variance. See text for discussion.

100 m vertical scale. With inertial currents weak, the semidiurnal tide plays a proportionally more significant role. Tidal velocity vertical wavelengths are in excess of 800 m, much longer than near inertial. Tidal shear has a characteristic vertical scale more comparable to near-inertial shear. The first harmonic of the tide has vertical scales similar to the tide and larger than the higher frequency motions in the wavefield.

With attention focused on the depth region 200–300 m, where CTD and sonar measurements overlap, a variety of spectral comparisons are made. The ratio of variance of horizontal to vertical velocity agrees well with internal wave WKB theory. Notable exceptions occur at tidal and twice-tidal frequencies, where near-surface effects are seen, and above 1 cph where the WKB approximation becomes less applicable. Vertical coherences of vertical and horizontal velocity are quite comparable. There is little need to invoke the presence of a finestructure contamination field to explain a significant disparity, as in previous experiments. This might be due to the absence of energetic inertial shears in MILDEX, which would serve to advect the "finestructure" to suitably high encounter frequency, where its variance would be comparable to that of propagating wave motions.

Power spectra of shear and vertical strain are similar in form. Both have $\sim \omega^{-1.5}$ slope with indication of inertial peaks. The influence of the tidal and twice-tidal motions is small, as these signals have such long vertical wavelengths. For linear, inviscid motions the $\omega^{-1.5}$ form for the strain spectrum suggests a similar form for the spectrum of the vertical component of relative vorticity. Similarly, the spectrum of the horizontal Laplacian of pressure, $\langle (\nabla_h^2 p)^2 \rangle (\omega)$, is of the form $\omega^{2.5}$ to be consistent with the strain spectrum.

Ratios of strain to vertical displacement and shear to horizontal velocity are used to estimate scale vertical wavenumbers. The dominant scale identified is approximately 300–500 m. This is remarkably constant with frequency, with the exception of the inertial and subinertial bands, where it is shorter, and the tidal and twice-tidal frequencies, where it is much longer. The changing modal structure of the wavefield at high frequency is due to the changing thickness of the waveguide rather than the changing characteristic vertical scale of the waves.

The attempt to estimate horizontal scales from the ratio of strain to horizontal velocity and shear to vertical velocity produces an interesting result. The normalized shear to vertical velocity ratio yields an estimate of the horizontal wavenumber, $\kappa(\omega)$, which nearly parallels a typical low-mode dispersion line, except at low frequency. The ratio of strain to horizontal velocity produces a wavenumber estimate that changes linearly with frequency, suggesting a scale horizontal group velocity of 30 cm s^{-1}. WKB internal-wave theory suggests that the two scales be identical. Less strain or vertical velocity variance or, conversely, more variance in the

sonar derived measurements is required to reduce this disparity.

While the analyses of these data are just beginning, several differences in future measurement technique are suggested. Clearly, an effort should be made to obtain data while FLIP is in a moored reference frame. FLIP has been routinely tri-moored in the deep sea since 1971, and it is worth the logistical inconvenience to attempt to determine the sensitivity of observed spectral harmonics to the ship's drift. Will fictitious harmonic signals "go away" when the component of drift which is coherent with the signal is removed? Alternatively, will true harmonics, which have been smeared by the Doppler shifting of the drifting measurements, appear with greater clarity?

Additional work should be directed toward improving the vertical range resolution of the sonars. The 37-m vertical differencing interval is too coarse to permit detailed comparison with the CTD, and only marginally adequate for the present task. A smaller, pulse-to-pulse coherent sonar has recently been created. This has cubic meter resolution with a maximum range of 40 m. It should complement the long-range low-resolution view obtained from the sonars used in the study.

APPENDIX A

Response Correction in the CTD

Following the cruise, a simple procedure was used to match the time response of the conductivity (C) and temperature (T) sensors (Williams, 1985). From a representative set of profiles the C and T data were first differenced and Fourier transformed. The coherence and the transfer function between the two records were estimated as a function of vertical wavenumber. Coherence was very high (>0.9) for vertical wavelengths greater than 1 m. It dropped very rapidly at shorter scales. It was assumed that the conductivity cell functioned without distortion to 1 m scale. Corrections to the phase and amplitude of the temperature signal were then determined, under the assumption that conductivity fluctuations of 1–10 m scale were entirely due to temperature, not salinity variations. All 6000 T and C profiles were subsequently first-differenced and Fourier transformed. The transfer function was then applied to match the spectral response of the T signal to that of the C. Also, power at scales shorter than 1 cpm was removed from both T and C. The records were then

inverse-transformed back into the space domain. The gradients were then integrated to produce "corrected" T and C profiles.

APPENDIX B

Doppler Sonar Signal Processing

The acoustic data were complex homodyned and sampled at 400 Hz. Estimates of the autocovariance of the echo (as a function of range and time lag) were formed at lags of 2.5 and 5 ms for each sonar. Averages of these estimates were formed over 30 s intervals and recorded on magnetic tape at sea. Subsequent to our return, the autocovariances were averaged over 3 min and 11 m in range to further increase precision. Velocity estimates are derived from the autocovariance information. Subsequent corrections to the velocity estimates were applied to account for FLIP tilt (Plueddemann, 1987) using the mean tilt over the 3 min intervals. The velocity estimates were also corrected for a bias toward zero velocity which occurs at low signal to noise ratio. The bias correction was typically significant in the last few hundred meters of the data. Three, six and twelve minute averages were formed for use in the studies presented below. Corrections for azimuth fluctuation were unnecessary, as the automatic orientation system kept heading constant to within a few degrees. Unfortunately, in periods of high wind toward the end of the experiment, the acoustic noise generated by the orientation system was sufficient to degrade sonar performance. The maximum useful depth was reduced to less than 800 m for a two-day period on November 10–12. These data have not been used in the present analyses.

REFERENCES

Briscoe, M. G., 1975: Preliminary results from the Trimoored Internal Wave Experiment (IWEX). *J. Geophys. Res.*, **80**, 3872–3884.

Fofonoff, N., 1969: Spectral characteristics of internal waves in the oceans. *Deep-Sea Res.*, **16**(Suppl.), 58–71.

Garrett, C. J. R., 1972: Space-time scales of internal waves. *Geophys. Fluid Dyn.*, **2**, 225–264.

——, 1975: Space-time scales of internal waves: A progress report. *J. Geophys. Res.*, **80**, 291–299.

——, and W. H. Munk, 1971: Internal wave spectra in the presence of fine structure. *J. Phys. Oceanogr.*, **1**, 196–202.

McKean, R. S., 1974: Interpretation of internal waves measurements in the presence of fine structure. *J. Phys. Oceanogr.*, **4**, 200–213.

Müller, P., D. J. Olbers and J. Willebrand, 1978: The IWEX spectrum. *J. Geophys. Res.*, **83**, 479–500.

Phillips, O. M., 1971: On spectra measured in an undulating layered medium. *J. Phys. Oceanogr.*, **1**, 1–6.

Pinkel, R., 1975: Upper ocean internal wave observations from FLIP. *J. Geophys. Res.*, **80**, 3892–3910.

——, 1981: Observations of the near-surface internal wavefield. *J. Phys. Oceanogr.*, **11**, 1248–1257.

——, 1984: Doppler sonar observations of internal waves: The wavenumber frequency spectrum. *J. Phys. Oceanogr.*, **14**, 1249–1270.

——, 1985: A wavenumber–frequency spectrum of upper-ocean shear. *J. Phys. Oceanogr.*, **15**, 1457–1469.

Plueddemann, A. J., 1987: Observations of the upper ocean using a multibeam Doppler sonar. Ph.D. thesis, University of California, San Diego, La Jolla, CA.

Smith, J., R. Pinkel and R. A. Weller, 1987: Velocity structure in the mixed layer during MILDEX. *J. Phys. Oceanogr.*, **17**, 425–439.

Williams, R. G., 1985: The internal tide off Southern California. Ph.D. thesis, University of California, San Diego, La Jolla, CA.

Zalkan, R. L., 1970: High frequency internal waves in the Pacific Ocean. *Deep-Sea Res.*, **17**, 91–108.

Craters, Calderas, and Hyaloclastites on Young Pacific Seamounts

RODEY BATIZA,[1] DANIEL J. FORNARI,[2] DAVID A. VANKO,[1,4] AND PETER LONSDALE[3]

Craters, calderas, and bedded hyaloclastites are commonly associated with seamounts. New Sea MARC I side-looking sonar data for the summit of MOK seamount located near the East Pacific Rise (EPR) at 10°N show that MOK has a large caldera consisting of three coalesced circular depressions. These data also reveal many features such as stepped crater walls, talus deposits, ring faults, intracaldera flows, small cones, lava tubes and channels, and other features. Results of an ALVIN submersible dive in the crater of seamount "F" near the EPR at 21°22'N, 108°37'W revealed the presence of bedded hyaloclastite deposits; bedded hyaloclastites were also recovered by dredging of six other volcanoes all with summit craters. The bedded hyaloclastites are thin blankets of several types of basalt glass shards in a matrix of bottom sediment, clay, and ferromanganese minerals. The glass shards are chemically homogeneous and similar to midocean ridge basalts and transitional basalt lavas typical of young seamounts. Hyaloclastite deposits are crudely inverse graded with tabular, platy shards parallel to bedding. The characteristics of bedded hyaloclastites on seamount suggest an origin by rapid eruption rate, explosive mixing of magma and seawater, followed by rapid transport and deposition, such as may occur during submarine lava fountaining.

INTRODUCTION

This paper has two main purposes. The first purpose is to present new data on the occurrence, morphology, and characteristics of craters and calderas of two young volcanic seamounts. Seamount "F" (21°22'N, 108°37'W) has a relatively flat summit, a summit crater that is ~2 km in diameter and ~60 m deep, and a pit crater 200 m deep. These features were studied with the ALVIN submersible. A single dive on the summit region also revealed the presence of bedded hyaloclastite deposits on the crater walls and on the floor of the caldera. These deposits were sampled by the submersible and also by dredges of the summit and flanks of F. New Sea MARC I side scan sonar data for the summit area of MOK seamount near the East Pacific Rise at 10°N detail the morphology of the walls and floor of a complex summit caldera. The caldera on MOK and the crater of F strongly resemble features on better studied subaerial basaltic shield volcanoes. For this reason we interpret their origin and evolution by processes known to occur on subaerial shield volcanoes of Hawaii and the Galapagos islands.

The second purpose of this paper is to present field and laboratory data on the bedded hyaloclastite on seamount F and other young seamounts near the East Pacific Rise. All the seamounts known to contain bedded hyaloclastites also have summit craters or calderas. Our data constrain the types of eruptions that produce bedded hyaloclastites on seamounts. Although similar bedded hyaloclastites are also found within normal ocean crust [Schmincke et al., 1978], we speculate that on seamounts the eruptive activity near summit craters can produce bedded hyaloclastites of the type we have observed. The question of genetic links between caldera collapse and the formation of bedded hyaloclastite on seamounts remains unanswered.

[1] Department of Earth and Planetary Sciences and McDonnell Center for the Space Sciences, Washington University

[2] Lamont-Doherty Geological Observatory.

[3] Marine Physical Laboratory, Scripps Institution of Oceanography.

[4] Now at Department of Geology, Georgia State University.

SEAMOUNT CRATERS AND CALDERAS

Background

Since small summit craters were first recognized on seamounts [Menard, 1964], sonars of higher resolution have revealed that summit craters ($\leq$1-km diameter) and calderas (>1-km diameter) are very common on small seamounts [Lonsdale and Spiess, 1979; Lonsdale and Batiza, 1980; Hollister et al., 1978; Batiza and Vanko, 1983; Fornari et al., 1983a, b, 1984; Searle, 1983]. Probably more than half of the many thousands of seamounts in the main ocean basins have surficial craters or calderas, and many of the remainder may have buried ones [Batiza, 1982; Batiza and Vanko, 1983].

The collapse features on seamounts vary from tiny pits only a few tens or hundreds of meters in diameter [Lonsdale and Spiess, 1979; Lonsdale et al., 1982] to large complex calderas more than 5 km long, like that on MOK seamount and some in the western Pacific and Philippine Basin [Hollister et al., 1978]. Many are about 1-2 km in diameter [Searle, 1983; Batiza and Vanko, 1983] and a few tens to hundreds of meters deep. There are insufficient data to determine systematic relations among crater diameter, crater depth, and volcano height for submarine volcanoes as observed for subaerial volcanoes [Basaltic Volcanism Study Project, 1981, p. 744].

Most seamount craters and calderas are roughly circular or elliptical in plan [Menard, 1964; Lonsdale and Spiess, 1979; Hollister et al., 1978; Batiza and Vanko, 1983; Malahoff et al., 1982; Lonsdale, 1983; Edwards et al., 1984]. Most craters are single collapse features floored by flat ponded lava flows. Other craters are more complex and consist of multiple collapse features that may be nested or coalesced in chains. Many craters are scalloped by collapse and mass wasting [Edwards et al., 1984; Delaney et al., 1983].

Most crater walls are vertical and truncate subhorizontal lava flows. Some walls are stepped and consist of vertical or slightly overhanging sections that alternate with talus ramps. Talus ramps and irregular projecting buttresses occur around the margins of the crater floors. The height of the outer walls often varies around the perimeter of a crater (e.g., seamount F), owing to irregular topography on the volcano summit, gentle tilting of the summit or crater floor, and breaching of the crater [Lonsdale et al., 1982; Lonsdale and Spiess, 1979; Fornari et al., 1984; Edwards et al., 1984; Hollister et al., 1978; Batiza and Vanko, 1983; Malahoff et al., 1982].
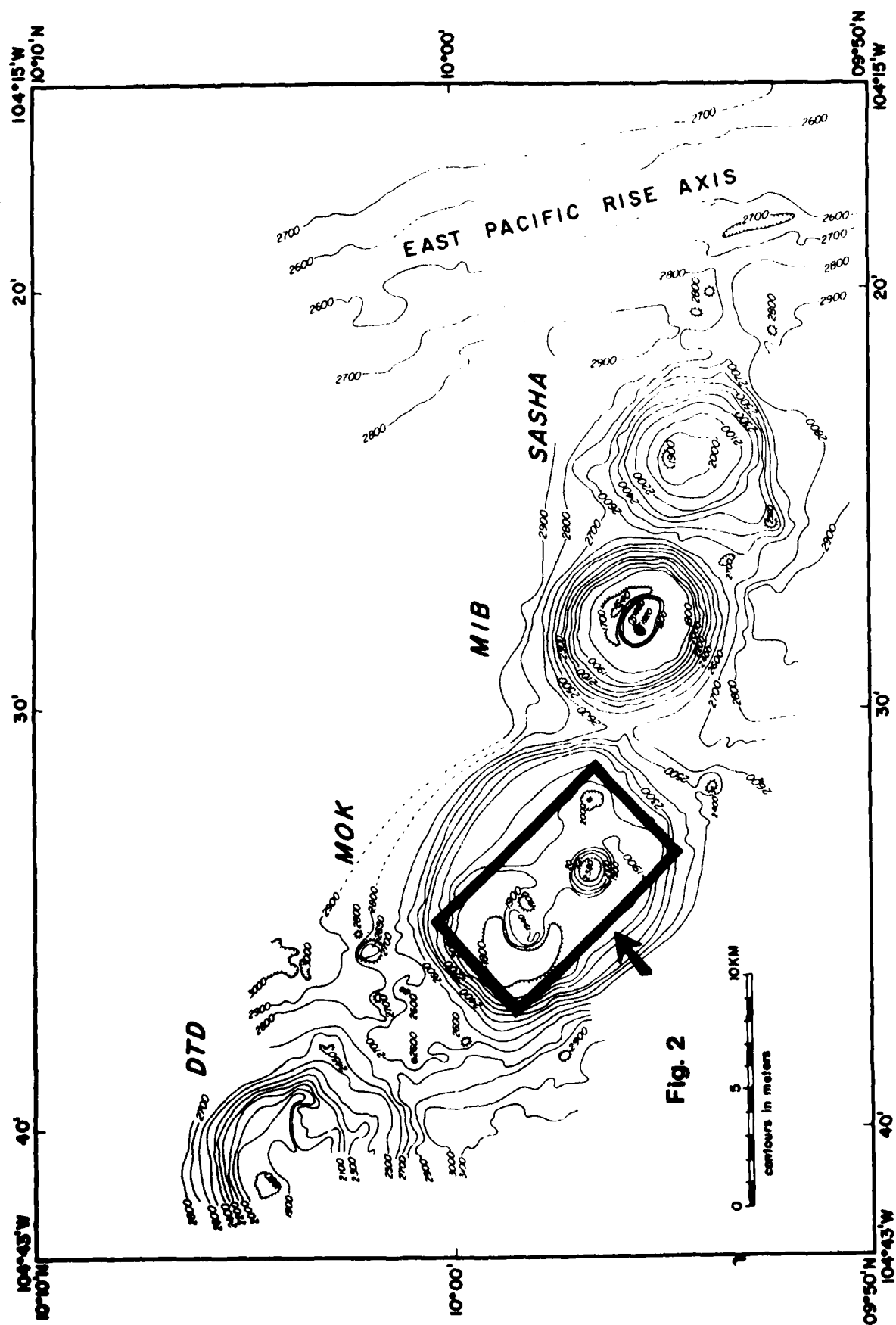
Fig. 1. Simplified base map of seamount group surveyed with Sea MARC 1 side scan and SEABEAM sonar systems [Fornari et al., 1984]. The area covered by the Sea MARC 1 acoustic image of Figure 2a is outlined.

MOK Seamount and Caldera

MOK seamount is an elliptical volcano measuring 11 by 13 km at its base rising from a depth of about 2800 m to a summit plateau that varies between 1900-m and 2000-m depth. MOK is the largest (~90 km³) of four volcanoes that form a linear group trending NW near the East Pacific Rise just west and south of the Clipperton fracture zone (Figure 1). All four volcanoes were bathymetrically surveyed with a SEA-BEAM swath mapping system (10-m contours), and the summits of Sasha, MIB, and MOK were surveyed with the Sea MARC 1 side scan sonar. Details of these surveys are presented by Fornari et al. [1983a, b, 1984].

Figure 2a shows the bathymetry of MOK's summit, and Figure 2b shows the side scan acoustic image of the summit of MOK seamount obtained with the Sea MARC 1. On this image, black regions represent strong reflectors, white areas are acoustic shadows, and grey regions have intermediate reflectivity. An interpretive sketch map of the Sea MARC 1 image is shown in Figure 2c. The side scan sonar (Figure 2b) resolves bottom features on the basis of contrasting acoustic reflectance, which varies with composition, slope angle, and roughness. For this reason, Sea MARC 1 plus SEABEAM data in combination provide more information than either type alone.

The summit of MOK has three coalesced craters, each about 2 km in diameter, arranged in a line roughly parallel to the direction of elongation of the volcano (Figure 2). The depth of the southeastern crater (Cauldron Crater) is 380 m along its north rim and 480 m along its south rim because the summit of MOK slopes down to the north. This is the deepest submarine crater known. The middle and northwest craters have coalesced. The middle crater is 10-20 m deep along its southern rim, and its northern wall is poorly defined, especially on the northeast side. The northwest crater has walls about 100 m high on the north side and lower on the south side. Partly surrounding the west side of this triple caldera is a broad, arcuate ridge 100 m high (Figures 1 and 2a). Broad, arcuate ridges of this type are very common on cratered seamounts having fairly flat tops [Lonsdale et al., 1982; Batiza and Vanko, 1983], and we refer to them as summit benches (Figure 3).

The triple caldera on MOK is so similar in size and shape to Mokuaweoweo caldera on Mauna Loa that we have named it (in abbreviated form) after the Hawaiian caldera. Figure 2b shows that the floors and walls of the three coalesced craters differ from each other. The Sea MARC 1 image also shows several volcanic and structural features on the summit outside the caldera (Figure 2c). These include several small volcanic cones, lava tube and channel systems, several features that we interpret as eruptive fissures, and normal faults that are circumferential to the western part of the caldera.

The walls of Cauldron Crater consist of nearly vertical cliffs (black in Figure 2b) separated in several places by narrow, discontinuous horizontal benches that are white in Figure 2b. The floor of the crater is characterized by hummocky topography that may represent primary eruptive constructional topography. The floor of the middle crater is much smoother than that of Cauldron Crater. This smooth surface could be the surface of a lava lake, or alternatively it could be flat because it is partly filled with sediment. Two narrow lobate features oriented north-south are present on the north side of the crater floor. These features have a furrowed surface and we interpret them to be lava flows that originated near the north

wall of the crater and spread south across the crater floor for a distance of about 0.75 km. Their relatively low reflectivity suggests that they may be partly covered with sediments which typically are good absorbers of acoustic energy. SEA-BEAM data (Figure 2a) show that the floor of the middle and northwestern craters slopes to the east about 0.6° [Fornari et al., 1984]. If the lobate features on the north side of the middle caldera are lava flows, the flow directions inferred from their shapes seem to be qualitatively consistent with a component of eastward downslope movement.

The northwestern crater exhibits the greatest acoustic diversity and contains many features that are probably sediment-free constructional volcanic features on the basis of their high reflectivity (Figure 2b) and relief (Figure 2a). Because it appears to have little sediment, we believe that the western crater floor has been volcanically active more recently than the other two. Along the bases of both the northern and southern walls of the western crater is a discontinuous band of moderately reflective seafloor that we interpret as talus.

South of the talus deposits on the north side of the western crater are three distinct lobate, highly reflective features that we interpret as lava flows. On the basis of superposition, the smallest, northernmost of these appears to be the youngest. Near its northwestern rim and within the western crater there is an arcuate ridgelike feature (Figures 2a and 2b) concentric to the crater wall. We interpret this feature as an eruptive fissure. Subparallel and to the south of this arcuate feature is another stubby linear feature that we also interpret as an eruptive fissure. The southeast trending lobate features on its south side we interpret as lava flows. Finally, just west of the western caldera is an arcuate reflector which parallels the crater walls. We interpret this as a ring fault circumferential to the westernmost crater.

The Crater of Seamount F

Figure 3 is a bathymetric chart of seamount F, based on a conventional wide-beam echo sounder survey. This volcano was studied in detail in 1982 with the ALVIN submersible (one dive: number 1178) and the ANGUS deep-tow camera (one lowering: number 166). In addition, two dredges of F were made: one at the summit (PL-D5) and one on the SSE flanks between 2480-m and 2450-m depth (PL-D4, Table 1). Both of these dredges recovered bedded hyaloclastite. Seamount F rises from ~2900 m to a height of about 2100 m (Figure 3). It has an elliptical sloping caldera about 2 km in diameter whose floor on the southwest side contains a pit crater about 600 m in diameter and 200 m deep.

Dive 1178 of ALVIN began at a point about 100 m south of the pit crater on the caldera floor (Figure 3). Between this point and the pit crater the caldera floor is fairly flat and consists of about 30–40% outcrop of volcanic rock separated by younger ponds of cream colored calcareous ooze. The outcrops are about 5 m to 15 m across and consist of lobate flow surfaces and low piles of loose pillow fragments, all of which are coated with ferromanganese material and partly covered by sediment. Within about 50 m of the pit crater, outcrops of much fresher looking pillow basalt were encountered. These pillows are elongated in the downslope direction (south), and later in the dive they were seen to cover loose rubble on the upper southwest walls of the pit crater. In general, along the short traverse toward the pit crater, the proportion of rock outcrop to sediment increased and the thickness of ferro-manganese coatings on pillows decreased. Early in the trav-

Fig. 2
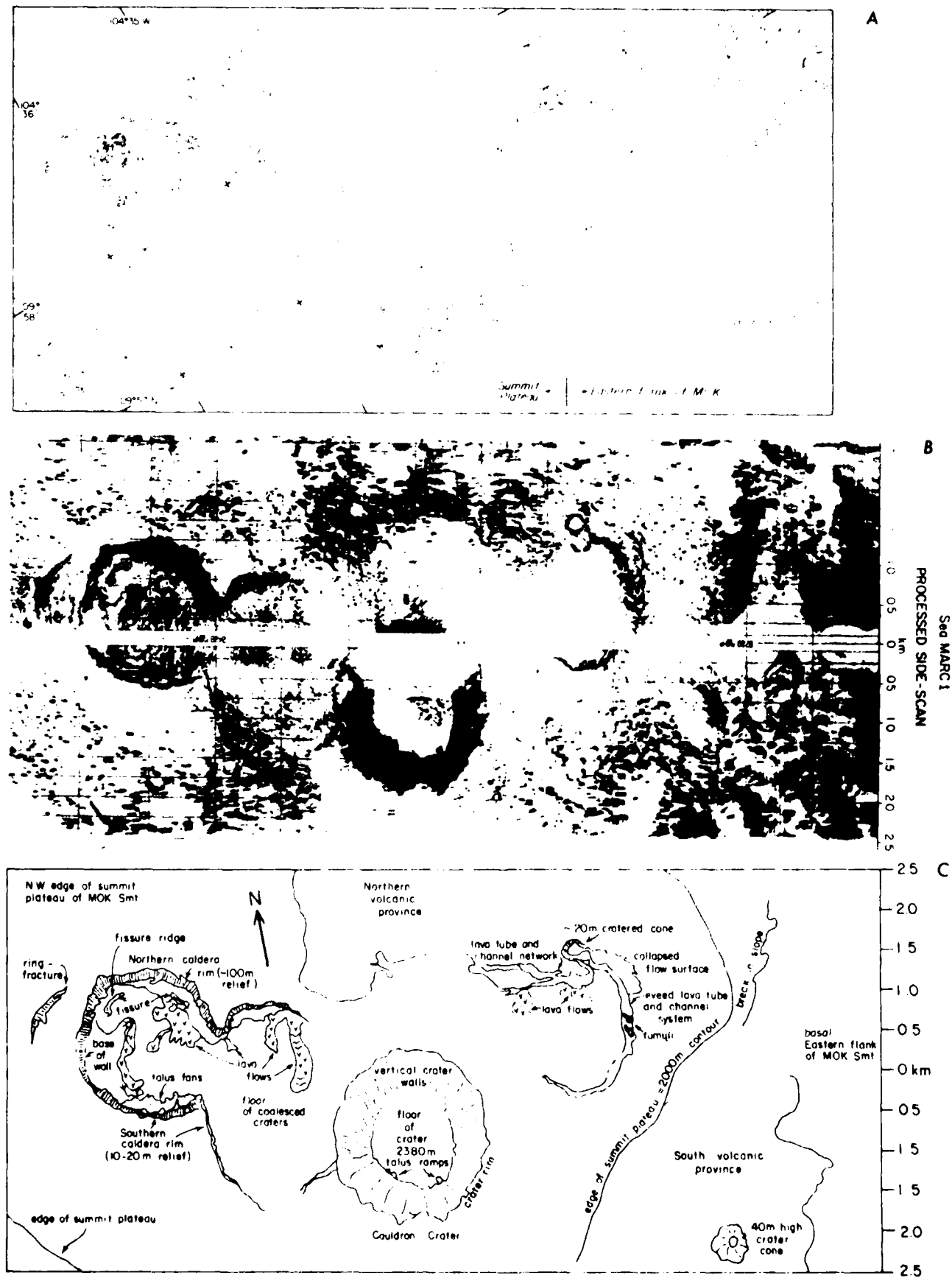
erse, we recognized a thin disrupted hyaloclastite pavement on the caldera floor.

The walls of the pit crater are step like, having average slopes of 40° in which vertical cliffs that truncate pillows alternate with rubbly talus slopes. The talus consists generally of loose blocks up to 30–40 cm in size, but in some parts the talus is mixed with fine grained sediment. In one place a thin hyaloclastite pavement coat the talus. The floor of the pit crater is covered with sediment and gravel-sized rock fragments. The caldera floor on the east side of the pit crater consists of wrinkled and folded surfaced basalt flows partly covered by sediment. About 700 m east of the pit crater, we encountered outcrops 2–3 m high consisting of entrail pillow lava having shiny glass surfaces. From this point the ALVIN submersible turned southeast to intersect the east-west trending south wall of the caldera. Before reaching the wall, we encountered mainly pillow basalt, partly covered with sediment, cut by several small (2- to 3-m displacement) east-west trending normal faults. These faults also cut a hyaloclastite pavement deposit that overlies the pillow lavas and sediment.

Just before reaching the south wall of the caldera, we encountered very fresh pillow lava and wrinkle-textured lava erupted directly onto a sediment-covered surface. These are the freshest volcanic rocks that we encountered during the dive. The wrinkle-textured lava is apparently younger than the pillow lava because in several places we observed it partly covering outcrops of pillow lava. The caldera wall resembles the stepped walls of the pit crater, with cliffs of truncated lava flows alternating with aprons of talus.

These observations suggest that the caldera and pit crater both formed before the eruption of hyaloclastites and that pillows and wrinkle-textured flows may have erupted after the hyaloclastite. The youngest basalt eruptions that we observed originated within the caldera floor near the pit crater and at the southern margin of the caldera near the main caldera wall.

INTERPRETATION AND DISCUSSION OF CALDERA FEATURES

The collapse features on MOK and F greatly resemble their subaerially exposed counterparts, so in general we believe that it is reasonable to suggest that their origin and evolution may be quite similar to well-studied collapse features on Hawaii, the Galapagos islands, and elsewhere.

Craters and calderas formed by collapse are commonly found on many types of subaerially exposed volcanoes in various tectonic environments [Williams and McBirney, 1979]. On Hawaii, it has been possible to demonstrate that processes of caldera formation, coalescence, and enlargement are closely linked with processes of magma intrusion, transport, and eruption, seismic activity, and ground deformation [Ryan et

al., 1981, 1983; Wright and Fiske, 1971; Duffield et al., 1982; Epp et al., 1983; Thurber, 1984]. Specifically, there is strong evidence that summit collapse is probably caused by withdrawal of roof support due to lateral migration of magma outward to feed rift eruptions on Kilauea. Similar processes are thought to be important within Etna [Guest and Skelhorn, 1973; Sharp, 1982; Duncan and Guest, 1982]. On Galapagos volcanoes, which greatly resemble many seamounts in form (upturned soup bowl profile), circumferential fractures are present at the summit in close association with craters and calderas. These serve as magmatic conduits and may play a role in caldera enlargement [Simkin, 1972, 1984; Nordlie, 1973; Williams and McBirney, 1979]. On Piton de la Fournaise (Reunion Island) and Mauna Loa, coalescence of craters is thought to be an important process in the formation of large calderas [Jaggar, 1947; Duffield et al., 1982; Dana, 1890; Macdonald and Abbott, 1970]. In a related fashion, small pit craters are thought to form by stoping and magma withdrawal over subterranean magma conduits.

The results of previous studies of seamount craters and calderas together with the new data presented here provide evidence that summit craters and calderas on seamounts form by c   .pse. On MOK seamount the collapse mechanism may be very similar to that inferred for Kilauea [Fornari et al., 1984]. For volcano F there is less evidence for voluminous flank eruptions, so we speculate that withdrawal of roof support may be caused principally by summit eruptions. It is clear that submarine calderas and craters can have eruptive and structural histories that are as complicated as those of subaerial summit collapse features. Eruptions within calderas and craters are probably common. Much more detailed study will be required to determine how similar the origin and evolution of submarine calderas and craters are to the better studied subaerial ones.

SEAMOUNT HYALOCLASTITES

Background

Rittman [1960] first used the term hyaloclastite to describe rocks made of sand-sized basalt particles formed by in situ breakage of glassy pillow rims. Subsequently [Honnorez, 1963; Honnorez and Kirst, 1975; Schmincke et al., 1978], it has been shown that similar rocks may form in a variety of ways. Sand-sized particles of basalt glass may form by a variety of processes, and these particles may then be deposited during volcanic eruption or alternatively can be transported to form volcaniclastic sedimentary rock. Hyaloclastites are known to be common on seamounts [Bonatti, 1967; Batiza, 1980; Lonsdale and Batiza, 1980] and are also found within normal ocean crust in the deep sea [Schmincke et al., 1978; Dick et al., 1978; Robinson et al., 1979; Schmincke and von Rod, 1979].

Fig. 2 (a) Detailed bathymetry of the summit of MOK seamount. Contours were drawn by merging 10-m SEABEAM contours and Sea MARC I side scan reflectivity patterns. Final contours were hand drawn to insure consistency with side scan data which have the greatest resolution of vertical relief (approximately 2.5 m to 5 m). (b) Sea MARC I acoustic image of the summit plateau of MOK seamount. Width across swath (top to bottom) is 5 km. The image has been slant range corrected and orthorectified to a horizontal plane. Dark areas represent areas of high acoustic reflectivity such as walls, ridges, and flow fronts. White areas are flat or low areas in the acoustic shadow of the sonar beams. The instrument was towed almost 300 m off the bottom, so the average resolution on the image is about 2.5 m. (c) Interpretive geologic sketch map of the area covered by the Sea MARC I image shown in Figure 2a. The summit caldera consists of three coalesced craters: Cauldron Crater and the two adjoining craters to the west-northwest. Volcanic flows are clearly identified within the westernmost crater of the caldera as are eruptive fissures and fans of talus deposits shed from the steep caldera walls. Small cones are also present on the summit plateau. The cones are surrounded by acoustically rough terrain having well-developed lava tube and channel systems. (See text for additional discussion and details.)
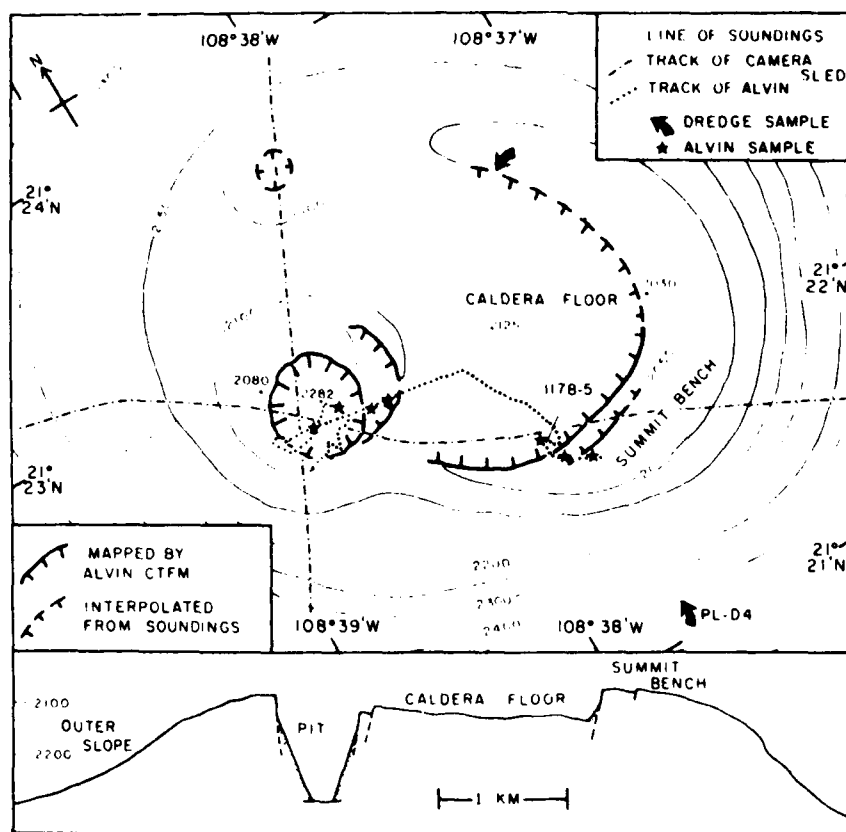
Fig. 3. Bathymetry of the summit area of seamount F, on the Rivera Plate 20 km northwest of the spreading center. Submersible and camera sled (ANGUS) tracks were transponder navigated. Northwest to southeast profile at twice vertical exaggeration is constructed from the bottom pinger trace of the camera sled. Location of samples PL-D4 and 1178-5 (Table 2) is shown.

Formation of glass fragments can occur by several processes [Schmincke et al., 1978]: (1) spalling of pillow rinds, (2) direct granulation (by thermal shock) of basalt magma [Schmincke et al., 1978; Bonatti, 1967; Carlisle, 1963; Moore et al., 1973], (3) vesiculation caused by expansion of magmatic gases, (4) steam explosions [McBirney, 1963], and (5) fuel-coolant interaction [Peckover et al., 1973]. Moreover, once the fragments are produced, they can be transported and deposited by a variety of mechanisms to form deposits. Transport may occur during or immediately after shard production [Schmincke et al., 1978] (i.e., the hyaloclastite is essentially produced as a primary igneous deposit), but very little is known about these processes in the deep sea. Furthermore, many other types of marine volcanic fragmental rocks such as pillow breccias, hyaloclastite breccias, and breccias of tectonic origin occur on seamounts, volcanic islands, normal ocean crust, and in the rock record [Batiza, 1980; Bonatti, 1967; Dimroth and Lichtblau, 1979; Carlisle, 1963; Natland, 1976; Staudigel and Schmincke, 1984]. Much more study is needed to develop criteria for recognizing various types of submarine fragmental rocks and understanding their origins [Honnorez and Kirst, 1975].

In the next section we describe the field occurrence of bedded hyaloclastite on seamount F and report the results of study of hyaloclastite specimens from seamount F and several other seamounts (Table 1). These new data, particularly for the bedded hyaloclastites, provide some constraints on the mechanism of shard production, transport, and deposition of this type of seamount hyaloclastite.

Field Occurrence of Hyaloclastite on Seamount F

During ALVIN dive 1178 we found hyaloclastite deposits at three localities. The first is on the caldera floor (~2100-m depth) about 100 m south of the pit crater (Figure 4). The hyaloclastite here forms a thin (3-5 cm) deposit overlying pelagic calcareous ooze. The deposit was probably once a continuous blanket deposit but now consists of large (10 cm to

TABLE 1. Hyaloclastite Localities

Dredge Number	Depth Interval, m	Volcano Name	Approximate Summit Depth, m	Reference*	Crater
D-3	2180-2000	1	1300	1, 2, 3	yes
D-19	2650 1860	6			
D-20	1860-1820	6	1100	2, 3	yes
D-24	2450-2160	8			
D-25	2450 2320	8	1200	2, 3	yes
D-27	1700-1580	9			
D-28	1810 1570	9	1700	2	'
CD-11	3115-2660	N-5	2400	3	yes
CD-12	2692 2299	N-5			
CD-14	3150-2551	N-2	1900	3	yes
PL-D-4	2520-2470	F			
ALVIN 1178	2200-2100	F	2100		yes

*References: 1, Lonsdale and Spiess [1979]; 2, Batiza [1981]; 3, Batiza and Vanko [1983].
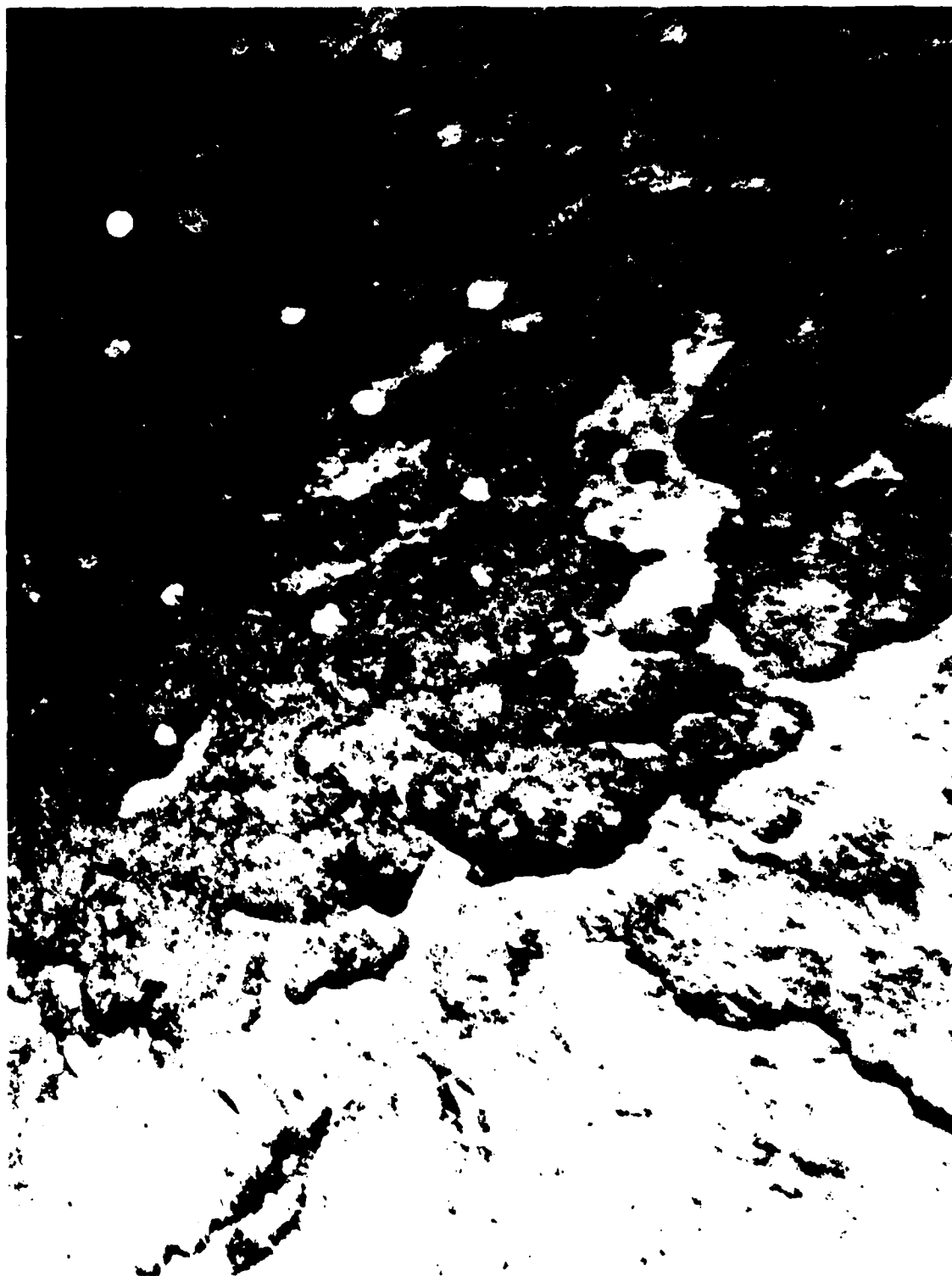
Fig. 4. Enlarged portion of a bottom photograph of a thin hyaloclastite deposit within the caldera of volcano F taken through the view port of the ALVIN submersible. The width of the field is approximately 1.5 m.

several m) polygonal sheets that are separated from one another by distance of up to several centimeters. Each polygonal sheet has a gently undulating surface with about 2-3 cm of relief. At the second locality, on the south wall of the pit crater, at ~2230-m depth, the hyaloclastite is deposited on a steeply dipping (30-40) fine-grained talus deposit. Apart from differences in original dip, the deposits at these two localities are very similar in appearance.

The third hyaloclastite outcrop we found is near the base of the south wall of the caldera (Figure 3). Hyaloclastite is exposed on the upper surfaces of several benches that are offset from one another by stepped normal faults of small displacement. The hyaloclastite here (Figure 5) partly covers pillow lava and is itself partly covered by talus deposits derived from pillow lava. A specimen of hyaloclastite collected from this locality at 2096-m depth (1178-5) has an upper surface that is
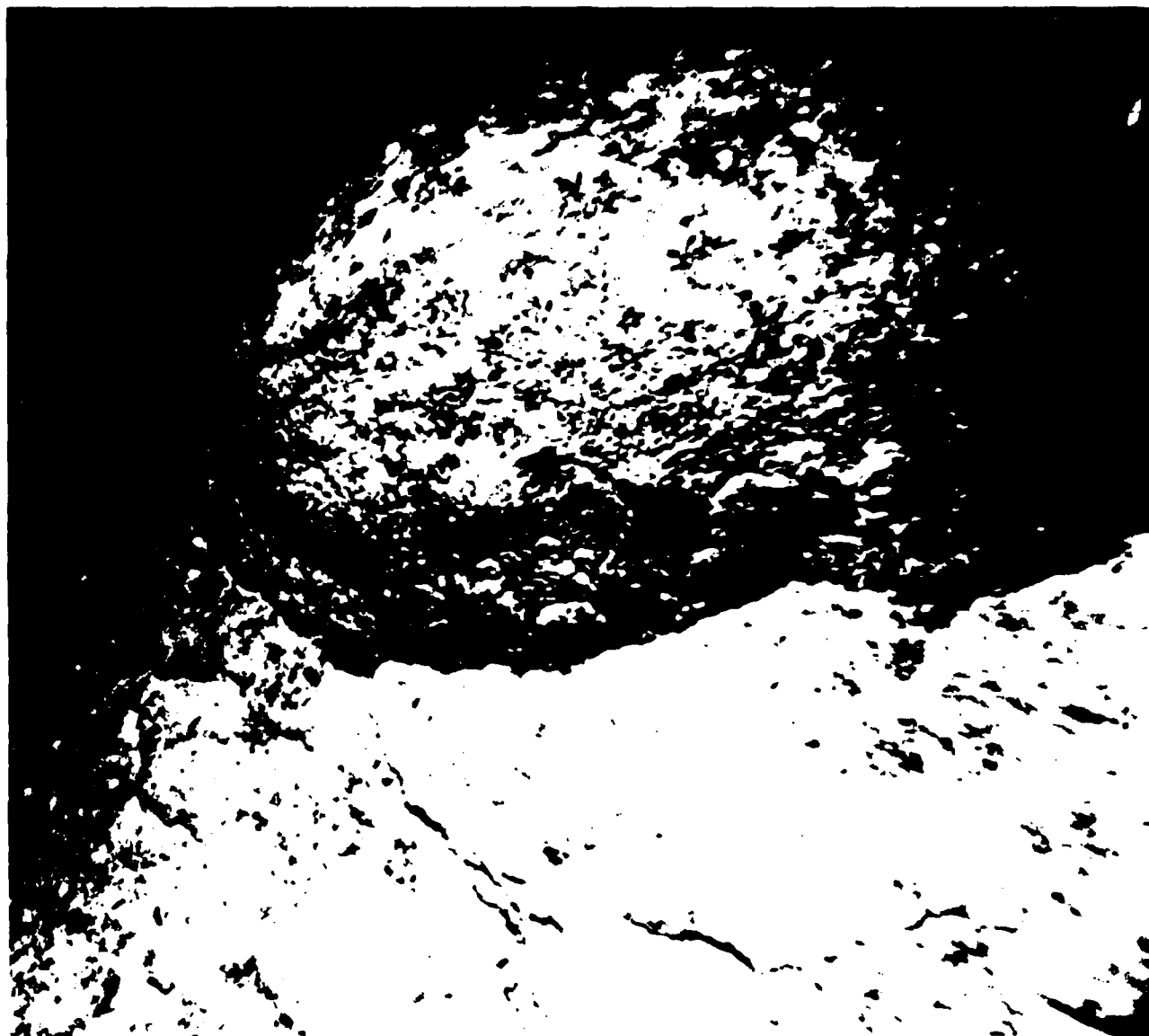
Fig. 5   ALVIN bottom photograph like Figure 4 showing the top of a Mn-encrusted pillow (0.5 ma cross) surrounded by hyaloclastite. This photo was taken near the southern crater wall of volcano F. This relativley proximal portion of the hyaloclastite deposit is probably at least 0.5 to 1.5 m thick.

relatively smooth and flat and is coated by about 1 cm of brown laminated ferromanganese crust. The bottom surface is flat but has much more small-scale (1-2 cm) surface roughness and only about 1 mm of ferromanganese coating. The hyaloclastite at this locality clearly predates the circumferential normal faults near the south caldera wall of seamount F. This deposit is thicker than comparable deposits farther from the caldera wall on the caldera floor. Assuming that the hyaloclastite deposits we saw on the caldera floor are the relatively distal portions of a deposit originating at the summit or near the caldera wall, our observations at three outcrops plus laboratory data to be discussed later are consistent with the highly speculative cartoon shown in Figure 6. This interpretive cartoon is meant to emphasize that the deposits are probably localized, that they are thin blanket deposits that can coat steep slopes, as in the pit crater, and that they probably originate at the seamount summit. This speculative hypothetical model of the size, geometry, and distribution of bedded

hyaloclastites is consistent with all our field observations and laboratory study of seamount hyaloclastites.

HYALOCLASTITE ROCK DESCRIPTIONS

Table 1 shows the data for young volcanoes from which we have recovered hyaloclastites, hyaloclastite breccia, and pillow breccia. In this paper we focus on the characteristics of bedded hyaloclastites. With the exception of volcano 9, which is poorly surveyed [Batiza, 1980], all the volcanoes of Table 1 have summit craters or calderas.

Hyaloclastite specimens are typically flat slabs up to 10 cm thick (Figure 7). They consist of unusually fresh basalt glass shards loosely cemented in a fine grained matrix. Almost all specimens exhibit crude graded bedding and platy shards that are oriented parallel to bedding (Figure 8). Hyaloclastite specimen 1178-5, collected by ALVIN, could be oriented and has inverse grading (largest shards at the top). Because of the great similarity among all specimens of bedded hyaloclastite, we
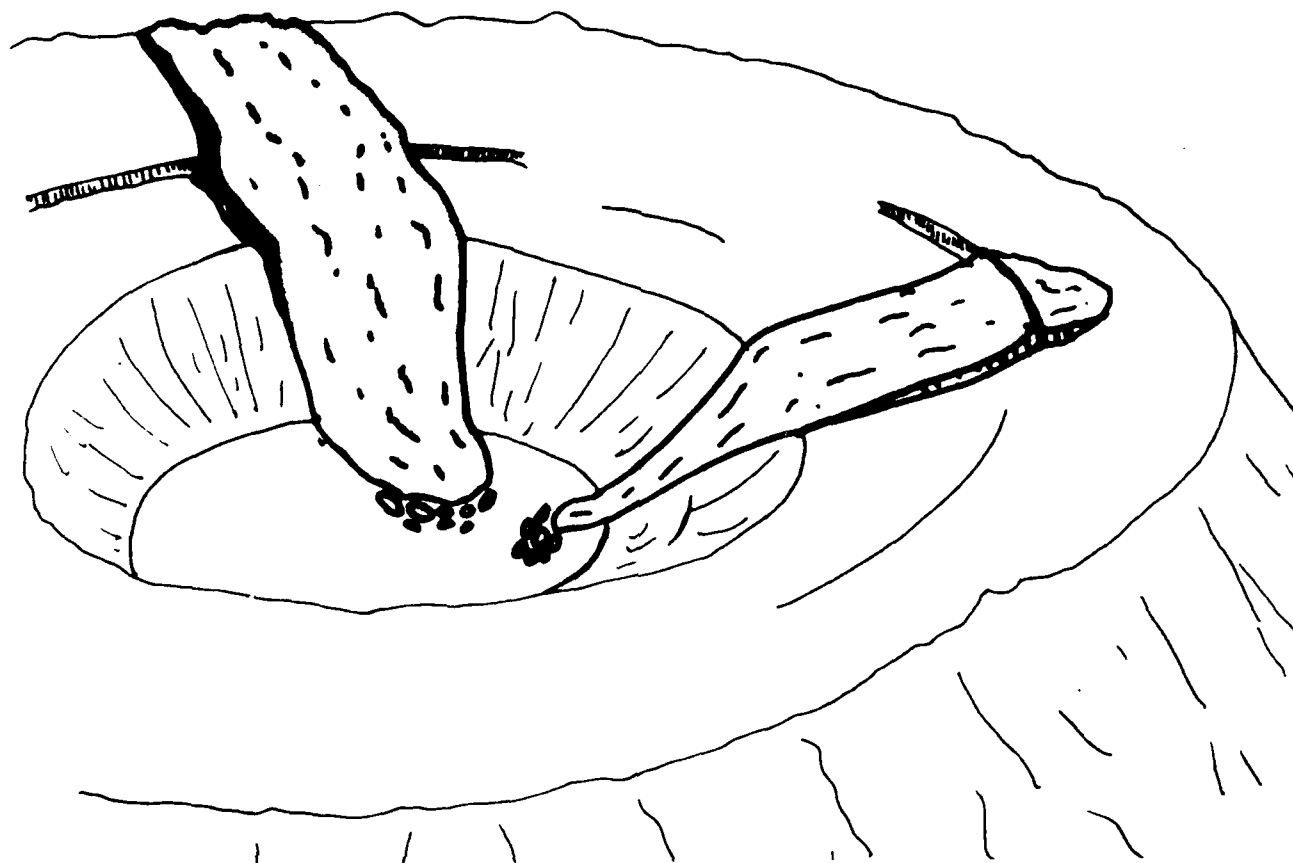
Fig. 6. A composite schematic drawing of the flat summit region of a small cratered seamount showing two hyaloclastite deposits. Their size, shape, and relative thickness are inferred from observations made during an ALVIN dive on volcano F. This is an interpretive composite, as no single deposit was traced continuously from its vent to its most distal part. In addition, no hyaloclastite vent area was recognized during the dive, though it is likely that they are localized along circumferential faults on the summit.

assume that the crude graded bedding of the dredged samples (unoriented) is also inverse rather than normal grading. This is supported by the observation that ferromanganese coating of many specimens (top) are on the side of the specimen with the largest shards. Individual specimens consist of either single (inversely) graded units about 3 6 cm thick or multiple inverse-graded units (up to three have been observed: Figure 7). In specimens with multiple, crudely graded units, the sense of grading is the same in each unit; however, the maximum particle size in each unit may differ.

All of the specimens we examined (about 40 specimens dredged on seven volcanoes plus one specimen collected by ALVIN on seamount F) are matrix-supported rocks. We recognize three distinct types of shards: (1) blocky and equant shards, (2) delicately curved shards including thin (10 30 μm) gently curved plates, and (3) small (5 30 μm) flake-shaped shards. The matrix material in which the shards are embedded consists of pelagic calcareous ooze which is replaced by clay minerals and ferromanganese oxides and hydroxides as the hyaloclastites weather. In the weathered specimens these secondary phases and palagonite also replace the margins of glass shards; in the most highly weathered ones, only the cores of the largest glass shards remain unaltered. In even the most weathered specimens, however, the relict fragments and bedded texture persist.

Morphology of the Glass Shards

The bedded hyaloclastites contain three morphologically distinct shard types. The most abundant are blocky, equant shards (Figure 9). These shards are usually crude cubes or tetrahedrons. The largest shards in each specimen are usually of this type, and they tend to be concentrated toward the tops of inversely graded units. The matrix material in which the equant shards are dispersed has a high concentration of tiny (usually 5 20 μm, rarely up to 50 μm) flakes of basalt glass. Shards of this second type greatly resemble the slivers and flakes pictured by Schmincke et al. [1978, Plate 3, Figures 3 and 4] and those produced by Carlisle [1963] from the shattering of molten basalt droplets immersed in water.

The third type are delicate glass shards with very complex and delicate shapes. Figures 10 and 11 show examples of delicately curved, infolded shards. Other shards in this group have thin, flat or curved tabular forms (Figures 8b and 11), recumbent folds and twisted and folded ribbon shapes. All these shards have linear striations on their surfaces, elongate stretched vesicles, and other features that provide evidence of stretching and elongation of the sort that occur in samples of Pele's hair [Heiken, 1972]. These shards are commonly found together with equant shards; however, they tend to be concentrated together toward the bottom, finer-grained parts of

Fig. 7. Hand specimen of hyaloclastite specimen CD14-2. Knife is 7 cm long. This specimen consists of three individual graded units that are difficult to recognize in the hand specimen. Since this specimen was dredged, we do not know whether the grading is normal or inverse. We infer, however, it is inverse grading because an oriented hyaloclastite sample from seamount F has crude inverse grading. If so, this specimen is correctly oriented with its top toward the top.

the hyaloclastite units (Figure 8). Furthermore, the straight and curved tabular shards tend to be oriented parallel to bedding (Figures 8b and 11). Rarely, these delicate shards exhibit welding (Figures 10b and 11d). These are the only shard types in the bedded hyaloclastite that are welded.

A common feature of the bedded hyaloclastites is the presence of groups of shards, separated by matrix material, that can be fitted together like pieces of a puzzle (Figure 12). These groups usually consist of both equant shards and fine flakes and are found most commonly toward the tops of the hyaloclastites. However, in some instances, delicate shards, particularly of tabular form, consist of many small unconnected fragments like puzzle shards (Figure 11b).

Chemical Composition of the Shards

Table 2 gives electron microprobe major element analyses for representative glass shards from specimens of bedded hya-

loclastites. Figure 13 shows chondrite-normalized rare earth element patterns for several of these. The hyaloclastites are mostly similar to light rare earth element depleted midocean ridge basalt (MORB), but some specimens are chemically transitional between MORB and alkalic basalt. Batiza and Vanko [1984] have shown that seamount lavas consist mostly of MORB compositions with minor amounts of transitional and alkalic basalt. Therefore the range of chemical compositions of hyaloclastite are similar to the composition of lavas on seamounts.

Hyaloclastites have only very rare lithic fragments (up to three or four per thin section, but usually one or none, see Figure 9c). In addition, most specimens contain few mineral fragments. Sparse angular fragments of plagioclase, olivine and pyroxene crystals are present in some specimens, and, much more rarely, euhedral phenocrysts are present within glass shards. In general, the hyaloclastite shards consist entirely of glass with only very rare microlites or crystallites such
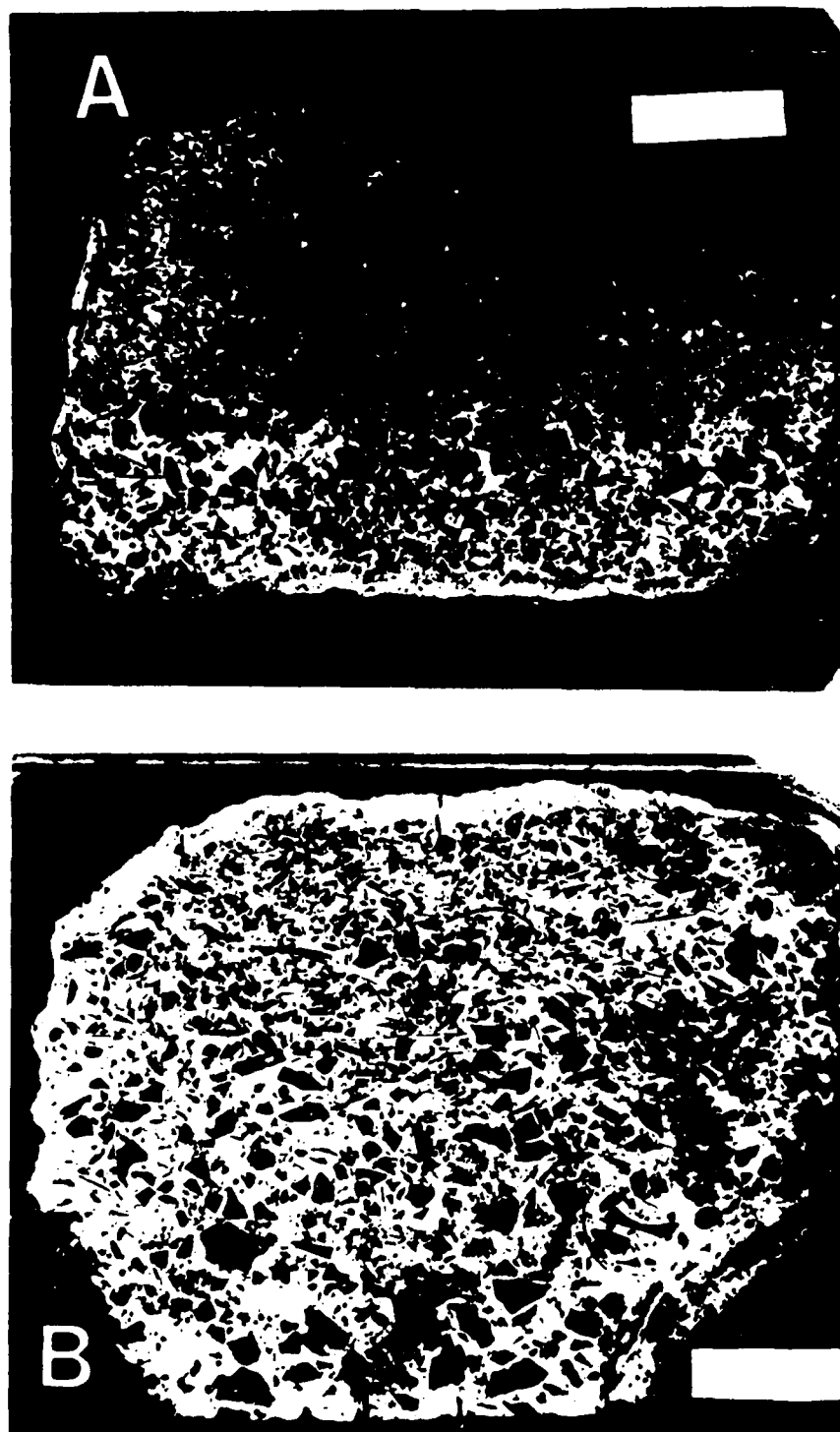
Fig. 8. Negative photomicrographs of two thin sections of hyaloclastite that show crude graded bedding. The sample in Figure 8a has been partly polished away at the upper right. Scale bars are about 7 mm long. Note that thin platy shards are oriented parallel to bedding. The sections are probably upside down, since hyaloclastites probably have crude inverse grading, not normal grading.

as those usually found in glassy pillow rinds. Figures 14 and 15 show that the glass shards of individual hyaloclastite specimens are chemically homogeneous. There are no systematic chemical differences among equant shards, delicate shards and small flakes. Instead, the various shard types belong to a single population on the basis of their chemistry. For specimens that consist of multiple reversely graded units, the

chemical composition of shards is the same within each unit and also among the different units.

Hyaloclastite Matrix

Several specimens of hyaloclastite possess a matrix that is nearly unaltered and consists of pelagic foraminiferal ooze (Figure 16d). The matrix of most specimens is moderately to
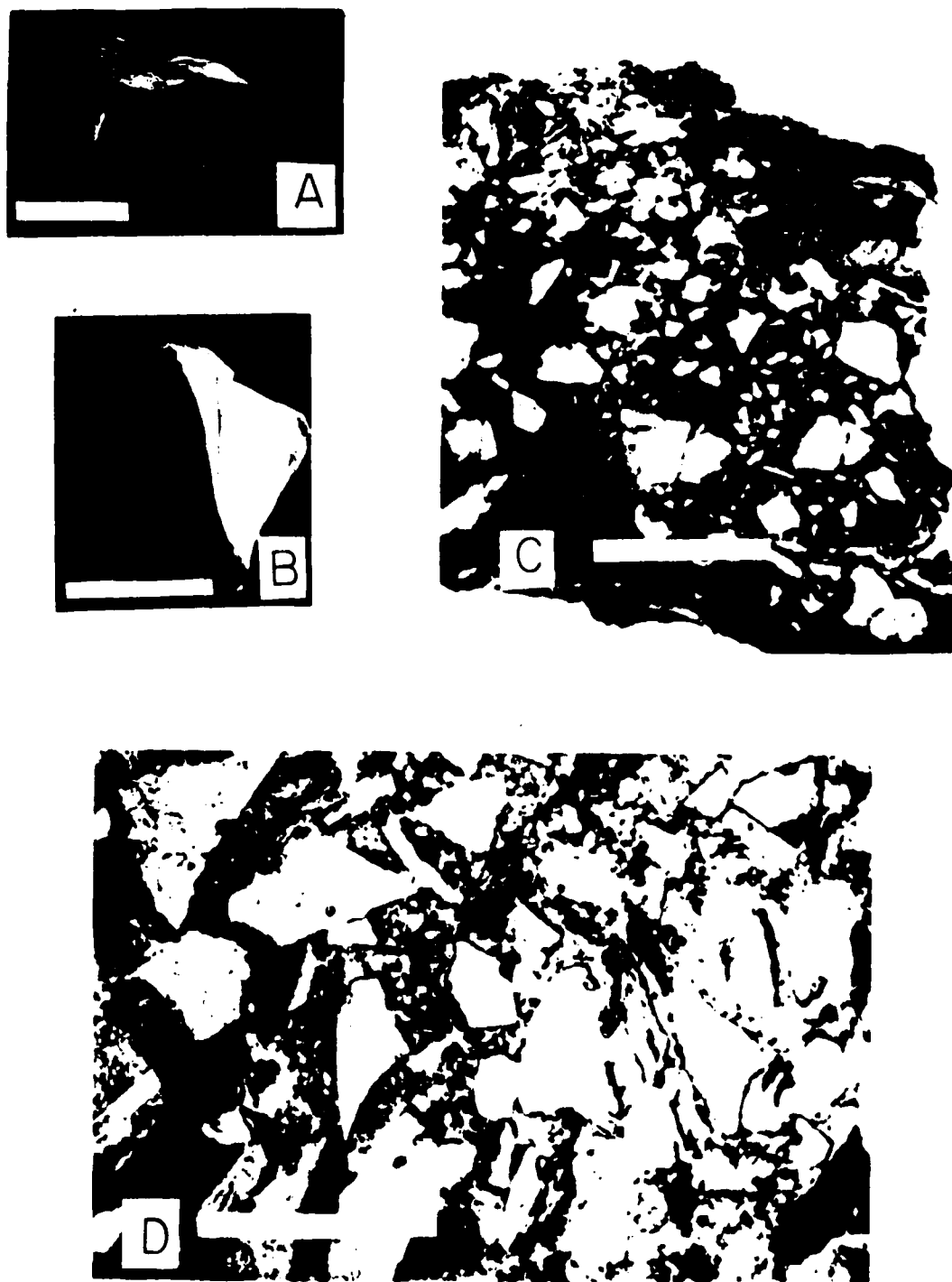
Fig. 9. Several views of equant shards of presumed explosive origin [*Heiken*, 1972]. (a) SEM photo of a roughly cubic glass shard from PL-D-4-21 (photo courtesy of M. Sheridan; scale bar is approximately 1 mm long). (b) SEM photo of an equant glass shard with a truncated tetrahedral form from specimen PL-D-4-21 Scale bar is 1 mm long. (c) Photomicrograph in plane-polarized light (scale bar is 8 mm) of a thin inverse-graded hyaloclastite unit (sample PL-D-4-4). This matrix-supported rock consists mostly of equant angular fragments of probable explosive origin. A rock fragment in the extreme upper right shows swirly, banded, partly crystallized flow texture in contrast with the other almost exclusively crystal-free glass shards. (d) Plane light photomicrograph of hyaloclastite PL-D-4-3 (scale bar is 3 mm) showing glass fragments which are mostly equant and presumably explosive in origin

almost completely replaced by clay minerals and ferromanganese oxides and hydroxides. Nevertheless, in most specimens, microfossils are still evident, which indicates that most of the hyaloclastites had a matrix that contained pelagic sediment prior to replacement (Figure 16). Progressive replacement of carbonate matrix starts with formation of fine grained yellow and light brown clay minerals. Next, after clay minerals have replaced most of the matrix, the remaining calcite and clay are replaced by opaque ferromanganese oxide and hydroxides. These opaque phases form patches between shards and also
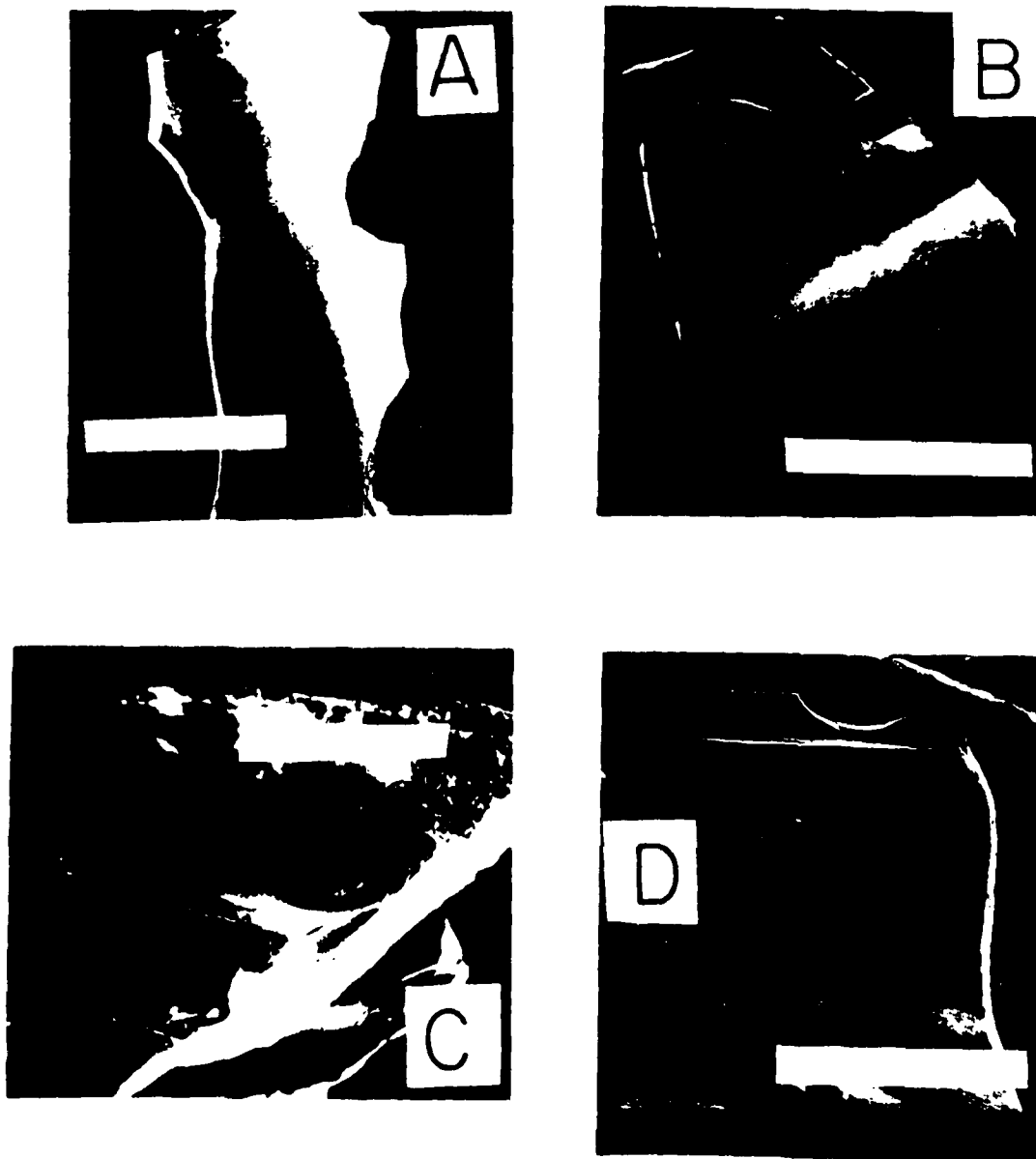
Fig 10 SEM photos of delicate fragile shards separated from sample PL-D-4-21 All scale bars are 1 mm. (a) An elongate curved shard which approximates a broken cylindrical shape Note the fine elongate surface striations. (b) A very delicate shard with a thin-walled branching form in cross section The thin sheetlike fragment on the surface is welded, and an oval weld mark is visible to its right (about 200 μm away) where another welded piece was intentionally broken off. (c) A delicate fragment showing stretched and circular vesicles of large size One such vesicle in the foreground is broken open at the edge of the shard partly revealing the open interior of the vesicle (d) A curved tabular shard with well developed striations similar to those produced when soft plastic is extruded through an orifice See text for discussion

form coatings around shards In some cases, these coatings replace the matrix surrounding the shard but in others, the coatings replace basalt glass. This replacement by opaque ferromanganese minerals proceeds inward from both the bottom and top surfaces of the hyaloclastites, however, the replacement zones are much thicker near the bottom surfaces compared with the tops

After the matrix is almost totally replaced, replacement of the glass shards begins The most abundant replacement products of glass shards are palagonite, birefringent orange clay, celadonite, and opaque ferromanganese minerals Replacement of glass shards begins at their outer surfaces and along cracks and proceeds inward Commonly, clay replacement of glass shards produces finely laminated planar and botryoidal masses of vari-colored clays

Hyaloclastite matrix also contains other secondary minerals including quartz, K-feldspar, and several different types of Ca- and Na-rich aluminosilicates that are probably zeolites. These may be of hydrothermal origin, as active hydrothermal vents and hydrothermal mineral deposits are known to exist on some seamounts [Lonsdale et al., 1982; Malahoff et al., 1982; Delaney et al., 1983]

INTERPRETATION OF THE ORIGIN OF BEDDED HYALOCLASTITES ON SEAMOUNTS

Many of the characteristics of the bedded hyaloclastites discussed before can be used to help constrain hypotheses of their origin In this section we discuss possible processes which could produce the different shard shapes we observed, possible transport processes which could give rise to the sedimentary

Fig. 11. Four photomicrographs (plane light) showing delicate curved shards. Scale bars are about 1 mm long, except for Figure 11b which is about 2.5 mm. (a) A cloverleaf-shaped shard. (b) Several very long tabular shards, in some cases broken into fragments ("puzzle" shards—see Figure 12). Upper right portion of Figure 11b is enlarged in Figure 11d, which shows a delicately curved ribbon of glass that is recumbently folded and welded at the point of contact. (c) A branched curvilinear ribbon of glass (like the one in Figure 11b) running diagonally from the lower left to the upper right.
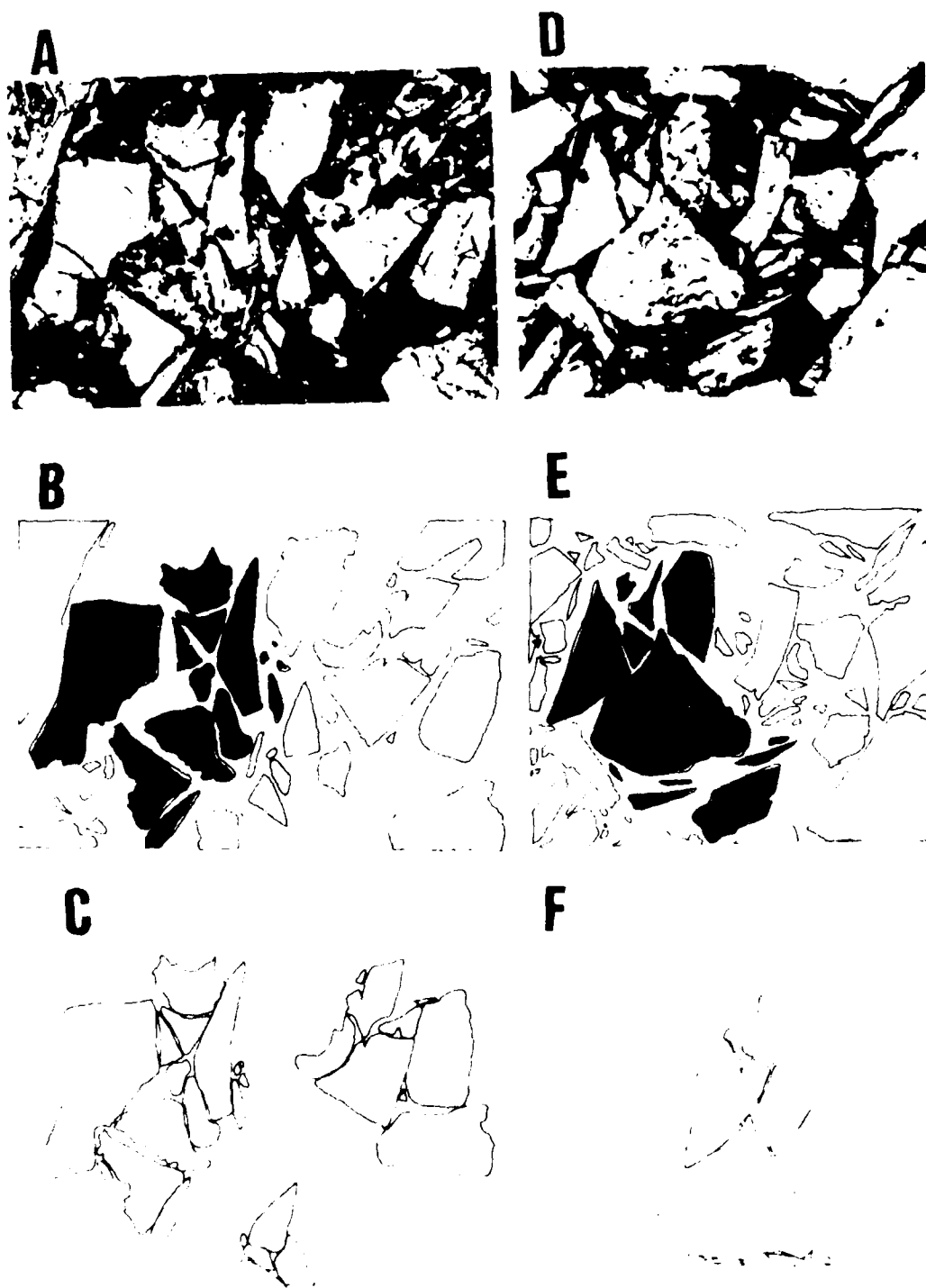
Fig. 12 Two photomicrographs of "puzzle" shards (Figures 12a and 12d) in plane light. Field of view is about 4 mm in each. Figures 12b and 12e show tracings to emphasize the glass shard outlines, and the pieces which are assembled in Figures 12c and 12f are shaded in the same pattern. Assembly of these fragments requires only small rotations and translations to achieve quite good fits. We interpret these groups of shards as pieces of glass fragments which were once larger and were surrounded by steam envelopes while they were hot. Carlisle [1963] showed fragmentation of shards occurs only after their steam envelope disperses during cooling. If so, these puzzle shards must have been still hot and surrounded by steam when they were deposited.

TABLE 2. Major Element Chemical Analyses of Glass Shards

	Sample Number										
	PL-D 4-1	PL-D 4-2	PL-D 4-5	PL-D 4-7	PL-D 4-11	PL-D 4-20	PL-D 4-21	1178 5	CD 11-1M	CD 12-9	CD 14-2
SiO_2	49.78	50.02	50.14	50.60	50.14	49.84	50.00	50.54	49.95	48.83	51.83
TiO_2	1.07	1.13	1.12	1.23	1.13	1.10	1.09	1.02	1.76	1.75	1.38
Al_2O_3	16.15	15.77	16.01	15.32	15.59	15.82	15.89	15.14	18.05	18.07	14.45
FeO^*	9.22	9.18	9.16	9.93	9.45	9.25	9.23	9.60	7.65	8.12	10.39
MgO	8.51	8.18	8.45	7.88	8.27	8.43	8.26	8.24	7.03	7.52	7.57
CaO	12.47	12.55	12.59	12.38	12.69	12.51	12.52	12.91	9.70	10.39	12.04
Na_2O	2.43	2.42	2.42	2.50	2.46	2.36	2.35	2.17	3.70	3.39	2.40
K_2O	0.06	0.05	0.06	0.05	0.06	0.05	0.03	0.04	1.17	0.78	0.08
P_2O_5	0.10	0.12	0.10	0.12	0.10	0.09	0.10	0.10	0.48	0.42	0.12
Total	99.79	99.42	100.05	100.01	99.89	99.45	99.47	99.76	99.49	99.27	100.26
$(Mg/Mg + Fe^{2+})$ $\times 100$	65.9	65.1	65.9	62.5	64.7	65.6	65.2	64.3	65.8	66.0	60.2

Analyses were performed by electron microprobe at the Smithsonian Institution. In computing the Mg number $((Mg/Mg + Fe^{2+}) \times 100)$, we assume that $Fe^{3+}/Fe^{2+} = 0.2$.

structures present in the hyaloclastites, and finally the possible types of eruptions that might produce hyaloclastite deposits.

First, we consider the possible origins of the abundant equant sharts. Heiken [1972] has shown that phreatomagmatic eruptions of high-viscosity magma can produce blocky and pyramidal, vesicle-poor shards of the type we find in the hyaloclastites. It is thus possible that steam explosions of seawater and hot basalt magma produce the blocky shards in the hyaloclastites. Table 1 shows that the rocks we have studied are all at sufficiently shallow depth (< 3100 m) for seawater (35‰ salinity) to boil with a sudden and large volume change [Delaney and Cosens, 1982]. The blocky hyaloclastite shards are all very vesicle poor and rarely have mineral crystallites or microlites. This suggests that they formed after very rapid quenching of volatile-poor magma, so we can confidently rule out shard formation from spallation of pillow rinds, which commonly have abundant microlites and crystallites. In addition, we can rule out the process of shard formation by vesiculation of magmatic gases.

We cannot rule out the possibility that equant shards formed by explosions resulting from fuel-coolant interactions [Peckover et al., 1973]. Such interactions involve the mixing of two molten materials that are at very different temperatures (e.g., basalt magma at 1200 C and seawater at 2 C) and that exchange heat rapidly and explosively. Such interactions have been invoked to explain certain hydromagmatic eruptions [Peckover et al., 1973], but we have no evidence that such processes are important for deep (> 2-km depth) submarine basalt eruptions. We also cannot rule out the possibility that direct granulation of basalt magma from thermal shock produced the equant shards. Usually, however, this process produces thin glass slivers and flakes, not blocky shards [Carlisle, 1963; Schmincke et al., 1978]. So, while it is possible that the equant shards were produced by direct granulation of basalt melt, fuel-coolant interactions, or steam explosions, we favor an origin by steam explosions.

The characteristics of the delicate, striated, and stretched shards discussed before favor an origin similar to that of Pele's hair, which they partly resemble [Heiken, 1972]. We suggest that they form by turbulent mixing of basalt magma and seawater. Their stretched and delicate shapes and the presence of welding suggest that they were deformed while still hot. They could form as moving basalt magma is mixed with, and rapidly chilled by, seawater.

The small flakes and puzzle shards found in the hyaloclastites seem to have formed by in situ shattering of larger glass fragments. Carlisle [1963] observed that droplets of basalt melt dropped into beakers of water did not shatter until their insulating envelopes of steam, which initially formed around the droplets, were dispersed. We suggest that the puzzle shards like those shown in Figure 12 formed in the same manner. If so, they provide evidence that the deposits were still hot when they were laid down, which in turn suggests relatively rapid transport.

The homogeneous chemical composition of the shards shows that they formed from a single magma batch. We can confidently rule out the possibility that the glass shards were formed and then transported much later, because if so, the shards would be expected to show more chemical diversity and, furthermore, to be somewhat rounded by sedimentary reworking. The rarity of lithic fragments suggests that if some of the glass shards formed explosively, the explosion probably
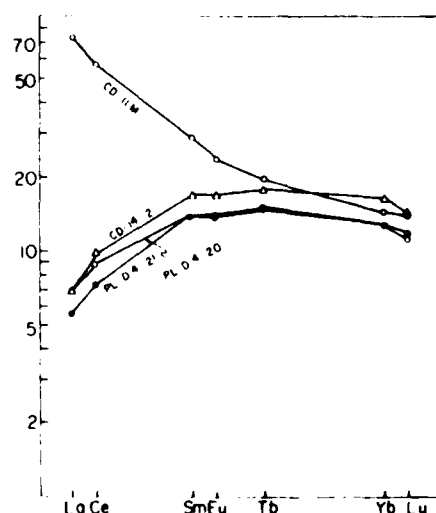
Fig. 13. Chondrite-normalized rare earth element abundances of glass shards separated from four hyaloclastite samples. Three are light rare earth element depleted and the fourth (open circles) is a transitional light rare earth element enriched basalt. Hyaloclastites and hyaloclastite breccias are not systematiclly different chemically from magmas which, under different conditions, form pillow lava and sheet flows.

Fig. 14. Tracing of a photomicrograph to show glass shard outlines This rock (sample PL-D-4-2) shows crude inverse graded bedding. The shaded shards (65 total) are the ones which we analyzed by electron microprobe. Results of these analyses are shown in Figure 15.
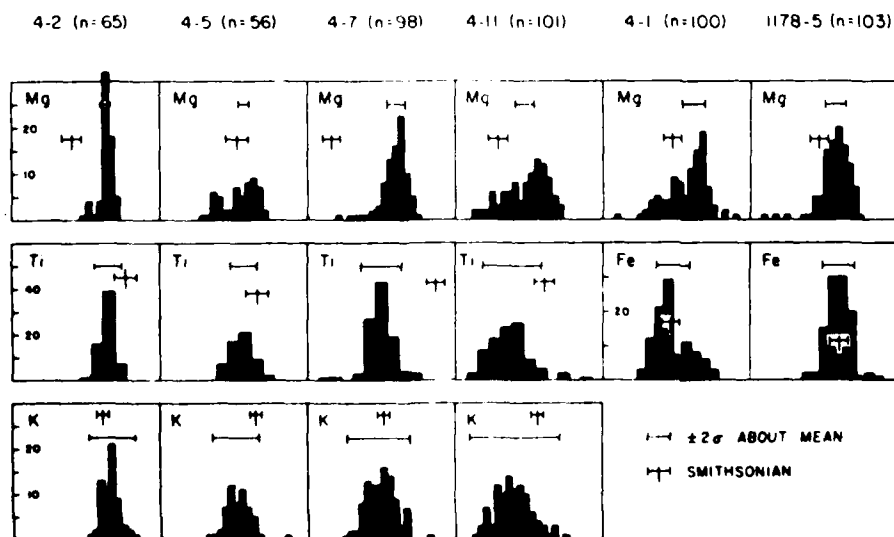
4-2 (n=65)   4-5 (n=56)   4-7 (n=98)   4-11 (n=101)   4-1 (n=100)   1178-5 (n=103)

Fig. 15. Results of partial microprobe analyses of a large number of grains in each of six hyaloclastites. Numbers at the top give sample number (PL-D-4), and n is the number of shards analyzed in each. Vertical axes in each panel are number of analyses, and horizontal axes represent a linear scale for peak intensity (abundance), increasing to the right in each diagram. The symbols labeled "± 2σ" show the extent of two standard deviations on each side of the mean, where the standard deviation was determined from counting statistics. The symbols labeled "Smithsonian" show the position of the reported element composition from Table 2, together with a conservative error bar (Mg, 2%, Ti and Fe, 2.5%, K, 10%). For example, in sample 4-2 the reported MgO content is 8.18 wt %. The symbol in the diagram for 4-2 shows the position corresponding to 8.18 wt % MgO, as well as the 2% error limits 8.02 and 8.34 wt % MgO. For 4-2 TiO₂, the symbol shows the nominal 1.13 wt % TiO, and error limits 1.10 and 1.16 wt %.
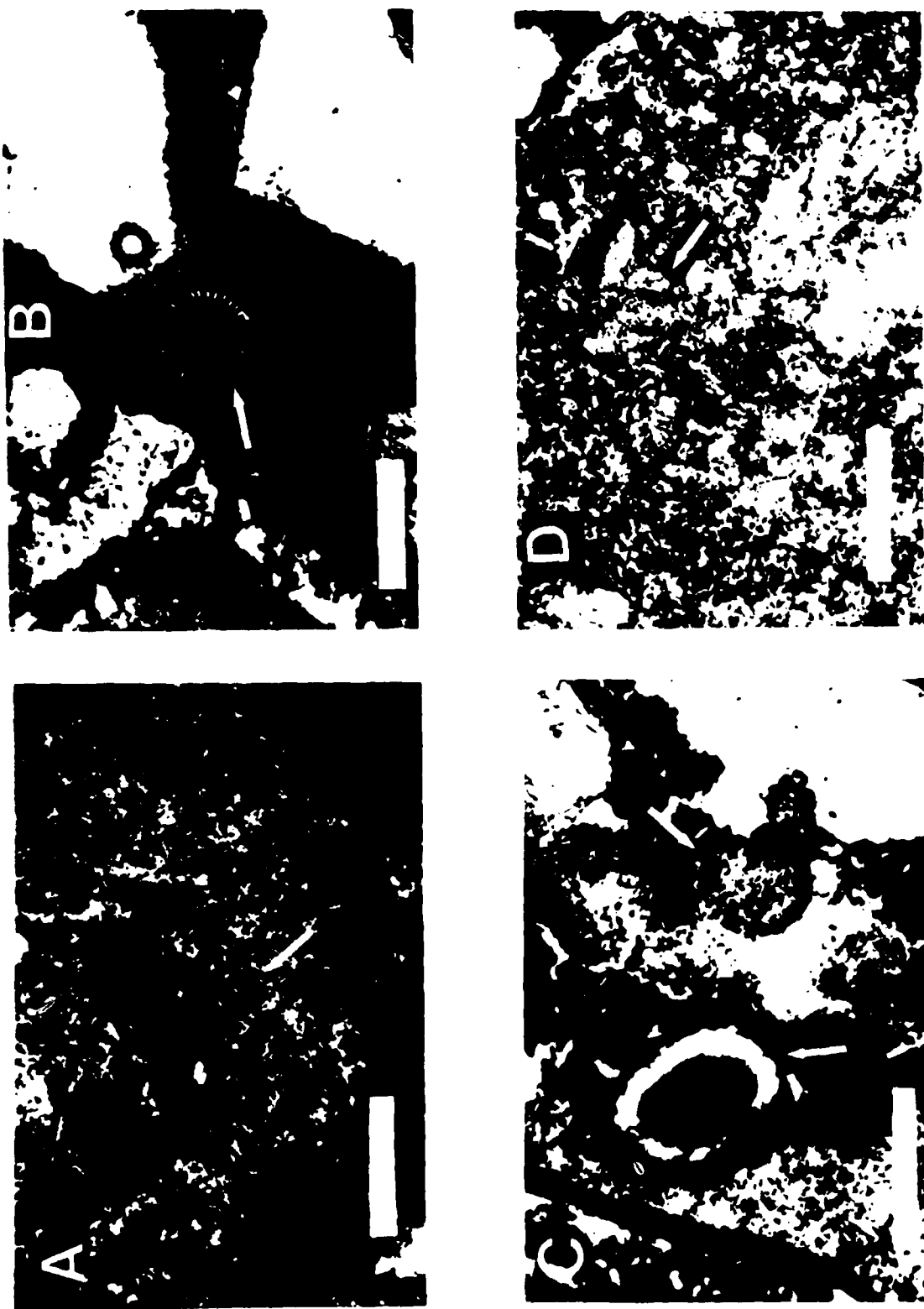
Fig. 16. Four plane light photomicrographs showing fossils and fossil fragments in the matrix material of hyaloclastites. The matrix material shows a range of preservational states with Figure 16d being the freshest. The matrix of Figure 16b is completely replaced by ferromanganese material. All scale bars are approximately 0.5 mm long. In freshest samples the matrix consists mostly of fossil fragments, unaltered calcite particles, and clay, indicating a large admixture of pelagic ooze in these hyaloclastites.

took place very near the surface or above the vent. The crude inverse grading and the observed bedding-parallel orientation of platy shards are consistent with transport in a high-viscosity, high-density flow characterized by a laminar flow regime. Such sedimentary structures are characteristic of many debris flows and some lahars [Reineck and Singh, 1980; Fisher, 1971; Schmincke, 1967].

The shapes and composition of the hyaloclastite shards, their sedimentary structures, their field occurrence as thin blanket deposits, and the abundance of pelagic sediment in the matrix are all consistent with an explosive origin followed by transport in a high-density flow. The inferred orgin of the puzzle shards is consistent with rapid deposition of a hot slurry of basalt glass shards, sediment, and seawater plus steam. These observations and inferences are consistent with submarine eruptions similar to subaerial lava fountaining. Submarine lava fountaining might be expected to produce the shard types observed. Moreover, column collapse of a lava fountain could provide enough kinetic energy to cause mixing of shards with bottom sediment and a relatively high transport velocity for a high-density flow. Pulsation during lava fountaining may have produced the multiple inversely graded units. While lava fountaining activity appears to be consistent with the observed features of seamount hyaloclastites, other eruption types might be capable of producing such deposits. More detailed work on the occurrence and characteristics of seamount hyaloclastites is needed to further constrain their origin and significance.

DISCUSSION OF POSSIBLE RELATIONS BETWEEN SEAMOUNT HYALOCLASTITES AND SEAMOUNT CRATERS AND CALDERAS

In many subaerially exposed volcanoes, pyroclastic rocks produced by explosive eruptions are closely associated with calderas and craters [Basalt Volcanism Study Project, 1981, chapter 5; Williams and McBirney, 1979]. In some cases, there is strong evidence that explosive eruptions are the result of processes in conduits and chambers beneath calderas (Smith [1979], Hildreth [1981], Spera and Crisp [1981], and other papers in this issue). For the much less studied young volcanic seamounts, we have shown that hyaloclastites are commonly associated with summit craters and calderas. However, these preliminary results do not allow us to confidently establish the reasons for this common association.

The existence of complex calderas such as the one of MOK seamount implies that processes of magma ascent, storage, migration, and eruption on seamounts are as complicated and episodic as those known to occur on well-studied subaerial volcanoes [Ryan et al., 1981; Fornari et al., 1984]. The association of bedded hyaloclastites with calderas on seamounts is consistent with their formation either during or after caldera formation and/or enlargement. If our inferrence that hyaloclastites are produced by submarine lava fountaining is correct, then such activity occurring along ring faults that are commonly associated with craters and calderas on seamount summits could produce bedded hyaloclastite deposits at the summits and on the caldera walls and floors. These deposits could thus be produced by relatively small summit eruptions during or after crater formation. Much more study is needed to determine whether bedded hyaloclastites are more common on seamount summits compared with their flanks and whether their production is restricted to periods when calderas are present.

CONCLUSIONS

1. Craters and calderas on seamounts may be either simple circular depressions or may be morphologically much more complex, like the caldera on MOK seamount.

2. Bedded hyaloclastites are commonly associated with seamount craters and calderas. This suggests a genetic link between them, but not enough is known to confirm this possible relation.

3. Bedded hyaloclastite deposits occur as thin blanket deposits on the caldera walls and floor of seamount F. These deposits consist of glass shards of several types cemented in a matrix that consists largely of calcareous sediment. The glass shards are chemically homogeneous midocean ridge basalt and the deposits exhibit crude inverse grading with tabular shards oriented parallel to bedding.

4. The characteristics of bedded hyaloclastites suggest formation by rapid eruption rates, turbulent mixing of magma with seawater, steam explosions, and rapid transport and deposition. Eruptions such as deep water lava fountaining might produce these deposits.

REFERENCES

Basaltic Volcanism Study Project, Basaltic Volcanism on the Terrestrial Planets, 1286 pp., Pergamon, New York, 1981.

Batiza, R., The origin and petrology of young oceanic central volcanoes: Are most tholeiitic rather than alkalic?, Geology, 8, 447–482, 1980.

Batiza, R., Abundances, distribution and sizes of volcanoes in the Pacific Ocean and implications for the origin of non-hotspot volcanoes, Earth Planet. Sci. Lett., 60, 195–206, 1982.

Batiza, R., and D. Vanko, Volcanic development of small oceanic central volcanoes on the flanks of the East Pacific Rise inferred from narrow beam echo sounder surveys, Mar. Geol., 54, 53–90, 1983.

Batiza, R., and D. Vanko, Petrology of young Pacific seamounts, J. Geophys. Res., in press, 1984.

Bonatti, E., Mechanisms of deep-sea volcanism in the South Pacific, in Researches in Geochemistry 2, edited by P. Abelson, pp. 453–491, John Wiley, New York, 1967.

Carlisle, D., Pillow breccias and their aquagene tuffs in Quadra Island British Columbia, J. Geol., 71, 48–71, 1963.

Dana, J. D., Characteristics of Volcanoes, 339 pp., Dodd, Mead, New York, 1890.

Delaney, J. R., and B. A. Cosens, Boiling and metal deposition in submarine hydrothermal systems, Mar. Technol. Soc. J., 16, 62–66, 1982.

Delaney, J. R., J. L. Karsten, H. P. Johnson, R. Chase, S. D. Scott, V. Tunnicliffe, and S. Hammond, Structural control of hydrothermal vents and sulfide structures on the 'Axial Seamount,' Juan de Fuca (abstract), Eos Trans. AGU, 64, 889, 1983.

Dick, H. J. B., J. Honnorez, and P. W. Kirst, Origin of the abyssal sand, sandstone and gravel from DSPD hole 396B, leg 46, Initial Rep. Deep Sea Drill. Proj., 46, 331–339, 1978.

Dimroth, E., and A. P. Lichtblau, Metamorphic evolution of Archean hyaloclastites, Noranda area, Quebec, Canada, 1, Comparison of Archaen and Cenozoic sea-floor metamorphism, Can. J. Earth Sci., 16, 1315–1340, 1979.

Duffield, W. A., L. Stieltjes, and J. Varet, Hugh landslide blocks in the growth of Piton de la Fournaine, La Reunion, and Kilauea Volcano, Hawaii, J. Volcanol. Geotherm. Res., 12, 147–160, 1982.

Duncan, A. M., and J. E. Guest, Mount Etna: Variations in its internal plumbing, Geophys. Surv., 5, 213–227, 1982.

Edwards, M. H., R. E. Arvidson, and E. A. Guinness, Digital image processing of SEABEAM bathymetric data for structural studies of seamounts near the East Pacific Rise, J. Geophys. Res., in press, 1984.

Epp, D., R. W. Decker, and A. T. Okamura, Relation of summit deformation to East Rift zone eruptions on Kilauea volcano, Hawaii, Geophys. Res. Lett., 10, 493–496, 1983.

Fisher, R. V., Features of coarse-grained, high-concentration fluids and their deposits, J. Sediment. Petrol., 41, 916–927, 1971.

Fornari, D. J., W. B. Ryan, and P. J. Fox, High resolution side-scan sonar imaging of a linear seamount group near the crest of the East Pacific Rise at 9 53'N (abstract), Eos Trans. AGU, 64, 239, 1983a.

Fornari, D. J., W. B. F. Ryan, and P. J. Fox, Sea MARC 1 and SEABEAM sonar studies of seamounts near the East Pacific Rise at 10 N: The evolution of seamount structure and morphology (abstract), Eos Trans. AGU, 64, 729, 1983b.

Fornari, D. J., W. B. F. Ryan, and P. J. Fox, The evolution of craters and calderas on young seamounts: Insights from Sea MARC 1 and SEABEAM sonar surveys of a small seamount group near the axis of the East Pacific Rise at 10°N, J. Geophys. Res., in press, 1984.

Guest, J. E., and R. R. Skelhorn (Eds.), Mount Etna and the 1971 eruption, Philos. Trans. R. Soc. London Ser. A, 274, 1–179, 1973.

Heiken, G. H., Morphology and petrography of volcanic ashes, Geol. Soc. Am. Bull., 83, 1961–1988, 1972.

Hildreth, W., Gradients in silicic magma chambers: Implications for lithospheric magmatism, J. Geophys. Res., 86, 10,153–10,192, 1981.

Hollister, C. D., G. E. Morris, and P. Lonsdale, Morphology of seamounts in the western Pacific and Philippine basin from multibeam sonar data, Earth Planet. Sci. Lett., 41, 405–418, 1978.

Honnorez, J., Sur l'origine des hyaloclastites, Note preliminaire, Bull. Volcanol., 25, 253–258, 1963.

Honnorez, J., and P. Kirst, Submarine basaltic volcanism: Morphometric parameters for discriminating hyaloclastites from hyalotuffs, Bull. Volcanol., 39, 1–25, 1975.

Jaggar, T. A., Origin and development of craters, Mem. Geol. Soc. Am., 21, 508 pp., 1947.

Lonsdale, P., Laccoliths (?) and small volcanoes on the flank of the East Pacific Rise, Geology, 11, 706–709, 1983.

Lonsdale, P., and R. Batiza, Submersible study of hyaloclastite and lava flows on young seamounts at the mouth of the Gulf of California, Geol. Soc. Am. Bull., 91, 545–554, 1980.

Lonsdale, P., and F. N. Spiess, A pair of young cratered volcanoes on the East Pacific Rise, J. Geol., 87, 157–173, 1979.

Lonsdale, P., R. Batiza, and T. Simkin, Metallogenesis at seamounts on the East Pacific Rise, Mar. Technol. Soc. J., 16, 54–61, 1982.

Macdonald, G. A., and A. T. Abbott, Volcanoes in the Sea, 400 pp., University of Hawaii Press, Honolulu, 1970.

Malahoff, A., G. M. McMurtry, J. C. Wiltshire, and H.-W. Yeg, Geology and chemistry of hydrothermal deposits from active submarine volcano Loihi, Hawaii, Nature, 298 234–239, 1982.

McBirney, A. R., Factors governing the nature of submarine volcanism, Bull. Volcanol., 26, 455–469, 1963.

Menard, H. W., Marine Geology of the Pacific, 271 pp., McGraw-Hill, New York, 1964.

Moore, J. G., R. L. Phillips, R. W. Grigg, D. W. Peterson, and D. A. Swanson, Flow of lava into the sea, 1969–1971, Kilauea Volcano, Hawaii, Geol. Soc. Am. Bull., 84, 537–546, 1973.

Natland, J. H., Petrology of volcanic rocks dredged from seamounts in the Line Islands, Initial Rep. Deep Sea Drill. Proj., 33, 749–777, 1976.

Nordlie, B. E., Morphology and structure of the western Galapagos

volcanoes and a model for their origin, Geol. Soc. Am. Bull., 84, 2931–2956, 1973.

Peckover, R. S., D. J. Buchanan, and D. E. T. F. Ashby, Fuel-coolant interactions in submarine volcanism, Nature, 245, 307–308, 1973.

Reineck, H.-E., and I. B. Singh, Depositional Sedimentary Environments, 2nd ed., 549 pp., Springer-Verlag, New York, 1980.

Rittman, A., Vulkane und ihre Tatigkeit, 335 pp., Enke, Stuttgart, Federal Republic of Germany, 1960.

Robinson, P. T., M. F. J. Flower, D. A. Swanson, and H. Staudigel, Lithology and eruptive stratigraphy of Cretaceous oceanic crust, western Atlantic Ocean, Initial Rep. Deep Sea Drill. Proj., 51–53, 1535–1555, 1979.

Ryan, M. P., R. Y. Koyanagi, and R. Fiske, Modeling the three-dimensional structure of macroscopic magma transport systems: Applications to Kilauea, Hawaii, J. Geophys. Res., 86, 7111–7129, 1981.

Ryan, M. P., J. Y. K. Blevins, A. T. Okamura, and R. Y. Koyanagi, Magma reservoir subsidence mechanics: Theoretical summary and application to Kilauea volcano, Hawaii, J. Geophys. Res., 88, 4147–4181, 1983.

Schmincke, H.-U., Graded lahars in the type section of the Ellensburg Formation, south central Washington, J. Sediment. Petrol., 37, 438–448, 1967.

Schmincke, H.-U., and U. von Rad, Neogene evolution of the Canary Island volcanism inferred from ash layers and volcaniclastic sandstones of DSDP site 397 (Leg 47A), Initial Rep. Deep Sea Drill. Proj., 47, 703–725, 1979.

Schmincke, H.-U., P. T. Robinson, W. Ohnmacht, and M. F. J. Flower, Basaltic hyaloclastites from holes 396B, DSDP Leg 46, Initial Rep. Deep Sea Drill. Proj., 46, 341–355, 1978.

Searle, R. C., Submarine central volcanoes on the Nazca plate—High resolution sonar observations, Mar. Geol., 53, 77–102, 1983.

Sharp, A. D. L., The seismic detection of a magma chamber beneath Mount Etna, Sicily, Geophys. Surv., 5, 229–244, 1982.

Simkin, T., Origin of some flat-topped volcanoes and guyots, Mem. Geol. Soc. Am., 132, 183–193, 1972.

Simkin, T., Geology of Galapagos, in The Galapagos, edited by R. Perry, Pergamon, New York, in press, 1984.

Smith, R. L., Ash-flow magmatism, Spec. Pap. Geol. Soc. Am., 180, 5–25, 1979.

Spera, F. J., and J. A. Crisp, Eruption volume, periodicity and caldera area: Relationships and inferences on development of compositional zonation in silicic magma chambers, J. Volcanol. Geotherm. Res., 11, 169–187, 1981.

Staudigel, H., and H.-U. Schmincke, The Pliocene seamount series of La Palma–Canary Islands, J. Geophys. Res., in press, 1984.

Thurber, C. H., Seismic detection of the summit magma complex of Kilauea Volcano, Hawaii, Science, 223, 165–167, 1984.

Williams, H., and A. R. McBirney, Volcanology, 397 pp., Freeman, Cooper and Co., San Francisco, Calif., 1979.

Wright, T. L., and R. S. Fiske, Origin of differentiated and hybrid lavas of Kilauea volcano, Hawaii, J. Petrol., 12, 1–65, 1971.

R. Batiza, Department of Earth and Planetary Sciences and McDonnell Center for the Space Sciences, Washington University, St. Louis, MO 63130.

D. J. Fornari, Lamont-Doherty Geological Observatory, Palisades, NY 10964.

P. Lonsdale, Marine Physical Laboratory, Scripps Institution of Oceanography, La Jolla, CA 92093.

D. A. Vanko, Department of Geology, Georgia State University, Atlanta, GA 30303.

Surface-generated noise under low wind speed at kilohertz frequencies

E. C. Shang and V. C. Anderson

Marine Physical Laboratory, Scripps Institution of Oceanography, University of California, San Diego, California 92152

Some experimental observations of the ocean surface under low wind speed conditions, carried out with the high gain acoustic distribution array, ADA, indicate that bubbles may play an important role in the noise generating mechanism in this wind speed regime. One of the mechanisms discussed in the theory is that of bubble collapse in the surface turbulence layer as first proposed by Furduev [Atmos. Ocean. Phys. 2, 314 (1966)]. Under typical ocean conditions, low wind speeds, and the available bubble population data, the calculated noise level agrees well with experimental results, both in magnitude and in the shape of the spectrum. The spectrum has a peak in the frequency range of 100 to 1000 Hz and an ω^{-2} behavior at high frequencies. Several geophysical parameters could influence the noise generation. Local wind speed probably controls the population of bubbles, and swell-induced static pressure variations could play an important role in the critical turbulence pressure for bubble collapse. There seems to be further evidence that additional structure within the water, perhaps bubble density associated with different water masses, generates a patch type of distribution on the sea surface in the low wind speed situation.

INTRODUCTION

For almost half a century, since the time of Knudsen's experimental measurements, it has been recognized that the surface winds play a dominant role in the generation of ambient noise in the ocean in the kilohertz frequency region. In spite of the large amount of research that has gone on in the interim, the actual mechanisms of noise generation have not been clearly identified. That is not to say that there has not been any thought given to the question. Kerman (1984) provides an excellent review of the work that has gone on in attempting to identify these mechanisms. He emphasizes particularly the kilohertz region and wind speeds above the critical speed, that speed for which the friction velocity exceeds the minimum phase velocity in the wave spectrum that lies between the capillary and gravity wave regimes. The formation of whitecaps and the associated bubble excitation or the occurrence of spray are obvious mechanisms that occur in the higher wind speed region where waves are generated with sufficient amplitude to cause rupture and breaking of the crests. However, for wind speeds below this (approximately 5.5 m/s at a standard height of 10 m) there is no obvious noise-generating mechanism, and yet, experimental measurements of ambient noise indicate that noise does exist, and is wind speed dependent at these lower wind speeds.

One of the problems in data that has been taken in the low wind speed case is that in many instances the measurements are contaminated by noise sources other than the wind generated surface noise. Consequently, the indication of the dependence of noise level on wind speed in this region is quite uncertain. For example, Kerman (1984) in his Fig. 2, which is a composite of data from several sources, shows a third power dependence for low wind speed based on Evans and Watts (1981) but an indication of a lower power dependence for the other sources. By way of contrast, shallow wa-

ter measurements reported by Wille and Geyer (1984) show essentially no dependence on wind speed for the minimum spectrum levels at kilohertz frequencies in the comparable wind speed region (wind speed below 6 kn).

The diversity of wind speed characteristics is illustrated in Fig. 1 where wind speed data from several authors have been combined. The data are normalized to a reference level
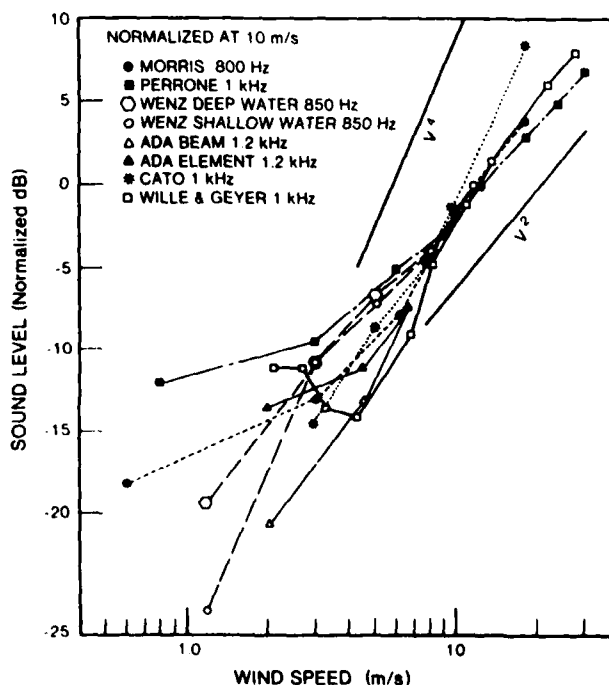

FIG. 1. Wind speed dependence of surface noise, various authors: Cato (1979), Morris (1978), Perrone (1969), Wenz (1962), Wille and Geyer (1984).

at 10 m/s. The slopes range from u^0 for Wille and Geyer to u^4 for shallow water data from Wenz (1962). The ADA data come from the same data set as that of Figs. 3 and 4. For this data set a significantly higher slope, approximately u^3, is observed for data from a beam directed toward the surface which preferentially receives the surface-generated noise, than for that from an individual element which has a broad cardioid response directed horizontally and is responsive to noise sources not located at the surface.

Without some degree of confidence in the power law dependence on wind speed or some visible manifestation of the mechanism, it is difficult to ascertain what the real sound generating process is.

In this paper we will present some of the clues of an indirect nature which relate to the low wind speed condition and also introduce conjectures as to the mechanism or mechanisms which could be generating the noise. The wind speed dependence of the noise intensity given by the theoretical analysis in the present paper is

$$I \sim u^\alpha \quad (\alpha = 3.0 \text{ to } 4.5).$$

I. EXPERIMENTAL OBSERVATIONS

The two data sets shown here were collected with the large Acoustic Distribution Array (ADA) illustrated in Fig. 2. This array is described in considerable detail in an earlier paper (Anderson, 1980). It is an array which has a planar aperture of roughly 20 by 5 m, filled with approximately 700 cardioid hydrophone units. Contained within the pressure case is a digital DIMUS beamformer which filters and hard limits the set of hydrophone signals and then transforms it into a set of directional beams. These beams cover one full hemisphere, formatted in subsets of constant elevation, with shoulder to shoulder beams in each elevation subset covering ± 90 deg in azimuth.

The first data set was taken in September 1979 at a very opportune time when the wind speed changed from an initial value of about 2 m/s in a quite linear manner up to 6.5 m/s as shown in Fig. 3. The hydrophone signals were filtered to a 200-Hz band centered at 1200 Hz. During this run the array was moored at a depth of about 300 m below the surface in 3600-m-deep water. In Fig. 4 the original beam data have been interpolated to reformat them into a display that maps uniform linear displacement on the ocean surface to a uniform linear displacement in the figure. Thus, a constant velocity track on the ocean surface will appear as a straight line with the appropriate slope. Two such tracks are identified in Fig. 4(a) with slope magnitudes of 1.0 and 4.4 m/s.

The top portion of the figure shows the start of the linear increase in wind speed. In interpreting the data, it should be
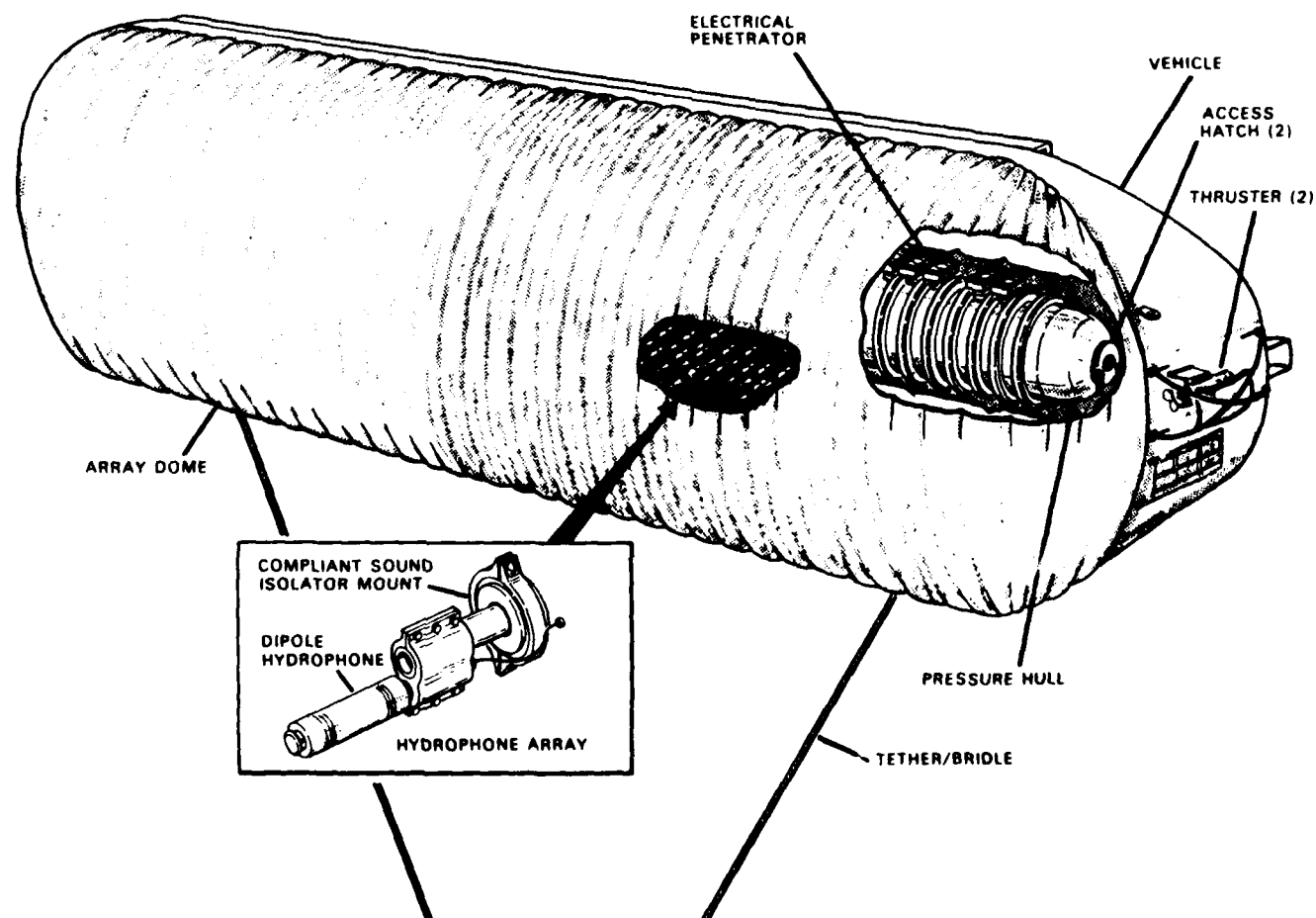

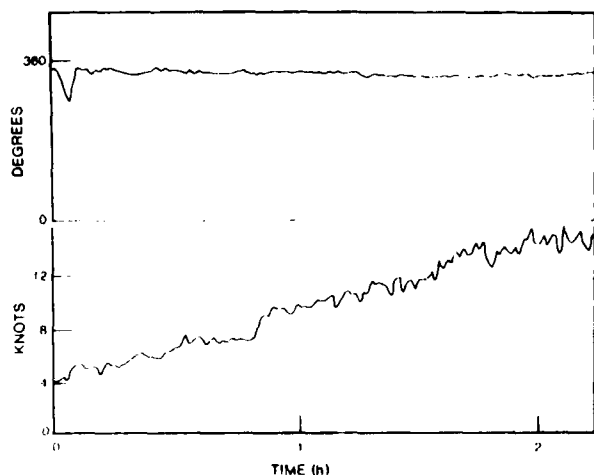FIG. 2. Artist's rendering of ADA, acoustic distribution array.

FIG. 3. Wind speed and direction versus time for data of Fig. 4.

FIG. 4. Surface noise structure as observed from ADA for wind speeds increasing from 2-6.5 m/s.

pointed out that the array itself was located almost a kilometer away from the surface platform ORB (Ocean Research Buoy) on which the wind speed sensor was mounted. Thus, there could be a significant time lag between the wind speed effect evidenced on the acoustic record and that recorded at ORB. Further, it should also be noted that the display has been normalized to constant total power by the inherent normalization of the DIMUS beamformer and by the image enhancement algorithm used in generating the display from the raw beamformer data. In the early part of the record the ambient noise level is quite low corresponding to the very low wind speed. The sea at this time was glassy smooth. Three horizontal bands can be seen at the early part of the record. These are caused by distant shipping noise (beyond our 40-mi radar range) entering through the sidelobes of the beams. As the wind speed increases with time these bands are suppressed by the rising ambient wind generated noise level.

The features of interest are the diagonal tracks having a slope comparable to the 4.4-m/s slope drawn on the figure. This velocity corresponds to the group velocity of gravity waves with a 6-s period. One thing is clear, that, whatever the physical phenomenon, the manifestation as a source of acoustic radiation undergoes a definite translation over the ocean surface. This same slope is observed for the remainder of the record, independent of wind speed, from which we infer that the 6-s waves would be associated with swell originating outside of the region of local wind activity. The effect of wind speed is to increase the occurrence of the noise tracks until, at the 6-m/s wind speed, they are barely distinguishable from a continuum of noise. Another word of explanation for the display: The lack of resolvable wave structure at the extreme ranges, top and bottom of the display, is caused by a combination of the reduced sensitivity of the directivity pattern of the individual cardioid hydrophone elements for these directions and the larger beam "footprint" on the surface associated with the shallow grazing angle at these longer ranges.

We consider this record to be direct evidence that ambient noise generation in the low wind speed region is governed by both the mag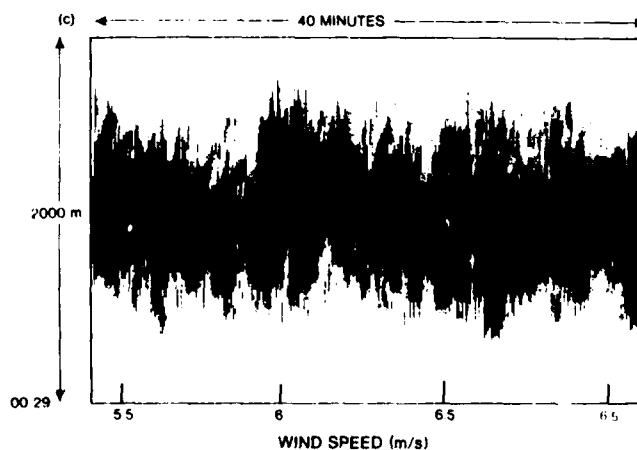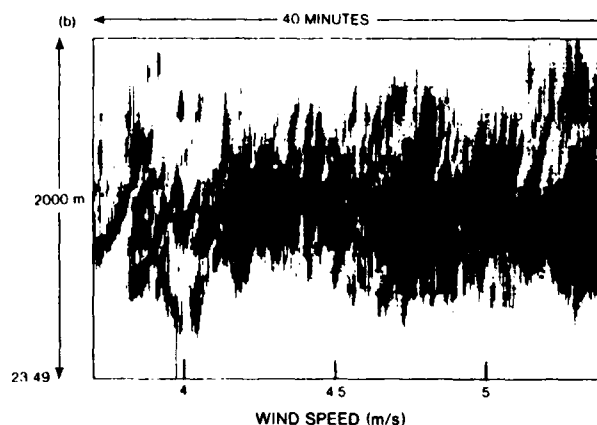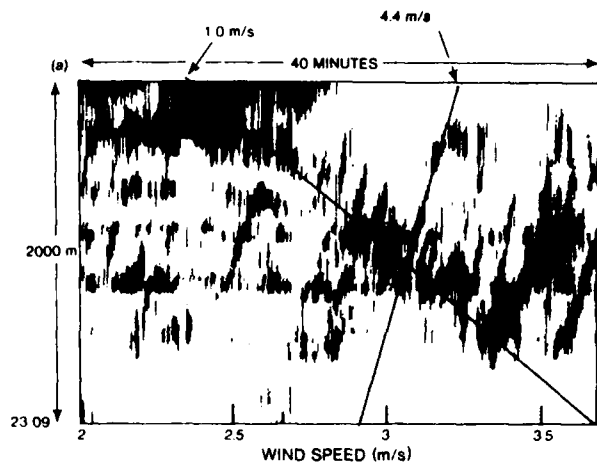nitude of the local wind speed, and the roughness of the sea surface, particularly that associated with the swell which originates outside of the influence of the local wind stress. This corroborates the findings of other authors, Wille and Geyer (1984) and Cato (1979), who concluded that both surface roughness, particularly swell, and local wind stress influence the noise level in the low wind speed region. It also shows that a mechanism, or mechanisms, governed by these factors exist for the generation of surface noise at wind speeds below that at which whitecaps are formed.

Another data set obtained in December 1980 provides further insight into the noise generating mechanisms at low wind speed. In particular, isolated noise bursts were observed indicating that the noise generation consisted of discrete events resolvable in space and time. In this experiment, acoustic radiation from patches on the sea surface was measured with ADA suspended in a deep water moor at a depth of 50–90 m below the surface. In the experiment the beamformer was configured to focus the array for surface sources lying approximately normal to the plane of the array. Figure 5 is an illustration of the fine scale acoustic radiation patterns observed in the experiment. The individual traces of the two waterfall displays represent 50-ms averages of the rectified beam outputs. The beam data have been interpolated and enhanced for the display. The fine scale structure is seen predominately in the central region of the display where the nearfield focusing of the array is at its best. For the 1.8-m/s wind speed record the individual events are quite short in duration, mainly one, or at the most two, scan times. At 3.6 m/s with a lower display gain, the events are of higher intensity and of longer duration, several hundred milliseconds.

At 1.8 m/s the wind speed is below the minimum required to excite capillary waves. Also, the events are of very short duration. Hence, the more probable candidate mechanisms at this very low wind speed would be cavitation collapse of bubbles in saturated water below the surface or bursting bubbles at the surface.

The 3.6-m/s wind speed will generate capillary waves, and, particularly in light of the extended duration of the acoustic events, unstable capillary waves or Crapper waves which entrain bubbles could play an important role here.

Although we have managed to observe these discrete acoustic events as components of the low wind speed generated surface noise, additional experiments will be required in order to obtain synoptic measurements of the physical events accompanying the acoustic emission.

II. BUBBLE CAVITATION MODEL

In this section, the mechanism of bubble cavitation under the surface is treated with a detailed theoretical analysis. Undersurface cavitation as a source of noise in the ocean was first proposed by Furduev (1966). In the intervening 18 years little note has been made of his work until recently when authors such as Kerman (1984) mention it as a possible mechanism. One reason that it may have been ignored is that there is a lack of theoretical estimation of the absolute level and its relation to the parameters of wind speed and surface roughness on the one hand, and there is a lack of observed experimental evidence on the other hand. The theoretical model which is presented here incorporates:

(1) Sound pressure radiated by the collapse of a vapor/air bubble derived by Khoroshev (1964).

(2) Bubble distributions given by Novarini and Bruno (1982).

(3) Turbulence under the surface layer from Kitaigorodskii (1961).

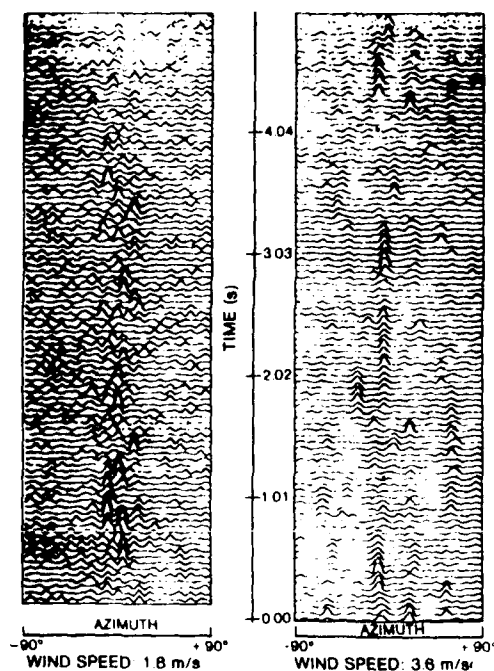(4) Surface roughness statistics given by Longuet-Higgins (1952).

FIG. 5. Short-time averaged directional structure of surface noise observed from ADA.

The presence of bubbles in the ocean is essential to this model. There are many sources in nature to supply an ample population of subsurface bubbles. Here, only surface-induced, wind-dependent bubbles are considered. Small scale capillary waves, possibly in the form of unstable Crapper waves, lead to bubble entrainment. Bubble cloud entrainment has also been observed above a threshold of about 2.5-m/s wind speed [Thorp and Humphries (1980)]. Probability distributions have been measured *in situ* by means of acoustics and optics [Medwin (1977), Glotov (1962), Johnson, Cooke (1979)], and several authors have given distribution functions recently [Crowther (1979), Novarini and Bruno (1982), Kerman (1982)].

Briefly, the process of bubble cavitation in the surface turbulent layer is initiated when the turbulent pressure surrounding a vapor–air cavity of sufficient radius (greater than 10^{-4} cm) is reduced to the Hsieh–Plesset (1961) threshold whereupon the bubble would grow to larger radius by rectified diffusion. Some of the larger bubbles will be transformed into a transient cavity determined by the dynamic equation. According to Flynn (1964), whether or not a cavity becomes a transient cavity, i.e., one which undergoes a rapid collapse, depends on the competition in the dynamic equation between the inertial function F_1, which represents the portion of acceleration due to the spherical contraction of the liquid, and the quasistatic function F_2, which is the net pressure divided by the radius. The condition for this transformation is that the relative maximum radius on expansion be greater than a critical value during the pressure fluctuation period. A shock wave will be radiated as a result of collapse of the transient cavity. The absolute noise level corresponding to this phenomenon will be estimated later in the paper.

There are two geophysical parameters playing different roles in the model of surface noise generation. First, local wind speed mainly controls the bubble entrainment or equivalently the distribution function of the bubbles, and second, the swell-induced static pressure variations will mainly control the turbulent features in the surface layer, so these turbulent features will be most strongly influenced by the distance fetch, wind history and travel time, but not by the local wind speed.

A. Critical radius of the expanding bubble under rectified diffusion

The relation between the critical radius of the expanding bubble and the fluctuating pressure p' was given by Hsieh and Plesset (1961):

$$p' = \sqrt{3} P_0 (1 + 2\alpha / R_c P_0 - \gamma)^{1/2}, \tag{1}$$

where P_0 is the static pressure, γ is the coefficient of saturation by dissolved air of the water surrounding the cavity, α is the coefficient of surface tension of the water ≈ 72 dyn/cm, and R_c is the critical radius for a bubble expanding by rectified diffusion.

Considering the saturation case for which $\gamma = 1$, one gets

$$R_c = \tfrac{4}{3} P_0 [\alpha / (p')^2] \tag{2}$$

or, from Bernoulli's law,

$$R_c = \tfrac{4}{3} P_0 [\alpha / (\rho V'^2)^2], \tag{3}$$

where V' is the particle motion velocity of the turbulence layer.

B. Sound pressure and spectrum from a single collapsing bubble

The sound pulse radiated by a collapsing bubble is a function of its radius R and air content of the bubble δ:

$$P(R,t) = P_A(R,\delta) S(t), \tag{4}$$

where the peak pressure P_A was given by Khoroshev (1964) for a vapor–air bubble collapsing:

$$P_A(R,\delta) = P_0(R_m/r) F(\delta) \times 10^{-6}$$
$$= P_0(K_E R /r) F(\delta) \times 10^{-6}, \tag{5}$$

where P_0 is the hydrostatic pressure, R_m is the maximum bubble radius (μm) at the moment collapse begins, K_E as defined here is the coefficient of expansion ($K_E \doteq 3-5$, Furduev; $K_E \doteq 2$, Flynn); r is the measurement distance (m) from the bubble, and the function $F(\delta)$ is

$$F(\delta) = [(1 + 3\delta)(1 + 3\delta - \delta^{1.6})]^2 / 27\delta^2, \tag{6}$$

where δ is the parameter of the air content. In general it ranges from 0.002 to 0.1 under typical conditions.

The pulse form $S(t)$ is an exponential pulse for a vaporous bubble observed by Harrison (1952) experimentally. Owing to the fact that the bubble is beneath a free surface, and taking into account the reflection effect, $S(t)$ can be modeled by an approximate pulse shape (Furduev, 1966)

$$S(t) = A e^{-t/\tau_0} \sinh(mt - \beta), \tag{7}$$

where the three parameters A, β, m are determined by the physical restriction

$$A = 1/\sinh(-m\tau_1), \quad \text{for } S(0) = 1, \tag{8}$$

$$\beta = m\tau_1, \quad \text{for } S(\tau_1) = 0, \tag{9}$$

$$m = \frac{1}{\tau_0} \tanh(\beta), \quad \text{for } \int_0^\infty S(t)dt = 0, \tag{10}$$

$$m \leqslant 1/\tau_0, \quad \text{for convergence.} \tag{11}$$

From Eq. (10) we get

$$\tau_0 = \tau_1 [\tanh(m\tau_1)/m\tau_1] \leqslant \tau_1. \tag{12}$$

Thus, we must have $\tau_0 \leqslant \tau_1$; and if the parameter m in the model is chosen to keep the convergence rate not too much slower than $1/\tau_0$, we have $m\tau_0 \ll 1$; then from Eq. (10) and Eq. (12) we get

$$\tau_0 \approx \tau_1 \tag{13}$$

and τ_1 is given by

$$\tau_1 = 2D/c_0, \tag{14}$$

where D is the effective depth of the bubble population and c_0 is the sound speed in water.

Although τ_0 and τ_1 represent two physically different parameters—one being the decay rate of the cavitation impulse and the other representing the travel time delay between the direct and image paths, the times are comparable as pointed out by Furduev and they have been set equal for convenience here.

From Eq. (7), the frequency spectrum of the radiating pulse is

$$S(\omega) = \frac{\omega}{[(2\omega/\tau_0)^2 + (1/\tau_0^2 - m^2 - \omega^2)^2]^{1/2}}. \tag{15}$$

There is a peak at ω_{max}:

$$\omega_{max} = 1/\tau_0 \cosh(m\tau_1) \approx 1/\tau_1. \tag{16}$$

The spectrum peak value is given by

$$\hat{S}(\omega_{max}) = \omega_{max}/(2\omega_{max}/\tau_0) = \tfrac{1}{2}\tau_0 \approx \tfrac{1}{2}\tau_1. \tag{17}$$

C. Pressure pulsation, surface layer turbulence, and surface roughness

In spite of the large body of knowledge about turbulence in pipes, in boundary layers near solid walls, in jets, and in the atmosphere, unfortunately little is known about turbulence in the ocean (Monin, 1977). Apparently surface waves play a particularly important role for the upper ocean layer turbulence. The disturbed sea surface can be regarded as a moving random surface. The random surface waves induce in the upper ocean layer a random field of wave motions, which can be described by a model called "turbulence waves of large amplitude" by Kitaigordskii (1961). Such a "turbulence wave" motion was characterized by an average orbital velocity $\bar{u}_{orb}$ superimposed by random turbulent pulsation of different scales:

$$v' = \bar{u}_{orb} + v'' \tag{18}$$

and the average orbital velocity $\bar{u}_{orb}$ was given by Kitaigordskii (1961):

$$\bar{u}_{orb} \approx \bar{H} \bar{\omega} e^{-\bar{K}z}, \tag{19}$$

where $\bar{H}$ is the average wave height of the large amplitude surface waves, $\bar{\omega}$ is the average angular frequency, and $\bar{K}$ is

the average wavenumber. The Reynolds number of the average motion is

$$R_{e\,wave} \approx \bar{u}_{orb}\bar{\lambda}/\nu, \qquad (20)$$

where ν is the molecular viscosity coefficient of water $[\nu = 10^{-2}(cm)^2/s]$. For a typical real condition the magnitude of $R_{e\,wave}$ is

$$R_{e\,wave} \approx 10^6\text{--}10^7. \qquad (21)$$

So, the criterion for turbulence generation

$$R_{e\,wave} > R_{e\,cr} \sim 3000 \qquad (22)$$

is satisfied by a large margin.

Measurements in shallow water (Bowden and White, 1966) indicated that the random component which is superimposed on the orbital component is approximately 20%. Thus, the pressure pulsation is mainly contributed by the periodic orbital motion, specified by the average wave height $\bar{H}$. Here, $\bar{H}$ can be regarded as one of the parameters of the surface roughness.

For a random sea surface, the statistical description was given by Longuet-Higgins (1980). If the sea surface is assumed to be the sum of many sine waves in random phase, and if the frequency spectrum is sufficiently narrow, then the wave amplitudes (a wave amplitude is here defined as one half of the height of a wave crest above the preceding trough) are distributed according to a Rayleigh distribution. That is, the probability P that the amplitude H of any given wave exceeds the value H_1 is given by

$$P(H_1) = \exp[-2(H_1/H_{1/3})^2] \qquad (23)$$

or

$$P(H_1) = \exp(-H_1^2/\sigma^2), \qquad (24)$$

where $H_{1/3}$ is the significant wave height, and σ is the rms wave height. In the derivation of this law it was implied that the sea surface slopes were sufficiently small that the component waves could be linearly superposed and hence that there was no correlation between the phases of the different Fourier components.

Obviously, under the low wind speed condition, the surface roughness influencing the orbital movement is mainly due to swell, not the wave height of "sea" induced by the local wind (because $H_{swell}^2 > H_{sea}^2$). So, for the model of surface noise generation, under low wind speed, the parameter $\bar{H}$ will be considered approximately as

$$\bar{H} \approx \bar{H}_{swell} \qquad (25)$$

and the orbital velocity at the upper layer in Eq. (19) is

$$\bar{u}_{orb} \approx \bar{H}_{swell} \cdot \bar{\omega}_{swell}. \qquad (26)$$

In addition to this orbital velocity it should be noted that there will also be a drift flow at the surface produced by a direct action of the wind.

D. Estimation of noise level

For the estimation of the noise field produced by the bubbles distributed under the surface, the interaction between bubbles is neglected and energy summation is assumed. The resulting noise level spectrum can be written as

$$I(\omega,R_c) = \Omega(R_c)\int_0^{ }\int_{R_c}^{\infty} K_T \eta(R,z)$$

$$\times [P_A S(\omega)]^2 D(\theta)dr\,dv, \qquad (27)$$

where $\Omega(R_c)$ is the collapse formation frequency for bubbles having a radius greater than R_c, K_T is the percentage of the bubbles that can be transformed into a transient cavity, $\eta(R,z)$ is the bubble distribution function, P_A is the peak pressure radiated by a transient cavity, given by Eq. (5), $S(\omega)$ is the spectrum of the radiated pulse, given by Eq. (15), and $D(\theta)$ is the directivity function of the bubble radiation. Because of the proximity of the free surface, $D(\theta)$ is a dipole,

$$D(\theta) = \cos^2(\theta), \qquad (28)$$

where θ and the element volume of integration dv are shown in Fig. 6, and dv is given by

$$dv = 2\pi l\,dl\,dz = 2\pi h^2\sec^2(\theta)\tan(\theta)d\theta\,dz. \qquad (29)$$

Substituting Eq. (29), Eq. (28), and Eq. (5) into Eq. (27), and completing the integral with respect to θ, we get

$$I(\omega,R_c)$$

$$= \Omega(R_c)\pi\int_{R_c}^{ }\int_0^{ }(K_T K_E)\eta(R,z)[P_0F(\delta)]^2$$

$$\times S^2(\omega)R^3\times 10^{-12}\,dR\,dz, \qquad (30)$$

where R is in μm. For simplicity, and because we have no knowledge of the dependence of K_T and K_E on r and u, $(K_T K_E)$ is considered as constant. Then we get the peak of the spectrum,

$$\hat{I}(\omega,R_c) = \Omega(R_c)\pi(K_T K_E)[P_0F(\delta)]^2S^2(\omega)$$

$$\times 10^{-12}\int_{R_c}^{\infty}\int_0^{\infty}\eta(R,z)R^2\,dR\,dz. \qquad (31)$$

A bubble distribution function given by Novarini and Bruno (1982) will be used:

$$\eta(R,u,z) = 8.6\times 10^9 R^{-4.3}(u/6)^2\exp(-z/D), \qquad (32)$$

where u is the wind speed in knots and D is the bubble-layer thickness in m that is wind speed dependent.

Since we are interested in larger bubbles and lower wind speeds, in view of reduced turbulent entrainment forces and larger bouyancy forces, the decay with bubble size may be more rapid. For simplicity, we take

$$\eta(R,u,z) = 8.6\times 10^9 R^{-5}(u/6)^2\exp(-z/D). \qquad (33)$$
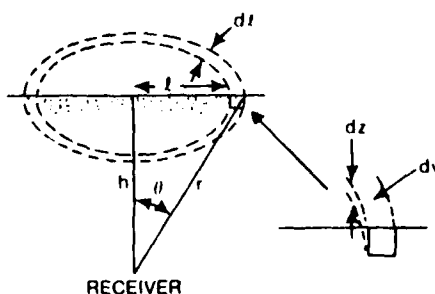

FIG. 6. Geometry for integration of surface noise.

Substituting Eq. (17) and Eq. (33) into Eq. (31), and completing the integral with respect to R, and z, we get

$$I(\hat{\omega},R) = 3.3 \times 10^{-1}(K_T K_E^2)\Omega(R_c)[P_0 F(\delta)]^2$$

$$\times \tau_0^2 (u/6)^2 D R_c^{-2}. \tag{34}$$

As analyzed above, the critical radius R_c of the cavitating bubble is dependent on the geophysical condition of the turbulence in the upper surface layer due to swell. From Eqs. (3), (18), and (19), if the given swell is specified by wave height H and circular frequency ω_c, we get

$$R_c = \tfrac{4}{3}[P_0\alpha/\rho^2(H\omega_c)^4]. \tag{35}$$

Taking account of Eq. (23), and the theory given by Rice (1945), the formation frequency Ω is given by

$$\Omega(H) = \exp\left[-2\left(\frac{H}{H_{1/3}}\right)^2\right]\left(\frac{\int_0^c f^2 E(f)df}{\int_0^c E(f)df}\right)^{1/2}, \tag{36}$$

where $E(f)$ is the power spectral density function of the surface wave process.

If H is considered as the average wave height $\bar{H}$, then

$$\Omega(\bar{H}) = \exp[-2(\bar{H}/H_{1/3})^2](\bar{\omega}/2\pi) = 0.46/T. \tag{37}$$

Substituting Eq. (37) into Eq. (34):

$$\hat{I}(\hat{\omega},u,\bar{H}) = (1.52 \times 10^{-3}/T)(K_T K_E^2)[P_0 F(\delta)]^2$$

$$\times \tau_0^2 (u/6)^2 D [R_c(\bar{H},\bar{\omega})]^{-2}. \tag{38}$$

Now, we may make a quantitative estimation for the absolute level under typical oceanic conditions:

wind speed: $u = 6$ kn,
typical swell parameters:
$\bar{H} = 2.3$ m,
$T = 9.4$ s,
effective bubble layer: $D = 0.2$ m,
coefficient of expansion: $K_E = 2$,
coefficient of transient transformation $K_T = 0.2$,
parameter of air content: $\delta = 0.1$.

From Eqs. (14) and (13):

$$\tau_1 \approx \tau_0 = 2D/C_0 = 0.26 \times 10^{-3} \text{ s.} \tag{39}$$
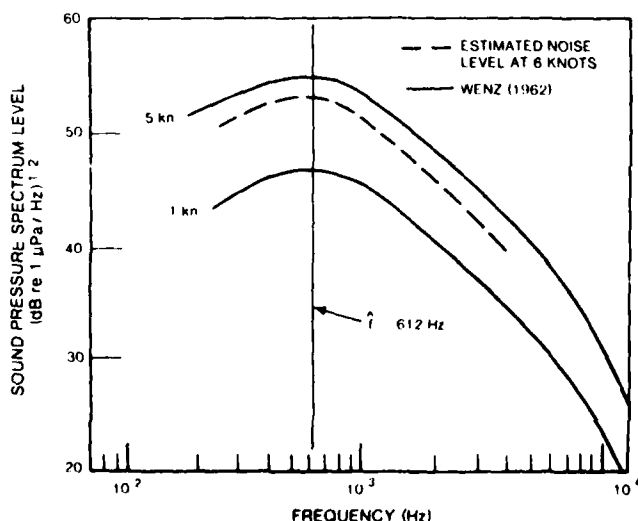
From Eq. (16):

$$\hat{\omega} \approx 1/\tau_1 = 3.8 \times 10^3 \text{rad/s},$$

$$f \approx 612 \text{ Hz.} \tag{40}$$

From Eq. (6):

$$F(\delta) = 6.3,$$

$$[P_0 F(\delta)]^2 = 3.9 \times 10^{13}. \tag{41}$$

From Eq. (37):

$$R_c(\bar{H},\bar{\omega}) = 1700 \,\mu\text{m.} \tag{42}$$

Substituting all the above quantities into Eq. (38), we get

$$I(\hat{\omega},u,H) = [(1.52 \times 10^{-3})/T](K_T K_E^2)$$

$$\times [P_0 F(\delta)]^2 \tau_0^2 (u/6)^2 DR_c^{-2}$$

$$= (0.16 \times 10^{-3})[0.8][3.9 \times 10^{13}]$$

$$\times [0.26 \times 10^{-3}][0.2](1700)^{-2}$$

$$\approx 0.07 \text{ W/m}^2/\text{Hz}$$

$$\approx -47 \text{ dB } re: 1 \text{ dyne/cm}^2/\sqrt{\text{Hz}}. \tag{43}$$

The result is demonstrated in Fig. 7. The absolute values computed above are near the 5-kn wind speed curve of Wenz and both the shape of the spectrum and the location of the maximum are in good agreement with his data.

The wind speed dependence of $\hat{I}$ given by Eq. (38) is up to $\sim (u)^2 D(u)$. Unfortunately, it seems that there is not a very clear expression of the wind speed dependence available. Novarini and Bruno (1982) suggested

$$D(u) \sim U^{2.5}$$

and Crowther (1979) suggested

$$D(u) \sim U^{1.0}.$$

So, in the present paper, the power law of the wind speed dependence of $\hat{I}$ will be described as:

$$\hat{I} \sim U^n \quad (\alpha = 3.0\text{--}4.5).$$

III. BURSTING BUBBLES AS SOUND SOURCES

Another possible mechanism for sound generation by bubbles is the rupture or bursting of bubbles on the ocean surface. The nature of the radiation from a bursting bubble is readily computed. We begin with the internal overpressure for a bubble on the surface which is given by

$$\Delta p = 2T\pi D/(\pi D^2/4) = 4T/R, \tag{44}$$

where R is the radius of curvature of the double-surfaced upper bubble wall. This pressure is balanced by a combination of the differential hydrostatic head associated with the lower surface of the bubble and the upward force created by the surface tension T of the water at the lower boundary. When the upper wall ruptures, the dimple left at the water surface provides a decaying step function restoring force over the depressed area.

The basic sound source of the breaking bubble then is modeled as an initial pressure step function of magnitude Δp acting over a circular area approximately equal to πR^2 at the pressure release boundary of an infinite half-space. The boundary conditions match closely the solution of a vibrat-

FIG. 7. Comparison of estimated noise spectrum with Wenz's data.

ing sphere in free field. The free field model is appropriate because the plane of the surface, normal to the motion of the sphere, is a plane of zero acoustic pressure corresponding to the pressure release of the air/water interface.

From Morse (1948), the radiated intensity from a dipole sound source or vibrating sphere, assuming that the source is very small compared to a wavelength, is given by

$$\Upsilon \simeq \frac{1}{8} \frac{\omega^4 \rho a^6 U_0^2 \cos^2(\theta)}{c^3 r^2}. \qquad (45)$$

In order to determine a value for u_0, from the driving pressure p, we use the expression for one-half of the impedance of the sphere, also given by Morse for $ka < 1$:

$$Z_r = F/u_0 \simeq -i(u/2)(\tfrac{4}{3}\pi \rho_0 a^3). \qquad (46)$$

The force F is equal to $\Delta p \pi a^2$, thus

$$U_0 = -3\Delta p/i\omega \rho_0 a = i(3\Delta p/\rho_0 cka). \qquad (47)$$

Combining Eqs. (45) and (47), the radiated intensity is then

$$\Upsilon = \tfrac{9}{8}[(ka)^2 a^2 \Delta p^2 \cos^2(\theta)/\gamma^2 \rho_0 c]. \qquad (48)$$

Now, assuming the pressure impulse to be approximated by an exponential step function, $\Delta p(t) = \Delta\ _{0} e^{-t/\tau}$, Δp^2 would have a pressure spectrum proportional to $1/\omega^2$. Then the spectral shape of the radiated intensity will be

$$\Upsilon(\omega) \propto (1/\rho)[a^4 \cos^2(\theta)/c^3 r^2], \qquad (49)$$

which represents a flat spectrum with no frequency dependence.

It is apparent that this bursting bubble model does not match the conventional Knudsen spectrum shape for wind noise in the kilohertz region, but it is still a viable candidate for the extremely low wind speeds under 2.5 m/s where no capillary wave action is produced, and when swell conditions are low. Because of the scarcity of uncontaminated measurements of wind generated noise in this extremely low wind speed regime, there is a question as to whether or not the conventional ω^{-2} spectrum is valid for this regime. For example, the limited data from Wenz (1962) in his Figs. 2 and 3 for 2-kn wind speeds do not support an ω^{-2} slope in the 10^3- to 10^4-Hz region.

The analysis shows that the signatures of collapsing subsurface bubbles and surface bursting bubbles are distinctively different. If close range wideband acoustic measurements can be carried out it should be possible to identify the events from the distinctive character of their respective acoustic signatures.

ACKNOWLEDGMENT

Anderson, V. C. (1980). "Nonstationary and Nonuniform Oceanic Background in a High-gain Acoustic Array," J. Acoust. Soc. Am. 67, 1170–1179.

Bowden, K. F., and White, R. A. (1966). "Measurements of the Orbital Velocity of Sea Waves and Use in Determining the Directional Spectrum," Geophys. J. R. Astron. Soc. 12, 33–54.

Cato, D. H. (1979). "Wind Dependent Sea Noise," Ocean Sciences Review, RAN Research Lab., NSW 2010, Australia.

Crowther, P. A. (1979). "Acoustical Scattering from Near-Surface Bubble Layers," in Cavitation and Inhomogeneities in Underwater Acoustics, edited by W. Lauterborn (Springer, New York).

Evans, D. L., and Watts, D. R. (1981). "Wind Speed and Stress at the Sea Surface from Ambient Noise Measurements," in Proceedings of International Symposium on Acoustic Remote Sensing of the Atmosphere and Oceans, Univ. Calgary, Calgary, Canada (21–25 June 1981)

Flynn, H. G. (1964). "Physics of Acoustic Cavitation in Liquids," in Physical Acoustics (Academic, New York), Vol. 1B.

Furduev, A. V. (1966). "Undersurface Cavitation As a Source of Noise in the Ocean," Atmos. Oceanic Phys. 2, 314.

Glotov, J. P. (1962). "Investigation of the Scattering of Sound by Bubbles Generated by an Artificial Wind in Seawater and the Statistical Distribution of Bubble Sizes," Sov. Phys. Acoust. 7, 341–345.

Harrison, M. (1952). "An Experimental Study of Single Bubble Cavitation Noise," J. Acoust. Soc. Am. 24, 776.

Hsieh, D. Y., and Plesset, M. S. (1961). "Theory of Rectified Diffusion of Mass into Gas Bubbles," J. Acoust. Soc. Am. 33, 206.

Johnson, B. D., and Cooke, R. C. (1979). "Bubble Population and Spectra in Coastal Waters: A Photographic Approach," J. Geophys. Res. 84, 3761–3766.

Kerman, B. R. (1982). "Underwater Sound Generation at Low Wind Speeds" (unpublished).

Kerman, B. R. (1984). "Sound Generation by Breaking Wind Waves," J. Acoust. Soc. Am. 75, 149–165.

Kitaigorodskii, G. A. (1961). "On Small Scale Turbulence in the Surface Layer of the Sea with Wind Swell," Trans. Inst. Ocean, Moscow 52, 87–96 (in Russian).

Khoroshev, G. A. (1964). "Collapse of Vapor–Air Cavitation Bubble," Sov. Phys. Acoust. 9(3), 275–279.

Longuet-Higgins, M. S. (1952). "On the Statistical Distribution of Heights of Sea Waves," J. Marine Res. 11, 245–266.

Longuet-Higgins, M. S. (1980). "On the Distribution of the Height of Seawaves: Some Effects of Nonlinearity and Finite Bandwidth," J. Geophys. Res. 85, 1519–1523.

Medwin, H. (1977). "In Situ Acoustic Measurements of Microbubbles at Sea," J. Geophys. Res. 82, 971–975.

Monin, A. S. (1977). "On the Generation of Oceanic Turbulence," Atmos. Ocean Phys. 1, 789–803.

Morris, G. B. (1978). "Depth Dependence of Ambient Noise in the North Eastern Pacific Ocean," J. Acoust. Soc. Am. 64, 581–590.

Morse, P. M. (1948). Vibration and Sound (McGraw-Hill, New York), p. 248.

Novarini, J. C., and Bruno, D. R. (1982). "Effects of the Sub-Surface Bubble Layer on Sound Propagation," J. Acoust. Soc. Am. 72, 510–514.

Perrone, A. J. (1969). "Deep Ocean Ambient Noise Spectra in the North West Atlantic," J. Acoust. Soc. Am. 46, 762–770.

Rice, S. O. (1945). Bell Syst. Tech. J. 23, 282.

Thorp, S. A., and Humphries, P. N. (1980). "Bubbles and Breaking Waves," Nature 283, 463–465.

Wenz, G. M. (1962). "Acoustic Ambient Noise in the Ocean: Spectra and Sources," J. Acoust. Soc. Am. 34, 1936–1956.

Wille, P. C., and Geyer, D. (1984). "Measurements on the Origin of the Wind-Dependent Ambient Noise Variability in Shallow Water," J. Acoust. Soc. Am. 75, 173–185.

Effect of pressure on sound absorption in synthetic seawater and in aqueous solutions of MgSO₄[a)]

C. C. Hsu[b)] and F. H. Fisher

University of California—San Diego, Marine Physical Laboratory, Scripps Institution of Oceanography, San Diego, California 92152

Measurements have been made, at 25 °C, of the effect of pressure on sound absorption in Lyman and Fleming (LF) synthetic seawater from 30–300 kHz up to 307 atm. Similar measurements were made in 0.02M MgSO₄ solution in a 0.02M MgSO₄–0.6M NaCl solution. The decrease with pressure of absorption per wavelength $(\alpha\lambda)$ in LF seawater differs substantially from those reported by other investigators. The relaxation frequency, within experimental error, was found to be independent of pressure. For LF seawater, increasing pressure to 307 atm reduced absorption by 26.3%, very nearly the same as was observed previously (28.2%) for 0.5M MgSO₄ solutions. The addition of 0.6M NaCl to the 0.02M MgSO₄ solution decreased the absorption by a factor of 4 and the effect of pressure was found to be independent of the NaCl concentration. The Eigen and Tamm multistate dissociation parameters which best describe the pressure dependence of sound absorption and electrical conductance in a 0.02M MgSO₄ solution predict a 21.4% decrease in absorption at 307 atm compared with the observed 19.6% decrease. However, these parameters yield an equilibrium constant which differs from the conductance derived value by a factor of 3.

PACS numbers: 43.30.Bp, 43.35.Bf, 43.35.Fj, 43.35.Ty

INTRODUCTION

Sound absorption in seawater above 10 kHz is essentially due to a relaxational process involving MgSO₄ as seen in Fig. 1.[1] Shortly after the discovery[2] of MgSO₄ as the cause of sound absorption in seawater, Liebermann[3] showed how a pressure-dependent chemical reaction could cause the absorption. Since both the magnesium and sulfate ions were required for the absorption to occur, the principal focus for various researchers[4–17] was that absorption was proportional to the concentration of MgSO₄ and more specifically, to the concentration of MgSO₄ ion pairs.[5,6,8,9,11–14] However a serious difficulty arose in explaining experimental data as seen in Fig. 2.[17]

For example, conductance data[9] in pure MgSO₄ solutions revealed only a 10% decrease in ion-pair concentration for an increase in pressure of 1000 atm [curve (c) in Fig. 2] compared to a decrease of 67% in sound absorption [curve (e) in Fig. 2]. This paradox was resolved by the Eigen and Tamm[8] multistate dissociation model which was developed to explain the extensive ultrasonic relaxation spectrometry data of Kurtze and Tamm[5] at 1 atm. Their results revealed a cation specific relaxation at ~100 kHz (for the magnesium ion) and another one at ~200 MHz which was common to all the divalent sulfates. By postulating pressure-dependent chemical equilibria governing the concentration of three species of neutral ion pairs, differing only in amount of solvation, Eigen and Tamm[8] not only explained the 1-atm data over a wide frequency range but also predicted the pressure dependence of absorption very well [curve (d) in Fig. 2] and conductance nearly exactly.[17]

In seawater, Bezdek's measurements in the ocean[15] [curve (f) in Fig. 2] disagreed substantially with the prediction by Schulkin and Marsh[10] which was based on a linear interpolation of laboratory data in 0.5M MgSO₄ solutions.[17] However, Bezdek's results disproved the contention by Kes-
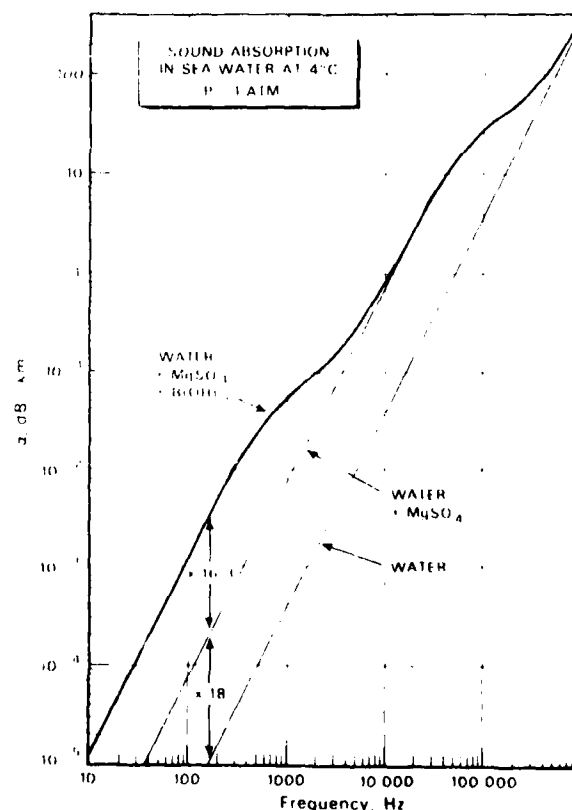

FIG. 1. Illustration of sound absorption in the ocean at 4 °C, $pH = 8$ taken from Simmons and Fisher.
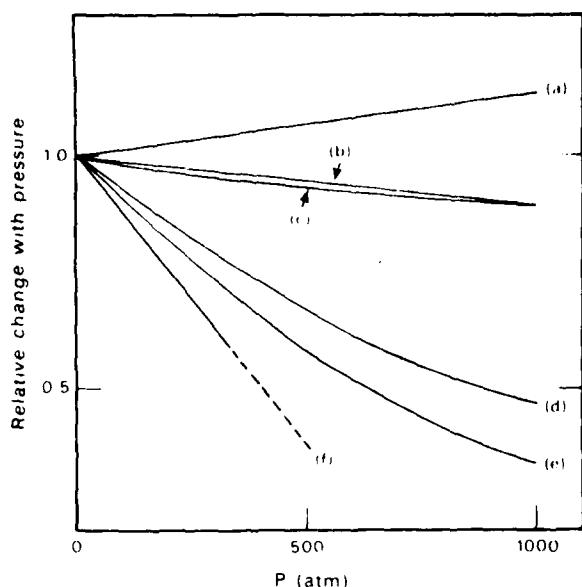
FIG. 2. Relative change with pressure of (a) MgSO$_4$ ion-pair concentration according to Kester and Pytkowicz, (b) MgSO$_4$ ion-pair concentration according to Millero, (c) MgSO$_4$ ion-pair concentration according to Fisher, (d) sound absorption according to one Eigen–Tamm multistate model for MgSO$_4$, (e) sound absorption in a 0.5M MgSO$_4$ solution measured by Fisher, (f) sound absorption in the ocean measured by Bezdek.

P (atm)	$(\alpha\lambda)_m \times 10^6$	f_r (kHz)	Solution
1	61.3 ± 0.5	140 ± 11	Lyman and Fleming seawater
71	57.8 ± 0.5	140 ± 11	
188	52.9 ± 0.3	133 ± 8	
307	45.2 ± 0.3	142 ± 7	
1	80.8 ± 0.6	149 ± 10	0.02M MgSO$_4$
307	65.0 ± 0.4	145 ± 8	
1	20.2 ± 0.3	162 ± 20	0.02M MgSO$_4$ + 0.6M NaCl
307	16.2 ± 0.2	150 ± 14	

ter and Pytkowicz[18] that sound absorption in the ocean should increase as a result of an increase in the concentration of MgSO$_4$ ion-pairs (according to their calculations). Millero[19] disagreed with Kester and Pytkowicz[18] and argued that the ion-pair concentration of MgSO$_4$ in the ocean decreased with pressure [curve (b) in Fig. 2]. Fisher[14] showed that even if there was a slight increase in ion-pair concentration with pressure, the multistate model of Eigen and Tamm[8] would still predict a decrease in absorption.

The object of this work is to make a definitive laboratory study of the pressure dependence of sound absorption in seawater and in pure MgSO$_4$ solutions at 25 °C in order to clear up the discrepancies between the ocean data and the laboratory data in 0.5M MgSO$_4$ solutions [curves (e) and (f) in Fig. 2]. For these measurements we have used seawater synthesized according to the Lyman and Fleming[20] formula. The use of a large titanium spherical resonator (105 l) on loan from Woods Hole Oceanographic Institution has made it possible to make such absorption measurements. Since sound absorption in seawater is equivalent to about a 0.014 molar solution of MgSO$_4$ we have made absorption measurements in an aqueous solution of 0.02M MgSO$_4$ to compare both with the seawater absorption results and with electrical conductance data. For dilute ($c < 0.02$M) aqueous MgSO$_4$ solutions conductance data[17] have been used to test predictions of multistate models for MgSO$_4$. The addition of 0.6M NaCl to the 0.02M MgSO$_4$ solution was made so that the effect of the principle ingredient in seawater on the pressure dependence of sound absorption may be studied.

I. MEASUREMENTS AND RESULTS

The absorption measurements were made using the acoustic resonator technique[4–6] in which measurements are

made of the decay rate of resonance modes of liquid in the 105 l titanium sphere which is supported by piano wires inside a vacuum chamber. Pressure inside the sphere was regulated to ± 0.000021 atm at elevated pressures by a Ruska automatic dead-weight gauge controller. Temperature probes at the two polar caps on the sphere indicated temperature variations inside the sphere were less than ± 0.5 °C at 25 °C. Details of the experimental technique apparatus have been discussed by Hsu[21] elsewhere. A digital frequency synthesizer was particularly useful inasmuch as resonance modes had high Q's; at 25 kHz, for example, a mode with a Q of 1.2×10^6 was found in measurements[22] with water as the calibration liquid.

The theoretical curve for the frequency dependence of absorption per wavelength for a relaxational process is

$$\alpha\lambda = 2(\alpha\lambda)_m f f_r / (f^2 + f_r^2), \qquad (1)$$

where $(\alpha\lambda)_m$ is the value of absorption per wavelength when $f = f_r$, the relaxation frequency. The maximum absorption, per wavelength $(\alpha\lambda)_m$, and the relaxation frequency f_r, are obtained by fitting Eq. (1) to the data. The results for the values of $(\alpha\lambda)_m$ and f_r are summarized in Table I. The data along with the best fit curves are shown in Figs. 3–5. The maximum absorption per wavelength and the relaxation frequency are those for which the standard deviation σ was minimized as f_r was varied. In Fig. 6(a) we see that $(\alpha\lambda)_m$ shifts only slightly as f_r changes. The value $\sigma/\sigma_0 = 1.21$ was found empirically from our data to correspond to the maximum possible error in the relaxation frequency from our measurements, when residuals are all positive on one side of f_r and all negative on the other. For the data in this paper the error in $(\alpha\lambda)_m$ is ± 1.1% on the average and the maximum error of the relaxation frequency is estimated to be 7.6% on the average. While this analysis may overestimate the error on relaxation frequency, further efforts to refine the results would require weighting of the data to reflect the increasing difficulty in making measurements as frequency increases. This would be a subjective process at this point. Duplicate runs with newly prepared solutions would probably be the best method to evaluate the accuracy of the work.

II. DISCUSSION OF RESULTS

The value of $(\alpha\lambda)_m$ for seawater was found to be linearly dependent on the pressure in the range of 1–307 atm. Second-order fits were not significantly better. We used the following equation to calculate our data
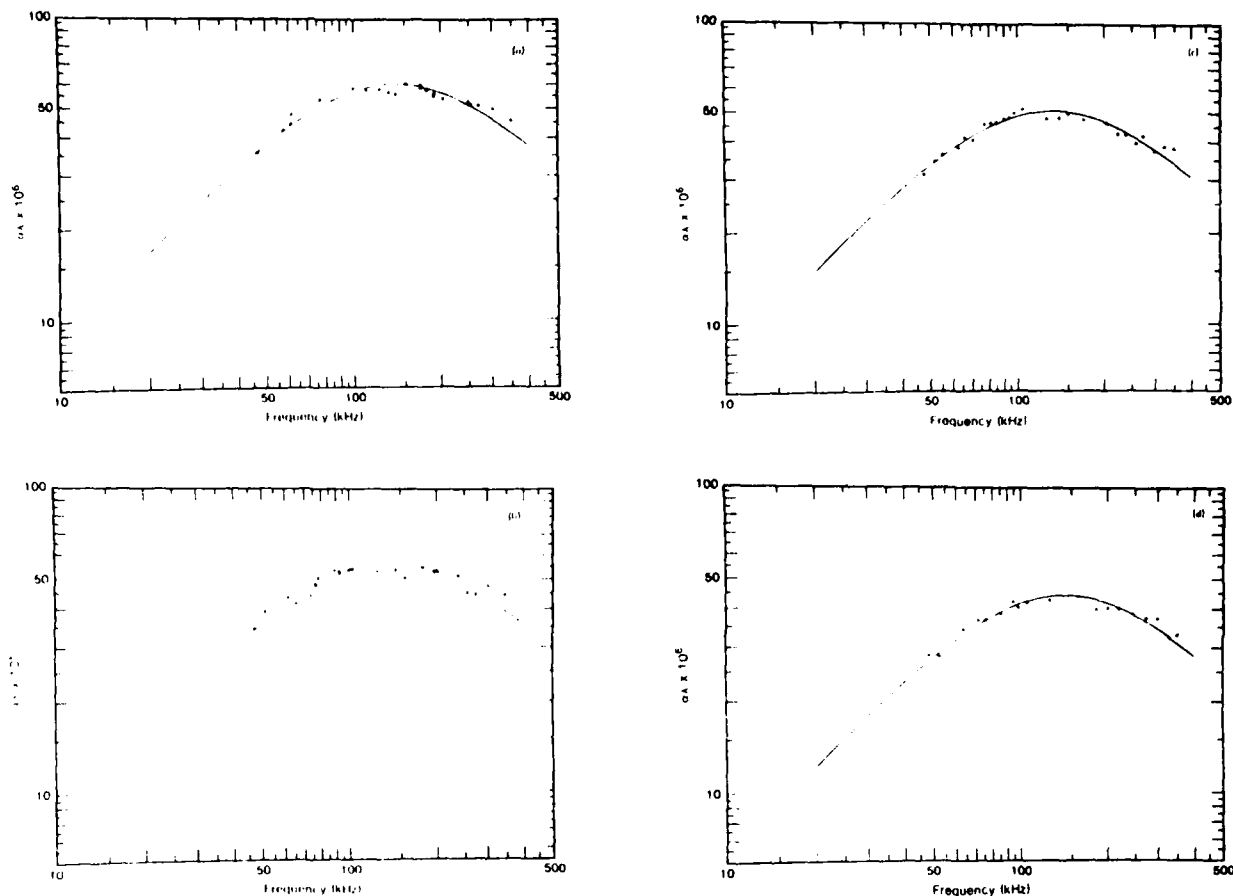
FIG. 3. Sound absorption versus frequency at 25 °C for Lyman and Fleming seawater at (a) 1 atm, (b) 71 atm, (c) 188 atm, and (d) 307 atm.

$$(\alpha\lambda)_m(P)/(\alpha\lambda)_m(1) = 1 + b_1(P-1) + b_2(P-1)^2, \quad (2)$$

where $(\alpha\lambda)_m(P)$ is the maximum absorption per wavelength obtained at P atm and $(\alpha\lambda)_m$ is that at atmospheric pressure. Values of b_1 and b_2 obtained from our results are summarized in Table II and compared with those obtained by previous investigators.

The magnesium sulfate solution and the mixture of magnesium sulfate and sodium chloride show virtually the same decrease in absorption at 307 atm as seen in Table II. This indicates that the addition of sodium chloride up to the ionic strength of seawater does not produce a significant effect on the volume changes or the reaction rates of the steps coupled with the primary relaxation of the magnesium sulfate equilibrium. The greater pressure effect on sound absorption in LF seawater could be interpreted as a larger relative decrease in the concentration of $MgSO_4$ ion-pairs at high pressure for LF seawater than for the pure magnesium sulfate solution or the $MgSO_4$–NaCl mixture.

From our results we have found that the pressure dependence of both absorption and relaxation frequency in LF seawater are substantially different from the results obtained by Bezdek.[15] In fact, for a pressure change of 306 atm at 25 °C the absorption in LF seawater[20] decreases by 26.3%, very nearly the same as the 28.1% decrease observed in 0.5M $MgSO_4$ solutions. There was no change in relaxation frequency with pressure, contrary to the large increase reported by Bezdek[15]; however, this independence of f_r with pressure agrees with the results obtained by Fisher[7] in 0.5M $MgSO_4$ solutions to 1000 atm. For the 0.02M $MgSO_4$ solution as well as the 0.02M $MgSO_4$–0.6M NaCl mixture, the effect of pressure on absorption was essentially identical, a decrease of 19.6% and 19.8%, respectively, at 307 atm. This decrease is in good agreement with the 21.4% decrease predicted by one set of parameters for the Eigen and Tamm[8] multistate model[14] as discussed in the next section.

III. MULTISTATE DISSOCIATION MODEL
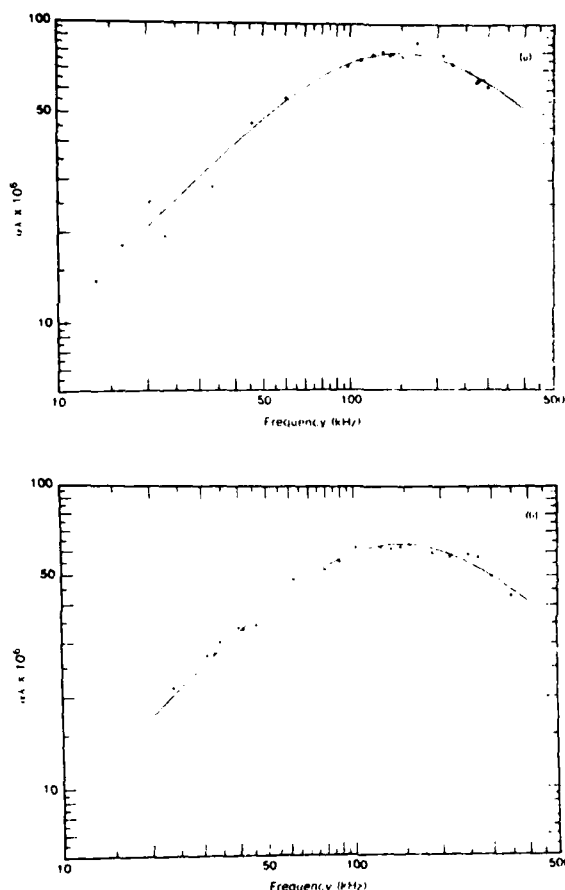
The multistate model referred to in the Introduction is

$$Mg^{++} + SO_4 \overset{k_{12}}{\underset{k_{21}}{\rightleftharpoons}} MgOH_2OH_2SO_4 \cdot MgOH_2SO_4 \cdot MgSO_4, \quad (3)$$
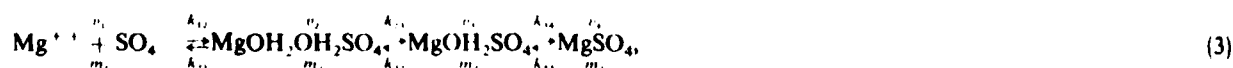
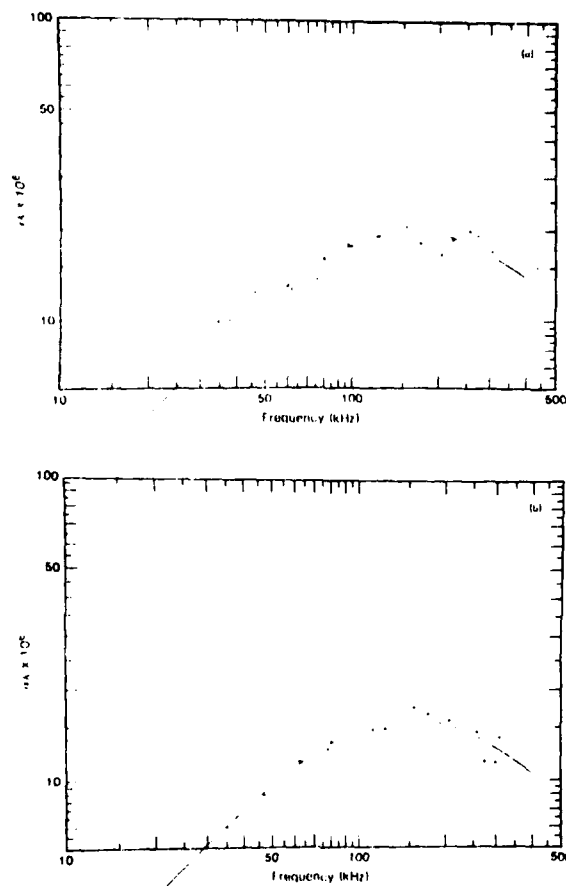FIG. 4. Sound absorption versus frequency at 25 °C for 0.02M magnesium sulfate solution at (a) 1 atm and (b) 307 atm.

FIG. 5. Sound absorption versus frequency at 25 °C for 0.02M magnesium sulfate and 0.6M sodium chloride mixture at (a) 1 atm and (b) 307 atm.

where v_i and m_i are the partial volumes and the concentrations of the species in the four states, and k_{ij} are the corresponding reaction rates. Eigen and Tamm[8] specified a range of parameters for the molal equilibrium constants K_{ij} ($\pm 50\%$) and partial molal volume change ΔV_{ij} ($\pm 20\%$) which could be used to fit the atmospheric pressure absorption data in MgSO$_4$ solutions. Since chemical equilibria shift with pressure according to the equation

$$\left(\frac{\partial \ln K_{ij}}{\partial P} \right)_T = - \frac{\Delta V_{ij}}{RT}, \qquad (4)$$

where R is the gas constant and T is the absolute temperature, we can calculate the pressure dependence of both electrical conductance and sound absorption in MgSO$_4$ solutions using the multistate dissociation parameters. As Fisher and Fox[17] mentioned, there are other multistate models for MgSO$_4$ of the range of parameters for the four-state Eigen and Tamm model[8] but only those not in parentheses below describe the pressure dependence of both conductance and acoustic data

$$K_{12} = m_1^2 f^2 / m_2, \quad \Delta V_{12} = 0(0)\text{cc/mole},$$

$$K_{12} = 0.04(.024); \qquad (5)$$

$$K_{23} = m_2 / m_3 = k_{32}/k_{23},$$

$$\Delta V_{23} = - 18(- 14)\text{cc/mole}, \quad K_{23} = 1(0.5); \qquad (6)$$

$$K_{34} = m_3 / m_4 = k_{43}/k_{34},$$

$$\Delta V_{34} = - 3(- 3)\text{cc/mole}, \quad K_{34} = 9(7.5); \qquad (7)$$

here (assuming the activity coefficient of ion-pair is unity) $f_\pm$ is the mean activity coefficient of the magnesium and sulfate ions and can be calculated from Debye–Huckel theory.[7,17] For $f_\pm$ we use the same equation and distance parameter as Fisher and Fox did in analyzing their conductance data.

From the above parameters, m_4 is about 5% of the total neutral ion-pair concentration, $m_2 + m_3 + m_4$. The contact ion-pair in state four is the one whose concentration m_4 governs the ~100 kHz relaxation measured and the relaxation frequency if principally governed by k_{43}. In pure MgSO$_4$ solutions, according to the Eigen and Tamm theory, the maximum absorption per wavelength is expressed by

$$(\alpha \lambda)_m = \frac{\pi}{2\beta_0} \frac{(m_1' + m_2 + m_3)m_4(\Delta V_{III}^2)}{(m_1' + m_2 + m_3 + m_4)1000RT}, \qquad (8)$$

where β_0 is the static compressibility of the solution, $m_1' = m_1 [2 + (\partial \ln f_\pm^2 / \partial \ln m_1)]^{-1}$ is the concentration of the species in state 1 when activity coefficients are considered. The quantity ΔV_{III} is a normal coordinate volume
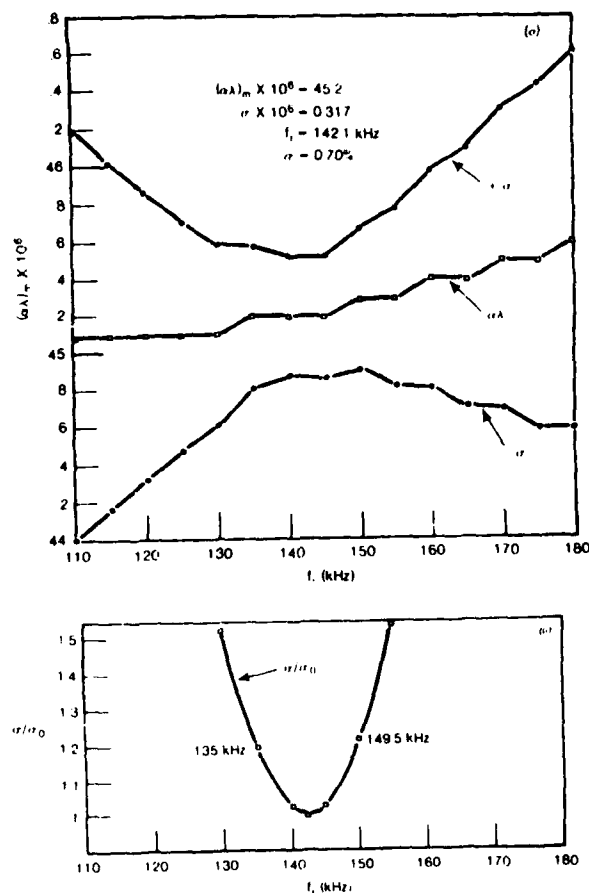
FIG. 6(a). $\alpha\lambda_m$ and σ versus relaxation frequency f_r. (b). The ratio σ/σ_0 versus relaxation frequency f_r.

change that is a linear combination of the ΔV_{ij}. The conventional molal dissociation constant for MgSO$_4$ is given by

$$K_m = m_1^2 f^2_{\pm} /(m_2 + m_3 + m_4) \qquad (9)$$

and its pressure dependence is given by

TABLE II. Summary of pressure effect on maximum excess sound absorption at 25 °C for the equation $(\alpha\lambda)_m(P)/(\alpha\lambda)_m(1) = 1 + b_1(P-1) + b_2(P-1)^2$, where P is in atmospheres.

Investigator	$b_1 \times 10^4$ (atm^{-1})	$b_2 \times 10^8$ (atm^{-2})
Hsu and Fisher (0.02M MgSO$_4$)	− 6.39 ± 0.35	0
Hsu and Fisher (0.02M MgSO$_4$ + 0.6M NaCl)	− 6.47 ± 0.81	0
Hsu and Fisher (LF seawater)	− 8.06 ± 1.08	0
Schulkin and March (seawater using Fisher data)[a]	− 6.54	0
Francois and Garrison (seawater, using Bezdek and Fisher data)	− 11.8	0
Bezdek (seawater)[a]	− 12.90	0
Fisher (0.5M MgSO$_4$)[10]	− 10.30	+ 37.00

[a]Schulkin and Marsh used a straight line to represent Fisher's data rather than the parabola Fisher used; hence the difference between the coefficients.

$$\left| \frac{\partial \ln K_m}{\partial p} \right|_T = - \frac{\Delta V^0}{RT}. \qquad (10)$$

By using Eq. (8) and the numerical parameters (not in parentheses) given in Eqs. (5)–(7) a decrease in absorption of 21.4% is predicted compared to the observed 19.6% decrease for a pressure change of 307 atm.

Using conductance data at elevated pressures one can evaluate the pressure dependence of K_m and arrive at a value of ΔV^0 using Eq. (10). As we see from Eqs. (5)–(7) and (9) and (10), such a ΔV^0 is really a composite of all the ΔV_{ij}. From conductance data Fisher and Fox[17] found $\Delta V^0 = -9.0$ cc/ mole at 1 atm compared to $\Delta V^0 = -9.4$ cc/mole predicted from the Eigen and Tamm parameters.

Thus we have good agreement with the observed and predicted pressure dependence of both sound absorption and electrical conductance in MgSO$_4$ solutions. However, there is a substantial disagreement between values of $K_m = 0.0062$ obtained from conductance data[17] and $K_m = 0.019$ calculated from the parameters in Eqs. (5)–(7). Eigen and Tamm considered K_{12} a free parameter (and therefore K_m a free parameter) in explaining the acoustic data, rather than constraining K_m to fit conductance data.

The other four-state model parameters (those in parentheses) proposed by Eigen and Tamm which yield a K_m of 0.00735, and a ΔV^0 of − 9.7 cc/mole predict only a 14% reduction in absorption for a pressure change of 306 atm compared to the 19.6% observed decrease. Thus we see that neither of the Eigen–Tamm multistate models fully describe both conductance and acoustic data. These models, therefore, need to be re-examined critically.

IV. COMPARISON OF PREDICTIONS AND MEASUREMENTS FOR SEAWATER

Francois and Garrison[23] have recently published the most comprehensive review to date of both laboratory and ocean measurements of sound absorption measurements in seawater. Our results for Lyman and Fleming synthetic seawater at 25 °C as a function of pressure are shown in Table III along with theirs for natural seawater. We see that their predictions exceed our measurements at atmospheric pressure by 15% for the magnitude of $(\alpha\lambda)_m$ and by 22% for the relaxation frequency. We also differ in the effect of pressure on the decrease in $(\alpha\lambda)_m$; our measurements show a decrease of 26% compared to their predicted decrease of 36%. We agree on the independence of the relaxation frequency with respect to pressure. In making this comparison, however, it must be noted that their results at 1 atm empha-

TABLE III. Comparison of predictions by Francois and Garrison (FG) with our results (HF) for $(\alpha\lambda)_m$ and f_r at 25 °C.

P(atm)	$(\alpha\lambda)_m \times 10^6$		f_r, kHz	
	FG	HF	FG	HF
1	70	61	172	140
71	64	58	172	140
188	54	53	172	140
307	45	45	172	140

size data in the ocean at temperatures from $-2°$ to $10°$ and the pressure data of Bezdek from $1°$ to $7°$ while our results are for synthetic seawater in the laboratory. It remains to be seen how those differences can be reconciled. We plan to make pressure measurements in Lyman and Fleming seawater in the laboratory at lower temperatures in seawater as a first step and then make some laboratory measurements with natural seawater.

V. SUMMARY

We have measured the pressure dependence of sound absorption in Lyman and Fleming synthetic seawater and in aqueous solutions of $MgSO_4$ at 25 °C. For seawater, we find a greater decrease in absorption, 26% for a pressure increase of 306 atm than for a pure 0.02M $MgSO_4$ solution or a 0.02M $MgSO_4$–0.6M NaCl solution which exhibit decreases of 19.6% and 19.8%, respectively. The addition of 0.6M NaCl reduced absorption in the 0.02M $MgSO_4$ solution by a factor of four. The reasons for such a large reduction at atmospheric pressure have been treated by Hsu[21] in a preliminary manner.

For 0.02M $MgSO_4$ solutions we find that the measured values of the pressure dependence of both sound absorption and electrical conductance are in agreement with those predicted by the Eigen and Tamm multistate dissociation theory. However, since there exists such a large discrepancy for the overall equilibrium constant, the parameters for the multistate model need to be re-evaluated.

For seawater, our results are the first laboratory measurements as a function of pressure. The reasons for the difference of our results with predictions of Francois and Garrison are not clear at this time. We will extend our work to lower temperatures and natural seawater and then re-evaluate the disagreements.

Our intent was to do definitive work to clear up discrepancies between ocean and laboratory measurements. While we regard this work as definitive, it obviously did not clear up the discrepancies. We are dealing only with chemical absorption and ocean measurements can include other loss mechanisms such as volume and surface scattering[24] which were present in the early work by Marsh and Schulkin.[25] Wilson and Leonard[6] and Simmons[16] both showed that laboratory measurements in synthetic and natural seawater were in good agreement. Nevertheless, we feel that this should be checked again in our laboratory in an effort to resolve these discrepancies.

ACKNOWLEDGMENTS

[1] F. H. Fisher and V. P. Simmons, "Sound Absorption in Seawater," J. Acoust. Soc. Am. 62, 558–564 (1977).

[2] R. W. Leonard, P. C. Combs, and L. R. Skidmore, Jr., "Attenuation of Sound in Synthetic Seawater," J. Acoust. Soc. Am. 21, 63 (1949).

[3] L. N. Liebermann, "Origin of Sound Absorption in Water and in Seawater," J. Acoust. Soc. Am. 20, 868–873 (1948).

[4] R. W. Leonard, "The Attenuation of Sound in Liquids by a Resonator Method," Tech. Rep., No 1, Phys. Dept., UCLA (1950).

[5] G. Kurtze and K. Tamm, "Absorption of Sound in Aqueous Solutions of Electrolytes," Nature 168, 346 (1951); "Measurements of Sound Absorption in Water and in Aqueous Solutions of Electrolytes," Acustica 3, 33–48 (1953).

[6] O. B. Wilson and R. W. Leonard, "Measurements of Sound Absorption in Aqueous Salt Solutions by Resonator Method," J. Acoust. Soc. Am. 26, 223–226 (1954).

[7] F. H. Fisher, "Effect of Pressure on Sound Absorption and Chemical Equilibrium," J. Acoust. Soc. Am. 30, 442–448 (1958).

[8] M. Eigen and K. Tamm, "Sound Absorption in Electrolyte Solutions due to Chemical Relaxation," Z. Elektrochem. 66, 93–121 (1962).

[9] F. H. Fisher, "The Effect of Pressure on the Equilibrium on Magnesium Sulfate," J. Phys. Chem. 66, 1607–1611 (1962).

[10] M. Schulkin and H. W. Marsh, "Sound Absorption in Seawater," J. Acoust. Soc. Am. 34, 864–865 (1962); "Low-frequency Sound Absorption in the Ocean," J. Acoust. Soc. Am. 63, 43–48 (1978).

[11] F. H. Fisher, "Ultrasonic Absorption in $MgSO_4$ Solutions as a Function of Pressure and Dielectric Constant," J. Acoust. Soc. Am. 38, 805–812 (1965).

[12] (a) K. Tamm, "Acoustic Relaxation in Electrolyte Solutions," Proceedings of the International School of Physics "Enrico Fermi," Course XXVII, edited by D. Setta (Academic, New York, 1963), pp. 175–222. (b) J. Stuehr and E. Yeager, "The Propagation of Ultrasonic Waves in Electrolytic Solutions," in Physical Acoustics, edited by W. P. Mason (Academic, New York, 1965), Vol. II, Part A, Chap. 6III, pp. 376–452

[13] F. H. Fisher, "Multistate Dissociation and the Effect of Pressure on the Equilibrium of Magnesium Sulfate," J. Phys. Chem. 69, 695–696 (1965).

[14] F. H. Fisher, "Effect of Pressure on Sulfate Ion Association and Ultrasonic Absorption in Sea Water," Geochim. Cosmochim. Acta 36, 99–101 (1972).

[15] H. F. Bezdek, "Pressure Dependence of Sound Attenuation in the Pacific Ocean," J. Acoust. Soc. Am. 53, 782–788 (1973), "Pressure Dependence of the Acoustic Relaxation Frequency Associated with $MgSO_4$ in the Ocean," J. Acoust. Soc. Am. 54, 1062–1065 (1973).

[16] V. P. Simmons, "Investigation of the 1 kHz Sound Absorption in Sea Water," Ph.D. dissertation, University of California, San Diego, CA (1975).

[17] F. H. Fisher and A. P. Fox, "Divalent Sulfate Ion Pairs in Aqueous Solutions at Pressures up to 2000 atm," Jr. Solution Chem. 8, 309–328 (1979).

[18] D. R. Kester and R. M. Pytkowicz, "Effect of Temperature and Pressure on Sulfate Ion Association in Sea Water," Geochim. Cosmochim. Acta 34, 1039–1051 (1970).

[19] F. J. Millero, "Effect of Pressure on Sulfate Ion Associations in Sea Water," Geochim. Cosmochim. Acta 35, 1089–1098 (1971).

[20] J. Lyman and R. H. Fleming, "Composition of Sea Water," J. Marine Res. III, 134–146 (1940).

[21] C. C. Hsu, "Differential Sound Absorption Technique and Effect of Ion-Pairing and Pressure on Sound Absorption in Seawater and Aqueous Mixtures of Magnesium Sulfate and Sodium Chloride," Ph.D. dissertation, University of California, San Diego, CA (1 November 1981), pp. 105 (SIO Reference 81–34).

[22] C. C. Hsu and F. H. Fisher, "Observation of Q of 1 Million in a Water-filled 100-liter Titanium Spherical Resonator at 25 kHz," J. Acoust. Soc. Am. Suppl. 1 69, S44 (1981).

[23] R. E. Francois and G. R. Garrison, "Sound Absorption Based on Ocean Measurements. Part 1: Pure Water and Magnesium Sulfate Contributions," J. Acoust. Soc. Am. 72, 896–907 (1982).

[24] R. J. Urick, Principles of Underwater Sound (McGraw-Hill, New York, 1975), 2nd ed.

[25] H. W. Marsh, Jr. and M. Schulkin, "Report on the status of project AMOS," USL Res. Rep. #255 (U. S. Navy Underwater Sound Laboratory, New London, CT, 1955).

Persistence of a Pattern of Surface Gravity Waves

KENNETH M. WATSON

Marine Physical Laboratory of the Scripps Institution of Oceanography,
University of California, San Diego

The observation of ship Kelvin wakes by the Seasat synthetic aperture radar raises a question concerning the persistence of patterns of surface gravity waves. Time scales vary with wavelength and environmental conditions. The range extends from fractions of a second at the shortest wavelengths to many days for ocean swell. Several mechanisms for destroying a wave pattern are investigated here. These are viscous dissipation, direct wind-wave interaction, and nonlinear hydrodynamic interaction with ambient surface waves. The nonlinear hydrodynamic interactions appear to be the most significant.

1. INTRODUCTION

The imaging of surface ship Kelvin wakes by the Seasat synthetic aperture radar (SAR) raises an interesting question: How long will a given "pattern" of surface waves persist? Under conditions of light wind and low sea state the Kelvin wake of a vessel may be seen to persist astern for some kilometers. Under more robust sea conditions the wake persistence seems to be greatly reduced. In this paper we shall discuss several mechanisms contributing to the decay of such a "pattern."

Deterministic mechanisms, such as linear wave propagation and dispersion and the interaction with known large-scale currents, can distort a wave pattern. This, however, is in principle predictable and will not be considered as "pattern decay." Stochastic mechanisms, such as interaction with wind and ambient sea, do lead to a genuine decay of the pattern. We note, however, that the quantitative criteria for decay may be sensitive to the detection algorithm used.

We shall be principally concerned here with the decay of gravity waves in the 0.1- to 4-m range of wavelengths. The mechanisms considered for decay imply a strong sensitivity to wavelength. For wavelengths less than 10 cm the time scales as predicted are too short (of the order of a second, or less) to be of interest in the present context. For wavelengths greater than a few meters the predicted time scales become so long that changing environmental conditions may be a factor. Patterns of swell have been observed to propagate across ocean basins [*Snodgrass et al.*, 1966]. The Bragg wavelengths for the Seasat SAR were in the 30-cm range [*Vesecky and Stewart*, 1982], which is well within the scope of our analysis.

There are evidently several mechanisms that contribute to wave pattern decay. Viscous dissipation seems to be the simplest of these. Wind-wave interaction, while physically complex, is phenomenologically modeled as a simple exponential pattern decay. These mechanisms are reviewed in section 3.

Nonlinear hydrodynamic interactions of the pattern with ambient surface waves provide other decay mechanisms.

In the terminology of wave-wave weak interaction theory, both "three-wave" and "four-wave" interactions must be considered. It is well-known that for gravity waves the three-wave interactions do not admit resonant frequency conditions. We shall see that these lead to only partial pattern decay. Only if this decay brings the signal-to-noise level below the threshold for detectability, can we consider the pattern destroyed. The four-wave interactions act on a slower time scale than do the three-wave interactions, but lead to total decay of the pattern (according to weak interaction theories).

In section 4 we discuss first the three- and four-wave interactions of pattern waves with ambient waves of much longer wavelengths. The response to a matched filter in the space time domain will be described using a technique due to *Van Kampen* [1974].

In section 4 we also analyze the pattern response to interaction with waves of similar wavelengths. A formulation of the *Hasselmann* [1967] equations given by *Dungey and Hui* [1979] is used for this.

The evolution of the pattern spectrum is investigated in section 5. For the case of three-wave interactions this is done explicitly. The effect of four-wave interactions with long waves is formulated in terms of diffusion equation in wave number space.

The conclusions of this paper are summarized in section 6. It is observed that the fastest decay rates obtained result from three-wave interaction with long ambient waves. When this mechanism is not effective, the dominant decay mechanism is four-wave resonant interactions with long ambient waves, with the wind mechanism being somewhat comparable.

2. DESCRIPTION OF THE DECAY PHENOMENA

In a specified "rectangular area of ocean" we use a Fourier expansion for the surface wave displacement $\zeta(x, t)$ ($x = x, y, a$ vector in the plane of the quiescent ocean surface):

$$\zeta(x, t) = -Im [Z(x, t)]$$

$$Z(x, t) = \sum_l b_l \exp [il \cdot x - \omega_l t)] \qquad (1)$$

Here $\omega_l = (gl)^{1/2}$. In the approximation that the waves are

linear and not forced, the b_l are constants. In general, $b_l(t)$ is time dependent.

We shall suppose that (1) refers to the ambient sea. For the pattern waves we take as a special case of (1),

$$\zeta_p(x, t) = -Im\ (Z_p)$$

$$Z_P = \sum_k B_k(t)\ \exp\ [i(k \cdot x - \omega_k t)] \tag{2}$$

We shall suppose that the $B_k(0)$ are fixed, specified amplitudes (they determine the pattern) at some reference time, say, $t = 0$.

Over an ensemble of realizations of the ocean surface the b_l will be considered to be uncorrelated Gaussian variables. The ensemble averaged spectrum Ψ_a of vertical displacement is

$$\Psi_a(l)\ d^2l = \sum_l \tfrac{1}{2} < |b_l|^2 > \tag{3}$$

In this paper we shall use a *Pierson and Moskowitz* [1964] spectrum for the ambient sea:

$$\Psi(l) = (\tfrac{\eta}{l^4})\ \exp\ [-0.74\ (\tfrac{l_o}{l})^2]G(\theta)$$

$$\eta = 4 \cdot 10^{-3}, \qquad l_o = g/W^2 \tag{4}$$

Here W is the wind velocity, g $= 9.8$ m/s^2, and θ is the angle between l and W. We shall specify models of $G(\theta)$ later, but now note the normalization

$$\int_{-\pi}^{\pi} G(\theta)\ d\theta = 1 \tag{5}$$

For the pattern waves, we introduce the *Wigner* [1932] correlation function

$$\Gamma_p(r, x, t) = \tfrac{1}{2} < Z_p(x - r/2, t)Z_p^*(x + r/2, t) > \tag{6}$$

Here $<\ \ >$ represents an ensemble average over the ambient sea, as in (3). In performing this ensemble average the pattern amplitudes $B_k(0)$ are considered deterministic and fixed. The spectrum of vertical displacement is

$$\Psi_p(k, x, t) = \int \Gamma_p\ \exp\ (ik \cdot r)\ d^2r/(2\pi)^2 \tag{7}$$

(It is assumed that x varies slowly over distances comparable to pattern wavelengths of interest.)

The spectrum of wave action F and energy E are related to the spectrum of vertical displacement Ψ by the relations

$$F = (g\rho_o/\omega_k)\Psi = E/\omega_k \tag{8}$$

where ρ_o is the density of seawater. The *Hasselmann* [1967] equation for the evolution of F is of the form

$$\frac{\partial F}{\partial t} + \dot{x} \cdot \nabla_x F = S_{nl} + S_v + S_w \tag{9}$$

Here $\dot{x} = \nabla_k \omega_k$, and S_{nl}, S_v, and S_w represent the effects of wave-wave interactions, viscosity, and wind, respectively. We have omitted the term in (9) describing diffraction by large-scale surface currents or shoaling. To the extent that such effects are known, their influence on the pattern is predictable and would not lead to pattern decay. These effects are sensitive to detail and seem best omitted in the present general discussion.

We may write

$$F = F_a + F_p \tag{10}$$

where F_a refers to the action spectrum of ambient waves and F_p to that of the pattern waves. For simplicity, we take F_a to be a (quasi) stationary solution to (9). Then, on inserting (10) into (9) and linearizing in F_p, we obtain

$$\frac{\partial F_p}{\partial t} + \dot{x} \cdot \nabla_x F_p = S_n' + S_v' + S_w' \tag{11}$$

The quantities on the right depend linearly on F_p and will be specified later.

3. EFFECTS OF VISCOSITY AND WIND

Viscosity will lead to exponential damping of the pattern waves. In the notation of (11) this is expressed as [*Phillips*, 1977]

$$S_v' = -\beta_v F_p$$

$$\tag{12}$$

$$\beta_v = 4\nu_o k^2$$

where $\nu_o \cong 1.1 \cdot 10^{-6}\ m^2/s$ is the kinematic viscosity of seawater. The decay time

$$T_d(v) \equiv \beta_v^{-1} \tag{13}$$

is shown as a function of wavelength $\lambda = 2\pi/k$ in Figure 1.

The rate of wind-induced growth for surface waves has recently been reviewed by *Plant* [1982; see also, *Mitsuyasu and Honda*, 1982]. He concludes that for the growth rate of small amplitude waves,

$$S_w' = \beta_w F_p \tag{14}$$

in (9). Here

$$\beta_w = 0.04u_*^2 k^2 \cos \theta/\omega_k \tag{15}$$

where u_* is the friction velocity of the wind and θ is the angle between k and W.

It seems plausible for our purposes to interpret

$$T_d(w) \equiv \beta_w^{-1} \tag{16}$$

as a pattern decay time.

To evaluate (16) we use the analysis of *Garratt* [1977] to relate u_* to the wind speed W at 10-m height. The resulting time $T_d(w)$ is shown in Figure 2 as a function of W for several wavelengths λ and angle $\theta = 0$. We note from Figures 1 and 2 that for $W > 2\ m/s$, $T_d(w) < T_d(v)$ when $\lambda > 0.1$ m.

4. EFFECTS OF WAVE-WAVE INTERACTIONS

One simple descriptor of pattern decay is given by the correlation function, which we may consider as the output of a "matched filter."

$$\Gamma_0(t) = < P[\zeta_p(x, 0); t]\zeta_p(x, t) > \tag{17}$$

Here $t = 0$ is considered to be the reference time at which the pattern is first observed. The quantity
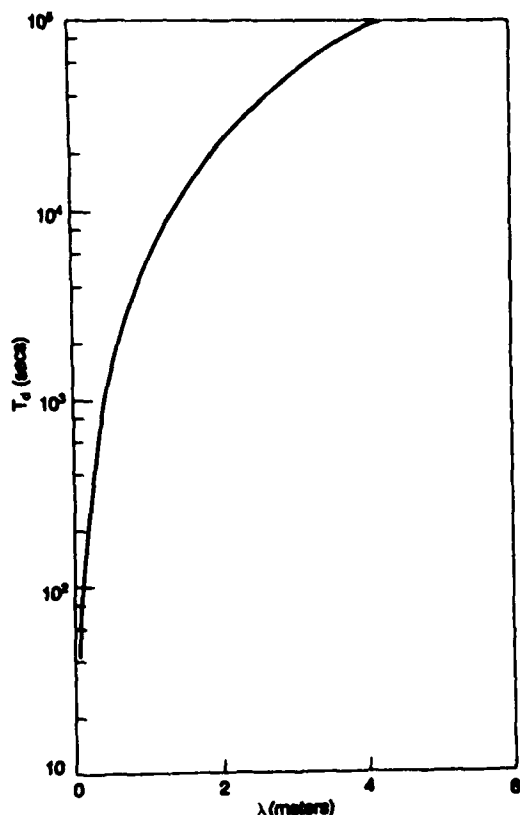
$$P[\zeta_p(x, 0; t)]$$

Fig. 1. The decay time (13) due to viscous dissipation as a function of wavelength.

represents the predicted field at t, given the initial field $\zeta_p(x, 0)$. The prediction is to be obtained using known deterministic phenomena that may distort the pattern. For example, if linear wave propagation is the only deterministic phenomenon, then

$$P[\zeta_p(x, 0); t] = -Im \sum_k \left\{ B_k(0) \exp [i(k \cdot x - \omega_k t)] \right\} \quad (18)$$

where $B_k(0)$ is the value of B_k at $t = 0$.

The ensemble average in (17) is considered to be one over realizations of the ambient field amplitudes b_k (see (1)) with the initial pattern amplitudes $B_k(0)$ being fixed, as in (6). If the pattern could be predicted exactly at time t, then $\Gamma_0(t)$ would represent the mean square pattern vertical displacement. Interaction of the pattern with the ambient wave field reduces the accuracy of this prediction and leads to a mismatch between the predicted and actual patterns, causing the correlation, or "filter output," Γ_0 to decay with time.

In this paper we shall assume that (18) applies to evaluating (17). Then it is sufficient to calculate the set of correlations

$$\gamma_{kk'}(t) = <B_k(t)B_{k'},(0)> = <B_k(t)> B_{k'},(0) \quad (19)$$

We shall refer to a given Fourier amplitude in the pattern as a "test wave."

Under certain conditions we might expect $< B_k >$ to be determined from a Langevin equation of the form

$$\frac{d}{dt} < B_k > = -\nu(k) < B_k > \quad (20)$$

where $\nu(k)$ is the Langevin "rate constant." In this case we would evaluate (19) as

$$\gamma_{kk'} = B_k(0)B_{k'},(0) \exp [-\nu(k)t] \quad (21)$$

We shall see that four-wave interactions, with frequency resonance, lead asymptotically to equations of the form (20) and (21).

4.1. Interaction with Ambient Wave Orbital Currents

As a first illustration of (17) and (19) we consider the advection of a test wave k due to the orbital velocity $U(x, t)$ of the ambient waves. This current is of the form

$$U(x, t) = \sum_l (\frac{i}{2})\hat{l}\omega_l \left\{ b_l \exp [i(l \cdot x - \omega_l t)] - c.c \right\} \quad (22)$$

where $\hat{l} \equiv l/l$, using the notation of (1). We may assume here that the ambient waves are linear, so the b_l are constants. We shall also assume that

$$l << k \quad (23)$$

or the wavelength of the test wave is small compared with that of those ambient waves which are of most importance for pattern decorrelation. This assumption can be tested for verification when we evaluate the decay using the spectrum (4).

If the test wave is advected with the local velocity U, we use (23) to write

$$B_k(t) \cong B_k(0) \exp [-ik \cdot \int_0^t U(t') dt'] \quad (24)$$
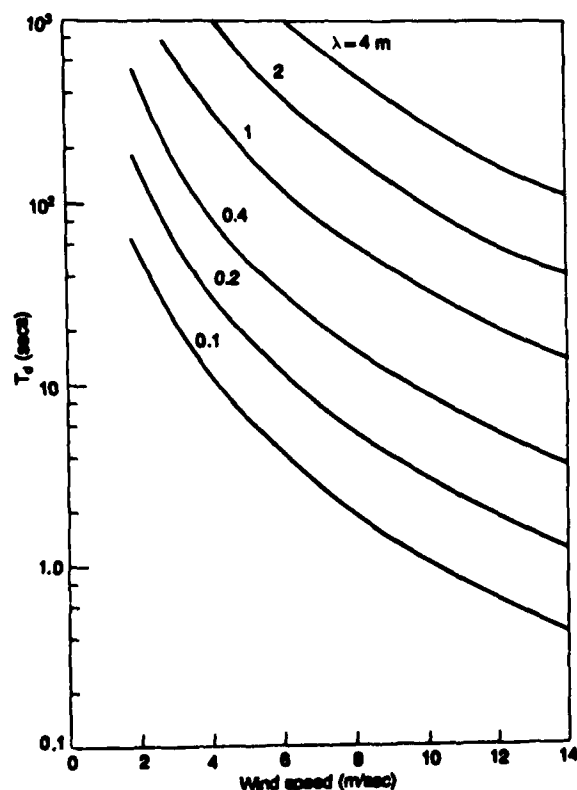

Fig. 2. The decay time (16) due to wind-sea interaction as a function of wind speed for several wavelengths.

Using the assumed Gaussian distribution of the b_k's and the relation (3), we obtain

$$< B_k (t) > = B_k (0) \exp [-D_3(k, t)] \qquad (25)$$

where

$$D_3(k, t) = \int d^2l (k \cdot \hat{l})^2 [1 - \cos (\omega_l t)] \Psi_a (l) \qquad (26)$$

For small t this becomes

$$D_3(k, t) \cong \sigma^2 t^2 / 2 \quad , \quad \omega_{l_0}(t) << 1 \qquad (27)$$

where

$$\sigma^2 = < (k \cdot U)^2 > = \int d^2l (k \cdot \hat{l})^2 \omega_l^2 \Psi_a (l) \qquad (28)$$

For $t \rightarrow \infty$, on the other hand, we have

$$D_3(k, \infty) = \int d^2l (k \cdot \hat{l})^2 \Psi_a (l) \qquad (29)$$

We note that for the spectrum (4) the assumed condition (23) appears to be valid for the evaluation of D_3.

When (27) is valid, we may define an e-folding decay time as

$$T_d (3) = 2^{\frac{1}{2}} / \sigma \qquad (30)$$

More generally, we may define the decay time with the relation

$$D_3[k, T_d (3)] = 1 \qquad (31)$$

This equation may or may not have a solution. When there is no solution, the advection mechanism is ineffective in destroying the pattern. The single e-folding condition (31) is arbitrary, and one may wish to define the decay time to correspond to several e-foldings.

The decay relation (25) is not of the form (21). This is due to the lack of a frequency resonance in the wave interactions.

4.2 Decay Due to Three-Wave Interaction

A more systematic and formal description of the decay of (19) can be obtained using the method of *Van Kampen* [1974]. To develop this, we begin with the formulation of *Watson and West* [1975]. Their equation of motion, when linearized in the pattern amplitudes B_k, is of the form

$$\dot{B}_k = T_2(B, b) + T_3(B, b) + \ldots \qquad (32)$$

Here T_2 and T_3 are quadratic and cubic, respectively, in wave amplitudes. If we ignore all but the T_2 term, (32) takes the form

$$\dot{B}_k = \sum_p A_k{}^p B_p \qquad (33)$$

where

$$A_k^p = \sum_l \delta_{k-l-p} \left\{ 2 \Gamma_p^k b_l \exp [(\omega_k - \omega_p - \omega_l)t] \right.$$

$$\left. + \Gamma_p^{k-l} b_{-l}^* \exp [i(\omega_k - \omega_p - \omega_l)t] \right\} \qquad (34)$$

The coefficients Γ are defined in Appendix A of *Watson and West* [1975].

The Van Kampen equation is

$$\frac{d}{dt} < B_k > = -K (t) < B_k > \qquad (35)$$

where

$$K (t) = -\int_0^t d\tau < A_k^p (t) A_p^k (t - \tau) > \qquad (36)$$

Evaluation of this is straightforward, assuming that the b_l are constant and Gaussian and that $l << k, p$. The result is

$$K (t) = \int d^2l (k \cdot \hat{l})^2 \omega_l \sin (\omega_l t) \Psi_a (l) \qquad (37)$$

Integration of (35) leads to the expression (25) with D_3 given by (26).

The three-wave interaction model (33) is thus equivalent to the simple advection model described by (24). The fact that our decay function D_3 does not increase indefinitely with time reflects the lack of a three-wave resonance. To find true decay to a vanishing pattern amplitude, we include the effects of T_3 in (32). This contains four-wave interactions. Higher order terms arising from T_2 also contribute four-wave interactions and must also be included.

4.3. Decay Due to Four-Wave Interactions

Taking account of the four-wave interactions with long wavelength ambient waves, we again have an equation of the form (33), but with the definition

$$A_k^p = \frac{i}{2} \sum_{l,n} \delta_{k+n-l-p} C_p^{k n} b_l b_n^*$$

$$\cdot \exp [i (\omega_k - \omega_p + \omega_n - \omega_l)t] \qquad (38)$$

The coefficients C here are defined in Appendix B of *Watson and West* [1975] (see specifically their equation (47)). Some rapidly oscillating terms have been dropped from (38), since these do not contain frequency resonance and so do not lead to a true pattern decay. It is assumed in (38) that $l, n << k, p$.

Evaluation of (36) using (38) now gives the decay rate

$$\nu(t) = \text{Re} [K (t)]$$

$$\cong \frac{49}{128} \int d^2l\, d^2n\, \Psi_a (l) \Psi_a (n) \left[k \cdot (\omega_n l + \omega_l n) \right]^2$$

$$\cdot \frac{\sin(\beta t)}{\beta} \qquad (39)$$

where

$$\beta = \omega_l - \omega_n + \omega_k - \omega_{k+l-n}$$

$$\cong \omega_l - \omega_n + c(k) \cdot (n - l) \qquad (40)$$

and $c(k) = \nabla_k \omega_k$. As $t \rightarrow \infty$, we obtain

$$\nu(\infty) = \frac{49\pi}{128} \int d^2l\, d^2n\, \Psi_a (l) \Psi_a (n)$$

$$\left[k \cdot (\omega_n l + \omega_l n) \right]^2 \delta(\beta) \qquad (41)$$

We see that asymptotically the four-wave resonance leads to a Langevin decay law of the form (21).
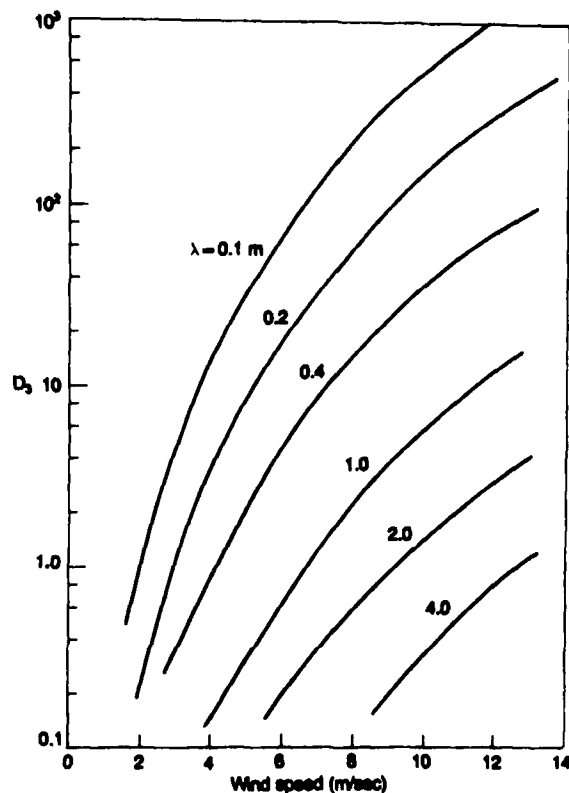
For finite times, we have the relation

Fig. 3. The limiting decay function (29) due to three-wave interactions as a function of wind speed for several wavelengths.

$$< B_k (t) > = B_k (0) \exp [-D_4(k, t)] \qquad (42)$$

where

$$D_4(k, t) = \int_0^t \nu (t') dt'$$

$$= \frac{49}{128} \int d^2l\ d^2n\ \Psi_a (l)\Psi_a (n) [k \cdot (l\omega_n + n\omega_l)]^2$$

$$\cdot [1 - \cos (\beta t)]/\beta^2 \qquad (43)$$

As $t \to \infty$, we obtain

$$D_4(k, t) = \nu (\infty) t \qquad (44)$$

To describe the implication of (26) and (43), we first assume an isotropic ambient spectrum

$$G (\theta) = 1/(2\pi) \qquad (45)$$

Although not realistic as a wind wave spectrum, (45) leads to reasonably accurate decay rates because of the integration over wave angles. A more realistic spectrum will be considered later.

Using (45), we can readily express (26) in the form

$$D_3(k, t) = (\frac{\eta}{2})(k/l_o)^2 J_3(s)$$

$$J_3(s) = \int_1^\infty [1 - \cos (x^{\%}s)\ dx/x^3 \qquad (46)$$

where

$$s \equiv \omega_{l_0} t \qquad (47)$$

and we have replaced the exponential factor in (4) by a simple cutoff at $l = l_0$. Similarly, we may evaluate (43) as

$$D_4(k, t) = (\frac{49}{96}\eta^2(k/l_o)^2 s J_4(s)$$

$$J_4(s) = \frac{\pi}{2} + s^3 \int_0^\infty \frac{[1 - \cos u] du}{(u+s)^3 u^2} \qquad (48)$$

In Figure 3 we show the limiting decay (29) for three-wave interactions for several wavelengths $\lambda = 2\pi/k$ as functions of wind speed W. When $D_3(k, \infty)$ is small enough that the pattern cannot be considered destroyed, the three-wave mechanism is ineffective. We have arbitrarily chosen here

$$D_3(k, \infty) \geqslant 1 \qquad (49)$$

as the condition of pattern destruction by three-wave interactions.

We now define a decay time T_d as being the smaller of T_3, T_4 where

$$D_3(k, T_3) = 1$$

$$D_4(k, T_4) = 1 \qquad (50)$$

In Figure 4 we show T_d as a function of wind speed for several wavelengths λ. The dashed lines represent an
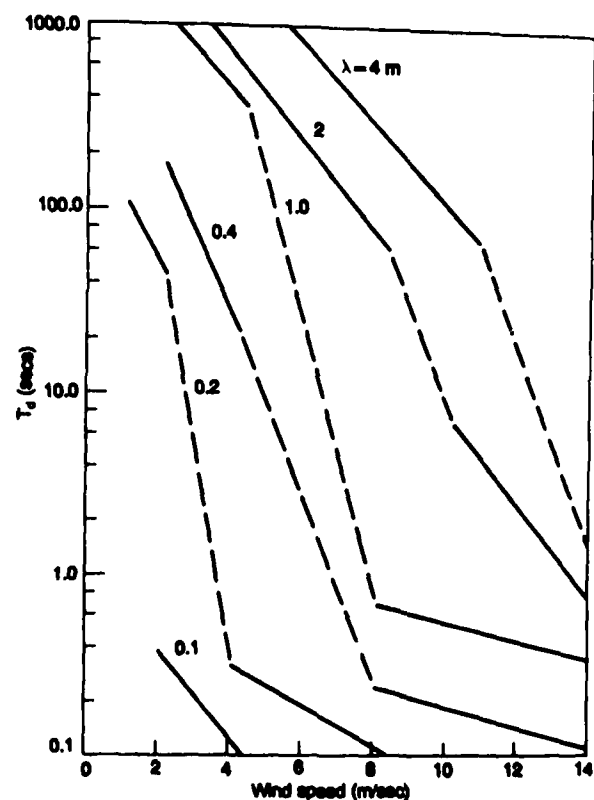
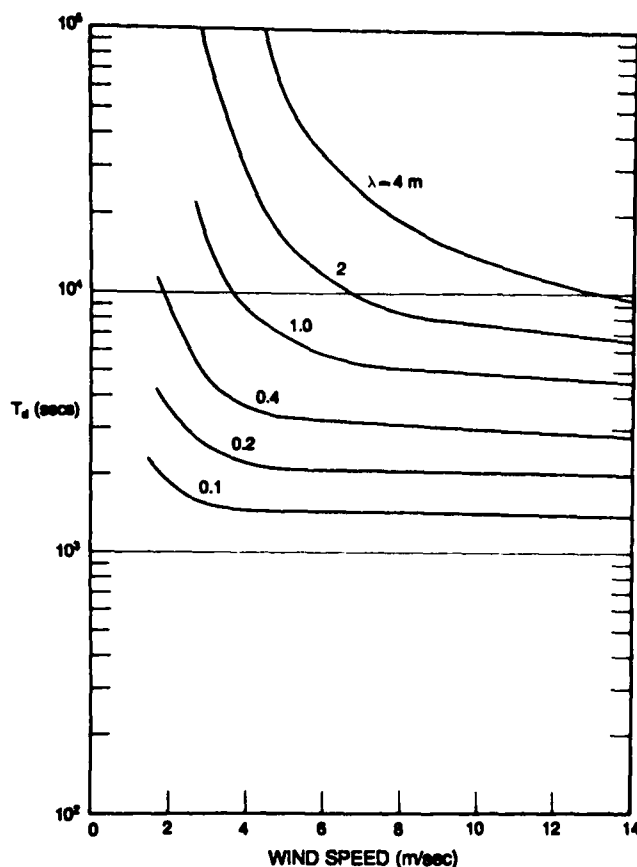Fig. 4. The decay time (50) due to three- and four-wave interaction.

Fig. 5. The decay time (58) due to four-wave interactions.

interpolation made from T_4 (upper region) to T_3 (lower region).

A more realistic spectrum than (45) is that of Tyler et al. [1974]:

$$G(\theta) = \cos^S(\theta)/L(S)$$

$$L(S) = 2(\pi)^{1/2}\Gamma(\tfrac{1}{2}S + \tfrac{1}{2})/\Gamma(\tfrac{1}{2}S + 1) \qquad (51)$$

where S is a function of k.

Using (51) we evaluate (28) as

$$\sigma^2 = \eta g (k^2/l_0)[0.8 \cos^2\alpha + 0.2 \sin^2\alpha]$$

or

$$\sigma = 0.4(W/\lambda)(\cos^2\alpha + 0.25 \sin^2\alpha)^{1/2} \qquad (52)$$

Here α is the angle of k with respect to W. Use of (45), on the other hand, would replace (52) by $\sigma = 0.3(W/\lambda)$. The consequence of using the spectrum (51) does not seem very significant.

The decay time (30) obtained using the simple expression (52) is expected to be valid when

$$T_d \ll \frac{W}{g} \qquad (53)$$

4.4. Decay Due to Waves of Comparable Wavelength

For our discussion of three- and four-wave interactions we have assumed the ambient waves to have wavelengths

much longer than the pattern wavelengths. This has been justified because of the peaking of the spectrum (6) at wave numbers near l_0. To further clarify this, we return to the Hasselmann equation (11). We have already considered the effects of wind and viscosity, so we now write this as

$$\frac{\partial F_p(k,t)}{\partial t} = S_{nl}' \qquad (54)$$

If we assume that F_p represents a very small perturbation on the ambient spectrum, we can write

$$S_{nl}' = -2\nu(k)F_p(k,t) \qquad (55)$$

where

$$2\nu(k_1) = \int d^2k_2\, d^2k_3\, d^2k_4\, G(k_1, k_2, k_3, k_4)$$

$$\cdot \left\{ F_a(k_2)[F_a(k_3) + F_a(k_4)] - F_a(k_3)F_a(k_4) \right\}$$

$$\cdot \delta(k_1 + k_2 - k_3 - k_4)\, \delta(\omega_{k_1} + \omega_{k_2} - \omega_{k_3} - \omega_{k_4}) \qquad (56)$$

Here G is a function of the indicated four wave numbers. A convenient simplification of this equation is given by Dungey and Hui [1979] for the case that F_a describes a narrow spectrum centered near k_1. These authors also show that evaluation of (56) can be reduced to a single numerical integration when F_a can be represented as a sum of Gaussian functions.

To use the method of Dungey and Hui [1979], we have written

$$F_a(l) = \left\{\left[\frac{\rho_0 g}{2\pi\omega_{k_1}}\right]\left[\frac{\eta}{k_1^4}\right]\right\} \exp -\left[\frac{[l - k_1 - (\tfrac{\alpha}{2})]^2}{\beta^2 k_1^2}\right]$$

$$\cdot \exp[-0.74(l_0/k_1)^2] \qquad (57)$$

Here α and β are considered to be small parameters and (57) represents a "cut" out of the spectrum (4) for l near k_1.

Equation (56) was evaluated for a range of values of α and β. The results are illustrated in Figure 5 for the case $\alpha = 0$, $\beta = 1/3$. The quantity shown is

$$T_d = [\nu(k)]^{-1} \qquad (58)$$

We estimate that the "narrow band" approximation of Dungey and Hui is valid for $0 < \beta < 0.5$. Over this range the decay time (58) scales approximately as β^{-2}. The variation of (58) with α is less than a factor of 2 for $\alpha/k_0 \le 1$. We are thus led to conclude from the results given in Figure 4 and 5 that the decay rate is dominated by contributions from long ambient waves.

5. Evolution of the Pattern Spectrum

In this section we first study the evolution of the pattern spectrum (7) due to the three-wave mechanism. Using (24) we write

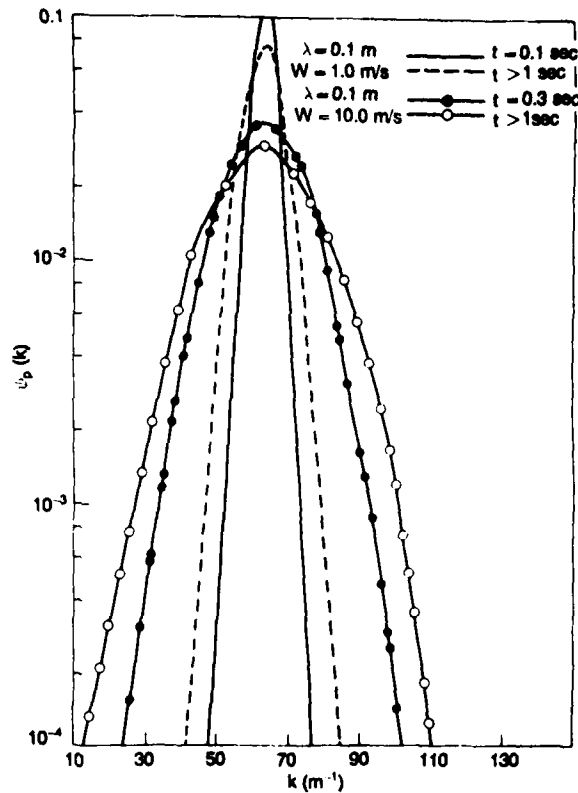$$Z_p(x,t) = B_p(0) \exp[i(p \cdot x - \omega_p t - p \cdot R)] \qquad (59)$$

where

Here

$$K = k - p$$

$$c_1 = \cos^2 \phi a_1 + \sin^2 \phi a_2 - 2\sin \phi \cos \phi b$$

$$c_2 = \sin^2 \phi a_1 + \cos^2 \phi a_2 + 2\sin \phi \cos \phi b$$

$$\tan 2\phi = 2b/(a_2 - a_1), \qquad -\frac{\pi}{4} < \phi < \frac{\pi}{4}$$

$$a_1 = \int d^2 l \Psi_a (l)(i \cdot \hat{l})^2 (p \cdot l)^2 [1 - \cos (\omega_l t)]$$

$$a_2 = \int d^2 l \Psi_a (l)(j \cdot \hat{l})^2 (p \cdot l)^2 [1 - \cos (\omega_l t)]$$

$$b = \int d^2 l \Psi_a (l)(i \cdot \hat{l})(j \cdot \hat{l})(p \cdot l)^2 [1 - \cos (\omega_l t)] \quad (63)$$

It is straightforward to evaluate these expressions for the spectral form (51). This is tedious and seems overly elaborate for our purpose. We therefore consider only the "peaked" spectrum corresponding to

$$G (\theta) = \delta (\theta) \quad (64)$$

and the isotropic spectrum (45).

For the peaked spectrum (64) we may simplify (62) to the form

$$\Psi_P (k, t) = \frac{|B_p (0)|^2}{4(\pi a_1)^{1/2}} \delta (k_y - p_y)$$

$$\cdot \exp [-K_x^2/ (4a_1)] \quad (65)$$

In this case

$$a_1 = p_x^2 h \quad (66)$$

Fig. 6. The pattern spectral function (65) integrated over k_y, for the case that $\lambda = 0.1$ m and $p_y = 0$. Wind speeds and times are indicated.

$$p \cdot R = p \cdot \int_0^t U \, dt'$$

$$= \Sigma_l [(p \cdot \hat{l})/l] \left\{ b_l e^{il \cdot x} [\exp (-i\omega_l t) - 1] + c.c. \right\} \quad (60)$$

In (59) we have assumed the initial pattern at $t = 0$ to be a plane wave of wave number p. A more general pattern, representing a superposition of plane waves, can readily be analyzed by the present method.

The wind velocity vector $W = \hat{i} W$ is assumed to be directed parallel to the x-axis. The b_l's are supposed to be constant and to have a Gaussian distribution, with the ambient spectrum described by (4). The expression (6) can be evaluated analytically. It is consistent with the condition (23) to assume that $rl \ll 1$, so we obtain

$$\Gamma_p (r, t) = \frac{1}{2} |Bp (0)|^2 \exp (-ip \cdot r) \exp \left\{ -\int d^2 l \Psi_a (l) \right.$$

$$\cdot (r \cdot \hat{l})^2 (p \cdot l)^2 [1 - \cos (\omega_l t)] \right\} \quad (61)$$

Equation (7) may also be evaluated analytically using the expression (61). The result gives the pattern spectrum as a function of time:

$$\Psi_P (k, t) = |B_p (0)|^2/ [8\pi (c_1 c_2)^{1/2}]$$

$$\cdot \exp \left[-(K_x \cos \phi - K_y \sin \phi)^2/ (4c_1) \right.$$

$$- (K_x \sin \phi + K_y \cos \phi)^2/ (4c_2) \right] \quad (62)$$
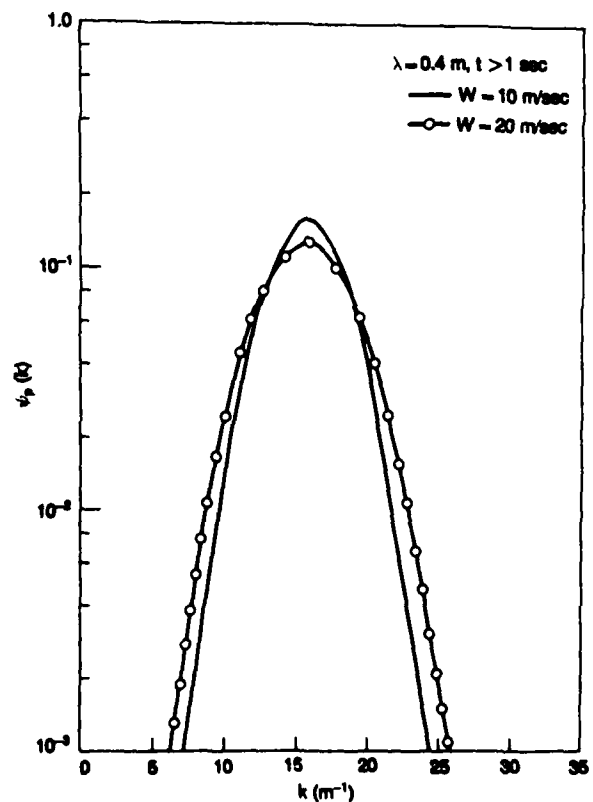

Fig. 7. The pattern spectral function for the conditions of Figure 5 for the case $\lambda = 0.4$ m.
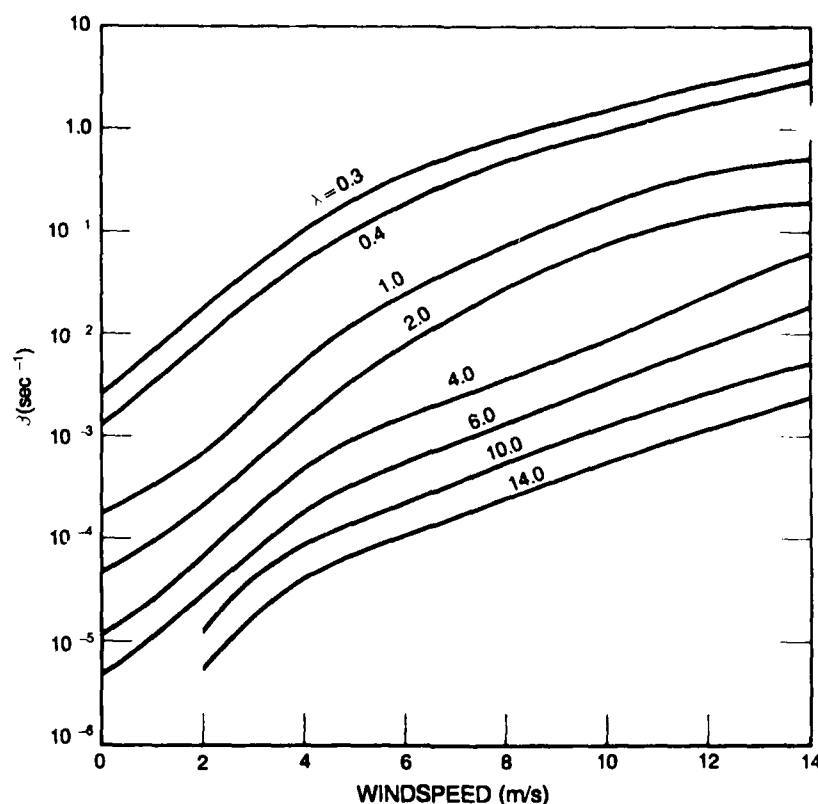
Fig. 8. The decay rate constant β of (74) as a function of wind speed for several wavelengths λ.

where

$$h = \eta \int \frac{dl}{l} \exp [-0.74 \ (l_0/l)^2] \ [1 - \cos (\omega_l t)] \quad (67)$$

For the isotropic spectrum (25) we suffer no loss of generality in setting $p_v = 0$. Then

$$\Psi_p (k, t) = \frac{|B_p (0)|^2}{8\pi (a_1 a_2)^{1/2}} \exp [-(k_x - p_x^2/(4a_1)]$$

$$\cdot \exp [-k_v^2/(4a_2)] \quad (68)$$

Now,

$$a_1 = \frac{3}{8} p_x^2 h \ , \qquad a_2 = \frac{1}{8} p_x^2 h \ , \qquad b = 0 \quad (69)$$

where h is given by (67).

The integral (67) requires a cutoff at large l and depends logarithmically on this cutoff. Thus the scale separation condition (23) is not automatically satisfied by the spectrum (4), but must be imposed. For numerical evaluation we have done this by inserting a factor $[1 + (2l/p_v)^2]^{-1}$ into the integrand in (67). In spite of the arbitrary imposition of a scale separation, our spectral evolution equations appear to be of some interest.

As was the case with the decay, as described by (29), the spectral spreading reaches an asymptotic limit for large t. To illustrate our model, we consider the peaked model (65) for the case that $P_v = 0$. The spectrum is shown in Figure 6 for $\lambda = 2\pi/P = 0.1 \ m$ and $W = 1$ and 10 m/s. In Figure 7 we show the spectrum for $\lambda = 0.4 \ m$ and $W = 10$ and 20 m/s. The spectrum described by (68) is similar but evolves in both horizontal dimensions.

For these examples the asymptotic variance in the wave number is much less than the initial wave number of the wave train. Nevertheless, this spreading can decorrelate the wave phase coherence for a wave train of many wavelengths.

We have seen that four-wave interactions lead to an irreversible redistribution of wave energy in wave number space. This is described by the term S_{nl}' in (11). In the general case this is a very complex phenomena and beyond our present scope to discuss. For the case that the scale separation condition (23) can be assumed, S_{nl}' reduces to a simple diffusion mechanism

$$S_{nl}' = \frac{\partial}{\partial k_i} D_{ij} \frac{\partial F_p}{\partial k_j} \quad (70)$$

Weak interaction theory leads to the expression (see, for example, Appendix A of McComas and Bretherton [1977]

$$D_{ij} = \frac{1}{t} < \int_0^t k \cdot \frac{\partial U}{\partial x_i} dt' \int_0^t k \cdot \frac{\partial U}{\partial x_j} dt'' > \ , \quad t \to \infty \quad (71)$$

Here U is given by (22). For our application with the spectrum (4), the scale separation condition must be imposed by introducing a cutoff for wave numbers greater than some value, say, l_{max}. For this reason, only a brief qualitative discussion of (70) and (71) seems justified. A scalar diffusion coefficient, $D = \frac{1}{2}[D_{11} + D_{22}]$, appears sufficient, then, to characterize the diffusion. For the spectrum (51) we obtain

$$D \cong 3 \cdot 10^{-4} k^2 \omega_c \ , \qquad \omega_c = (g l_{max})^{1/2} \quad (72)$$

The variance Δk in an initial wave of wave number k is estimated at time t as

$$\Delta k = (Dt)^{\frac{1}{2}} = 2 \cdot 10^{-2} k \, (\omega_c t)^{\frac{1}{2}} \qquad (73)$$

If we assume $\omega_c \approx 1 \, s^{-1}$ as reasonable, (73) implies times of the order of 10^3 s for significant pattern distortion. This is not incompatible with the four-wave time scales of Figure 4.

6. SUMMARY AND CONCLUSIONS

We have seen that persistence times for surface gravity waves can vary from fractions of a second to many days for ocean swell [Snodgrass et al., 1966]. Mechanisms studied in this paper that lead to wave pattern decay are viscous damping, air-sea interaction, and three-wave and four-wave interactions.

The three-wave interactions tend to have short time scales but do not lead to wave decay or energy transport across the surface wave spectrum. As is seen in Figures 6 and 7, these interactions lead to only a very limited spreading in wave number. If this fine spectral detail is not important for a specific application, the three-wave process should be omitted in assessing decay rates.

In this case it is convenient to summarize our calculations of surface wave relaxation in the form of single decay constant β (see Hughes [1978] and Phillips [1984] for a related model):

$$S_{nl} + S_v + S_\omega = -\beta F_p \qquad (74)$$

Here we have set

$$\beta = \beta_v + \beta_w + 2\nu \qquad (75)$$

(see (12), (15), and (39)), neglecting the three-wave contribution. The assumption of additivity made here appears reasonable, since for any given set of wavelengths and wind speeds, one of the three terms in (75) tends to dominate.

The relaxation rate β is shown in Figure 8 as a function of wind speed w for several wavelengths λ. At the two longest wavelengths shown the air-sea interaction gives the most significant contribution to θ. (The four-wave contribution in Figure 8 is negligible unless $\lambda \ll 2\pi w^2/g$).

REFERENCES

Dungey, J. C., and W. W. Hui, Nonlinear energy transfer in a narrow gravity-wave spectrum, Proc. R. Soc. London Ser, A, 368, 239-265, 1979.

Garratt, J. R., Review of drag coefficients over oceans and continents, Mon. Weather Rev., 105, 915-922, 1977.

Hasselmann, K., Nonlinear interactions treated by the methods of theoretical physics, Proc. R. Soc. London Ser., A, 299, 77-100, 1967.

Hughes, B. A., The effect of internal waves on surface wind waves, 2, Theoretical analysis, J. Geophys. Res., 83, 455-465, 1978.

McComas, C. H., and F. P. Bretherton, Resonant interaction of oceanic internal waves, J. Geophys. Res, 82, 1397-1412, 1977.

Mitsuyasu, H. and T. Honda, Wind induced growth of water waves, J. Fluid Mech., 123, 425-442, 1982.

Phillips, O. M., The Dynamics of the Upper Ocean, 2nd ed., Chap. 3, Cambridge University Press, New York, 1977

Phillips, O. M., On the response of short ocean wave components at a fixed wavenumber to ocean current variations, J. Phys. Oceanogr., 14, 1425-1433, 1984.

Pierson, W. J., and L. Moskowitz, A proposed spectral form for fully developed wind seas based on the similarity theory of S. A. Kitaigorodskii, J. Geophys. Res., 69, 5181-5190, 1964.

Plant, W. J., A relationship between wind stress and wave slope, J. Geophys. Res., 87, 1961-1967, 1982.

Snodgrass, F. E., G. W. Groves, K. F. Hasselmann, G. R. Miller, W. H. Munk, and W. H. Powers, Propagation of ocean swell across the Pacific, Philos. Trans. R. Soc. London Ser., A, 259, 431-497, 1966.

Tyler, G. L., C. C. Teague, R. H. Stewart, A. M. Peterson, W. H. Munk, and J. W. Joy, Wave directional spectra from synthetic aperture observations of radio scatter, Deep-Sea Res., 21, 988-1016, 1974.

Van Kampen, N. G., Stochastic differential equations, Physica, 74, 215-238. 1974.

Vesecky, J. F., and R. H. Stewart, The observation of ocean surface phenomena using imagery from the Seasat synthetic aperture radar: An assessment, J. Geophys. Res., 87, 3397-3413, 1982.

Watson, K. M., and R. J. West, A transport-equation description of nonlinear ocean surface wave interactions, J. Fluid Mech., 70, 815-826, 1975.

Wigner, E. P., On the quantum correction for thermodynamic equilibrium, Phys. Rev., 40, 749-759, 1932.

K. M. Watson, Marine Physical Laboratory, Scripps Institution of Oceanography, University of California, San Diego, CA 92152.

U3.5

ELEMENT-LEVEL REVERBERATION TIME SERIES SYNTHESIS

W.S. Hodgkiss and D. Almagor

Marine Physical Laboratory
Scripps Institution of Oceanography
San Diego, CA   92152

ABSTRACT

An alternative to the point scattering model approach for simulating reverberation will be discussed. Reverberation is synthesized by passing a vector white noise process through a multichannel IIR filter whose time-varying transfer function matches the time-evolving spectral characteristics of the expected auto and cross range-Doppler maps.

I. INTRODUCTION

The ocean's boundaries (surface and bottom) and particulate matter in the ocean volume scatter energy from an active sensor ping back to the transducer. As depicted in Figure 1, one approach to estimating the expected range-Doppler map is to propagate the pulse outward and calculate the expected backscattered return at successive range increments [1]. At each range, the shell representing the ensonified portion of the ocean and its boundaries is split into cells subtending a small azimuth and elevation angle spread. The expected spectrum contributed by each cell is summed across all cells yielding the expected spectrum at that range (i.e. a slice of the range-Doppler map at a given range).

Although the expected range-Doppler map is useful in many instances for active sonar system performance characterization, often the actual reverberation time series is desired. Such reverberation time series are generated by REVGEN (REVerberation GENerator) [2]. REVGEN is a direct implementation of the point-scattering model of oceanic reverberation where the returns from a large number of discrete scatterers distributed randomly throughout the volume and on the boundaries are summed coherently to obtain the (complex basebanded) reverberation time series at the output of each hydrophone element. The backscattering coefficient (strength) for each reverberation type (surface, volume, and bottom) is specified along with random scatterer motion, platform trajectory, absorption, and beam pattern.

Although very good, REVGEN also is very computationally intensive and is not suitable for generating large numbers of pings for a given environment. An alternative to the point scattering approach taken in REVGEN is to synthesize reverberation by passing a vector white noise process through a multichannel IIR filter whose time-varying transfer function matches the time-evolving spectral characteristics of the expected range-Doppler map [3-4]. Of specific interest is the generation array element-level reverberation time series which have appropriate element-to-element cross-correlations.

II. MULTICHANNEL REVERBERATION SYNTHESIS

A. Expected Range-Doppler Map Generation (RVMD)

A multibeam extension of the approach discussed in [1] is used to model the environment in an expected value sense. Array elements can be viewed simply as beams with broad spatial response characteristics. A matrix of auto and cross range-Doppler maps is generated.

B. Time-Varying IIR Filter Derivation

The fundamental goal is to pass a vector white noise process through a multichannel IIR filter as shown in Figure 2 yielding a vector time series at the output which approximate the time-evolving (auto and cross) spectral characteristics of reverberation as it would be seen at the output of the elements of a transducer array. The time-varying coefficients of the multichannel filter can be derived in a number of ways. Here, slices at a given range from the set of expected (auto and cross) range-Doppler maps will be viewed as the multichannel power spectrum of a stationary vector random process. After inverse Fourier transforming the multichannel power spectrum, to yield the corresponding multichannel correlation function, the Levinson-Durbin algorithm is used to derive the whitening or inverse filter (one-step forward prediction error filter) shown in Figure 3 which provides the IIR filter coefficients [5-6]. Each increment in range is processed in exactly the same way yielding successive sets of IIR filter coefficients.

C. Element-Level Reverberation Time Series Synthesis (REVSIM)

The sets of IIR filter coefficients (one set per range increment) then are used as the coefficients of a time-varying, multichannel IIR filter. A vector white noise process is passed through the filter yielding a vector output time series which simulates the outputs of a real transducer array in an ocean whose environmental parameters are those input to RVMD.

III. SURFACE SHIP ACTIVE SONAR SIMULATION

As an example of this approach to reverberation time series synthesis, consider the following active sonar system. An array of hydrophones is mounted on the bow of a surface ship and pointed 45° downward as shown in Figure 4. The ship is traveling at 10 knots (5.1 m/s) and the ocean depth is 300 m. The sonar operates at $f_c = 75$ kHz and transmits a 100 ms, rectangularly windowed pulse.

The 9x9 rectangular array has a sensor spacing of $\lambda/2$ at the operating frequency of the sonar. A conventional beam is formed by simply summing the outputs of all elements. A vertical slice through the corresponding beam pattern normal to the array plane is shown in Figure 5. A difference beam is formed by subtracting two row sums. The corresponding beam pattern similar to Figure 5 is shown in Figure 7. A transmit beam is assumed which uniformly illuminates the medium over a sector ±30° in both bearing and elevation normal to the array plane.

The backscattered return to this sonar was simulated using REVGEN and the multichannel IIR filter approach discussed above. In this case, an isovelocity sound speed profile was assumed (c = 1500 m/s) along with the following parameters: (a) volume backscattering coefficient, $s_v = -70$ dB, (b) bottom backscattering coefficient, $s_b = -20$ dB, and (c) attenuation due to absorption, $\alpha = 23$ dB/km.

REVGEN range-Doppler maps of the returning reverberation for the conventional (sum) and difference beams as

2701

well as the the corresponding cross-power range-Doppler map are
shown in Figure 6 ($f_s = 2$ kHz). These were generated by taking
successive 128-point FFT's (Kaiser-Bessel window, $\alpha=2.5$)
overlapped by 87.5% (16 points). In addition, the range-Doppler
maps have been left-shifted to compensate for ship velocity (a 5.1
m/s velocity imparts a 515 Hz Doppler shift to stationary targets
in line with the direction of ship motion at $f_c = 75$ kHz). In
Figure 6a (sum beam), volume reverberation dominates early in
the range-Doppler map. Later (at approximately 0.4 s in range),
the onset of bottom reverberation arriving through the lower edge
of the main lobe is seen. Bottom reverberation at approximately
0.6 s in range corresponds to backscatter arriving through the
center of the main lobe. In Figure 6b (difference beam), volume
reverberation also dominates early in the range-Doppler map.
The onset of bottom reverberation is more pronounced here than
in Figure 6a due to the response characteristics of the difference
beam pattern.

Figure 1.   Reverberation model geometry.

The multichannel IIR filter results will be presented
following the three steps discussed in Section II. The RVMD
parameters were identical to those used in the REVGEN
simulation with the exception that circularly symmetric beams
were implemented (Figures 9 and 11 show the bottom projection
of these beam patterns where the symbols represent 6 dB
contours). First, Figure 8 shows the RVMD auto and cross
range-Doppler maps (the plots are offset by 33 dB from the actual
RVMD results). Second, the corresponding time-evolving inverse
linear predictor spectral estimates are shown in Figure 10. They
indicate how closely the derived IIR filter matches the expected
auto and cross range-Doppler maps. Lastly, Figure 12 shows the
results of passing a vector white noise process through the
multichannel IIR filter and processing the output as done with the
REVGEN time series. As is easily seen, the results are quite
similar to the REVGEN range-Doppler maps in Figure 6.

Figure 2.   Autoregressive process generation model.

IV. SUMMARY

The point scattering model approach used by REVGEN is
very computationally intensive and not suitable for generating
large numbers of pings for a given environment. Large numbers
of pings are required by Monte Carlo simulations of
detection/estimation structures for the purpose of performance
evaluation. Characterizing active sonar reverberation as a time-
evolving, multichannel, autoregressive process facilitates the
derivation of a multichannel, time-varying, IIR filter. Large
numbers of pings for a given environment can be generated easily
by simply passing different sample functions of a vector white
process through the filter.

Figure 3.   Whitening or inverse filter (one-step forward prediction
error filter).

References

[1]   W.S. Hodgkiss, "An Oceanic Reverberation Model," IEEE J.
Oceanic Engr., OE-9(2): 63-72 (1984).

[2]   R.P. Goddard, "REVGEN-4 High-Fidelity Simulation of
Sonar Pulses," APL-UW-8505, Applied Physics Laboratory,
University of Washington, Seattle, WA (1986).

[3]   S. Chamberlain and J. Galli, "A model for numerical
simulation of nonstationary sonar reverberation using linear
spectral prediction," IEEE J. Oceanic Engr., OE-8: 21-36 (1983).

[4]   J. Luby and D. Lytle, "Autoregressive Modeling of
Nonstationary Multibeam Sonar Reverberation," IEEE J.
Oceanic Engr., OE-12: 116-129 (1987).

[5]   P. Whittle, "On the fitting of multivariate autoregressions,
and the approximate canonical factorization of a spectral
matrix," Biometrika 50: 129-134 (1963).

[6]   R.A. Wiggins and E.A. Robinson, "Recursive solution to the
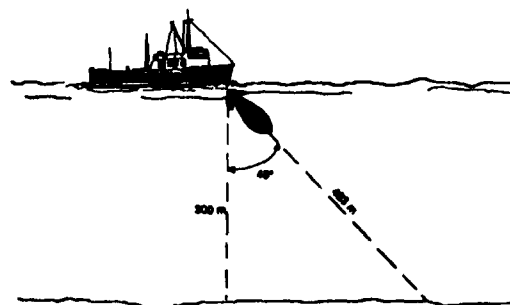multichannel filtering problem," J. Geophys. Res. 70: 1885-1891
(1965).

Figure 4.   Surface ship sonar example.
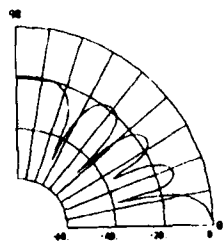
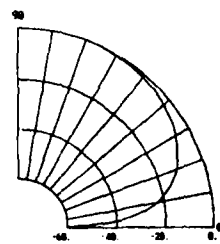Figure 5.   Sum beam pattern.

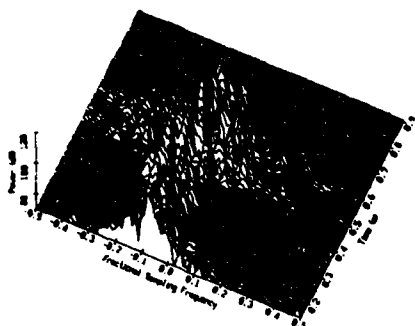Figure 7.   Difference beam pattern.

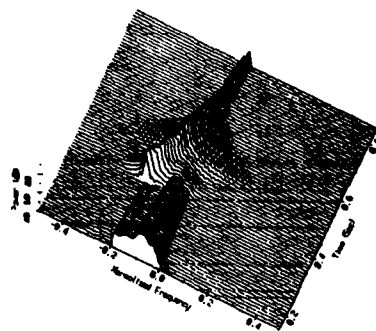Figure 6a.   REVGEN: Sum beam power spectrum vs time.

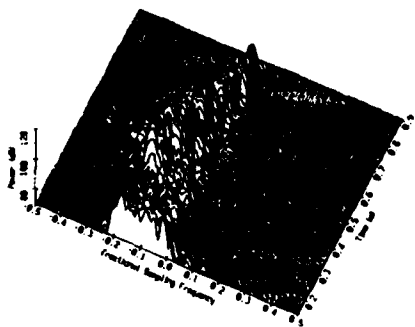Figure 8a.   RVMD: Sum beam power spectrum vs time.

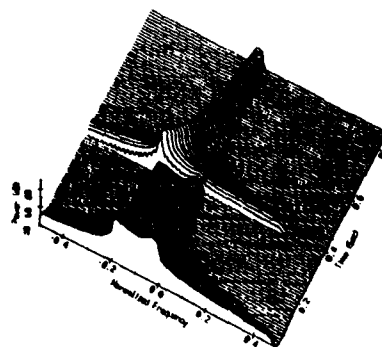Figure 6b.   REVGEN: Difference beam power spectrum vs time.

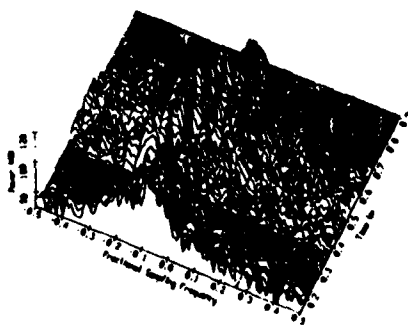Figure 8b.   RVMD: Difference beam power spectrum vs time.

Figure 6c.   REVGEN: Cross-beam power spectrum vs time.
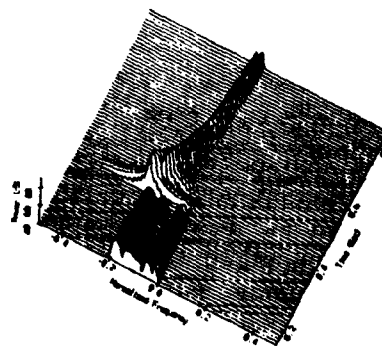

Figure 8c.   RVMD: Cross-beam power spectrum vs time.
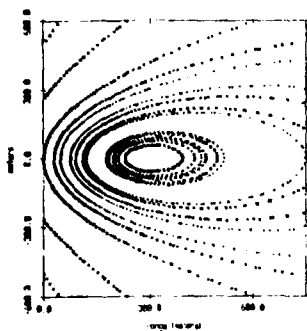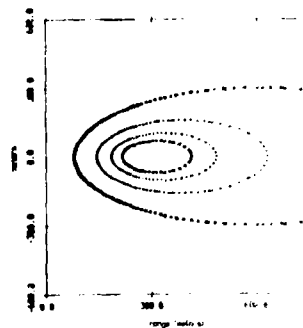
Figure 9.   Sum beam bottom projection.

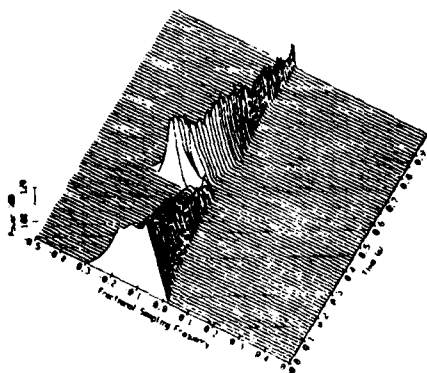Figure 11.   Difference beam bottom projection.

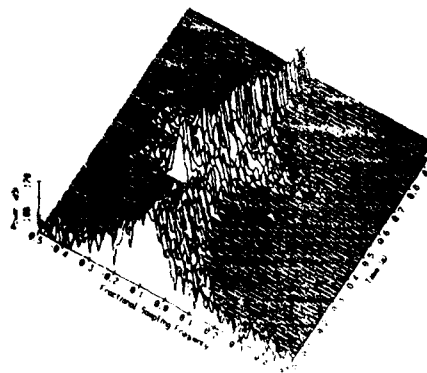Figure 10a.   Inverse linear predictor: Sum beam power spectrum vs time.

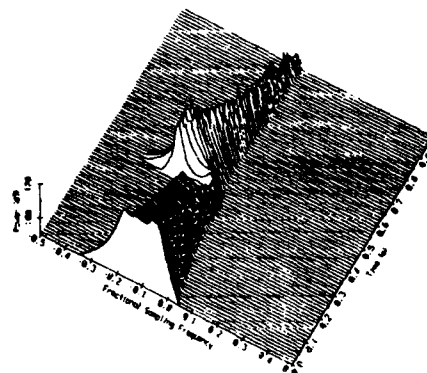Figure 12a   REVSIM: Sum beam power spectrum vs time.

Figure 10b.   Inverse linear predictor: Difference beam power spectrum ys time.
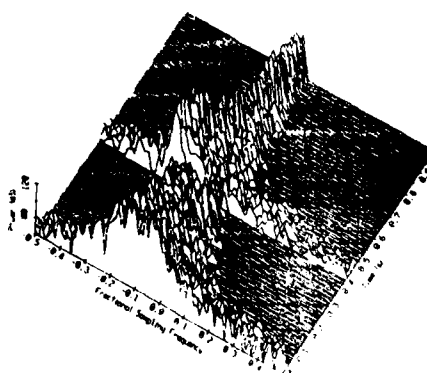

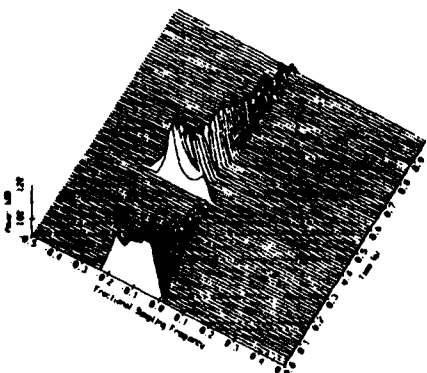Figure 12b.   REVSIM: Difference beam power spectrum vs time.

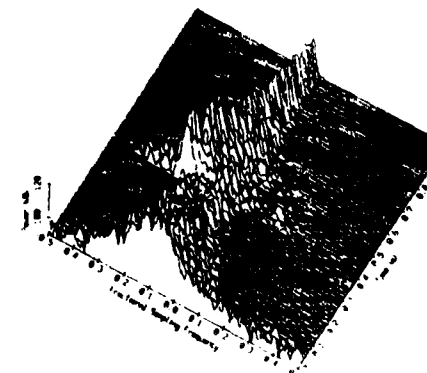Figure 10c.   Inverse linear predictor: Cross-beam power spectrum vs time.

Figure 12c.   REVSIM: Cross-beam power spectrum vs time.

APPENDIX B

BIBLIOGRAPHY

OFFICE OF NAVAL RESEARCH
CONTRACT N00014-79-C-0472

University of California, San Diego
Marine Physical Laboratory
Scripps Institution of Oceanography
San Diego, CA 92152

Journals

1. J. A. Smith and R. Pinkel, "Observations of waves and Langmuir circulation with Doppler sonars," in *Dynamics of the Oceanic Surface Mixed Layer*, edited by P. Muller and D. Henderson (Honolulu, Hawaii, 1977). Proceedings of the 'Aha Huliko'a, Hawaii Winter Workshop on Internal Waves and Small Scale Turbulence.

2. R. Pinkel, "Acoustic Doppler techniques," in *Air-Sea Interaction*, edited by F. Dobson, L. Hasse, R. Davis (Plenum Publ. Corp., 1980), pp. 171-199.

3. P. Lonsdale, "Manganese-nodule bedforms and thermohaline density flows in a deep-sea valley on Carnegie Ridge, Panama Basin," J. Sediment. Petrol. **50**, 1033-1048 (1980).

4. P. Lonsdale, V. Burns, and M. Fisk, "Nodules of hydrothermal birnessite in the caldera of a young seamount," J. Geol. **88**, 611-618 (1980).

5. R. Pinkel, "On the use of Doppler sonar for internal wave measurements," Deep-Sea Res. **28A**, 269-289 (1981).

6. R. Pinkel, "Observations of the near-surface internal wavefield," J. Phys. Oceanogr. **11**, 1248-1257 (1981).

7. W. C. Cummings and P. O. Thompson, "Sounds from Byrd and Finback whales in the Gulf of California," Fishery Bulletin (1981). Final Report to Contract N00014-79-C-0472 (Low Frequency Bioacoustics).

8. P. Lonsdale, R. Batiza, and T. Simkin, "Metallogenesis at seamounts on the East Pacific Rise," Mar. Technol. Soc. J. **16**, 54-61 (1982).

9. F. H. Fisher, J. M. Gieskes, and C. C. Hsu, "$MgSO_4$ ion association in seawater," Mar. Chem. **11**, 279-283 (1982).

10. F. H. Fisher, J. M. Gieskes, and C. C. Hsu, "Analysis of Johnson's response to our paper 'MgSo$_4$ ion association in seawater'," Mar. Chem. **11**, 287-288 (1982).

11. C. C. Hsu and F. H. Fisher, "Effect of pressure on sound absorption in synthetic seawater and in aqueous solutions of MgSO$_4$," J. Acoust. Soc. Am. **74**, 564-569 (1983).

12. K. M. Watson, "Relaxation processes for internal waves in mesoscale flow," Proc. Nat. Acad. Sci. USA **80**, 1144-1146 (1983).

13. P. B. Rhines and W. R. Young, "How rapidly is a passive scalar mixed within closed streamlines?," J. Fluid Mech. **133**, 133-145 (1983).

14. K. M. Watson, "A model for nonlinear wave interactions," Pure Appl. Geophys. **121**, 401-415 (1983).

15. W. R. Young, "Topographic rectification of tidal currents," J. Phys. Oceanogr. **13**, 716-721 (1983).

16. G. R. Ierley and W. R. Young, "Can the western boundary layer affect the potential vorticity distribution in the Sverdrup interior of a wind gyre," J. Phys. Oceanogr. **13**, 1753-1763 (1983).

17. R. Pinkel, "Doppler sonar observations of internal waves: the wavenumber frequency spectrum," J. Phys. Oceanogr. **14**, 1249-1270 (1984).

18. H. D. I. Abarbanel, D. D. Holm, J. E. Mardsen, and T. Ratiu, "Richardson number criterion for the nonlinear stability of stratified flow," Phys. Rev. Lett. **52**, 2352-2355 (1984).

19. H. D. I. Abarbanel, "Stability of inviscid stratified flows under nonlinear perturbations," Proc. of the Hawiian Winter Aha Huliko'a Workshop, 263-276 (1984).

20. W. S. Hodgkiss and R. Brienzo, "Coherent recombination of sediment borne and water path acoustic signals," IEEE Intl. Conf. on Acoust., Speech, Signal Process. **2**, 24.5.1 - 24.5.2 (1984).

21. W. K. Dewar, P. B. Rhines, and W. R. Young, "The nonlinear spin-up of a stratified ocean," Geophys. & Astrophy. Fluid Dyn. **30**, 169-197 (1984).

22. W. S. Hodgkiss and D. Alexandrou, "Applications of adaptive array processing," in *Appears in: Adaptive Methods in Underwater Acoustics, Heinz G. Urban, Ed. (Boston: D. Reidel, 1985), pp. 447-460* (NATO Advanced Study Institute on Adaptive Methods in, Luneburg, Germany, 1984).

23. R. Batiza, D. J. Fornari, D. A. Vanco, and P. F. Lonsdale, "Craters, calderas and hyoclastites on young Pacific seamounts," J. Geophys. Res. **89**, 8371-8390 (1984).

24. K. M. Watson, "Interactions of internal waves of near inertial frequencies," Presented at the Aha Huliko's Winter Workshop, Honolulu, Hawaii (1984).

25. R. Pinkel, "The wavenumber frequency spectrum of the internal wavefield," 2nd Annual Aha Huliko's Hawaiian Winter Workshop on Internal Waves and Small Scale Turbulence, 113-127 (1984).

26. W. R. Young, "The role of boundary layers in the gyre-scale ocean mixing," J. Phys. Oceanogr. 14, 478-483 (1984).

27. K. M. Watson, "Interaction between internal wave and mesoscale flow," J. Phys. Oceanogr. 15, 1296-1311 (1985).

28. H. D. I. Abarbanel, "Hamiltonian description of nearly geostropic flow," Geophys. Astrophys. Fluid Dyn. 33, 145-171 (1985).

29. C. de Moustier, "Inference of manganese nodule coverage from Sea Beam acoustic backscattering data," Geophysics 50, 989-1001 (1985).

30. W. R. Young, "Some interactions between small numbers of baroclinic, geostrophic vortices," Geophys. Astrophys. Fluid Dyn. 33, 35-61 (1985).

31. R. Pinkel, "A wavenumber-frequency spectrum of upper ocean shear," J. Phys. Oceanogr. 15, 1453-1469 (1985).

32. C. de Moustier, "Beyond bathymetry: mapping acoustic backscattering from the deep sea floor with Sea Beam," J. Acoust. Soc. Am. 79, 316-331 (1986).

33. P. F. Lonsdale, "Comments: "East Pacific Rise from Siqueiros to Orozco fracture zones: Along-strike continuity of axial Neovolcanic zone and structure and evolution of overlapping spreading centers" by K. Macdonald, J. Sempere and P. J. Fox.," J. Geophys. Res. 91, 10,493-10-499 (1986).

34. J. A. Smith, "Short surface waves with growth and dissipation," J. Geophys. Res. 91 (C2), 2616-2632 (1986).

35. J. F. Price, R. A. Weller, and R. Pinkel, "Diurnal cycling: Observations and models of the upper ocean response to diurnal heating, cooling, and wind mixing," J. Geophys. Res. 91, 8411-8427 (1986).

36. K. M. Watson, "Persistence of a pattern of surface gravity waves," J. Geophys. Res. 91 (C2), 2607-2615 (1986).

37. C. de Moustier and M. Kleinrock, "Bathymetric artifacts in Sea Beam data: how to recognize them, what causes them," J. Geophys. Res. 91, 3407-3424 (1986).

38. H. D. I. Abarbanel, "Nonlinear stability of inviscid fluid equilibria," Fourth Symposium of Energy Engineering Sciences (1986).

39. H.D.I. Abarbanel and W. R. Young, "General Circulation of the Ocean," Proc. of the First Scripps Institution of Oceanography Advanced Study Program in Physical Oceanography (1986).

40. C. de Moustier, "Approaches to acoustic backscattering measurements from the deep seafloor," Trans. Am. Soc. Mech. Eng. Ocean Engineering Symposium OED-11, 137-143 (1986). Invited paper. Also appears with minor revision in J. Energy Resources Tech., Vol. 110, pp. 77-84 (1988). (See A.19).

41. H.D.I. Abarbanel, S. Buchsbaum, and J. Keeler, "A low dimensional interated map with an apparent continuum of attractors," in *Perspectives in Nonlinear Dynamics*, edited by M. F. Shlesinger, R. Cawley, A. W. Saenz, and W. Zachary (World Scientific Publishing Co. Pte Ltd, 1986), pp. 167-208.

42. Amatzia Genin, Paul K. Dayton, Peter F. Lonsdale, and Fred N. Spiess, "Corals on seamount peaks provide evidence of current acceleration over deep-sea topography," Nature **322**, 59-61 (1986).

43. H.D.I. Abarbanel, "Chaos across disciplines," Proc. Navy Dynamics Institute Conf. on Perspectives on Nonlinear Dynamics (1986).

44. R. Pinkel, S. Beck, and J. Morison, "Doppler acoustic velocity profiling in the Arctic," Proceedings of the IEEE Third Working Conference on Current Measurements **86CH2305-1**, 163-168 (1986).

45. E. C. Shang and V. C. Anderson, "Surface generated noise under low wind speed at kilohertz frequencies," J. Acoust. Soc. Am. **79**, 964-971 (1986).

46. C. de Moustier and F. V. Pavlicek, "On-line Sea Beam acoustic imaging," Pro. MTS/IEEE Oceans '87, 1197-1201 (1987).

47. Jerome Smith, "On surface waves crossing a step with horizontal shear," J. Fluid Mech. **175**, 395-412 (1987).

48. H.D.I. Abarbanel and S. Rouhi, "Phase space density representation of inviscid fluid dynamics," Phys. of Fluids **30**, 952 (1987).

49. Jerome Smith, Robert Pinkel, and Robert Weller, "Velocity structure in the mixed layer during MILDEX," J. Phys. Oceanogr. **17**, 425-439 (1987).

50. C. de Moustier and V. Pavlicek, "A fully transportable Seabeam complex acoustic data acquisition system," Proceedings of the Offshore Technology Conference, 269-274 (1987).

51. Henry D.I. Abarbanel and Darryl D. Holm, "Nonlinear stability analysis of inviscid flows in three dimensions: Incompressible fluids and barotropic fluids fluids," Physics of Fluids **30**, 3369 (1987).

52. J. A. Smith and R. Pinkel, "Open ocean surface wave measurement using Doppler sonar," J. Geophys. Res. **92**, 12,967-12,973 (1987).

53. J. Gee, L. Tauxe, J. A. Hildebrand, H. Staudigel, and P. Lonsdale, "Non-uniform magnetization of Jasper Seamount," J. Geophys. Res. **93**, 12,159-12,175 (1988).

54. W. S. Hodgkiss and D. Almagor, "Element-level reverberation time series synthesis," IEEE Int'l Conf. Acoustics, Speech & Signal Processing **5**, 2701-2704 (1988).

55. W. S. Hodgkiss and D. Almagor, "A pole-zero complex adaptive joint process least-squares lattice," IEEE Conf. Acoust., Speech, and Sign. Proc. **5**, 2789-2792 (1988).

56. P. F. Lonsdale, "Structural pattern of the Galapagos Microplate and evolution of the Galapagos Triple Junctions," J. Geophys. Res. **93** (1988).

57. P. Lonsdale, "Geography and history of the Louisville hot spot chain in the Southeast Pacific," J. Geophys. Res. **93**, 3078-3104 (1988).

58. R. Pinkel, A. Plueddemann, and R. Williams, "Internal wave observations from FLIP in MILDEX," J. Phys. Oceanogr. **17**, 1737-1757 (1988).

59. D. Alexandrou and C. de Moustier, "Adaptive noise cancelling applied to Sea Beam sidelobe interference rejection," IEEE J. Ocean Eng. **13**, 70-76 (1988).

60. J. A. Hildebrand, "Technology of geophysical exploration on the ocean bottom," in *Gorda Ridge: A Frontier Area in the United States Exclusive Economic Zone*, edited by G. R. McMurray (Springer-Verlag, New York, 1989).

61. J. F. Allen, R. Batiza, and P. Lonsdale, "Petrology of lavas from seamounts flanking the East Pacific Rise, 21°N.," J. Geophys. Res. (in prep).

62. J. Hawkins, R. Batiza, and P. Lonsdale, "Petrology of the Louisville seamount chain," in *Seamounts* (American Geophysical Union, in prep).

63. Roscoe Collette and Peter Lonsdale, "Geologic interpretation of SEASAT altimetry across South Pacific transform faults and their fracture zones," J. Geol. Res. (in prep).

64. W. R. Young, "On the interaction between numbers of baroclinic, geostrophic vortices," Geophys. Astrophys. Fluid Dyn. (in prep).

65. H.D.I. Abarbanel, S. Buchsbaum, J. Keeler, and Y-M Yang, "Transient dissipative behavior in Hamiltonian dynamics," Physica D. (in prep).

66. P. Lonsdale and R. Batiza, "Pattern and geomorphology of seamounts near the Pacific-Rivera spreading center," in *Seamounts* (American Geophysical Union, 851510).

67. Mark R. Legg, Bruce P. Luyendyk, Jacqueline Mammerickx, Christian de Moustier, and Robert C. Tyce, "Sea Beam survey of an active strike-slip fault," J. Geophys. Res. (in press).

68. A. J. Plueddemann and R. Pinkel, "Biasing of the covariance-based spectral mean estimator in the presence of correlated noise," J. Atmos. Oceanic Technol. (submitted - revision).

Technical and Miscellaneous Reports

1. "Seamount seminar," Seamount Seminar held at the Marine Physical Laboratory, 10-11 January 1985, Marine Physical Laboratory, Scripps Institution of Oceanography, San Diego, CA (1985).

Ph.D Dissertations

1. R. G. Williams, "The internal tide off the California coast," Ph.D. Thesis, University of California, San Diego, San Diego, CA (1985).

2. W. S. Hodgkiss and D. Almagor, "Element-level reverberation time series synthesis," IEEE Int'l Conf. Acoustics, Speech & Signal Processing **5**, 2701-2704 (1988).

SIO References Series

1. C. C. Hsu, "Differential sound absorption technique and effect of ion-pairing and pressure on sound absorption in seawater and aqueous mixtures of magnesium sulfate and sodium chloride," SIO Reference 81-34, (1981).

2. C. Neuberger, C. C. Hsu, and F. H. Fisher, "Effect of ionic strength and ion pairing on sound absorption in aqueous solutions of $MgSO_4$ and NaCl," SIO Reference 82-9, (1982).

3. C. de Moustier, "Deep seafloor acoustic backscattering measurements using Sea Beam," SIO Reference 85-33, Scripps Institution of Oceanography, San Diego, CA, San Diego, CA, 143 pgs. (1985). Ph.D. Dissertation.

4. R. G. Williams, "The internal tide off the California coast," SIO Reference 86-1, Scripps Institution of Oceanography, San Diego, CA, 169 pgs. (1986).

5. A. J. Plueddemann, "Observations of the upper ocean using a multi-beam Doppler sonar," SIO Reference 87-15, Scripps Institution of Oceanography, San Diego, CA (1987).

6. Barbara J. Sotirin, "Large aperture acoustic array," SIO Reference 89-10, Scripps Institution of Oceanography, San Diego, CA (1989).

Technical Memorandums

1. W. S. Hodgkiss (Editor), "VLF Workshop: 24-25 January 1985," MPL TM-376, Marine Physical Laboratory, Scripps Institution of Oceanography, San Diego, CA (1985). UNCLASSIFIED.

2. W. S. Hodgkiss (Editor), "VLF Workshop: 24-25 January 1985 (U)," MPL TM-377, Marine Physical Laboratory, Scripps Institution of Oceanography, San Diego, CA (1985). (SECRET).

3. C. B. Bishop and F. N. Spiess, "Seamount seminar (U)," MPL TM-377, Marine Physical Laboratory, Scripps Institution of Oceanography, San Diego, CA (1985). SECRET.

4. C. de Moustier and V. Pavlicek, "A fully transportable Sea Beam complex acoustic data acquisition system," MPL TM-390, Marine Physical Laboratory, Scripps Institution of Oceanography, San Diego, CA (1987).

5. C. de Moustier, "Sea Beam calibration," MPL TM-370, Marine Physical Laboratory, Scripps Institution of Oceanography, San Diego, CA (in prep).

Patents

1. C. de Moustier, *Acoustic imaging with multi narrowbeam sonar U.S. Patent Pending* (Marine Physical Laboratory, Scripps Instituion of Oceanography, San Diego, Ca, submitted).

Abstracts

1. C. C. Hsu and F. H. Fisher, "Differential sound absorption technique for ion-pairing studies in $MgSO_4$-NaCl solutions," J. Acoust. Soc. Am. **68**, S107 (1980).

2. C. C. Hsu and F. H. Fisher, "Sound absorption in seawater at pressures up to 307 atmospheres," J. Acoust. Soc. Am. **69**, S45 (1981).

3. C. C. Hsu and F. H. Fisher, "Sound absorption in a 0.02 M $MgSo_4$ solutions and in a 0.02 M $MgSO_4$-0.6 NaCl mixture at 25°C and pressures up to 307 atm," J. Acoust. Soc. Am. **70**, S90 (1981).

4. C. C. Hsu and F. H. Fisher, "Sound absorption in sodium sulfate (1 atm) and sodium chloride (1-307 atm) solutions from 30 to 300 kHz," J. Acoust. Soc. Am. **69**, S45 (1981).

5. *C. C. Hsu and F. H. Fisher, "Observation of Q of 1 million in a water-filled 100-liter titanium spherical resonator at 25 kHz,"* J. Acoust. Soc. Am. **69**, S44 (1981).

6. C. de Moustier and R. C. Tyce, "Sea floor acoustic backscatter measurements using Sea Beam," EOS, Trans. Am. Geophys. Union **63**, 1107 (1982).

7. C. de Moustier, "Seafloor acoustic backscatter measurements using Sea Beam II," J. Acoust. Soc. Am. **74**, S44 (1983).

8. C. de Moustier, "Beyond bathymetry: Sea Beam can also contour variations in sea floor reflectivity," AGU, Ocean Sciences Meeting **64**, 1031 (1983).

9. A. J. Plueddemann, "Measurement of oceanic Reynolds stresses during MILDEX using a multi-beam Doppler sonar," EOS, Am. Geophys. Un. **66**, 1281 (1985).

10. J. Smith, R. Pinkel, and R. Weller, "Observations of small scale structure in the surface layer," EOS, Am. Geophys. Un. **66**, 1281 (1985). Presentation given at Ocean Science Meeting, New Orleans, 1986 January.

11. R. Pinkel, A. J. Plueddemann, and R. G. Williams, "Internal wave observations from FLIP in MILDEX," EOS, Am. Geophys. Un. **66**, 1281 (1985).

12. D. Alexandrou and C. de Moustier, "Angular dependence of acoustic backscattering of a Mn nodule field," J. Acoust. Soc. Amer. **80**, S99 (1986).

13. J. Sherman and R. Pinkel, "Investigation of fine scale shear with a coherent Doppler sonar," EOS, Trans. Amer. Geophys. Union **67**, 1060 (1986).

14. R. Pinkel, A. Plueddemann, and R. Williams, "Doppler sonar observation from FLIP in MILDEX," EOS, Trans. Amer. Geophys. Union **67**, 1060 (1986).

15. R. Pinkel and J. A. Smith, "Surface wave detection by Doppler sonar," EOS, Trans. Amer. Geophys. Union **44**, 1060 (1986).

16. S. Beck, R. Pinkel, and J. Morison, "Doppler acoustic velocity profiling in the Arctic," EOS, Trans. Amer. Geophys. Union **67**, 1052 (1986).

17. C. de Moustier and D. Alexandrou, "A 3D look at oceanic sound scattering layers in Sea Beam," EOS, Trans. Amer. Geophys. Union **67**, 1002 (1986).

ONR/MPL GENERAL DISTRIBUTION LIST

Chief of Naval Research
Department of the Navy
Arlington, Virginia 22217-5000
  Code 12, 122(2), 125
  1121, 112, 1122,
  1123, 1125, 1125 OA,
  1125 GG, 23

ONRDET
Stennis Space Center
Bay St. Louis, Mississippi 39529-5004
  Code 125

Commander
Naval Sea Systems Command
Washington, D. C. 20362
  Code 63DB, 933A

Commanding Officer
Naval Ocean Research and
  Development Activity
Stennis Space Center
Bay, St. Louis, Mississippi 39529-5004
  Code 100, 110, 300, 330,
  200, 220, 240, 250, 270,
  320, 360, 350

Commander
U.S. Naval Oceanographic Office
NSTL Station
Bay St. Louis, Mississippi 39522-5004
  Atten: Bill Jobst

Assistant Secretary of the Navy
(Research Engineering & Systems)
Department of the Navy
Washington, D. C. 20350

Defense Advanced Res. Proj. Agency
TTO - Tactical Technology Office
1400 Wilson Boulevard
Arlington, Virginia 22209-2308
  Atten: John N. Entzminger

National Oceanic & Atmospheric
  Administration
Ocean Engineering Office
6001 Executive Boulevard
Rockville, Maryland 20852

Commander
Space and Naval Warfare
  Systems Command
Washington, D. C. 20360-5100
  Code PMW-180T, PMW-180-5

Commander
Naval Ship Res. & Dev. Center
Bethesda, Maryland 20084

Executive Secretary
Naval Studies Board
National Academy of Sciences
2101 Constitution Avenue, N.W.
Washington, D.C. 20418

Director
Strategic Systems Proj. Ofc.
Department of the Navy
Washington, D. C. 20361
  Code NSP-20

Commander
Naval Ocean Systems Center
San Diego, California 92152
  Code 00, 01, 16, 94,
  54, 541, 605, 71, 72, 701

Commander
Submarine Development Group ONE
139 Sylvester Road
San Diego, California 92106

Commanding Officer
Civil Engineering Laboratory
Naval Construction Battalion Center
Port Hueneme, California 93043
  Code L40, L42

Commanding Officer
Naval Underwater Systems Center
Newport, Rhode Island 20844
  Atten: E.L. Sullivan

Officer in Charge
Naval Underwater Systems Center
New London Laboratory
New London, Connecticut 06320
  Code 900, 905, 910, 930, 960

Director of Research
U.S. Naval Research Laboratory
Washington, D. C. 20375
  Code 2620, 2627, 5000, 5100, 5800

Officer in Charge
Naval Surface Warfare Center
10901 New Hampshire Avenue
White Oak Laboratory Detachment
Silver Spring, Maryland 20903-5000
  Attn: E232 Tech Library

Commanding Officer
Naval Coastal Systems Laboratory
Panama City, Florida 32401

STOIAC
Battelle Columbus Laboratories
505 King Avenue
Columbus, Ohio 43201

Commander
Naval Air Systems Command
Washington, D. C. 20361
  Code 370

Commanding Officer
U.S. Naval Air Development Center
Attention: Bruce Steinberg
Warminister, Pennsylvania 18974

Director
Defense Documentation Center
(TIMA), Cameron Station
5010 Duke Street
Alexandria, Virginia 22314

Institute for Defense Analyses
1801 North Beaugard Street
Arlington, Virginia 22311

Superintendent
U.S. Naval Postgraduate School
Monterey, California 93940

Chief Scientist
Navy Underwater Sound Reference Div.
U.S. Naval Research Laboratory
P.O. Box 8337
Orlando, Florida 32806

Supreme Allied Commander
U.S. Atlantic Fleet
ASW Research Center, APO
New York, New York 09019
  Via: ONR 100 M, CNO OP092D1,
  Secretariat of Military,
  Information Control, Committee

Director
Institute of Marine Science
University of Alaska
Fairbanks, Alaska 99701

Director
Applied Physics Laboratory
Johns Hopkins University
Johns Hopkins Road
Laurel, Maryland 20810
  Atten: J. R. Austin

Director
College of Engineering
Department of Ocean Engineering
Florida Atlantic University
Boca Raton, Florida 33431

Director
Marine Research Laboratories
c/o Marine Studies Center
University of Wisconsin
Madison, Wisconsin 53706

Director
Applied Research Laboratory
Pennsylvania State University
P.O. Box 30
State College, Pennsylvania 16802

Director
Applied Physics Laboratory
University of Washington
1013 NE 40th Street
Seattle, Washington 98195

Director
The Univ. of Texas at Austin
Applied Research Laboratory
P.O. Box 8029
Austin, Texas 78712

Director
Lamont-Doherty Geological Observatory
Torrey Cliff
Palisades, New York 10964

Director
Woods Hole Oceanographic Institution
Woods Hole, Massachusetts 02543

Director
Inst. of Ocean Science Engineering
Catholic University of America
Washington, D.C. 20017

National Science Foundation
Ocean Sciences Division
Washington, D. C. 20550

Office of Naval Research
Resident Representative
c/o Univ. of California, San Diego
Mail Code Q023
La Jolla, California 92093

University of California, San Diego
Marine Physical Laboratory
Branch Office
La Jolla, California 92093